FACULTY OF
SCIENCE AND
ENGINEERING

MACQUARIE
University

Glow with the flow: Quantifying blood flow and photoluminescence signal in biological tissue

by

Annemarie Nadort

A thesis submitted to Macquarie University
for the degree of
Doctor of Philosophy
Department of Physics and Astronomy
September 2015

The research in this thesis was kindly funded by:

Academic Medical Center Amsterdam

Macquarie Universtiy

Microscan Inc.

Prins Bernhard Cultuur Fonds

Ocean Optics Inc.

Technology Foundation STW / iMIT programme

Optofab / Australian National Fabrication Facility

The Russian Foundation of Basic Research

Gerbarnd de Jong Fonds

This thesis is being submitted for examination simultaneously to Macquarie University and The University of Amsterdam under a cotutelle co-supervision agreement between the two universities, in fulfilment of the requirements of the degree of Doctor of Philosophy. Otherwise, the thesis has not been previously submitted to any institution.

To comply with the thesis guidelines of both universities, the lay-out of this thesis might deviate from usual. A thesis summary in Dutch is added. This is a thesis by publication, including multi-authored publications of which my contributions are specified on page 183.

I certify that, to the best of my knowledge, all sources used and assistance received in the preparation of this thesis have been acknowledged. This thesis does not contain any material which is defamatory of any person, form or corporation and is not in breach of copyright or breach of other rights which shall give rise to any action at Common Law or under Statute.

For this thesis Ethics Committee approval has been obtained described in protocol number ARA2013/007-2.

Annemarie Nadort

Thesis Abstract

This thesis contributes to the development of optical techniques to assess microcirculation functionality for the diagnosis, monitoring, therapy guidance and understanding of many diseases ranging from the onset of septic shock to the delivery of drugs to tumours. The first part of this thesis aims to develop a non-invasive technique to quantify microcirculatory blood flow velocity based on laser speckle flowmetry. The key results are the experimental and theoretical investigation of the characteristic decorrelation times of speckle dynamics, and the relationship with the flow velocity and optical properties of the scatterers, specifically multiple scattering in blood vessels and the scattering phase function of red blood cells. The second part is devoted to the quantification of optical signals arising from photoluminescent upconversion nanoparticles (UCNPs) for sensitive detection in biomedical tissues. The key results demonstrate that the UCNP optical properties enable the detection of small amounts of particles in UCNP-guided imaging applications, ranging from the detection of a single nanoparticle in biological liquid to modeling of a small UCNP-labeled tumour lesion embedded in biological tissue. The combination of these techniques is particularly useful in the context of tumour therapy by providing information on tumour angiogenesis, enabling molecular contrast and delivering nanoparticle-based drugs.

Table of Contents

1

General Introduction

1

Abstract This introductory chapter starts with an overview of the biomedical imaging scene in which this thesis is set. The area of interest for the optical imaging techniques that will be discussed is the microcirculation, therefore this chapter continues with a description of the microcirculation and the assessment of its functioning by quantifying the blood flow velocity. The microcirculation plays a role in many pathologies and a dysfunctional microcirculation can be the cause, mediator or result of other pathologies. Many tumours for example, thrive and survive due to increased microcirculatory blood supply invoked by tumour signalling molecules. However, quantifying the blood flow does not always provide adequate information, for example it does not provide adequate contrast to localize small tumour lesions. Therefore, the second part of the introduction focuses on achieving high-sensitivity molecular contrast in tumours using photoluminescent nanoparticles. Finally an overview of the thesis chapters covering quantitative flowmetry and photoluminescence techniques is given.

1.1 THE SCENE

Visual inspection is one of the oldest diagnostic tools used in medicine. In the early 1900's William Osler advised his students "Let not your conceptions of disease come from words heard in the lecture room or read from the book. See, and then reason and compare and control. But see first" [1]. In modern medicine, the importance of visual observation is still a critical part of teaching [2, 3]. The physician's eye and patient alone, however, do not always result in the true diagnostic outcome. Enhancing human vision has long been recognized as a valuable technique in medicine, from simple magnifying glasses and microscopes (flourishing since the 1680's) to advanced neurosurgical microscopes that allow 3-dimensional visualization through binoculars during intracranial neurovascular procedures [4-6]. Not only magnification, but also other light interactions with tissue can enhance clinical vision. For example the use of only a small part of the spectral range of light (colour) can result in a substantial increase in contrast. In Fig. 1.1 an example is shown of an image of microcirculatory blood vessels obtained using sidestream dark field (SDF) microscopy [7] (a technique that will be discussed in Chapters 2 - 4) using respectively unfiltered (white) and filtered (green) light for illumination. The large contrast in Fig. 1.1b is due to a large absorption difference between blood and surrounding tissue for green light, whereas this absorption difference is reduced when the whole visible spectrum is used (Fig. 1.1a).

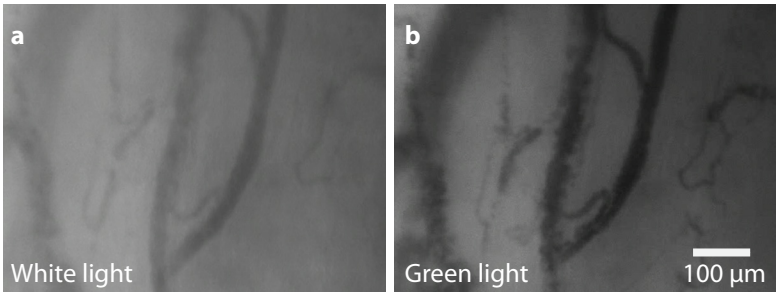

Figure 1.1 Spectral imaging | *Sidestream dark field (SDF) microscopy image of human sublingual microcirculation using white **(a)** and green **(b)** illumination light.*

The addition of magnifying and contrast enhancing tools to visual inspection allowed advancement of the area of optical biomedical imaging. Although the most common clinical imaging modalities (20th century inventions like X-ray, CT, ultrasound imaging and MRI) are non-optical, optical imaging is currently emerging due to the following advantages: optical radiation is nonionizing and safe; optical instruments are generally cheap and portable; and optical tissue interactions provide both structural and physiological information, usually at a higher resolution compared to the aforementioned modalities [8].

In the biomedical imaging field the goal is to obtain functional information about the tissue of interest to aid in a true diagnostic outcome, to monitor therapy or more generally to improve the understanding of life in health and disease. Tissue constituents like cells, organelles, proteins and biomolecules interact with light. Tissue can absorb, scatter and depolarize light, fluoresce or phosphoresce, or all at the same time. Interpreting the result of this complex, multiscale interaction can reveal information about the tissue of interest. Diseased tissue, or samples from a diseased organism (blood, urine, biopsies, etc.) can have a different structure or composition compared to healthy tissue. The task of biomedical imaging is to use the different optical signatures of healthy and diseased tissue to improve the differentiation between them.

Using light-tissue interactions for diagnostics is not limited to imaging. Biomedical imaging is a subfield of the larger research area called biophotonics, covering all techniques that study light-tissue interactions in aid of the differentiation between (or understanding of) healthy and diseased tissues. To complete the biophotonics landscape, a last but certainly not least application is the use of light for clinical interventions and therapy, for example laser surgery [9] or photodynamic therapy for the treatment of cancer [10]. An upcoming research area is 'theranostics', where therapy and diagnostics are integrated, often in the field of nanophotonics [11]. Ongoing research efforts to understand the complex interactions of light with tissue will result in more effective optics-based therapies.

The challenges in biophotonics arise from the complex interactions of light with tissue. In particular the highly scattering nature of tissue at optical wavelengths requires sophisticated algorithms to obtain functional information or reconstruct images. In addition, scattering, and also absorption, reduces the penetration depth of light in tissue to maximally a few centimetres in the near infrared region. The identification of potential application niches for optical techniques and the optimization of illumination, detection and signal processing methods are the driver behind the expansion of biophotonics in the biomedical field.

The versatile nature of tissue interactions with light logically results in a versatile field of biophotonics. Many excellent applications have already made their way to the clinic, such as the relatively simple pulse-oximeter [12] or advanced retinal imaging systems based on optical coherence tomography [13]. The advantages of adopting optics in the clinical setting are the potential for minimally invasive techniques, point-of-care diagnostics, and safe and affordable devices. In addition, the enhanced functional information (structural and physiological) that optical techniques can provide is arguably the most important added value to the clinic. However, before functional, robust and practical devices can be made, they have been preceded by in-depth, thorough and comprehensive research. This thesis is set in this particular scene where the quantification and interpretation of optical interactions with tissue are key concerns.

1.2 Microcirculation: where perfusion meets metabolism

The particular biotissue of interest in this thesis is the microcirculation: a network of blood vessels less than 100 μm in diameter. The microcirculation is the central region in the circulation system where the total vessel surface area is at its largest, and the blood flow slows down to allow exchange of gases, nutrients and metabolites providing the environment necessary for cells to function. Adequate tissue perfusion by microcirculatory blood flow is essential for healthy tissues and organs. Due to its function to meet the metabolic needs of tissues the microcirculation is found in almost all parts of the body, thus also close to the surface of tissues such as internal organs, muscles and skin (see Fig. 1.2). As light has a limited penetration depth in tissue the microcirculation is an excellent target for optical assessment with considerable clinical relevance.

Adequate tissue perfusion by the microcirculation is essential for organ health, so inadequate perfusion by the microcirculation can result in diseases and eventual organ failure. In the metabolic disease diabetes, common complications such as retinopathy and renal disease are the results of impaired microcirculation. Microangiopathy is caused by increased microvascular pressure and flow, but the exact cellular mecha-

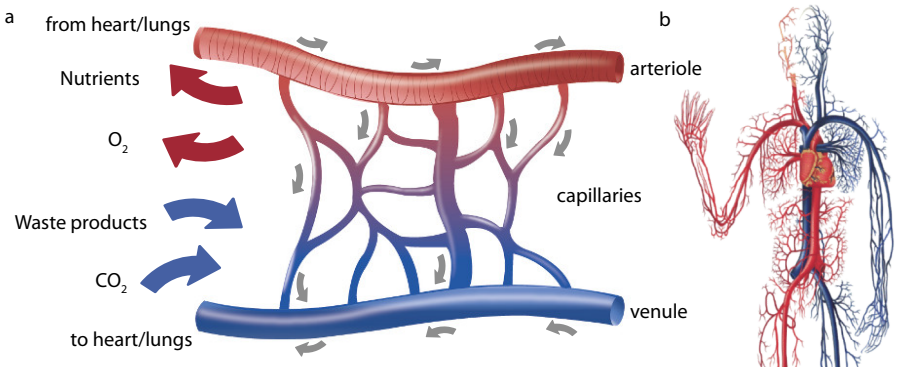

Figure 1.2 Microcirculation | ***(a)*** *Simple representation of metabolism in the microcirculation.* ***(b)*** *The microcirculation is everywhere (adapted from blog of Dr. S. Venkatesan, MD).*

nisms causing this are unknown. However, microangiopathy appears to precede cardiovascular diseases in diabetic patients, and in turn, functional microvascular changes precede microangiopathy [14, 15]. Assessing microvascular functionality thus aids in early diagnosis of diabetes and its related complications and can also function as an indicator for effectiveness of treatment [16].

Another relevant area where microcirculation assessment can aid in both diagnosis and therapy monitoring is at the intensive care unit (ICU). Sepsis is defined as the clinical syndrome characterized by the presence of infection and a systemic inflammatory response of the body, and septic shock refers to acute circulatory failure characterized by persistent arterial hypotension unexplained by other causes [17]. One of the major features of septic shock is a heterogeneous distribution of microcirculatory blood flow and in more advanced states a dysfunctional microcirculation leading to oxygen extraction deficit, severe functional shunting and organ failure [18, 19]. The pathological causes for this are not yet fully understood but suggestions includes triggers by inflammatory mediators, endothelial alterations, loss of neural control, altered leukocyte adhesion, altered red blood cell deformability and the presence of micro thrombi [20-22]. Regardless of cause, the indicators of septic shock are apparent in the microcirculation early on in disease development [23]; microcirculatory changes are more severe in nonsurvivors [24]; and an improved microcirculation functionality is associated with successful therapy and patient survival [25, 26]. In addition, during septic shock microvascular changes are independent of systemic haemodynamic variables [26, 27]. Other critical diseases where the microcirculation has been reported to play a role are cardiac arrests, heart failure and cardiogenic shock [28, 29]. In circulatory failure blood flow is diverted from the less vital tissues (skin, muscle, gastrointestinal tract) to the vital organs (heart, brain, kidneys). Consequently, monitoring the less vital tissues can be an early marker for hypoperfusion of vital organs with the advantage that the peripheral circulation is more accessible [30]. Microcirculatory function and capillary recruitment have therefore been proposed as end-points for therapy in sepsis and as potential parameters in other critical diseases [29, 31].

The microcirculation does not only provide adequate tissue perfusion to ensure healthy organs, it also provides oxygen and nutrients to unwanted tissue such as tumours. Without blood vessels tumours cannot grow beyond a critical size due to the limited diffusion distance of oxygen (100 - 200 µm) [32]. At the beginning of their development, tumours are usually not angiogenic (triggering blood vessel growth) due to a balance between pro- and anti-angiogenic molecules. Various processes occurring around tumours (metabolic or mechanical stress, immune or inflammatory response, genetic mutations) trigger the cells to

secrete pro-angiogenic signalling molecules to derail this balance and turn the angiogenic 'switch' to 'on' [32, 33]. The subsequent growth of blood vessels around the tumour allows the tumour to expand and facilitates transport of tumour cells to create metastasis elsewhere in the body. On the other hand, tumour microcirculation also enables anti-cancer drugs to be delivered to the tumour [32-34].

The microcirculation's ability or inability to accommodate the tissue's metabolic needs is thus an important pathological marker for various diseases, including those outlined above. The causes for microcirculatory dysfunction, pro- and anti-angiogenic behaviour and microangiopathy are complex, broad and warrant further investigations. However there is strong evidence that the microcirculation functionality and cellular processes are interdependent [32, 35], and hence the study of microcirculation can elucidate the related cellular processes and clinical physiology and can help to understand causes of diseases and mechanisms of diagnosis and therapy.

1.3 Functional microcirculation imaging

An important perception is that assessing a single capillary is not sufficient to verify (in)adequate supply of oxygen to tissue. The functional parameters that have been identified to be relevant in septic shock are a measure of vessel density and geometry; assessment of capillary perfusion and the heterogeneity of microvascular perfusion [36]. This method of microcirculation scoring was developed due to the availability of a new-generation microcirculation microscopes that allowed capturing videos of the microcirculation of approximately 1 mm^2 field of view, usually containing 20 or more capillaries, venules and/or arterioles. The first imager was based on orthogonal polarization spectroscopy (OPS) [37] and the improved version on sidestream dark field (SDF) imaging [7]. In both versions the contrast is obtained by illumination with green light (higher absorption by blood compared to surrounding tissue, see Fig. 1.1) and they share the common property that the specularly reflected light is rejected from the imaging path, resulting in detailed videos of subsurface microcirculatory vessels with flowing red blood cells (RBCs). Importantly, the techniques can be implemented in hand-held and small instruments, which can be used at the ICU as opposed to the bulky nailfold capillaroscopy microscopes that are historically used for microcirculation assessment [38-40]. In addition, these devices can be placed sublingually where the mucosal tissue overlaying the capillaries is quite transparent and the images contain much more detail compared to the nailfold. SDF and OPS devices have extensively been used for research on microcirculatory function during critical diseases [18, 19, 22-29, 41-44]. The non-invasiveness of SDF and OPS imaging is favourable for patients in critical circumstances especially for vulnerable patients such as in the paediatric intensive care unit [45]. SDF microscopy was for example used to monitor the microcirculation in relation to illness severity and therapy response in children with meningococcal disease [46], hypothermia [47], and hypotension [48]. The quantitative parameters proportion of perfused small vessels (< 20 μm) [24, 25, 27, 29, 46], microvascular flow index [26, 28, 46, 47, 49] and flow velocity [23, 44, 46] are found to be decreased in critically ill patients, while the microvascular heterogeneity increased [23]. Not all critical diseases lead to a change in functional microcirculatory parameters [42, 43], however this does not negate clinical relevance. On the other hand, concern has been raised about the requirement for time consuming off-line data analysis [42] and the difficult interpretation of microcirculation images [50], which could also be the reason for absence of significant microcirculatory changes in the data.

Quantification of the SDF or OPS images is currently semi-automatic using commercially available software (AVA3.0 Microvision Medical, Amsterdam, The Netherlands). The algorithm for flow assessment to determine the important microvascular parameter vessel perfusion (and the proportion and heterogeneity thereof) is based on tracking of RBCs and plasma gaps in a space-time diagram [51]. However, the maximal flow velocity measurement is limited by the frame rate and exposure time of the camera, which is around 1 - 2 mm/s in the current system. In addition, the analysis needs to be performed off-line and involves considerable user-interaction limiting its use at the bedside. An alternative range of techniques to visualize microcirculatory flow is based on the temporal statistics of coherent light backscattered from dynamic structures, referred to as Dynamic Light Scattering (DLS) techniques [52, 53]. In this case, the contrast is not based on absorption but on scattering by flowing RBCs. Techniques such as Laser Doppler Flowmetry (LDF) [54], Laser Speckle Contrast Imaging (LSCI) [55] and Diffusing Wave Spectroscopy (DWS, also called diffuse correlation spectroscopy) [56] fall in this category. These techniques are sensitive to a wide flow range, but generally lack a quantitative representation of flow velocity. Often their measurement quantities can be determined automatically with simple algorithms, but are expressed in quantities such as 'flux' or 'relative blood flow' or 'perfusion units' [57-59], related to the product of the number of moving RBCs and their average velocity. These techniques can therefore be used to visualize blood flow or quantify relative flow metrics, but are not a measure of absolute blood flow velocity. The techniques are discussed in more detail in Chapter 2 and their key differences in technology, temporal and spatial resolution, field of view and probing depth are listed. DLS techniques often use wavelengths within the so-called 'tissue transparency window' (approx. range 650 - 1300 nm) [60] and therefore probe deeper, but with reduced spatial resolution compared to SDF video-microscopy [61-63]. The handheld SDF microscope uses green light for high contrast but with limited penetration depth in tissue due to the high scattering and absorption properties of tissue for green light. The maximum focus depth of the device is 0.4 mm. SDF microscopy can only acquire microcirculation images at locations where the vessels are superficial and in optically transparent tissues, such as mucosal tissue (sublingual, conjunctiva, nail-fold) [7, 64], organ surfaces [65] or neonatal skin [47]. LDF, DWS and LSCI have the ability to image the microcirculation through e.g. skin or skull [58, 59, 66].

Besides diagnosis and monitoring of critical diseases, imaging techniques that quantify microvascular parameters have also been used e.g. to assess neurovascular changes to gain insight in brain metabolism under normal or pathological conditions [67]; skin grafts and burn wounds [68, 69] and microvascular disorders in metabolic [15], cardiovascular [70] or oncologic diseases. Microcirculatory parameters such as vessel geometry, vascular pattern and blood flow were assessed using OPS imaging on oral squamous cell carcinoma [71] and brain tumours [72]. Dilated and chaotic vessels or vessels with low flow compared to healthy areas were found to characterize cancerous regions [71, 72]. This suggests that microcirculatory imaging can be a useful tool in the detection of cancer-related vascular aberrations, the effects of therapy on the tumour microvasculature or for guidance during tumour neurosurgery. Ideally, a blood flow imager should be objective, non-invasive, and capable of performing instantaneous and reproducible readings (for some diseases continuously) [30, 73]. Therefore, a substantial part of this thesis is devoted to optimizing optical technologies to comply with these requirements.

1.4 Microcirculatory delivery in tumours

The observation that tumour angiogenesis occurs around tumours and that the vessels display 'chaotic irregularity' was made more than 100 years ago [74]. The imbalance of angiogenic regulators and the vigorous nature of tumour and blood vessel growth cause tumour vessels to be structurally and functionally abnormal. In contrast to healthy vessels, tumour vessels are dilated, tortuous, have uneven diameters, and show excessive branching and shunting [32]. As elucidated in the previous section, the appearance of the microcirculation can be an indicator for the presence of tumours making direct visualization an important non-invasive clinical tool. At the same time, it is expected that cancerous angiogenic regions are visible in microcirculation images only when the tumour has grown to a reasonable size and is superficial enough for vessel image details to be retained in the presence of scattering. In addition, inflamed areas can also induce changes in microcirculatory perfusion similar to malignancies, as measured by LDF [75]. However, for the detection of small or deep tumours the microcirculation can still be useful as a delivery system for contrast enhancing particles to enable detection by advanced optical imaging techniques [76].

The delivery of macromolecular complexes to tumours is mediated by the enhanced permeability and retention (EPR) effect [77]. Not only do tumour vessels look distorted on a µm to mm scale (dilated, tortuous, irregular, etc.) the composition of the tumour vessel wall also differs from normal on a nm to µm scale. The pathological angiogenesis process during tumour growth as a result of dysregulation of pro- and anti-angiogenic signalling molecules can result in a defective cellular lining of tumour vessels composed of disorganized, loosely connected, branched, overlapping or sprouting endothelial cells [78]. The resulting vessel wall is 'leaky' and exhibits an enhanced permeability to macromolecules. In normal tissue such macromolecules would be cleared by the lymphatic system, however, other characteristics of tumour tissue are compressed and damaged lymphatic vessels, possibly due to the high interstitial fluid pressure built up by the growing tumour mass [32, 79]. The absence of lymphatic drainage results in macromolecules retaining in the tumour for prolonged periods. This passive targeting of macromolecules to tumours through the EPR effect results in a higher concentration inside the tumour as compared with the surrounding tissue [80, 81]. As a result, when the macromolecular complexes have photoluminescent properties, the tumour imaging contrast can be enhanced [76, 82, 83].

The macromolecular complexes need to exhibit certain physical and biochemical properties to take full advantage of the EPR effect. Obviously the size is important since particles that are too large cannot diffuse through the permeable vessel wall, while small particles quickly diffuse through the tumour and are not retained [84]. Endothelial intercellular openings in the range 0.3 - 4.5 µm and transcellular holes of 0.6 µm in diameter were measured using scanning electron microscopy images of mouse mammary tumour, as shown in Fig. 1.3 [78]. In a human colon tumour xenograft a cut-off size of 400 - 600 nm was found by observing transvascular transport of liposomes [85]. Optimal sizes of macromolecules for the EPR effect around 60 - 100 nm are reported [84, 86]. In addition, these nanoscale particles must remain in the circulation long enough for accumulation in the tumour, escaping clearance by the immune system, liver and spleen and without interaction with components in the blood vessels or vessel walls [80]. Engineering nanoparticles using biocompatible molecules or coating nanoparticles with biocompatible surface groups increases their circulation time [87]. Other properties such as surface charge, hydrophobicity and

shape also play a role [80, 81]. In addition, co-administration of nanoparticles with factors that increase the permeability of tumour vessels has been shown to enhance the EPR effect [80, 83], for example by increasing the blood pressure and widening the endothelial cell-cell gaps [88].

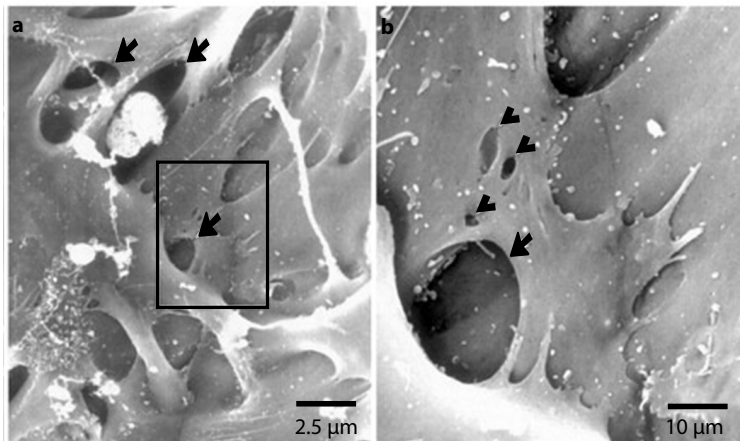

Figure 1.3 Tumour vessel leakiness | *Scanning electron microscopy image of a mouse mammary tumour blood vessel.* ***(a)*** *Multiple intercellular openings (arrows) in endothelial cell lining of a tumour vessel. Region in box in (a) is shown at higher magnification in* ***(b)****, where the arrowheads (<) point at three transcellular holes, much smaller than the intercellular hole (arrow). Figure adapted from ref. [78].*

The EPR effect essentially links the microcirculation to the cellular processes leading to tumour angiogenesis, enabling a passive way of enhancing molecular contrast in tissue. An active approach to enhancing molecular contrast is to conjugate the nanoparticles with tumour-specific recognition molecules (antibodies, ligands) that actively target tumour cells [89]. Targeted nanoparticles are recognised by tumour cell surface receptors, followed by nanoparticle binding and receptor-mediated endocytosis. Pre-clinical data on targeted nanoparticle delivery to tumours has shown an increased cellular uptake compared to non-targeted nanoparticles [90].

Drug delivery is another attractive application to use nanoparticles. The important advantage of engineering drugs as nanoparticles instead of the free drug, is the increased efficiency of delivery (either passively or targeted) to the tumour compared to the healthy tissues, as healthy vessels are not permeable for nanoparticles. This reduces side effects for patients and lowers the drug dosage necessary for tumour response (or detection). Currently, there are at least six clinically approved nanoparticle-based cancer therapies and another few hundred companies are developing novel nanoscale therapeutics [81]. The first approved form of loading drugs in a nanoparticle was the encapsulation of doxorubicin (standard chemotherapy for e.g. breast and ovarian cancer) in liposomes of around 100 nm. In comparison with conventional doxorubicin, equi-effective (and lower) doses of liposomal doxorubicin show a decreased rate of cardiotoxicity, impaired bone marrow activity, hair loss and nausea/vomiting [91].

The utility of targeted and non-targeted contrast enhancing agents aiming for a higher therapy success has been demonstrated in humans during surgical procedures. The success of surgery, measured as thorough removal of all tumour tissue while leaving as much healthy tissue as possible, can be increased by enhancing intraoperative tumour visibility for the surgeon, exemplified by the realization of tumour-specific targeted fluorescence-guided ovarian cancer surgery in humans [92]. And recently, surgeons

equipped with fluorescence goggles saw an enhanced tumour-to-healthy tissue contrast while resecting liver carcinomas during fluorescence-guided surgery [93]. These studies were accomplished using clinically approved fluorescent dyes. The design and approval of new nanotechnology based delivery of contrast enhancing agents can further enhance the specificity and sensitivity of visualizing tumour regions.

In spite of the above drug delivery and surgery prospects, the clinical effects of tumour therapy are confounded. This is illustrated by the withdrawal of the drug bevacizumab for patients with metastatic breast cancer, where impressive tumour reductions were seen but there was no improvement in overall survival [94]. This reveals the limitations and challenges in understanding tumour development where structural, cellular and molecular imaging can help to improve cancer treatments and guide the adaptation of nanotechnology based drug delivery approaches. The heterogeneity of angiogenesis in tumours, both spatially and temporally, is one of the problems resulting in unreachable areas of the tumours for nanoparticles. The high interstitial fluid pressure, which is on the one hand responsible for reduced lymphatic drainage and retention, on the other hand forms a barrier for transvascular transport [95]. In addition, the tumour size, type and location, immune system activity, co-medication and other patient specific characteristics all influence the EPR effect, nanoparticle delivery and the tumour response to therapy [32, 94]. Understanding and predicting EPR effects, assessing angiogenesis in primary and metastatic tumours and correlating EPR activity to clinical response are key considerations to improve nanomedicine in oncology [32, 33, 94]. Quantitative imaging of the microcirculation perfusion, geometry, permeability and delivery of nanoparticles can contribute to this quest.

1.5 Glow with the flow: Quantifying blood flow and photoluminescence signal in biological tissue

Understanding the complexity of microcirculation pathology during the course of diseases is aided by minimally invasive techniques that do not interfere with the physiology and bias results (ranging from changing the blood flow to interfering with the immune system). Optical techniques have advantageous characteristics that allow repeated monitoring, obtain functional information or allow sensitive detection using photoluminescent nanoparticles. The complex interactions of light with tissue represent important challenges in biophotonics. Understanding the complexity of these interactions can be the basis for novel biomedical imaging techniques. Designated niches for optical techniques are just below the surface of tissues. Since the microcirculation is in virtually all parts of the body, probing this part of the circulation is feasible and allows minimally invasive monitoring, even at the cellular and molecular level.

1.5.1 Thesis aim

This thesis aims to assess 2 optical imaging techniques for clinical applications in order to: 1. quantify microcirculatory flow velocities using laser speckle contrast imaging and 2. quantify photoluminescence signal from luminescent nanoparticles in biological tissues. The combination of these techniques can be especially useful in the context of tumour therapy by providing information on tumour angiogenesis, enabling molecular contrast and delivering nanoparticle-based drugs.

1.5.2 Thesis overview

The first part of this thesis addresses the problem of obtaining quantitative information on blood flow velocity, while maintaining technical simplicity. Using a hand-held microscope, a laser, LEDs and a software-controlled camera, two complementary flowmetry techniques were integrated into one device. SDF flowmetry, based on light absorption by RBCs, is excellent for visualizing blood vessels and quantifying low flows, while LSCI, based on dynamic light scattering by RBCs, is sensitive to a wide range of flow dynamics. Combining the two techniques potentially reduces their individual shortcomings: processing time and flow range (SDF), and quantification (LSCI). Building upon existing theoretical frameworks [54, 56, 96, 97] and recent advances in the understanding of optical scattering by blood [98] the quantitative abilities of LSCI are reassured in the first part of this thesis. The theoretical framework is described in **Chapter 2**, as well as the specific challenges and gaps for quantitative flowmetry. **Chapter 3** describes the validation of integrated SDF-LSCI using a flow phantom and a first *in vivo* calibration of the technique in humans. **Chapter 4** further explores the effects of light scattering with flowing particles of different sizes and concentrations to enable quantitative blood flow measurements *in vivo* for variable vessel diameters and blood volume fractions. LSCI can be used continuously, non-invasively and automated algorithms can be developed. The results of chapters 2 - 4 allow the quantitative visualization of blood flow, flow velocity and perfusion of microcirculatory beds, without being limited to relative flow measures. This enables SDF-LSCI to study microcirculation within and between organs and organisms, during the course of disease and therapy and resulting from different metabolic requirements.

Assessing the EPR effect and (targeted) delivery of macromolecules into tumours, whether it is for contrast-enhanced diagnosis, therapy, or both, is aided by highly sensitive and high contrast imaging. Therefore, macromolecules are often designed to enhance optical contrast due to their specific fluorescent, photoluminescent, scattering or absorption properties. High contrast is achieved when the macromolecules exhibit optical properties distinct from biological tissue. Since biological tissues can absorb, scatter and emit fluorescent light (autofluorescence), a novel type of luminophore capable of nonlinear 'upconversion' of light might be an excellent candidate for contrast-enhanced imaging *in vivo* [99, 100], given that tissues do not exhibit this property. The upconversion process and the unique optical properties of upconversion nanoparticles (UCNPs) are discussed in **Chapter 5**. To assess their utility for biomedical imaging a thorough quantification of the optical properties in the context of tissue scattering and absorption is a necessity, which is experimentally realized in **Chapter 6**. Their unique properties are exploited to achieve single UCNP imaging through an absorbing layer of haemolysed blood. This result is extended towards *in vivo* applications by theoretically modelling the ability to detect a single UCNP at different depths in skin. In **Chapter 7** we further advance this approach to include biological complexity by preparing UCNPs equipped with tumour-specific mini-antibodies and assessing their targeting abilities to human breast cancer cells *in vitro*. To model the *in vivo* detection limits of a cluster of breast cancer cells, we covered the labelled cancer cells with breast tissue simulating phantom layers and quantified the detectable upconversion signal at increasing thickness. This novel class of nanoparticles holds promise for future clinical tumour detection and therapy, especially in the context of the growing abilities of nanoscale engineering and technology. Quantitative experimental and theoretical modelling of optical upconversion signals in biomedical context is important to identify the opportunities and limitations of this unique class of photoluminescent nanomaterials, and identify feasible application niches. Chapters 5 - 7 are aimed at the

quantification of optical upconversion signals in the context of biological tissue scattering, absorption and labelling performance of UCNPs. Other biologically relevant parameters of UCNPs (biological toxicity of UCNPs, blood circulation times and microvascular delivery of UCNPs to tumours in a chick embryo model) are presented in the Discussion and Conclusion **Chapter 8**. Chapter 8 also discusses additional results on quantitative laser speckle flowmetry and recommendations to further improve the LSCI technique. **Chapter 9** presents a short summary and outlook on the results presented in this thesis, in particular the potential combination of photoluminescence and perfusion imaging in the context of the challenges in diagnosing and treating tumours, and the role of the microcirculation herein.

1.6 REFERENCES

1. W. S. Thayer, "Osler the teacher," Bulletin of Johns Hopkins Hospital 30, 198-200 (1919).
2. R. C. Anderson, M. J. Fagan, and J. Sebastian, "Teaching students the art and science of physical diagnosis," American Journal of Medicine, The 110, 419-423 (2001).
3. S. Naghshineh, J. P. Hafler, A. R. Miller, M. A. Blanco, S. R. Lipsitz, R. P. Dubroff, S. Khoshbin, and J. T. Katz, "Formal art observation training improves medical students' visual diagnostic skills," J. Gen. Intern. Med. 23, 991-997 (2008).
4. J. Hogg, "History of the invention and improvements of the microscope," in The microscope; its history, construction and application (Routledge, London, 1867), pp. 1-14.
5. T. C. Kriss and V. M. Kriss, "History of the operating microscope: from magnifying glass to microneurosurgery," Neurosurgery 42, 899 (1998).
6. K. Uluç, G. C. Kujoth, and M. K. Baskaya, "Operating microscopes: past, present, and future," Neurosurg. Focus 27, 4 (2009).
7. P. Goedhart, M. Khalilzada, R. Bezemer, J. Merza, and C. Ince, "Sidestream Dark Field (SDF) imaging: a novel stroboscopic LED ring-based imaging modality for clinical assessment of the microcirculation," Optics express 15, 15101-15114 (2007).
8. L. V. Wang and H.-i. Wu, Biomedical optics: principles and imaging (John Wiley & Sons, 2012).
9. S. L. Trokel, R. Srinivasan, and B. Braren, "Excimer laser surgery of the cornea," Am. J. Ophthalmol. 96, 710-715 (1983).
10. T. J. Dougherty, C. J. Gomer, B. W. Henderson, G. Jori, D. Kessel, M. Korbelik, J. Moan, and Q. Peng, "Photodynamic therapy," J. Natl. Cancer Inst. 90, 889-905 (1998).
11. X. S. Chen, "Introducing theranostics journal-from the editor-in-chief," Theranostics 1, 1 (2011).
12. I. Yoshiya, Y. Shimada, and K. Tanaka, "Spectrophotometric monitoring of arterial oxygen saturation in the fingertip," Med. Biol. Eng. Comput. 18, 27-32 (1980).
13. D. Huang, E. A. Swanson, C. P. Lin, J. S. Schuman, W. G. Stinson, W. Chang, M. R. Hee, T. Flotte, K. Gregory, and C. A. Puliafito, "Optical coherence tomography," Science 254, 1178-1181 (1991).
14. H.-H. Parving, G. Viberti, H. Keen, J. Christiansen, and N. Lassen, "Hemodynamic factors in the genesis of diabetic microangiopathy," Metabolism. 32, 943-949 (1983).
15. W. D. Strain, D. D. Adingupu, and A. C. Shore, "Microcirculation on a large scale: techniques, tactics and relevance of studying the microcirculation in larger population samples," Microcirculation 19, 37-46 (2011).
16. A. Jaap, C. Pym, C. Seamark, A. Shore, and J. Tooke, "Microvascular Function in Type 2 (Non-insulin-dependent) Diabetes: Improved Vasodilation After One Year of Good Glycaemic Control," Diabet. Med. 12, 1086-1091 (1995).
17. M. M. Levy, M. P. Fink, J. C. Marshall, E. Abraham, D. Angus, D. Cook, J. Cohen, S. M. Opal, J.-L. Vincent, and G. Ramsay, "2001 sccm/esicm/accp/ats/sis international sepsis definitions conference," Intensive Care Med. 29, 530-538 (2003).
18. C. Ince, "The microcirculation is the motor of sepsis," Crit. Care 9, S13 (2005).
19. C. Ince and M. Sinaasappel, "Microcirculatory oxygenation and shunting in sepsis and shock," Crit. Care Med. 27, 1369-1377 (1999).
20. D. Annane, E. Bellissant, and J.-M. Cavaillon, "Septic shock," The Lancet 365, 63-78 (2005).
21. F. G. Bonanno, "Physiopathology of shock," J. Emerg. Trauma Shock 4, 222 (2011).
22. D. De Backer, "Microcirculatory alterations: potential mechanisms and implications for therapy " in Continuous Renal Replacement Therapies Online, 2012),
23. S. Trzeciak, R. P. Dellinger, J. E. Parrillo, M. Guglielmi, J. Bajaj, N. L. Abate, R. C. Arnold, S. Colilla, S. Zanotti, and S. M. Hollenberg, "Early microcirculatory perfusion derangements in patients with severe sepsis and septic shock: relationship to hemodynamics, oxygen transport, and survival," Ann. Emerg. Med. 49, 88-98. e82 (2007).
24. D. De Backer, J. Creteur, J.-C. Preiser, M.-J. Dubois, and J.-L. Vincent, "Microvascular blood flow is altered in patients with sepsis," Am. J. Respir. Crit. Care. Med. 166, 98-104 (2002).
25. Y. Sakr, M.-J. Dubois, D. De Backer, J. Creteur, and J.-L. Vincent, "Persistent microcirculatory alterations are associated with organ failure and death in patients with septic shock*," Crit. Care Med. 32, 1825-1831 (2004).
26. S. Trzeciak, J. V. McCoy, R. P. Dellinger, R. C. Arnold, M. Rizzuto, N. L. Abate, N. I. Shapiro, J. E. Parrillo, and S. M. Hollenberg, "Early increases in microcirculatory perfusion during protocol-directed resuscitation are associated with reduced multi-organ failure at 24 h in patients with sepsis," Intensive Care Med. 34, 2210-2217 (2008).
27. D. De Backer, J. Creteur, M.-J. Dubois, Y. Sakr, M. Koch, C. Verdant, and J.-L. Vincent, "The effects of dobutamine on microcirculatory alterations in patients with septic shock are independent of its systemic effects*," Crit. Care Med. 34, 403-408 (2006).
28. Y. G. Omar, M. Massey, L. W. Andersen, T. A. Giberson, K. Berg, M. N. Cocchi, N. I. Shapiro, and M. W. Donnino, "Sublingual microcirculation is impaired in post-cardiac arrest patients," Resuscitation 84, 1717-1722 (2013).
29. D. De Backer, J. Creteur, M.-J. Dubois, Y. Sakr, and J.-L. Vincent, "Microvascular alterations in patients with acute severe heart failure and cardiogenic shock," Am. Heart J. 147, 91-99 (2004).
30. A. Lima and J. Bakker, "Noninvasive monitoring of peripheral perfusion," Intensive Care Med. 31, 1316-1326 (2005).
31. C. Ince, "Microcirculation in distress: A new resuscitation end point?*," Crit. Care Med. 32, 1963-1964 (2004).
32. P. Carmeliet and R. K. Jain, "Angiogenesis in cancer and other diseases," Nature 407, 249-257 (2000).
33. J. Folkman, "Angiogenesis in cancer, vascular, rheumatoid and other disease," Nat. Med. 1, 27-30 (1995).
34. J. Fang, H. Nakamura, and H. Maeda, "The EPR effect: unique features of tumor blood vessels for drug delivery, factors involved, and limitations and augmentation of the effect," Adv. Drug Delivery. Rev. 63, 136-151 (2011).
35. B. Fagrell and M. Intaglietta, "Microcirculation: its significance in clinical and molecular medicine," J. Intern. Med. 241, 349-362 (1997).
36. D. De Backer, S. Hollenberg, C. Boerma, P. Goedhart, G. Büchele, G. Ospina-Tascon, I. Dobbe, and C. Ince, "How to evaluate the microcirculation: report of a round table conference," Crit. Care 11, R101 (2007).
37. W. Groner, J. W. Winkelman, A. G. Harris, C. Ince, G. J. Bouma, K. Messmer, and R. G. Nadeau, "Orthogonal polarization spectral imaging: a new method for study of the microcirculation," Nat. Med. 5, 1209-1212 (1999).
38. M. Roustit and J.-L. Cracowski, "Non-invasive Assessment of Skin Microvascular Function in Humans: An Insight Into Methods," Microcirculation 19, 47-64 (2012).
39. M. Cutolo, A. Sulli, M. Secchi, S. Paolino, and C. Pizzorni, "Nailfold capillaroscopy is useful for the diagnosis and follow-up of autoimmune rheumatic diseases. A future tool for the analysis of microvascular heart involvement?," Rheumatology 45, iv43-iv46 (2006).
40. K. R. Mathura, K. C. Vollebregt, K. Boer, J. C. De Graaff, D. T. Ubbink, and C. Ince, "Comparison of OPS imaging and conventional capillary microscopy to study the human

microcirculation," J. Appl. Physiol. 91, 74-78 (2001).
41. C. A. Den Uil, E. Klijn, W. K. Lagrand, J. J. Brugts, C. Ince, P. E. Spronk, and M. L. Simoons, "The microcirculation in health and critical disease," Prog. Cardiovasc. Dis. 51, 161-170 (2008).
42. N. Vellinga, E. C. Boerma, M. Koopmans, A. Donati, A. Dubin, N. I. Shapiro, R. M. Pearse, F. R. Machado, M. Fries, and T. Akarsu-Ayazoglu, "International Study on Microcirculatory Shock Occurrence in Acutely Ill Patients," Crit. Care Med. (2014).
43. L. Maddison, J. Karjagin, M. Buldakov, M. Mäll, R. Kruusat, K. Lillemäe, Ü. Kirsimägi, and J. Starkopf, "Sublingual microcirculation in patients with intra-abdominal hypertension: A pilot study in 15 critically ill patients," J. Crit. Care 29, 183. e181-183. e186 (2014).
44. M. Fries, M. H. Weil, Y.-T. Chang, C. Castillo, and W. Tang, "Microcirculation during cardiac arrest and resuscitation," Crit. Care Med. 34, S454-S457 (2006).
45. A. Top, R. C. Tasker, and C. Ince, "The microcirculation of the critically ill pediatric patient," Crit. Care 15, 213 (2011).
46. F. Paize, R. Sarginson, N. Makwana, P. B. Baines, A. P. Thomson, I. Sinha, C. A. Hart, A. Riordan, K. C. Hawkins, and E. D. Carrol, "Changes in the sublingual microcirculation and endothelial adhesion molecules during the course of severe meningococcal disease treated in the paediatric intensive care unit," Intensive Care Med. 38, 863-871 (2012).
47. E. Ergenekon, I. Hirfanoğlu, S. Beken, O. Turan, F. Kulali, E. Koç, and K. Gücüyener, "Peripheral microcirculation is affected during therapeutic hypothermia in newborns," Archives of Disease in Childhood-Fetal and Neonatal Edition 98, F155-F157 (2013).
48. A. Schwepcke, F. D. Weber, Z. Mormanova, B. Cepissak, and O. Genzel-Boroviczény, "Microcirculatory mechanisms in postnatal hypotension affecting premature infants," Pediatr. Res. 74, 186-190 (2013).
49. P. E. Spronk, C. Ince, M. J. Gardien, K. R. Mathura, H. M. Straaten, and D. F. Zandstra, "Nitroglycerin in septic shock after intravascular volume resuscitation," The Lancet 360, 1395-1396 (2002).
50. I. H. Koh, J. L. Menchaca-Diaz, T. H. Koh, R. L. Souza, C. M. Shu, V. E. Rogerio, and A. M. Liberatore, "Microcirculatory evaluation in sepsis: a difficult task," Shock 34, 27-33 (2010).
51. J. G. Dobbe, G. J. Streekstra, B. Atasever, R. Van Zijderveld, and C. Ince, "Measurement of functional microcirculatory geometry and velocity distributions using automated image analysis," Med. Biol. Eng. Comput. 46, 659-670 (2008).
52. B. J. Berne and R. Pecora, Dynamic light scattering: with applications to chemistry, biology, and physics (Courier Dover Publications, 2000).
53. V. V. Tuchin, Tissue optics: light scattering methods and instruments for medical diagnosis (SPIE press Bellingham, 2007), Vol. 642.
54. M. Stern, "*In vivo* evaluation of microcirculation by coherent light scattering," Nature 254, 56-58 (1975).
55. A. Fercher and J. Briers, "Flow visualization by means of single-exposure speckle photography," Opt. Commun. 37, 326-330 (1981).
56. D. Pine, D. Weitz, P. Chaikin, and E. Herbolzheimer, "Diffusing wave spectroscopy," Phys. Rev. Lett. 60, 1134 (1988).
57. G. E. Nilsson, T. Tenland, and P. A. Oberg, "A new instrument for continuous measurement of tissue blood flow by light beating spectroscopy," Biomedical Engineering, IEEE Transactions on, 12-19 (1980).
58. M. Roustit, C. Millet, S. Blaise, B. Dufournet, and J. Cracowski, "Excellent reproducibility of laser speckle contrast imaging to assess skin microvascular reactivity," Microvasc. Res. 80, 505-511 (2010).
59. C. Cheung, J. P. Culver, K. Takahashi, J. H. Greenberg, and A. Yodh, "*In vivo* cerebrovascular measurement combining diffuse near-infrared absorption and correlation spectroscopies," Phys. Med. Biol. 46, 2053 (2001).
60. R. Weissleder, "A clearer vision for *in vivo* imaging," Nat. Biotechnol. 19, 316-316 (2001).
61. G. Dietsche, M. Ninck, C. Ortolf, J. Li, F. Jaillon, and T. Gisler, "Fiber-based multispeckle detection for time-resolved diffusing-wave spectroscopy: characterization and application to blood flow detection in deep tissue," Appl. Opt. 46, 8506-8514 (2007).
62. M. Ninck, M. Untenberger, and T. Gisler, "Diffusing-wave spectroscopy with dynamic contrast variation: disentangling the effects of blood flow and extravascular tissue shearing on signals from deep tissue," Biomedical optics express 1, 1502-1513 (2010).
63. K. Johansson, H. Ahn, J. Lindhagen, and O. Lundgren, "Tissue penetration and measuring depth of laser Doppler flowmetry in the gastrointestinal application," Scand. J. Gastroenterol. 22, 1081-1088 (1987).
64. K.-D. Schaser, U. Settmacher, G. Puhl, L. Zhang, T. Mittlmeier, J. Stover, B. Vollmar, M. Menger, P. Neuhaus, and N. Haas, "Noninvasive analysis of conjunctival microcirculation during carotid artery surgery reveals microvascular evidence of collateral compensation and stenosis-dependent adaptation," J. Vasc. Surg. 37, 789-797 (2003).
65. C. A. den Uil, R. Bezemer, D. R. Miranda, C. Ince, W. K. Lagrand, J. M. Hartman, A. J. Bogers, P. E. Spronk, and M. L. Simoons, "Intra-operative assessment of human pulmonary alveoli *in vivo* using sidestream dark field imaging: a feasibility study," Med Sci Monit 15, 141 (2009).
66. G. A. Holloway and D. W. Watkins, "Laser Doppler measurement of cutaneous blood flow," J. Investig. Dermatol. 69, 306-309 (1977).
67. A. K. Dunn, H. Bolay, M. A. Moskowitz, and D. A. Boas, "Dynamic imaging of cerebral blood flow using laser speckle," J. Cereb. Blood Flow Metab. 21, 195-201 (2001).
68. C. M. Choi and R. G. Bennett, "Laser Dopplers to determine cutaneous blood flow," Dermatol. Surg. 29, 272-280 (2003).
69. H. van Herpt, M. Draijer, E. Hondebrink, M. Nieuwenhuis, G. Beerthuizen, T. van Leeuwen, and W. Steenbergen, "Burn imaging with a whole field laser Doppler perfusion imager based on a CMOS imaging array," Burns 36, 389-396 (2010).
70. K. Farkas, E. Kolossváry, Z. Járai, J. Nemcsik, and C. Farsang, "Non-invasive assessment of microvascular endothelial function by laser Doppler flowmetry in patients with essential hypertension," Atherosclerosis 173, 97-102 (2004).
71. J. A. Lindeboom, K. R. Mathura, and C. Ince, "Orthogonal polarization spectral (OPS) imaging and topographical characteristics of oral squamous cell carcinoma," Oral Oncol. 42, 581-585 (2006).
72. K. R. Mathura, G. J. Bouma, and C. Ince, "Abnormal microcirculation in brain tumours during surgery," The Lancet 358, 1698-1699 (2001).
73. M. D. Stern, D. L. Lappe, P. D. Bowen, J. E. Chimosky, G. Holloway, H. Keiser, and R. Bowman, "Continuous measurement of tissue blood flow by laser-Doppler spectroscopy," Am. J. Physiol. 232, H441-H448 (1977).
74. E. Goldmann, "The growth of malignant disease in man and the lower animals, with special reference to the vascular system," Proc. R. Soc. Med. 1, 1 (1908).
75. M. Stücker, I. Horstmann, C. Nüchel, A. Röchling, K. Hoffmann, and P. Altmeyer, "Blood flow compared in benign melanocytic naevi, malignant melanomas and basal cell carcinomas," Clin. Exp. Dermatol. 24, 107-111 (1999).
76. S. Luo, E. Zhang, Y. Su, T. Cheng, and C. Shi, "A review of NIR dyes in cancer targeting and imaging," Biomaterials

32, 7127-7138 (2011).
77. Y. Matsumura and H. Maeda, "A new concept for macromolecular therapeutics in cancer chemotherapy: mechanism of tumoritropic accumulation of proteins and the antitumor agent smancs," Cancer Res. 46, 6387-6392 (1986).
78. H. Hashizume, P. Baluk, S. Morikawa, J. W. McLean, G. Thurston, S. Roberge, R. K. Jain, and D. M. McDonald, "Openings between defective endothelial cells explain tumor vessel leakiness," The American journal of pathology 156, 1363-1380 (2000).
79. G. Helmlinger, P. A. Netti, H. C. Lichtenbeld, R. J. Melder, and R. K. Jain, "Solid stress inhibits the growth of multicellular tumor spheroids," Nat. Biotechnol. 15, 778-783 (1997).
80. H. Maeda, H. Nakamura, and J. Fang, "The EPR effect for macromolecular drug delivery to solid tumors: improvement of tumor uptake, lowering of systemic toxicity, and distinct tumor imaging *in vivo*," Adv. Drug Delivery. Rev. 65, 71-79 (2013).
81. A. Z. Wang, R. Langer, and O. C. Farokhzad, "Nanoparticle delivery of cancer drugs," Annu. Rev. Med. 63, 185-198 (2012).
82. E. I. Altınoglu, T. J. Russin, J. M. Kaiser, B. M. Barth, P. C. Eklund, M. Kester, and J. H. Adair, "Near-infrared emitting fluorophore-doped calcium phosphate nanoparticles for *in vivo* imaging of human breast cancer," ACS Nano 2, 2075-2084 (2008).
83. D. B. Pink, W. Schulte, M. H. Parseghian, A. Zijlstra, and J. D. Lewis, "Real-time visualization and quantitation of vascular permeability *in vivo*: implications for drug delivery," PLoS One 7, e33760 (2012).
84. S. D. Perrault, C. Walkey, T. Jennings, H. C. Fischer, and W. C. Chan, "Mediating tumor targeting efficiency of nanoparticles through design," Nano Lett. 9, 1909-1915 (2009).
85. F. Yuan, M. Dellian, D. Fukumura, M. Leunig, D. A. Berk, V. P. Torchilin, and R. K. Jain, "Vascular permeability in a human tumor xenograft: molecular size dependence and cutoff size," Cancer Res. 55, 3752-3756 (1995).
86. A. L. Seynhaeve, S. Hoving, D. Schipper, C. E. Vermeulen, G. aan de Wiel-Ambagtsheer, S. T. van Tiel, A. M. Eggermont, and T. L. ten Hagen, "Tumor necrosis factor α mediates homogeneous distribution of liposomes in murine melanoma that contributes to a better tumor response," Cancer Res. 67, 9455-9462 (2007).
87. S. M. Moghimi, A. C. Hunter, and J. C. Murray, "Long-circulating and target-specific nanoparticles: theory to practice," Pharmacol. Rev. 53, 283-318 (2001).
88. M. Suzuki, K. Hori, I. Abe, S. Saito, and H. Sato, "A new approach to cancer chemotherapy: selective enhancement of tumor blood flow with angiotensin II," J. Natl. Cancer Inst. 67, 663-669 (1981).
89. W. Arap, R. Pasqualini, and E. Ruoslahti, "Cancer treatment by targeted drug delivery to tumor vasculature in a mouse model," Science 279, 377-380 (1998).
90. M. Wang and M. Thanou, "Targeting nanoparticles to cancer," Pharmacol. Res. 62, 90-99 (2010).
91. R.-D. Hofheinz, S. U. Gnad-Vogt, U. Beyer, and A. Hochhaus, "Liposomal encapsulated anti-cancer drugs," Anti-Cancer Drugs 16, 691-707 (2005).
92. G. M. van Dam, G. Themelis, L. M. Crane, N. J. Harlaar, R. G. Pleijhuis, W. Kelder, A. Sarantopoulos, J. S. de Jong, H. J. Arts, and A. G. van der Zee, "Intraoperative tumor-specific fluorescence imaging in ovarian cancer by folate receptor-[alpha] targeting: first in-human results," Nat. Med. 17, 1315-1319 (2011).
93. Y. Liu, Y.-M. Zhao, W. Akers, Z.-Y. Tang, J. Fan, H.-C. Sun, Q.-H. Ye, L. Wang, and S. Achilefu, "First in-human intraoperative imaging of HCC using the fluorescence goggle system and transarterial delivery of near-infrared fluorescent imaging agent: a pilot study," Transl. Res. 162, 324-331 (2013).
94. U. Prabhakar, H. Maeda, R. K. Jain, E. M. Sevick-Muraca, W. Zamboni, O. C. Farokhzad, S. T. Barry, A. Gabizon, P. Grodzinski, and D. C. Blakey, "Challenges and key considerations of the enhanced permeability and retention effect for nanomedicine drug delivery in oncology," Cancer Res. 73, 2412-2417 (2013).
95. C.-H. Heldin, K. Rubin, K. Pietras, and A. Östman, "High interstitial fluid pressure—an obstacle in cancer therapy," Nat. Rev. Cancer 4, 806-813 (2004).
96. R. Bonner and R. Nossal, "Model for laser Doppler measurements of blood flow in tissue," Applied optics 20, 2097-2107 (1981).
97. D. Weitz, J. Zhu, D. Durian, H. Gang, and D. Pine, "Diffusing-wave spectroscopy: The technique and some applications," Phys. Scr. 1993, 610 (1993).
98. N. Bosschaart, G. J. Edelman, M. C. Aalders, T. G. van Leeuwen, and D. J. Faber, "A literature review and novel theoretical approach on the optical properties of whole blood," Lasers Med. Sci. 29, 453-479 (2014).
99. S. Heer, K. Kömpe, H. U. Güdel, and M. Haase, "Highly Efficient Multicolour Upconversion Emission in Transparent Colloids of Lanthanide-Doped NaYF4 Nanocrystals," Adv. Mater. 16, 2102-2105 (2004).
100. G. Yi, H. Lu, S. Zhao, Y. Ge, W. Yang, D. Chen, and L.-H. Guo, "Synthesis, characterization, and biological application of size-controlled nanocrystalline NaYF4: Yb, Er infrared-to-visible up-conversion phosphors," Nano Lett. 4, 2191-2196 (2004).

2

Laser Speckle Contrast Imaging

2

Abstract Dynamic light scattering techniques obtain information about the medium of interest by measuring the intensity fluctuations in dynamically scattered coherent light. The intensity fluctuations relate to the medium dynamics. Laser speckle contrast imaging, laser Doppler flowmetry and diffusing wave spectroscopy make use of this principle to obtain information about tissue perfusion. In this chapter the techniques are introduced and in particular the theoretical background of laser speckle contrast imaging is given, followed by the identification of the essential aspects that need further investigation in order to enable quantitative blood flow velocity measurements.

2.1 Introduction

The clinical need for a non-invasive microcirculation imaging device at the bedside to monitor the onset and development of critical diseases was illustrated in Chapter 1. Besides non-invasive and compact, other preferential properties are continuous monitoring, and an instantaneous, reproducible and quantitative measurement of microcirculation functionality [1, 2]. Such a device could additionally be relevant for internal, surgical and oncologic medicine [3-8]. A clinically approved tool currently used for microcirculation monitoring at the intensive care unit (ICU) is the sidestream dark field (SDF) microscope. SDF videos contain a high level of detail to determine the relevant parameters such as vessel density and geometry; proportion of perfused vessels and microcirculatory heterogeneity [9]. However, the image analysis requires user-interaction, limiting its use at the bedside. In addition, accurate flow measurements require high-contrast images showing red blood cells (RBCs) and plasma gaps [10]. Fast flowing, out of focus, or fully RBC-filled vessels can therefore not be analyzed. An alternative method for measuring flow is based on the dynamical properties of scattered light, as introduced in Chapter 1. Techniques based on this approach do not depend on the aforementioned image properties and their flow sensitivity is based on different principles. In the next section their mechanisms and prospects as the favoured flowmetry techniques are discussed.

2.2 Dynamic Light Scattering techniques to measure blood flow

The notion that phase shifts in dynamically scattered coherent light give rise to measurable intensity fluctuations was discovered soon after the launch of the laser in 1960 [11, 12]. The intensity fluctuations are caused by the constructive and destructive interference of the electromagnetic waves (light) and are referred to as ‘speckles’. The cause of these phase differences is explained in two ways: by the Doppler-shift in the frequency of the scattered light (Laser Doppler Flowmetry, LDF [13]) and by the path length differences in the reflected light (Laser Speckle Contrast Imaging (LSCI) [14]) and Diffusing Wave Spectroscopy (DWS) [15]). In general, the temporal autocorrelation of the interference pattern (strictly speaking, the temporal autocorrelation of the electric field as detected by a stationary detector element) of the dynamically scattered light is related to the movement of the scattering particles.

In the case of LDF, the light scattered by moving particles undergoes a frequency shift (Doppler-shift) proportional to the velocity of the moving particle. This frequency shift is very small (10 - 100 kHz) compared to the high frequencies of light (100 THz), therefore the Doppler-shifted light is combined (‘mixed’) with a non-shifted reference beam resulting in a ‘beat’ frequency equal to the frequency shift [16]. This is called ‘heterodyne’ detection. In the case of flowing RBCs, however, not all the cells will have the same velocity but more likely the flow shows a velocity distribution about a mean value. Now the beat frequency will display a spread of frequencies, or a frequency spectrum, centred around the mean frequency shift. In addition, the reflected light from two RBCs with different velocities will also have slightly different Doppler shifts and therefore beat with each other. Thus, all cells together give rise to another self-beating frequency spectrum, centred around zero [17]. This is the homodyne signal detection. Even without a separate reference beam, a heterodyne signal is present from the self-mixing of non-shifted light reflected from static scatterers and the dynamically scattered light. Only for single scattered light

for which the exact angles between blood flow direction, and the incident and the reflected light are known the Doppler shift can be related to the flow velocity. In practice, this has been shown to be very complicated and troublesome [18]. Most commercial LDF devices do not use a separate reference beam and measure the self-mixing spectrum as a result of dynamic and static scattering in tissue [16]. In LDF the frequency spectrum is generated by recording the temporal intensity fluctuations of the interference pattern by a photodetector and calculating the temporal autocorrelation. By the Wiener-Khintchine theorem, the autocorrelation function (ACF) and the power spectral density (PSD) of the intensity (Doppler frequency spectrum) are the Fourier transform of each other [19]. A narrower ACF results in a broader frequency spectrum, and thus a larger Doppler frequency shift implicating a higher velocity. Usually the first moment of the intensity PSD is used as the designated measurement parameter, which is related to the speed of the scatterers and their concentration [20, 21].

The second description for the generation of a fluctuating interference (speckle) pattern is based on phase differences that arise from path length differences between detected photons scattered from different positions within the tissue. When the photons are scattered by moving structures such as flowing RBCs, the optical path lengths will change and the detected speckle pattern fluctuates, referred to as time-varying speckle. Techniques derived from this principle measure these fluctuations either directly (DWS) or indirectly (LSCI). The interference pattern resulting from either fluctuations in optical path lengths or from the fluctuations in frequency is identical, which is intuitively not obvious: the speckle explanation is based on the superposition of waves of the same optical frequency, whereas in the Doppler explanation the superimposed waves have different frequencies [22]. However, it can be shown mathematically that the two explanations lead to identical equations that link the intensity fluctuations to the tissue dynamics [17, 23] which was later confirmed by simulation and experiment [21, 24].

Similar to LDF, DWS measures the speckle intensity fluctuations of single speckles and calculates the temporal ACF [25]. Because DWS seeks to probe light travelling long path lengths in the diffusion regime it probes the photon correlation in the multiple scattering regime [26]. This is ensured by a distance of several centimetres between the illumination source and detector. This results in longer photon paths through tissue and deeper probing of tissue dynamics. Multiple scattering events with dynamic scatterers result in faster decorrelation of the photons. Consequently, speckle decorrelation happens on a shorter timescale and the ACF is measured at high sampling rates. The characteristic timescale for the decay of the ACF is referred to as the decorrelation time τ_c. The tissue dynamics and τ_c are inversely related, making τ_c an important measurement parameter in DWS.

Alternatively, the time-fluctuating speckle pattern can also be imaged as an ensemble of speckles using a camera. It is easy to see that a fluctuating pattern will look blurry in an image when the exposure time is long. The faster the fluctuations, the more blur in the imaged speckle pattern. This is the basic principle of laser speckle flowmetry techniques first introduced by Fercher and Briers [14]. The speckle blur, or speckle contrast, can be quantified mathematically since a blurred pattern will have a low standard deviation in intensity (σi) as compared to a sharp pattern, but the mean intensity ($<I>$) is unchanged. The speckle contrast K is therefore defined as the ratio $\sigma_i/<I>$ and depends on the integration time of the detector and the velocity of the scatterers and is valued between 0 and 1 [27]. Laser speckle flowmetry techniques

quantify the speckle contrast to measure or image blood flow and have been named laser speckle contrast analysis (LASCA [27], including the variations tLASCA (temporal) and sLASCA (spatial) [28]), laser speckle imaging (LSI [29, 30]), laser speckle contrast imaging (LSCI [31-34]), speckle-visibility spectroscopy (SVS [35]) and multi-exposure speckle imaging (MESI [36]), amongst others. In this thesis I refer to the technique as Laser Speckle Contrast Imaging - LSCI. As will be mathematically shown in Section 2.4 the contrast depends on the integration of the ACF over the exposure time. The measured quantity *K* is an indirect measurement of the ACF and relates to tissue dynamics, similar to the LDF and DWS techniques.

2.3 PRACTICAL DIFFERENCES BETWEEN LDF, DWS AND LSCI

The theoretical frameworks of the discussed dynamic light scattering techniques to measure blood flow are highly related. I will therefore summarize the main practical differences between the techniques and their applicability to microcirculation assessment. Techniques based on LDF and DWS measure the temporal autocorrelation in a single speckle directly at high sampling frequencies (~kHz) at one measurement point and need fast sampling photodiodes, CMOS cameras or photomultiplier tubes. In addition, in DWS the signal is usually low, which reduces the signal-to-noise ratio and makes detection sensitivity important. This makes the technical requirements of LDF and DWS more complicated compared to LSCI, which quantifies the temporal autocorrelation of speckles integrated over camera exposure times in the millisecond timeframe. For an increased accuracy of LSCI multiple frames and exposure times are desirable, which a standard CCD camera permits. In addition, LSCI is a full-field technique while for LDF scanning of the laser beam (and detector) is needed to obtain an image, making LDF imaging much slower (minutes versus sub-seconds). DWS has a high temporal resolution (single-point measurement), but a very low spatial resolution, compensated by a deep probing of tissue (> 1 cm deep) [26, 37, 38]. For this reason, DWS is not suitable for microcirculation imaging since the dominant decorrelation will be due to the deeper, larger and faster flowing vessels. Spatial resolution and probing depth are often interrelated via the wavelength of light and the distance between the light source and detector. Like DWS, LSCI and LDF operate in the near infrared window (relatively deep tissue penetration) but with shorter source detector separations and are estimated to measure flow at depths of several mm's [18, 39]. The spatial resolution of LSCI and LDF are similar, and depend on the detection and tissue geometry (e.g. numerical aperture (NA) of detection optics, scattering of tissue layers like skin). The spatial resolution of LSCI is slightly further reduced since the speckle contrast is calculated using several spatial speckles, although ergodicity allows the speckle contrast to be measured temporally as well [40, 41]. AAnother microcirculation imaging technique as introduced in Chapter 1 (1.3 Functional microcirculation imaging), is side-stream dark field (SDF) microscopy. The SDF microscope is a clinically approved hand-held video microscope that can image flowing red blood cells (RBCs) in the superficial microcirculation located below non-scattering tissue, such as the sublingual mucosa or organ surfaces. The contrast is obtained by illumination by a ring of green LEDs surrounding the central imaging tube, where green light is absorbed more by the RBCs as compared with the surrounding tissue. Therefore, the RBCs look like dark grey globules flowing through tissue. Within certain velocity limits, the RBCs can be tracked from frame to frame giving exact blood flow velocities, as well as vessel geometry and density parameters. The disadvantages of this technique are the insensitivity to high flows, the semi-automatic video processing algorithms and the necessity for imaging through non-scattering tissues, unlike for example skin. For this reason, we will continue to investigate

in Laser Speckle Contrast Imaging, which can resolve these issues as explained in the next section, as well as in Chapters 3 and 4. An overview of the discussed dynamic light scattering techniques, in addition to SDF microscopy, is given in Fig. 2.1

2.4 LASER SPECKLE CONTRAST IMAGING

The instrumental simplicity of LSCI makes it a favourable candidate for microcirculation monitoring. Since LSCI does not put stringent requirements on the detector, it can easily be combined with the clinical SDF microcirculation imager (Microscan, Microvision Medical Inc. The Netherlands) equipped with a CCD camera. For the results of Chapters 3 and 4 we modified the Microscan for integrated SDF-LSCI microscopy. This allowed for the direct comparison of the measured speckle contrast *K* and blood flow velocities in the microcirculation measured using SDF. The exact relationship between *K* and blood flow is a much discussed topic in laser speckle flowmetry.

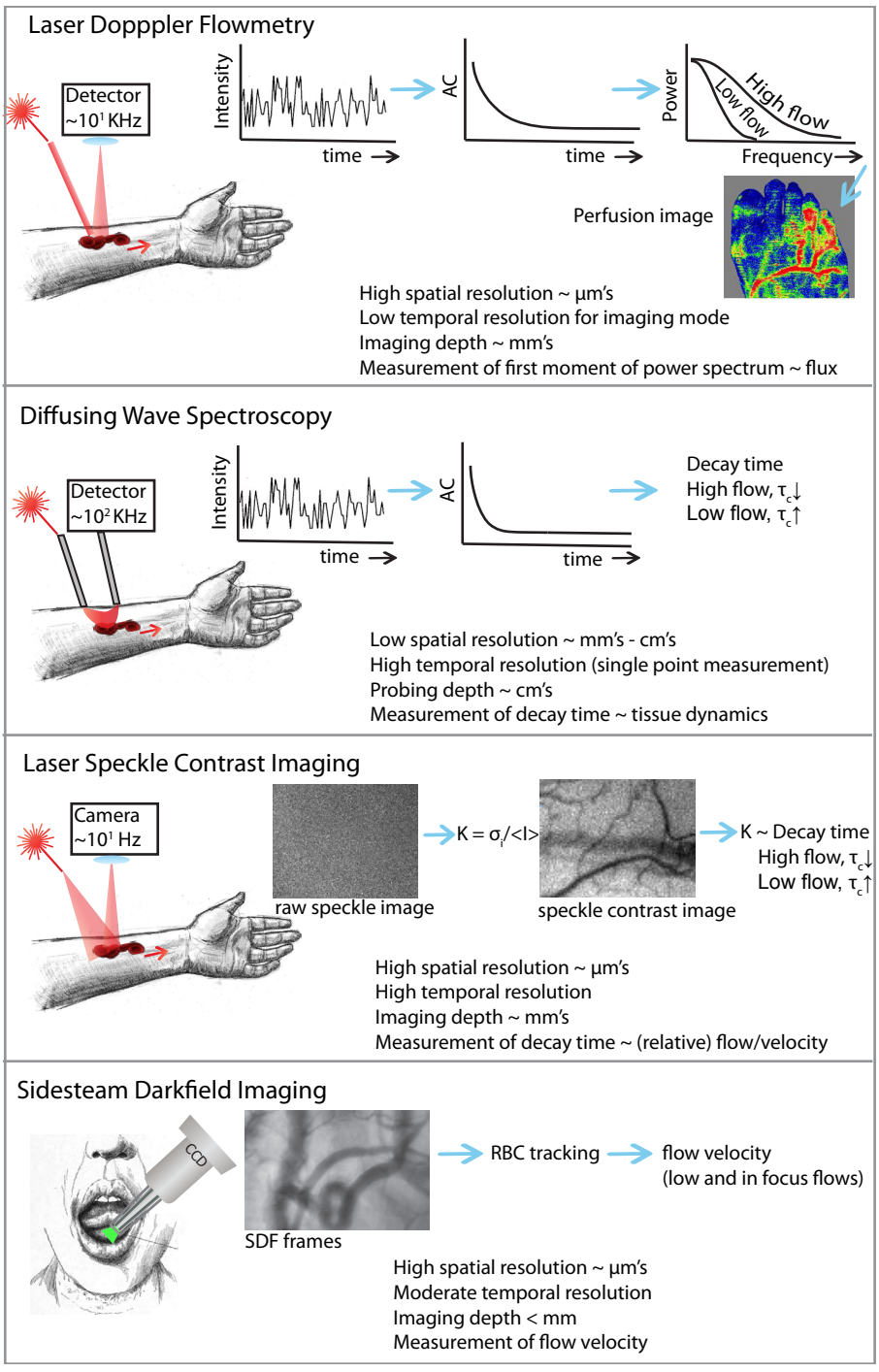

Fig. 2.1. | Schematic overview of blood flow imaging techniques. *Arm sketch adapted from Nobges, deviantART, LDF perfusion image adapted from Graduate School of Biomedical Sciences, Hiroshima University*

In Chapters 3 and 4 theoretical and experimental contributions to understand this complicated relationship are presented. Below, I start with the mathematical derivation of speckle contrast *K* from the ACF of the time-varying speckle pattern and introduce the challenges that are facing quantitative laser speckle flowmetry.

Goodman has shown that the spatial statistics of a time-integrated speckle pattern are related to the temporal statistics of speckle fluctuations [19]:

$$\sigma_s^2 = \frac{2}{T}\int_0^T \left(1-\frac{\tau}{T}\right) C_t(\tau) dt \tag{2.1}$$

here σ_s^2 is the spatial variance in the speckle pattern, T is the camera exposure time and $C_t(\tau)$ is the autocovariance of the temporal speckle intensity. Thus, the variance of the spatial intensity pattern depends on the time integrated autocovariance of the intensity fluctuations. Essentially, LDF and DWS measure the right-hand side of Eq. (2.1) while LSCI measures the left-hand side. $C_t(\tau)$ is defined as:

$$C_\tau(\tau) = \left\langle \left\{ I(t) - \langle I \rangle_t \right\} \left\{ I(t+\tau) - \langle I \rangle_t \right\} \right\rangle_t = \langle I(t) I(t+\tau) \rangle_t - \langle I \rangle_t^2 \tag{2.2}$$

Here $I(t)$ is the intensity measured at time t (or $t + \tau$), and $\langle ... \rangle_t$ is the time average. Assuming ergodicity, we can replace the time average/variance by the ensemble average/variance and vice versa (writing $\langle I \rangle$ and σ_i). Division by $\langle I \rangle^2$ relates Eq. (2.1) to speckle contrast *K* [14, 19, 35]:

$$K^2 = \frac{\sigma_i^2}{\langle I \rangle^2} = \frac{2}{\langle I \rangle^2 T}\int_0^T \left(1-\frac{\tau}{T}\right) C_\tau(\tau) d\tau \tag{2.3}$$

Substituting Eq. (2.2) in Eq. (2.3) gives:

$$K^2 = \frac{2}{\langle I \rangle^2 T}\int_0^T \left(1-\frac{\tau}{T}\right) \left\{ I(t) I(t+\tau) \right\} - \langle I \rangle^2 \, d\tau = \frac{2}{T}\int_0^T \left(1-\frac{\tau}{T}\right) \frac{\left\{ I(t) I(t+\tau) \right\}}{\langle I \rangle^2} - 1 \, d\tau \tag{2.4}$$

Though the speckle fluctuations are caused by electric field fluctuations, in practical set-ups the intensity fluctuations are measured. The normalized electric field autocorrelation function ($g_1(\tau)$) and the normalized intensity autocorrelation function ($g_2(\tau)$) are related through the Siegert relation [12]:

$$g_2(\tau) = 1 + \beta_M \left| g_1(\tau) \right|^2 \tag{2.5}$$

and are defined as:

$$g_1(\tau) = \frac{\left\langle E(t) E^*(t+\tau) \right\rangle_t}{\left\langle E(t) E^*(t) \right\rangle_t} \tag{2.6}$$

$$g_2(\tau) = \frac{\langle I(t)I(t+\tau)\rangle_t}{\langle I(t)\rangle_t^2} \tag{2.7}$$

Where β_M is a measurement-geometry specific constant [19], $E(t)$ represents the electric field at time t and $E^*(t)$ its complex conjugate. Finally, from equations (2.4)- (2.7) and the ergodicity principle we get the basic expression for K:

$$K(T) = \beta_M^{1/2}\left[\frac{2}{T}\int_0^T\left(1-\frac{\tau}{T}\right)\left|g_1(\tau)\right|^2 d\tau\right]^{1/2} \tag{2.8}$$

The assumption that Eq. (2.8) is valid for ergodic systems implies that the time and ensemble average of the speckle pattern are equal and K can be quantified using σ_i and $\langle I\rangle$ from image pixels in time (subsequent frames) and in space. However, if a purely static component is present in the scattered electric field this component will produce a constant speckle contrast independent of camera exposure time and in addition, this component will have different temporal and spatial statistics (e.g. a temporal σ_i of zero). In many practical LSCI geometries the static component needs to be taken into account. By defining the electric field as a summation of the fluctuating (E_f) and the static (E_s) component: $E(t) = E_f(t) + E_s(t)$, a modified Siegert relation was proposed [36, 42]:

$$g_2(\tau) = 1+\beta\left[\rho^2\left|g_1(\tau)\right|^2 + 2\rho(1-\rho)\left|g_1(\tau)\right| + (1-\rho)^2\right] \tag{2.9}$$

Which gives

$$K(T) = \beta_M^{1/2}\left(\frac{2}{T}\right)^{1/2}\left[\rho^2\int_0^T\left(1-\frac{\tau}{T}\right)\left|g_1(\tau)\right|^2 d\tau + 2\rho(1-\rho)\int_0^T\left(1-\frac{\tau}{T}\right)\left|g_1(\tau)\right| d\tau + (1-\rho)^2\right]^{1/2} \tag{2.10}$$

Where ρ is the fraction dynamic scattered light: $\rho = I_f / (I_f + I_s)$, with I_f the detected intensity of the fluctuating scattered light and I_s the detected intensity of the light scattered by static components. Parameters β_M and ρ depend on the measurement geometry and can be measured. To quantify the relation between K and blood flow dynamics an expression for the field ACF $g_1(\tau)$ is needed, which is parameterized by the characteristic decorrelation time of the scattered electric field, τ_c. In LSCI it is conventional to assume a Lorentzian form [$g_1(\tau) = \exp(-(\tau/\tau_c))$] for Brownian motion and a Gaussian form [$g_1(\tau) = \exp(-(\tau/\tau_c)^2)$] for directional motion. Substituting the appropriate form of $g_1(\tau)$ in Eq. (2.10) results in an analytical expression of $K(T)$ from which τ_c can be derived. This analytical expression is given in Chapters 3 and 4 (Eq. (3.6), Lorentzian and Eq. (3.7)/Supplementary Eq. (4.10), Gaussian).

From the above it is clear that accurate estimation of β_M and ρ is important, as well as choosing an appropriate model for of $g_1(\tau)$. Parthasarathy et al. [36] propose to use a multi-exposure speckle acquisition scheme to estimate β_M and ρ and τ_c accurately. It is commonly agreed that blood flow velocity and

τ_c are inversely proportional to each other, but the proportionality constant of this relationship is a topic of debate [24, 43], and *in vivo* quantification of the technique represents one of the challenges in LSCI. Since the integrated SDF-LSCI microcirculation imager can acquire raw speckle images and conventional SDF images of the same blood vessels, *in vivo* quantification is feasible. In Chapter 3 SDF-LSCI is explored using a multi-exposure acquisition scheme and assuming a Gaussian form of $g_1(\tau)$, for both an *in vitro* flow phantom and for the *in vivo* sublingual microcirculation. The relationship between $1/\tau_c$ and blood flow velocity is investigated, which gave interesting insight into the decorrelation by tissue dynamics relevant for LSCI. Another insufficiently explored area is the validity of the assumed forms of the ACF, often simply the Gaussian or Lorentzian form. In Chapter 4 $g_1(\tau)$ is revised within the theoretical frameworks of LDF and DWS, complemented by recent advances in the modelling of optical scattering of whole blood [44]. In addition, the influence of multiple scattering, a well-known bottleneck in LSCI (and also LDF) [45] is theoretically and experimentally assessed. The results are relevant to other dynamic light scattering flowmetry techniques for which the ability to accurately measure blood flow depends on the appropriateness of the assumed model for $g_1(\tau)$ and the accuracy in measuring $g_1(\tau)$, taking into account the optical properties of the scatterers and the geometry dependent multiple scattering in biological tissues. However, the acquisition simplicity, temporal and spatial measurement characteristics and automated analysis possibility of time-integrated speckle based methods (like LSCI) are advantageous for a non-invasive, compact, instantaneous and continuous microcirculation monitoring device.

2.5 References

1. A. Lima and J. Bakker, "Noninvasive monitoring of peripheral perfusion," Intensive Care Med. 31, 1316-1326 (2005).
2. M. D. Stern, D. L. Lappe, P. D. Bowen, J. E. Chimosky, G. Holloway, H. Keiser, and R. Bowman, "Continuous measurement of tissue blood flow by laser-Doppler spectroscopy," Am. J. Physiol. 232, H441-H448 (1977).
3. W. Groner, J. W. Winkelman, A. G. Harris, C. Ince, G. J. Bouma, K. Messmer, and R. G. Nadeau, "Orthogonal polarization spectral imaging: a new method for study of the microcirculation," Nat. Med. 5, 1209-1212 (1999).
4. A. Jaap, C. Pym, C. Seamark, A. Shore, and J. Tooke, "Microvascular Function in Type 2 (Non-insulin-dependent) Diabetes: Improved Vasodilation After One Year of Good Glycaemic Control," Diabet. Med. 12, 1086-1091 (1995).
5. M. Roustit and J.-L. Cracowski, "Non-invasive Assessment of Skin Microvascular Function in Humans: An Insight Into Methods," Microcirculation 19, 47-64 (2012).
6. K.-D. Schaser, U. Settmacher, G. Puhl, L. Zhang, T. Mittlmeier, J. Stover, B. Vollmar, M. Menger, P. Neuhaus, and N. Haas, "Noninvasive analysis of conjunctival microcirculation during carotid artery surgery reveals microvascular evidence of collateral compensation and stenosis-dependent adaptation," J. Vasc. Surg. 37, 789-797 (2003).
7. W. D. Strain, D. D. Adingupu, and A. C. Shore, "Microcirculation on a large scale: techniques, tactics and relevance of studying the microcirculation in larger population samples," Microcirculation 19, 37-46 (2011).
8. K. R. Mathura, G. J. Bouma, and C. Ince, "Abnormal microcirculation in brain tumours during surgery," The Lancet 358, 1698-1699 (2001).
9. D. De Backer, S. Hollenberg, C. Boerma, P. Goedhart, G. Büchele, G. Ospina-Tascon, I. Dobbe, and C. Ince, "How to evaluate the microcirculation: report of a round table conference," Crit. Care 11 (2007).
10. J. G. Dobbe, G. J. Streekstra, B. Atasever, R. Van Zijderveld, and C. Ince, "Measurement of functional microcirculatory geometry and velocity distributions using automated image analysis," Med. Biol. Eng. Comput. 46, 659-670 (2008).
11. J. Hecht, "Short history of laser development," Optical Engineering 49 (2010).
12. B. J. Berne and R. Pecora, Dynamic light scattering: with applications to chemistry, biology, and physics (Courier Dover Publications, 2000).
13. M. Stern, "*In vivo* evaluation of microcirculation by coherent light scattering," Nature 254, 56-58 (1975).
14. A. Fercher and J. Briers, "Flow visualization by means of single-exposure speckle photography," Opt. Commun. 37, 326-330 (1981).
15. D. Pine, D. Weitz, P. Chaikin, and E. Herbolzheimer, "Diffusing wave spectroscopy," Phys. Rev. Lett. 60, 1134 (1988).
16. P. Vennemann, R. Lindken, and J. Westerweel, "*In vivo* whole-field blood velocity measurement techniques," Experiments in fluids 42, 495-511 (2007).
17. J. D. Briers, "Laser Doppler, speckle and related techniques for blood perfusion mapping and imaging," Physiol. Meas. 22, R35 (2001).
18. Y. Aizu and T. Asakura, "Coherent optical techniques for diagnostics of retinal blood flow," J. Biomed. Opt. 4, 61-75 (1999).
19. J. W. Goodman, Speckle phenomena in optics: theory and applications (Roberts and Company Publishers, Greenwood Village, CO, 2007).
20. R. Bonner and R. Nossal, "Model for laser Doppler measurements of blood flow in tissue," Appl. Opt. 20, 2097-2107 (1981).
21. O. B. Thompson and M. K. Andrews, "Tissue perfusion measurements: multiple-exposure laser speckle analysis generates laser Doppler–like spectra," J. Biomed. Opt. 15 (2010).
22. V. V. Tuchin, Tissue optics: light scattering methods and instruments for medical diagnosis (SPIE press Bellingham, 2007)
23. J. D. Briers, "Laser Doppler and time-varying speckle: a reconciliation," JOSA A 13, 345-350 (1996).
24. M. J. Draijer, E. Hondebrink, M. Larsson, T. G. van Leeuwen, and W. Steenbergen, "Relation between the contrast in time integrated dynamic speckle patterns an the power spectral density of their temporal intensity fluctuations," Opt. Express 18 (2010).
25. D. Weitz, J. Zhu, D. Durian, H. Gang, and D. Pine, "Diffusing-wave spectroscopy: The technique and some applications," Phys. Scr. 1993, 610 (1993).
26. G. Dietsche, M. Ninck, C. Ortolf, J. Li, F. Jaillon, and T. Gisler, "Fiber-based multispeckle detection for time-resolved diffusing-wave spectroscopy: characterization and application to blood flow detection in deep tissue," Appl. Opt. 46, 8506-8514 (2007).
27. J. D. Briers and S. Webster, "Laser speckle contrast analysis (LASCA): a nonscanning, full-field technique for monitoring capillary blood flow," J. Biomed. Opt. 1, 174-179 (1996).
28. T. M. Le, J. Paul, and S. Ong, "Laser speckle imaging for blood flow analysis," in Computational Biology (Springer, 2010), pp. 243-271.
29. H. Cheng, Q. Luo, Q. Liu, Q. Lu, H. Gong, and S. Zeng, "Laser speckle imaging of blood flow in microcirculation," Phys. Med. Biol. 49, 1347 (2004).
30. P. Zakharov, A. Völker, A. Buck, B. Weber, and F. Scheffold, "Quantitative modeling of laser speckle imaging," Opt. Lett. 31, 3465-3467 (2006).
31. S. J. Kirkpatrick, D. D. Duncan, and E. M. Wells-Gray, "Detrimental effects of speckle-pixel size matching in laser speckle contrast imaging," Opt. Lett. 33, 2886-2888 (2008).
32. S. Yuan, A. Devor, D. A. Boas, and A. K. Dunn, "Determination of optimal exposure time for imaging of blood flow changes with laser speckle contrast imaging," Appl. Opt. 44, 1823-1830 (2005).
33. D. Zhu, W. Lu, Y. Weng, H. Cui, and Q. Luo, "Monitoring thermal-induced changes in tumor blood flow and microvessels with laser speckle contrast imaging," Appl. Opt. 46, 1911-1917 (2007).
34. Z. Wang, S. Hughes, S. Dayasundara, and R. S. Menon, "Theoretical and experimental optimization of laser speckle contrast imaging for high specificity to brain microcirculation," J. Cereb. Blood Flow Metab. 27, 258-269 (2006).
35. R. Bandyopadhyay, A. Gittings, S. Suh, P. Dixon, and D. Durian, "Speckle-visibility spectroscopy: A tool to study time-varying dynamics," Rev. Sci. Instrum. 76 (2005).
36. A. B. Parthasarathy, W. J. Tom, A. Gopal, X. Zhang, and A. K. Dunn, "Robust flow measurement with multi-exposure speckle imaging," Opt. Express 16, 1975-1989 (2008).
37. C. Cheung, J. P. Culver, K. Takahashi, J. H. Greenberg, and A. Yodh, "*In vivo* cerebrovascular measurement combining diffuse near-infrared absorption and correlation spectroscopies," Phys. Med. Biol. 46, 2053 (2001).
38. M. Ninck, M. Untenberger, and T. Gisler, "Diffusing-wave spectroscopy with dynamic contrast variation: disentangling the effects of blood flow and extravascular tissue shearing on signals from deep tissue," Biomedical optics express 1, 1502-1513 (2010).
39. K. Johansson, H. Ahn, J. Lindhagen, and O. Lundgren, "Tissue penetration and measuring depth of laser Doppler

flowmetry in the gastrointestinal application," Scand. J. Gastroenterol. 22, 1081-1088 (1987).
40. M. Draijer, E. Hondebrink, T. Van Leeuwen, and W. Steenbergen, "Review of laser speckle contrast techniques for visualizing tissue perfusion," Lasers Med. Sci. 24, 639-651 (2009).
41. P. Li, S. Ni, L. Zhang, S. Zeng, and Q. Luo, "Imaging cerebral blood flow through the intact rat skull with temporal laser speckle imaging," Opt. Lett. 31, 1824-1826 (2006).
42. D. A. Boas and A. K. Dunn, "Laser speckle contrast imaging in biomedical optics," J. Biomed. Opt. 15, 011109-011109-011112 (2010).
43. D. D. Duncan and S. J. Kirkpatrick, "Can laser speckle flowmetry be made a quantitative tool?," JOSA A 25, 2088-2094 (2008).
44. N. Bosschaart, G. J. Edelman, M. C. Aalders, T. G. van Leeuwen, and D. J. Faber, "A literature review and novel theoretical approach on the optical properties of whole blood," Lasers Med. Sci. 29, 453-479 (2014).
45. D. Briers, D. D. Duncan, E. Hirst, S. J. Kirkpatrick, M. Larsson, W. Steenbergen, T. Stromberg, and O. B. Thompson, "Laser speckle contrast imaging: theoretical and practical limitations," J. Biomed. Opt. 18, 066018-066018 (2013)

3

Quantitative Laser Speckle Flowmetry of the *In Vivo* Microcirculation using Sidestream Dark Field Microscopy

Adapted from:

A. Nadort, R. G. Woolthuis, T. G. van Leeuwen, and D. J. Faber, "Quantitative laser speckle flowmetry of the in vivo microcirculation using sidestream dark field microscopy," Biomedical optics express 4, 2347-2361 (2013).

My contribution to this publication:
Design and realization of all experiments, performing the experiments, supervising R.G.Woolthuis, data analysis, paper writing

ABSTRACT We present integrated Laser Speckle Contrast Imaging (LSCI) and Sidestream Dark Field (SDF) flowmetry to provide real-time, non-invasive and quantitative measurements of speckle decorrelation times related to microcirculatory flow. Using a multi-exposure acquisition scheme, precise speckle decorrelation times were obtained. Applying SDF-LSCI *in vitro* and *in vivo* allows direct comparison between speckle contrast decorrelation and flow velocities, while imaging the phantom and microcirculation architecture. This resulted in a novel analysis approach that distinguishes decorrelation due to flow from other additive decorrelation sources.

3.1 INTRODUCTION

The microcirculation comprises the smallest functional vessels of the vascular network, where blood and tissue interact to create an environment necessary for cell and tissue survival [1]. It provides the link between cellular processes and system physiology. Microcirculation imaging has been successfully applied in internal, surgical and intensive care medicine where its significance has become particularly apparent in the diagnosis and treatment of septic shock [2, 3]. Good image contrast and determination of functional parameters are key requirements for microcirculation imagers. Recently, sidestream dark field (SDF) video imaging has evolved from these clinical requirements [4] resulting in a handheld device, which captures light reflected from the subsurface tissue bed, focused onto a camera to visualize movement of red blood cells (RBCs) in the capillaries. High quality images can be acquired at locations where the microcirculation is superficial, such as mucosal tissue (e.g. sublingual), conjunctiva and organ surfaces.

Functional microcirculation parameters such as vessel geometry and density can be straightforwardly obtained from SDF images. The RBCs can be tracked to quantify the blood flow velocities within the vessels semi-automatically [5]. However, the maximum measurable flow velocities are limited by the frame rate of the camera (e.g. ~1 mm/s at 30 frames per second) [4, 5]. An alternative technique to quantify microcirculation dynamics is based on laser speckle photography [6], but only after digital cameras became readily available Laser Speckle Contrast Imaging (LSCI) increased in popularity [7-9]. Speckles are formed when coherent light is randomly reflected (scattered) and constructively or destructively interferes at the detector to form bright respectively dark spots ('speckles'). When the scatterers are in motion the speckle pattern fluctuates, resulting in blurring of speckles at the detector within a finite integration time. LSCI links the reduced speckle contrast to the dynamics of the scatterers (flowing RBC's). The speckle contrast depends on the combination of integration time and the decorrelation time of the speckle pattern. However, the quantitative relation between flow velocity and speckle contrast/decorrelation time remains a topic of debate [10]. On the other hand, the advantage of LSCI is the sensitivity to considerably higher flow velocities than SDF imaging (typically 10 mm/s for LSCI [11]).

Combining conventional SDF imaging with LSCI enhances the dynamic range of microcirculation perfusion measurements, and improves the quantification algorithm of perfusion. LSCI and SDF imaging have been shown to be sensitive to the same microcirculation perfusion dynamics, using the handheld SDF imaging system and a separate commercial LSCI system with different optics, magnification and resolution [12]. Here, we present an integrated system where both SDF and speckle contrast images can be obtained using one hand held SDF-LSCI system. This enabled us to acquire true RBC velocities (conventional SDF mode) and speckle contrast values (SDF-LSCI mode) of the same microcirculation region *in vivo*. We applied a multi-exposure acquisition scheme which has been shown to result in reliable estimates for speckle decorrelation times [11]. This dual-mode approach therefore provided fundamental insight in the quantitative relation between RBC flow velocities and time-integrated speckle contrast decorrelation. This resulted in the development of a novel speckle contrast analysis scheme that distinguishes decorrelation due to blood flow from other additive decorrelation sources, and is a first step towards absolute quantitative laser speckle flowmetry *in vivo*.

3.2 THEORY

After interaction of coherent light with tissue, each pixel on the camera receives light that has been scattered from various positions within the sample. The associated path length distribution leads to an interference amplitude that depends on the arrangement of the scattering medium with respect to the pixel, so that an image with randomly varying intensity (speckle pattern) is produced. Moving scatterers will naturally lead to fluctuations in the detected speckle intensity. Quantification of this fluctuation by calculating either temporal or spatial statistics of the speckle pattern provides information on the motion of the scatterers.

3.2.1 Temporal assessment of speckle dynamics

The rate of change of the speckle pattern is quantified through the characteristic decorrelation time(s) of the scattered electric field τ_C, which parameterize the electric field autocorrelation function $g_1(\tau) = \langle E^*(t+\tau)E(t)\rangle_t / \langle E(t)E^*(t)\rangle_t$, where $<...>_t$ is the time average This cannot be measured directly in most experiments so that in practice, the temporal autocorrelation of the detected intensity $g_2(\tau) = \langle I(t+\tau)I(t)\rangle_t / \langle I(t)^2\rangle_t$ is recorded. Both are related through the Siegert relation:

$$g_2(\tau) = 1 + \beta_M \left| g_1(\tau) \right|^2 \tag{3.1}$$

where β_M is a measurement-geometry specific constant discussed in Section 3.2.2. The characteristic time(s) of $g_1(\tau)$, can thus be obtained from measurements of $g_2(\tau)$ after proper assessment of β_M. For independent particles with isotropic dynamics, $g_1(\tau)$ is given in [13]:

$$|g_1(\tau)|^2 = \exp\left(-2q^2 \left\langle \Delta r^2(\tau) \right\rangle / 6\right), \tag{3.2}$$

where $q = 2k \sin(\theta/2)$, with k the wave number $k = 2\pi/\lambda$; λ the wavelength; and θ the angle between incident and reflected light. For low-NA detection optics in backscattering, $\theta \approx 180°$ and $q \approx 2k$§. The $<\Delta r^2(\tau)>$ is the mean-square displacement of the scatterer in time interval τ. Multiple sources of decorrelation can be present at the same time [10]. For example, particles in flow can also undergo Brownian motion due to finite temperatures. If Brownian motion is not affected by the velocity gradient, the total mean square displacement can be separated in a diffuse and convective part. The decorrelation of the scattered fields due to these two independent motions can then be treated separately [14]. For Brownian motion, $<\Delta r^2(\tau)> = 6D_b\tau$ [13] where D_b is the Brownian motion diffusion coefficient. For flows with a Gaussian velocity distribution, Bonner and Nossal [15] showed that $<\Delta r^2(\tau)> = <V^2>\tau^2$, where $<V^2>$ is the second moment of the velocity distribution. Neglecting other sources of decorrelation (e.g. rotations of the particles), we have:

$$\left|g_1(\tau)\right|^2 \approx \left|g_{1,Brown}(\tau)\right|^2 \times \left|g_{1,dir}(\tau)\right|^2 = \exp\left(-2\tau/\tau_{C,Brown}\right) \times \exp\left(-2\left[\tau/\tau_{C,dir}\right]^2\right), \tag{3.3}$$

§ This condition is often assumed in laser speckle flowmetry, but not always met. In Chapter 4, q will be calculated following Mie and Percus-Yevick scattering theories.

Both the Lorentzian and Gaussian form are encountered in the LSCI literature, often discussing which one is more appropriate [7, 9, 10, 16, 17]. However, the presence of multiple sources of decorrelation validates the use of a combinational model such as Eq. 3.3. Additionally, a sampled biological tissue volume likely consists of stationary structures and moving blood. The influence of the static component on $g_1(\tau)$ can be taken into account using a modified Siegert relation [11, 18, 19] introducing a dependence on $\rho = I_f/(I_f+I_s)$, with I_f the detected intensity of the fluctuating scattered light, I_s the detected intensity of the light scattered by static components.

3.2.2 Spatial assessment of speckle dynamics

Direct measurement of temporal statistics requires long acquisition times, or a small field of view, so that research has focused on spatial assessment of speckle dynamics. This approach relies on quantification of loss in speckle contrast due to temporal averaging of speckle fluctuations during the integration time of a camera. Speckle contrast K is defined as the ratio of the standard deviation (σ_I) to the mean ($\langle I \rangle$) of the intensity:

$$K = \frac{\sigma_i}{\langle I \rangle} \ . \tag{3.4}$$

Contrast K is related to the time integrated $g_1(\tau)$ [20]:

$$K(T) = \beta_M^{1/2}\left[\frac{2}{T}\int_0^T\left(1-\frac{\tau}{T}\right)\left|g_1(\tau)\right|^2 d\tau\right]^{1/2}, \tag{3.5}$$

where T is the exposure time of the camera and β_M is a factor propagating from Eq. (3.1). Although τ_c can be obtained from a measurement using a single T, it has been shown [11] that more robust estimates of τ_C can be obtained using a multi-exposure scheme, e.g. measuring $K(T)$ vs. T followed by non-linear curve fitting.

The probability density function of the measured intensity is a gamma-shaped PDF [20] with shape parameter $M = 1/\beta_M$, i.e. the maximum attainable speckle contrast $K_{max} = 1/\sqrt{M}$. A fully developed speckle pattern gives $K_{max} = 1$ ($\beta_M = 1$). In practice $K_{max} < 1$ due to depolarization; incoherence of the light source; vibrations in the experimental setup; etc. [7, 21, 22]. Another cause for reduced K_{max}, is failure to meet the Nyquist sampling criterion i.e. pixel size ≤ ½ speckle size (optical resolution in the camera plane).

An often used approximation is 'Brownian motion only' [6, 8, 11, 23], i.e. the first term in Eq. (3.3). Using the modified Siegert relation as before, Eq. (3.5) evaluates to:

$$K(T) = \beta^{1/2}\left[\rho^2\frac{\exp(-2x)-1+2x}{2(x)^2}+4\rho(1-\rho)\frac{\exp(-x)-1+x}{(x)^2}+(1-\rho)^2\right]^{1/2}+C_{noise} \tag{3.6}$$

where $x = T/\tau_c$ and C_{noise} an added noise term for measurement noise.

In case of directional dynamics, the second term of Eq. (3.3) is retained, and speckle contrast is given by

[16, 18]:

$$K(T)=\beta^{1/2}\left[\rho^2\frac{\exp\left(-2(x)^2\right)-1+\sqrt{2\pi}x\,erf(\sqrt{2}x)}{2(x)^2}+2\rho(1-\rho)\frac{\exp\left(-(x)^2\right)-1+\sqrt{\pi}x\,erf(x)}{(x)^2}+(1-\rho)^2\right]^{1/2}+C_{noise}\ . \quad (3.7)$$

The model choice has consequences for the retrieved τ_c and is a complicating factor in speckle contrast analysis [10]. A combinational model, as leading to Eq. (3.3) can be evaluated using e.g. Mathematica, but is not reiterated here because of the arguments in Section 3.2.4.

3.2.3 Relation between τ_C and V

Eq. (3.3) suggests an inverse linear relation between τ_C and V for both Brownian motion and directional flow, which has been observed in many independent experiments [8, 11, 24]. A common relation is $V = \lambda/(2\pi\tau_C)$, which reduces to approximately $V = 0.1/\tau_C$ [μm/ms] for visible laser light [21]. This relation differs by 1-2 orders of magnitude [9] from the analysis of Bonner [15] that takes into account the form factor of red blood cells, leading to $V = 3.5/\tau_{1/2}$ [μm/ms]. Also suggested is $V = \omega/\tau_C$; where ω is a measure of the point spread function of the system [10]. In the camera plane, ω corresponds to the minimal speckle size, and τ_C to the time it takes to "replace" a speckle pattern with an uncorrelated pattern. Yoshimura [25] gave an extensive overview of statistical properties of dynamic speckle patterns in different imaging geometries, demonstrating (again) an inverse relation between τ_C and V, but proportionality was highly dependent on the exact experimental layout. Imaging a speckle pattern on a camera, yields $V = r_s/M_{opt}\tau_C$, where r_s is the speckle size in the image plane and M_{opt} is the optical magnification of the imaging system. The relation between τ_C and V may thus depend on a combination of scatterer properties and imaging geometry, but remains unsettled. Another factor hampering quantification is multiple scattering by moving objects which reduces τ_C because of an apparent increase of $<\Delta r^2(\tau)>$ in a given time interval τ.

3.2.4 Practical considerations

Our preliminary *in vivo* measurements with the modified Microscan (see Fig. 3.1) showed that 'static tissue' also exhibits a non-negligible speckle decorrelation. We hypothesize that this is due to 1) dynamic processes encountered along the photon path before arriving at the image plane (tissue matrix, other vessels); 2) movement of muscles in the sublingual region (subject) and hand (operator) while holding the Microscan™. This 'offset' decorrelation is thus also present in data obtained from vessels in addition to the sought decorrelation due to flowing RBCs. Since, analogous to the derivation leading to Eq. (3.3), the total autocorrelation function is given by the product of the two (or more) autocorrelation functions we write:

$$g_{1,total}(\tau)=g_{1,flow}(\tau)\cdot g_{1,offset}(\tau)\ , \quad (3.8)$$

where *flow* refers to decorrelation due to blood flow and *offset* due to photon path dynamics and muscle movements. Likely, $g_{1,offset}$ is best modeled as random ("Brownian"). For simplicity we assume that a Gaussian form describes both processes, such that flow dynamics are characterized by the convolution

of two time constants:

$$\tau_{c,flow} = \tau_{c,offset} \cdot \tau_{c,total} \Big/ \left(\tau_{c,offset}^{\ 2} - \tau_{c,total}^{\ 2} \right)^{1/2}, \qquad (3.9)$$

where $\tau_{c,total}$ can be derived from a multi-exposure fit of K measured at the vessel region, while $\tau_{c,offset}$ can be measured at a tissue region adjacent to the vessel.

LSCI suffers from a trade-off between K-accuracy and spatial resolution, as K must be determined over a sufficient number of pixels. A practical approach [26-28] is to determine K in a small spatial region from subsequently acquired images, assuming ergodicity – ensemble statistics equal temporal statistics. Even if ergodicity is violated (e.g. the presence of a static fraction (1- ρ)) correct K-values are obtained as long as ρ is constant between frames, and the time between acquisitions is large compared to τ_C. It has been shown that a multi-exposure acquisition scheme and fit of Eq. (3.6) or (3.7) adequately corrects for differences in spatial and temporal sampling [11], and in this report we show similar assurance for spatiotemporal sampling.

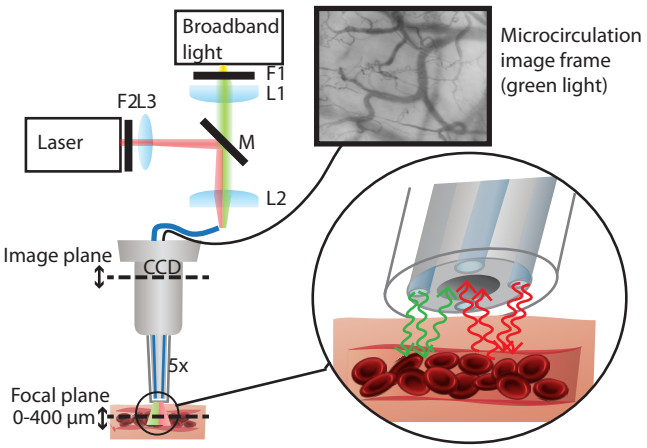

Figure 3.1 | Modified SDF-imaging system for non-invasive imaging of subsurface microcirculation in dual mode (SDF and SDF-LSCI). *Broadband green light (SDF) is highly absorbed by flowing RBCs, resulting in contrast between vessels and tissue. Red coherent light (SDF-LSCI) is scattered by tissue and moving RBCs, resulting in contrasting speckle dynamics between vessels and surrounding tissue. The optical set-up for sequential coupling of SDF light and SDF-LSCI light into the four optical illumination fibers involved 3 lenses (L1 = L2, f = 32 mm, L3, f = 10mm); two filters (F1, band pass interference filter, 550 ± 20 nm and F2, variable neutral density filter, OD 0.04 - 2.00); and a flip mirror M to swap between modes. A 5x magnifying lens system in the lens tube focuses the subsurface microcirculation image onto a CCD camera. Details of imaging modes are illustrated in the inset (green arrows: SDF, absorption; red arrows: SDF-LSCI, speckle).*

3.3 METHODS

3.3.1 Sidestream dark field and speckle microscope system

An SDF-imaging system (Microscan™, Microvision Medical, The Netherlands) was modified to allow flexible coupling between light sources for tissue illumination. The SDF-principle is based on a central imaging pathway surrounded by illumination light. Specular reflection is blocked while multiple scattered light illuminates the subsurface vessels and is focused on the camera. Absorption of green light by haemoglobin in red blood cells (RBCs) results in image contrast between tissue and flowing RBCs, an example can be viewed in Media 1[§]). In our system, four large multimode plastic optical fibers (POF ESKA™, fiber core 980 µm, NA 0.5) surrounding the central lens tube were used for light delivery. For conventional SDF

§ Media 1 can be downloaded at: http://www.opticsinfobase.org/boe/viewmedia.cfm?uri=boe-4-11-2347&seq=1

microcirculation imaging, green light provided by a band pass filtered (550 ± 20 nm) broadband light source (Xenon light, Karl Storz Endoskope, Germany) was coupled into the fibers. For SDF-LSCI imaging, red laser light (632.8 nm He/Ne, Spectra Physics, US) was coupled into the fibers using a flip mirror which simultaneously blocked the green light, see Fig. 3.1. To prevent overexposure a variable neutral density filter was placed in front of the laser. The tip of the Microscan™ including the four optical fibers is covered with a disposable sterile cap, and can be placed safely on organ and tissue surfaces. The camera plane can be axially translated with respect to the lens system within the tube (not shown, 5x magnification) which results in translation of the focal plane from tissue surface to a maximal depth of 400 µm. Light was detected with a monochrome camera (IEEE 1394, Guppy F-080B, Allied Vision Technologies, Germany), software controlled by self-written scripts (LabVIEW, National Instruments, US). By flipping the mirror between image sequences, conventional 'SDF-absorption mode' and 'LSCI mode' videos could be recorded sequentially. The principal imaging mechanisms are illustrated in the enlargement in Fig. 3.1: absorption of green light results in contrast between RBCs and tissue, while reflection (and minimal absorption) of red coherent light results in constructive and destructive interference patterns of which the temporal properties reflect the dynamic contrast between RBCs and tissue.

3.3.2 *In vitro* flow phantom imaging

We designed a sublingual tissue simulating optical phantom based on a protocol by De Bruin et al. [29]. Silicone elastomer (Sylgard® 184 Silicone Elastomer DOW/Corning, US) was mixed with titanium dioxide (TiO_2) particles (anatase form, Sigma Aldrich, US) to mimic tissue scattering ($[TiO_2]$ = 1 mg/ml, corresponding to a reduced scattering coefficient μ'_s = 1.5 mm^{-1} at 632.8 nm) [29]. A small glass tube (diameter d = 300 µm) was embedded in the silicone and connected to a reservoir of Intralipid® (2.5%), a scattering solution of fat particles, subject to a constant pressure to create a stable flow through the channel. The resulting flow velocity was estimated by measuring the throughput volume over an extended period of time. Fig. 3.2 shows an optical coherence tomography image of a cross-section of the flow phantom, together with a schematic drawing.

3.3.3 *In vivo* sublingual tissue imaging

In vivo sublingual microcirculation SDF and speckle images were obtained with the integrated SDF-LSCI device from a healthy volunteer. The handheld device was gently pressed against sublingual tissue ensuring undisruptive blood flow. The SDF and SDF-LSCI modes were alternated to record data from the same microcirculation region.

3.3.4 Data analysis

The SDF-LSCI device recorded 8-bit monochrome image frames, 1024 x 768 pixels at 30 frames-per-second (except for exposure times > 34 ms). Image and data analysis was performed using self-written software (Labview, National Instruments, US and Matlab, MathWorks, US). A prerecorded bias frame (average dark frame) was subtracted from each image frame before analysis, which made the noise-term in Eq. (3.6) and (3.7) negligible. The speckle contrast values recorded at multiple exposure times in the range 0.5 - 80 ms were calculated according to Eq. (3.4) using spatial and spatiotemporal sampling (see also Section 2.4), and were fitted to Eq. (3.6) and (3.7) using a nonlinear fitting procedure based on the

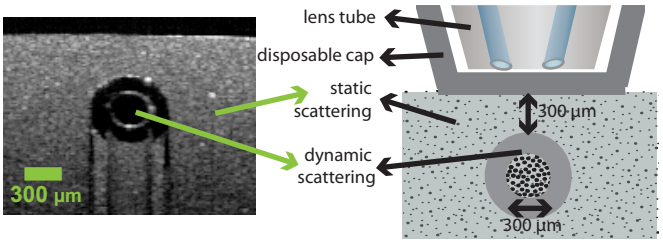

Figure 3.2 | Flow phantom design. *Optical coherence tomography image of cross-section of flow phantom (left), and schematic drawing of flow phantom (right).*

Levenberg-Marquardt algorithm. For our *in vitro* flow phantom measurements, β_M was a-priori estimated from the static part of the phantom, at short integration time T. The same approach is not possible for sublingual tissue measurements, since completely static regions are absent *in vivo* due to background tissue and/or probe movement. Therefore, for each individual vessel or tissue region β_M was estimated from an initial fit with fit parameters β_M, ρ and τ_c. We note that β_M is expected to be different in *in vitro* and *in vivo* situations, due to differences in optical properties affecting multiple scattering, depolarization, etc. which are likely to be different in both experiments. In subsequent evaluations of a given phantom or vessel/tissue region, β_M was kept fixed and ρ was estimated at $T >> \tau_c$, since the first two terms in Eq. (3.6)/(3.7) will be negligible ($K^2 = \beta_M (1-\rho)^2$). Finally, either Eq. (3.6) or (3.7) was fitted to the speckle contrast data with τ_c the only fitting parameter. Eq. (3.6) was used when no flow, but only Brownian motion was present in phantom experiments; Eq. (3.7) in all other cases. *In vivo*, determination of τ_c corresponding to flow regions and to non-flow regions allowed extraction of the speckle decorrelation time associated with flow only according to Eq. (3.9). Image frames acquired using conventional SDF-mode could be used to measure the blood flow velocities, using commercially available software (Automated Vascular Analysis, AVA3.0, Microvision Medical, The Netherlands).

3.4. RESULTS

3.4.1 Validation of SDF-LSCI device

Following Section 3.2.2 the intensity PDF of a static speckle pattern determines the maximum attainable speckle contrast. Fig. 3.3a shows the intensity PDF of the speckle pattern resulting from the static part of the flow phantom imaged with SDF-LSCI (green triangles), and the black line represents a gamma-PDF with $M = 2.2$ [20, 30]; the maximum contrast is $K_{max} = 0.67$ and $\beta_M = 0.45$. Spatial integration and undersampling of speckles can also reduce speckle contrast, therefore we estimate our speckle size using the second order statics of the intensity distribution [31, 32], such as the power spectral density (PSD) and the normalized autocovariance of the intensity in the spatial and the frequency domain respectively (Figs. 3.3b and 3.3c). The measured PSD (Fig. 3.3b) straightforwardly demonstrates that the speckles are sampled above the Nyquist frequency because there is no signal content at the maximum spatial frequency. More quantitatively, Alexander et al. calculate the average speckle diameter as half the full width of the autocovariance function [30], while Goodman relates the average size of a speckle to the 'equivalent area' of the normalized 2D autocovariance function [20], and Kirkpatrick et al. examine the FWHM of the autocovariance function to estimate the minimum speckle size [31]. Fig. 3.3c shows the normalized autocovariance of the speckle intensity with an equivalent area of ~2.5 pixels and a full width of ~5 pixels; resulting in a speckle size of 2.5 pixels. We estimated the FWHM of the PSD by fitting a Gauss-

ian and calculated the corresponding FWHM of the (also Gaussian) autocovariance function according to $FWHM_{autocov} = 8\ln(2)/FWHM_{PSD} = 2.2$ pixels. It is thus assured that the speckles are adequately sampled above the Nyquist frequency, with an estimated minimum speckle size ~2.2 pixels (10.2 µm) and average speckle size ~2.5 pixels (11.6 µm).

Lastly, the temporal behaviour of the light source and light delivery by multimode fibers is investigated. The Spearman correlation coefficient of subsequent image frames (T = 1 s), recorded from a static phantom region, showed a strong correlation ($r > 0.5$) up to 5 seconds. In view of the expected speckle decorrelation times *in vivo* this is sufficiently long.

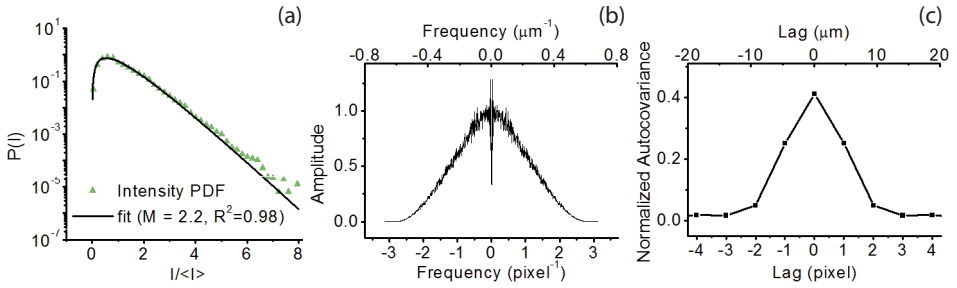

Figure 3.3 | First and second order statistics of the speckle intensity pattern *recorded using the static part of the flow phantom and an exposure time T = 1 ms.* ***(a)*** *Intensity probability density function (PDF) of static speckle pattern (green triangles) and plot of gamma-PDF with M = 2.2 (black line)* ***(b)*** *Power spectral density (PSD) of the static speckle intensity pattern showing sampling above the Nyquist frequency.* $FWHM_{PSD} \approx 2.5$ *pixel*$^{-1}$. ***(c)*** *Normalized autocovariance of static speckle intensity pattern, full width ≈ 5 pixels, equivalent area ≈ 2.5 pixels,* $FWHM_{autocov.} \approx 2.2$ *pixel.*

3.4.2 Validation of speckle contrast measurement

Accurate estimation of *K* benefits from a large number of sampled speckles and thus a large spatial region size for calculation of $\langle I \rangle$ and σ_i. The estimated *K*-value is reduced with respect to its true value for a small region-size to speckle-size ratio and the uncertainty in *K* is larger [27, 28, 32]. Large spatial regions result in a reduced spatial resolution. Spatiotemporal sampling can alleviate this resolution loss by (also) averaging over temporal pixels. In microcirculation imaging both spatial and temporal resolution are important, therefore we defined a spatiotemporal local region [27, 28].

To validate *K*-estimation we recorded 20 *in vitro* and *in vivo* images (T = 1 ms) and a large area representing the center of the flow channel respectively vessel was selected for which constant flow (thus constant *K*) was assumed. The flow velocity in the channel was 7 mm/s while that in the vessel was <2 mm/s resulting in lower absolute speckle contrast values for the channel compared to the vessel. To determine the smallest local region size that still gives an accurate estimation of *K* we varied the number of pixels in the spatial ($N_s \times N_s$) and temporal (N_t) dimension. For the varying local region sizes ($N_s \times N_s \times N_t$ pixels) *K*-values were calculated for the selected channel and vessel area (see Fig. 3.4a). Next, the mean $\langle K \rangle$ and coefficient of variance ($CV = \sigma_K/\langle K \rangle$) were determined, where σ_K is the standard deviation in *K*. For the largest local region size a total of 45 *K*-values could be obtained, thus, for fair comparison 45 *K*-values were selected for each local region size to calculate $\langle K \rangle$ and CV. The global *K*-value was calculated from all pixels comprising the area representing the channel respectively vessel in the raw speckle image, and is regarded as the 'true' *K*-value. In Fig. 3.4b the results for $\langle K \rangle$ *in vivo* and *in vitro*

are plotted as a dependency on N_s for 4 different N_t's, with global *K* represented by the dashed line. In Fig. 3.4c and 3.4d, the obtained CV is plotted for *in vitro* respectively *in vivo* *K*-values. As expected, the estimated <*K*> converges to the global value with increasing region size, and the CV decreases. Fig. 3.4 also shows that for a scenario with a large fraction of static scatterers, like the flow phantom, the estimated <*K*> is mostly dependent on the spatial dimension N_s, although the CV of <*K*> depends on both N_s and N_t. Based on Fig. 3.4 we defined our local region for subsequent analysis to be 7 x 7 x 20 ($N_s \times N_s \times N_t$) pixels, which means a negligible underestimation of *K* and a CV below 8%, while keeping the spatial resolution at 7 µm.

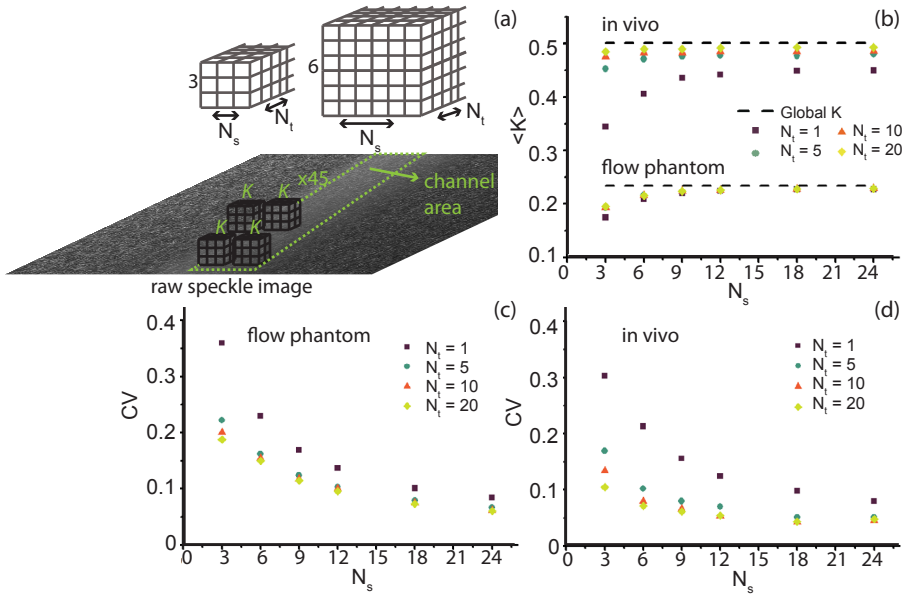

Figure 3.4 | Validation of local region size for accurate measurement of speckle contrast K. ***(a)*** *Schematic representation of local region size, where N_s is the number of pixels in the spatial dimension and N_t in the temporal dimension (total number of pixels: $N_s \times N_s \times N_t$) for which K is calculated.* ***(b)*** *Mean <K>, as calculated from 45 K-values selected in the processed speckle contrast image from the channel (in vitro) or vessel (in vivo) area. The dashed line represents the global K value.* ***(c)*** *+* ***(d)*** *Coefficient of variance ($CV = \sigma_K/\langle K \rangle$), where σ_K is the standard deviation in the 45 K-values. Both <K> and CV are plotted versus N_s, for 4 different temporal dimensions N_t. All images were recorded at exposure time 1 ms.*

3.4.3 SDF-LSCI *in vitro:* flow phantom

The flow phantom enabled recording of raw speckle images for a large range of Intralipid® flows (in the range V = 0 - 20 mm/s) and exposure times (0.5 - 80 ms). The raw speckle images were converted to speckle contrast images using a local region of 7 × 7 × 20 ($N_s \times N_s \times N_t$) pixels. In Fig. 3.5a the multi-exposure *K*-values are plotted for five different flow velocities and Brownian motion, as well as for a static (non-channel) region of the phantom. The flow data points are fitted to Eq. (3.7) (Gaussian autocorrelation function), while the Brownian motion data is fitted to Eq. (3.6) (Lorentzian autocorrelation function), $\langle R_{adj}^2 \rangle$ averaged over all 9 fits = 0.86 ± 0.08. β_M was estimated at 0.33, and ρ at 0.6 ± 0.02. To verify that spatiotemporal sampling resulted in a comparable fitting outcome compared to spatial sampling, we also estimated *K*-values using a spatial local region consisting of an equal amount of pixels (31 × 31 instead of 7 × 7 × 20) and repeated the same fitting procedure. Again, the goodness of fit was high ($\langle R_{adj}^2 \rangle$ averaged over all 9 fits = 0.94 ± 0.03). The obtained fitting parameter τ_c from both sampling procedures is plotted in Fig. 3.5b as a dependency of flow velocity. Fig. 3.5b shows that $1/\tau_c$ follows a linear relationship versus flow velocity for velocities up until 12 mm/s (r^2 = 0.99). The slope and intercept [95% upper CI - lower CI] of the linear fit were for the spatially sampled data: 2.7 [2.3 - 3.0]

[μm^{-1}] (slope) and 1.3 [-1.2 - 3.8] [ms^{-1}] (intercept), and for spatiotemporally sampled data: 2.4 [2.0 - 2.7] [μm^{-1}] (slope) and 1.8 [-0.7 - 4.2] [ms^{-1}] (intercept). The presence of static scatterers (as in the flow phantom) diverges the estimate of *K* when sampled spatially compared to spatiotemporally [18]. As can be seen in Fig. 3.5b, the absolute τ_c values from fitting the spatially and spatiotemporally sampled multi-exposure curves are similar (difference in slope linear fit <10%). Thus, the adopted model based on the modified Siegert relation properly corrects for the presence of a static component in the speckle images in the SDF-LSCI geometry, as was shown for other geometries before [11].

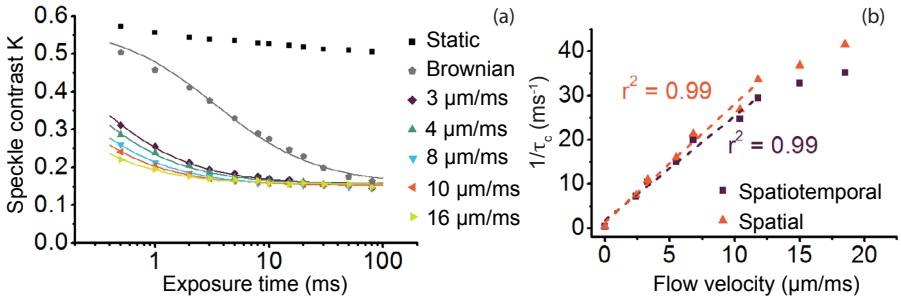

Figure 3.5 | Flow phantom speckle decorrelation results. (a) *Multi-exposure speckle contrast values (data points) and corresponding fit (lines) for several different flow velocities. The K values (N_s = 7, N_t = 20) are fitted to Eq. (3.7) for the flow data, while Eq. (3.6) is fitted to the Brownian motion data.* ***(b)*** *Fit parameter τ_c (plotted as $1/\tau_c$) from multi-exposure speckle contrast fits for several flow velocities between 0 - 20 μm/ms (mm/s), applying a spatiotemporal (purple squares) and a spatial (orange triangles) local region, consisting of 7×7×20 and 31×31 pixels respectively, and its linear fit (dashed line).*

3.4.4 SDF-LSCI *in vivo:* sublingual microcirculation

The *in vivo* data set consists of videos of several regions of the sublingual microcirculation acquired in SDF and SDF-LSCI mode sequentially, recorded with multiple exposure times (in the range 0.5 - 80 ms) for the SDF-LSCI mode. To illustrate the recording and analysis procedure and resulting processed images, a video is shown in Media 2 (1.6 Mb) and Media 3 (7.9 Mb)[§] and Fig. 3.6. Fig. 3.6 shows four panels each representing the same area of sublingual microcirculation. Fig. 3.6a and 3.6b (top left and top right panel in Media 2 and 3) represent unprocessed conventional SDF and raw speckle images respectively. The corresponding processed *K*-image at exposure time 10 ms is shown in Fig. 3.6c. In Media 3 (full video) raw speckle images and processed SDF-LSCI images are shown for T = 1, 2, 10, 20 and 50 ms consecutively, each as 2 second videos, and Media 2 only for T = 10 ms. Note that to enhance the contrast in Fig. 3.6c the scale bar for speckle contrast *K* ranges from 0.1 - 0.4, while in Media 2 and 3 (bottom left panel) the *K*-scale bar ranges from 0 - 1 to accommodate for *K*-values from short and long exposure times. To increase the spatial and temporal visualization, the raw SDF-LSCI videos in Media 2 and 3 (top right panel) were processed for each pixel (with local region N_s = 7, N_t = 20), thus only every 7th *K*-value in space and every 20th *K*-value in time are independent. For each exposure time 150 frames were recorded, consequently each pixel represented an average of 7 *K*-values to perform a multi-exposure fit (Eq.(3.7)), resulting in a $1/\tau_c$ map of the sublingual microcirculation region as shown in Fig. 3.6d and bottom right panel of Media 2 and 3.

To average the physiological variation in flow, SDF videos of 5 seconds were captured on average 5 times (at least twice) for each vessel before, during and after multi-exposure laser speckle imaging. SDF

§ Media 2 can be dowloaded at: http://www.opticsinfobase.org/boe/viewmedia.cfm?uri=boe-4-11-2347&seq=2 and the full version Media 3 at: http://www.opticsinfobase.org/boe/viewmedia.cfm?uri=boe-4-11-2347&seq=3

and SDF-LSCI images were recorded for 5 different sublingual regions in total. The minimum blood flow recoded was 0.2 mm/s and the maximum was higher than the reliable measurement range (>1.2 mm/s) using the RBC tracking algorithm in AVA3.0, resulting in reliably measurements for 15 out of 19 analyzed vessels. A multi-exposure speckle acquisition scheme (0.5 - 80 ms) was performed twice for each vessel, and for each exposure time 150 frames were recorded (≥ 5 sec) again averaging for physiological heterogeneity in flow. In these processed *K*-images for each vessel at least 25 (in space) x 15 (in time) independent *K*-values were selected to calculate mean <*K*>. The standard deviation in *K*-values was between 1 and 10% with an average of 4%. In Fig. 3.7a three examples of multi-exposure *K*-curves and their corresponding fit result (Eq.(3.7)) are shown for three blood vessels, ranging from 0.2 - 1.1 mm/s. We note that the maximum *K*-value of the multi-exposure speckle contrast curves *in vivo* (Fig. 3.7a) is higher than the static data points in Fig. 3.5a, likely due to differences in β_M as discussed in Section 3.3.4. The goodness of fit was high, $<R_{adj}^2>$ averaged over all 19 fits = 0.98 ± 0.01. The average value of β_M was 0.44 ± 0.06, and ρ 0.85 ± 0.02.

A bar plot of $\tau_{c,flow}$ according to Eq.(3.9) versus *in vivo* blood flow velocity is shown in Fig. 3.7b. Due to physiological variance in blood flow velocity we grouped the vessels, where each group consisted of minimally 3 vessels. Subscribing to our hypothesis, the correlation between blood flow velocity and $1/\tau_c$ was higher for the corrected $\tau_{c,flow}$ (r^2 = 0.95) than the uncorrected $\tau_{c,total}$ (r^2 = 0.40) for the grouped vessels. The slope and intercept [95% upper CI - lower CI] of the linear fit were for $1/\tau_{c,flow}$ versus flow: 0.32 [0.19 - 0.44] [μm^{-1}] (slope) and 0.37 [0.29 - 0.44] [ms^{-1}] (intercept). In addition, $\tau_{c,total}$ (uncorrected vessel τ_c) correlated highly to $\tau_{c,offset}$ (adjacent tissue region) (r^2 = 0.99).

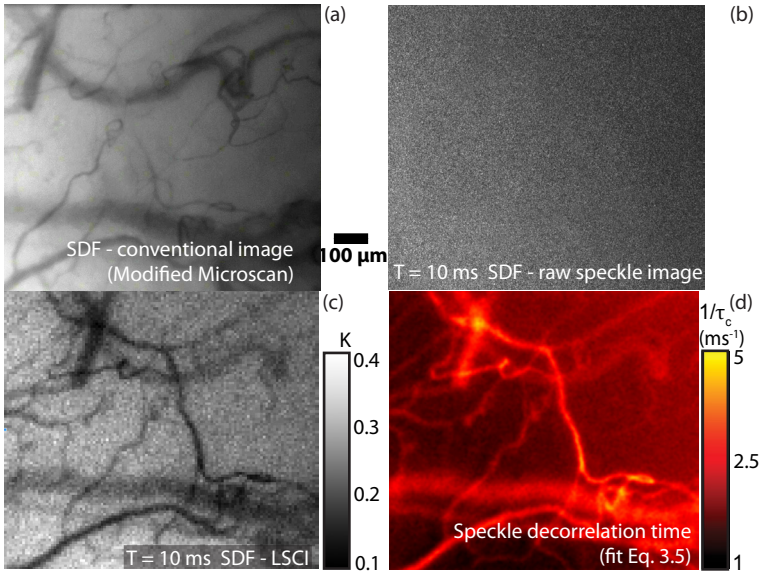

Figure 3.6 | In vivo SDF-LSCI recording and analysis procedure. ***(a)*** *Typical SDF image of sublingual microcirculation.* ***(b)*** *Raw speckle image and* ***(c)*** *processed K-image (N_s = 7, N_t = 20) of same region as in (a), recorded at T = 10 ms. For each pixel and exposure time, K was estimated to enable a pixel wise multi-exposure curve fit (Eq.(3.7)), resulting in a $1/\tau_c$ map of the same region as in (a), shown in* ***(d)****. In Media 2 and 3 the four panels are presented as a video, showing flowing RBC's (top left), raw speckle (top right) and speckle contrast (bottom left) images, and a still frame (bottom right) of the corresponding $1/\tau_c$ map. Media 2 represents SDF-LSCI at T = 10 ms, while Media 3 represents SDF-LSCI at T = 1, 2, 10, 20 and 50 ms consecutively.*

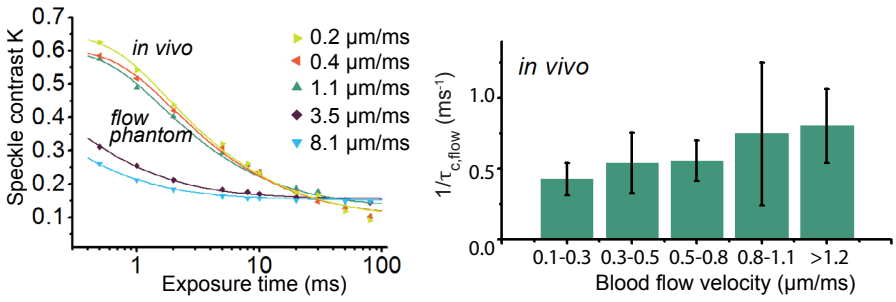

Figure 3.7 | In vivo SDF-LSCI results. (a) *Multi-exposure K-values (data points) and corresponding fit (lines) for several different flow velocities in vivo (upper curves). For comparison two in vitro multi-exposure K-curves are also plotted (lower curves). Eq. (3.7) is used as fitting model.* ***(b)*** *Bar plot of fit parameter $\tau_{c,flow}$ (represented as $1/\tau_{c,flow}$) of 19 in vivo blood vessels, corrected according to Eq. (3.9). The vessels were grouped in five different velocity ranges, with minimally 3 vessels per group.*

3.5 DISCUSSION

We validated sidestream dark field laser speckle contrast imaging (SDF-LSCI), for functional microcirculation imaging *in vivo* based on contrast due to RBC-concentration (absorption of green light, conventional SDF-mode) and on contrast due to RBC-flow (reflection of coherent light, SDF-LSCI mode). SDF-LSCI is sensitive to a large range of flows, from sub-mm/s to effectively unlimited velocities, making it a suitable tool to image low flows in angiogenic microvessels (wound healing, tumor neovascularization), or for high blood flow imaging during hyperthermia [33, 34]. A linear relationship between $1/\tau_c$ and flows up to 12 mm/s (equivalent to $\tau_c > 0.03$ ms) was found *in vitro*, suggesting that SDF-LSCI can be used to quantify changes in the microcirculation during the development of sepsis [3].

3.5.1 SDF-LSCI: a quantitative tool?

Duncan et al. highlighted 5 issues hindering LSCI to become a quantitative tool [10].

1. "a persistent erroneous formula expressing contrast as a function of integrated instantaneous covariance of intensity" – As pointed out by Bandyopadhyay [24], for robust absolute flow measurements the correct derivation is essential and thus applied in this study (Eq. (3.5)).

2. "the inappropriate use of the Lorentzian field correlation relationship" - Differences in τ_c fitted with Eq. (3.6) or (3.7) (Gaussian or Lorentzian) were small *in vitro* (data not shown), but since the error induced by incorrect autocorrelation model is more significant for low flows (small T/τ_c ratio) [17], for the subsequent *in vivo* analysis the Gaussian model, appropriate for directional flow, was applied in this study.

3. "a tendency to operate in the long-exposure asymptotic regime and the subsequent lack of sensitivity" - Fig. 3.5a shows that high flow velocities in the phantom experiment allowed only fitting the tail of the multi-exposure curve. The reduced linearity of $1/\tau_c$ vs. V for higher velocities (Fig. 3.5b) could thus be caused by a large T/τ_c ratio in the applied exposure range. Increasing the intensity to allow for shorter T is expected to result in an increased linear regime. For our *in vivo* data at $T = 0.5$ ms, $T/\tau_{c,total}$ is well below 1 and the speckle contrast is close to K_{max} (high sensitivity [10]).

4. "a common assumption that the requirements of quasi-elastic light scatter (QLS) and LSCI measurements are the same" - In the optimal QLS measurement, the speckle size matches the pixel size [7, 23]. However, in LSCI the speckle contrast (thus $<I>$ and σ_i) is highest when speckles are truthfully imaged. Fig. 3.3 shows that for the SDF-LSCI instrument we assure that the speckles are sampled above the Nyquist frequency, with an average speckle size of ~2.5 pixels. Thompson et al. showed that K continues to increase above Nyquist sampling, and is close to maximum at 3 pixels/speckle [32], but that any reduction in K is properly corrected for by a 'linear system factor', i.e. β_M.

5. "the oft-cited, nonphysical association between the decorrelation time and its associated flow velocity" - The key feature of the modified SDF-LSCI tool is the accessibility to speckle decorrelation times and actual blood flow velocities simultaneously. Having preliminary quantitative *in vivo* $1/\tau_c$ and absolute flow data in hand, investigating this relationship was plausible. The aforementioned association refers to $\tau_c = \lambda/2\pi V \approx 0.1/V$ [ms]. Interestingly, the (uncorrected) $\tau_{c,total}$ found *in vivo* was between 0.8 - 3 ms which according to this relation corresponds to a flow of 0.03 - 0.13 mm/s. Without knowledge of actual RBC velocities this seems a plausible range for microvessels, however the results of Section 3.4.4 show that using the uncorrected $\tau_{c,total}$ there is low correlation with flow velocity ($r^2 = 0.40$). After correction for offset decorrelation an improved relation between flow and τ_c could be established ($r^2 = 0.95$), Fig 3.7b. Two other suggested relationships between velocity V and τ_c exist in literature (Section 3.2.3). Adapting the model by Duncan et al. based on the PSF for this geometry results in $\tau_c = 4.2/V$ [ms] [10]. For our *in vivo* data (first 4 bars in Fig. 3.7b) we find $\tau_c = 3.3/V$ [ms], approaching the PSF-model. Conversely, phantom experiments yielded $\tau_c = 0.4/V$ [ms], significantly deviating from this model. The decrease in proportionality constant may be due a larger influence of photons that are multiply scattered from moving scatters, caused by a larger channel ($d = 300$ µm vs. $d = 30 \pm 16$ µm *in vivo*) and smaller scatterers (<700 nm fat particles vs. >10× larger RBCs [35]). The third suggested model [15], taking into account the size of scatterers yields $\tau_{1/2} \approx 3.5/V$ [ms] for RBCs (close to our values); our proportionality constant *in vitro* corresponds to a particle of diameter $D = 0.5$ µm, in excellent agreement with our recent determination of the effective scattering size for Intralipid® particles [35].

The different physical principles underlying the proposed models confound quantitative flow measurements, further complicated by possible multiple scattering and heterogenous flow profiles. However, we believe our approach addresses all of the five issues discussed above. Most importantly, the dual-mode operating SDF-speckle imager is a valuable method to increase the knowledge of the relationship between τ_c and V *in vivo*.

It should be noted that SDF-LSCI as presented here is used as a truly integrated technique: the SDF- capability is used to locate vessel and tissue regions and measure vessel diameters, while the LSCI-capability is used to obtain decorrelation times of the tissue dynamics corrected using the geometry information. In practice, the SDF-mode is crucial to enable quantitative LSCI, which is not ideal as SDF is limited to measurements through non-scattering tissues such as mucosal tissues and organ surfaces. In current LSCI the contrast is not high enough to establish the vessel geometry, especially for low flows. However, the insights gained from the SDF-LSCI combination may lead to improved LSCI techniques that have an increased contrast and become true quantitative flow imagers

3.5.2 Comments on hypothesis

Our proposed separation of $\tau_{c,offset}$ and $\tau_{c,flow}$ for *in vivo* measurements in Section 3.2.4 improved the correlation between actual flow velocity and $1/\tau_{c,flow}$, but needs further verification and explanation of the remaining intercept of $1/\tau_c$ at zero flow (fig. 3.7b). For our *in vitro* data (Fig. 3.5b), the intercept of the linear fit of $1/\tau_c$ versus V was 1.8 ms^{-1}, with 95% confidence range (-0.7 – 4.2). This result nearly matches the value of $1/\tau_c$ found for Brownian motion of Intralipid® at V=0 in the flow phantom channel: $1/\tau_c$=0.4 (0.32 - 0.53) ms^{-1}. Following Eq. (3.3), we interpret the dynamics in flowing Intralipid® as a combination of Brownian motion and directional flow, where the total autocorrelation function is given by the product of the individual functions [10]. Applying our analysis of Eq. (3.9) (all processes have Gaussian autocorrelation functions), we interpret decorrelation due to Brownian motion as an offset, e.g. $\tau_{c,offset} = \tau_{c,Brown}$. As there were no other sources of decorrelation in our phantom setup, this analysis indeed yields $1/\tau_{c,flow} =$ 0 at 0 mm/s. We again note that the assumption of two Gaussian autocorrelation functions is not strictly correct (since Brownian motion is associated with Lorentzian autocorrelation), but to gain mathematical simplicity the resulting small deviation is acceptable. This also suggests that the remaining intercept in the *in vivo* data, Fig. 3.7b ($\tau_{c,flow}$ = 3 ms), is partially due to the Brownian motion of RBCs in the vessels that is not corrected for using *in vivo* $\tau_{c,offset}$ (next to the vessel). A $\tau_{c,Brown,RBC}$ in the order of 10 ms was measured for rat RBCs in Brownian motion, which have similar size to human RBCs [36].

3.6 CONCLUSION

We studied the combination of two non-invasive *in vivo* flowmetry techniques, calibrated flowmetry (SDF microscopy) and laser speckle flowmetry (LSCI). This enabled us to compare *in vivo* microcirculation blood flow to speckle decorrelation characteristics. We found that decorrelation sources other than blood flow confound the relationship between flow and τ_c. We proposed an analysis scheme that reduces the contribution of additive decorrelation sources to advance towards absolute quantitative laser speckle flowmetry. The preliminary *in vivo* quantitative relationship of τ_c with blood flow velocity is promising in view of existing models, but warrants further study. The existing models have diverging parameters to describe the $1/\tau$c vs V dependency, such as scatterer parameters (size, concentration), or set-up parameters (resolution). A systematic study of the influence of these parameters on the $1/\tau$c vs V relationship is mandatory. In Chapter 4 we will investigate on the scatterer size and concentration in the context of this relationship We thoroughly validated the integrated instrument to ensure valid speckle sampling and speckle contrast calculations. Using the exposure range of 0.5 - 80 ms, the absolute value of fitting parameter τ_c was robust to sampling method (spatial or spatiotemporal sampling of K) and $1/\tau_c$ was found to scale linearly with flow velocities up to 12 mm/s *in vitro*. We have shown that SDF-LSCI has the potential to become a quantitative, automatic, non-invasive and affordable microcirculation monitoring tool.

3.7 ACKNOWLEDGMENTS

The authors kindly thank Microscan B.V. (Amsterdam) for providing a modified Microscan™. A.N. gratefully acknowledges the financial support from the Gerbrand de Jong Fonds (the Netherlands).

3.8 References

1. B. Fagrell and M. Intaglietta, "Microcirculation: its significance in clinical and molecular medicine," J. Intern. Med. **241**, 349-362 (1997).
2. K. R. Mathura, G. J. Bouma, and C. Ince, "Abnormal microcirculation in brain tumours during surgery," The Lancet **358**, 1698-1699 (2001).
3. Y. Sakr, M. J. Dubois, D. De Backer, J. Creteur, and J. L. Vincent, "Persistent microcirculatory alterations are associated with organ failure and death in patients with septic shock*," Critical care medicine **32**, 1825 (2004).
4. P. Goedhart, M. Khalilzada, R. Bezemer, J. Merza, and C. Ince, "Sidestream Dark Field (SDF) imaging: a novel stroboscopic LED ring-based imaging modality for clinical assessment of the microcirculation," Opt. Express **15**, 15101-15114 (2007).
5. J. G. G. Dobbe, G. Streekstra, B. Atasever, R. Van Zijderveld, and C. Ince, "Measurement of functional microcirculatory geometry and velocity distributions using automated image analysis," Medical and Biological Engineering and Computing **46**, 659-670 (2008).
6. A. Fercher and J. Briers, "Flow visualization by means of single-exposure speckle photography," Opt. Commun. **37**, 326-330 (1981).
7. Z. Wang, S. Hughes, S. Dayasundara, and R. S. Menon, "Theoretical and experimental optimization of laser speckle contrast imaging for high specificity to brain microcirculation," Journal of Cerebral Blood Flow & Metabolism **27**, 258-269 (2006).
8. H. Cheng, Q. Luo, Q. Liu, Q. Lu, H. Gong, and S. Zeng, "Laser speckle imaging of blood flow in microcirculation," Physics in medicine and biology **49**, 1347 (2004).
9. M. Draijer, E. Hondebrink, T. Van Leeuwen, and W. Steenbergen, "Review of laser speckle contrast techniques for visualizing tissue perfusion," Lasers in medical science **24**, 639-651 (2009).
10. D. D. Duncan and S. J. Kirkpatrick, "Can laser speckle flowmetry be made a quantitative tool?," JOSA A **25**, 2088-2094 (2008).
11. A. B. Parthasarathy, W. J. Tom, A. Gopal, X. Zhang, and A. K. Dunn, "Robust flow measurement with multi-exposure speckle imaging," Opt. Express **16**, 1975-1989 (2008).
12. R. Bezemer, E. Klijn, M. Khalilzada, A. Lima, M. Heger, J. van Bommel, and C. Ince, "Validation of near-infrared laser speckle imaging for assessing microvascular (re) perfusion," Microvascular Research **79**, 139-143 (2010).
13. T. Durduran, R. Choe, W. Baker, and A. Yodh, "Diffuse optics for tissue monitoring and tomography," Reports on Progress in Physics **73**, 076701 (2010).
14. D. Bicout and G. Maret, "Multiple light scattering in Taylor-Couette flow," Physica A: Statistical Mechanics and its Applications **210**, 87-112 (1994).
15. R. Bonner and R. Nossal, "Model for laser Doppler measurements of blood flow in tissue," Applied optics **20**, 2097-2107 (1981).
16. A. B. Parthasarathy, S. Kazmi, and A. K. Dunn, "Quantitative imaging of ischemic stroke through thinned skull in mice with Multi Exposure Speckle Imaging," Biomedical optics express **1**, 246-259 (2010).
17. J. C. Ramirez-San-Juan, R. Ramos-García, I. Guizar-Iturbide, G. Martínez-Niconoff, and B. Choi, "Impact of velocity distribution assumption on simplified laser speckle imaging equation," Opt. Express **16**, 3197-3203 (2008).
18. D. A. Boas and A. K. Dunn, "Laser speckle contrast imaging in biomedical optics," Journal of biomedical optics **15**, 011109-011109-011112 (2010).
19. P. Zakharov, A. Völker, A. Buck, B. Weber, and F. Scheffold, "Quantitative modeling of laser speckle imaging," Opt. Lett. **31**, 3465-3467 (2006).
20. J. W. Goodman, *Speckle phenomena in optics: theory and applications* (Roberts and Company Publishers, Greenwood Village, CO, 2007).
21. J. D. Briers, G. Richards, and X. W. He, "Capillary blood flow monitoring using laser speckle contrast analysis (LASCA)," Journal of biomedical optics **4**, 164-175 (1999).
22. J. W. Goodman, "Some fundamental properties of speckle," JOSA **66**, 1145-1150 (1976).
23. A. K. Dunn, H. Bolay, M. A. Moskowitz, and D. A. Boas, "Dynamic imaging of cerebral blood flow using laser speckle," Journal of Cerebral Blood Flow & Metabolism **21**, 195-201 (2001).
24. R. Bandyopadhyay, A. Gittings, S. Suh, P. Dixon, and D. Durian, "Speckle-visibility spectroscopy: A tool to study time-varying dynamics," Review of scientific instruments **76**, 093110-093110-093111 (2005).
25. T. Yoshimura, "Statistical properties of dynamic speckles," JOSA A **3**, 1032-1054 (1986).
26. H. Cheng, Q. Luo, S. Zeng, S. Chen, J. Cen, and H. Gong, "Modified laser speckle imaging method with improved spatial resolution," Journal of biomedical optics **8**, 559-564 (2003).
27. D. D. Duncan, S. J. Kirkpatrick, and R. K. Wang, "Statistics of local speckle contrast," JOSA A **25**, 9-15 (2008).
28. J. Qiu, P. Li, W. Luo, J. Wang, H. Zhang, and Q. Luo, "Spatiotemporal laser speckle contrast analysis for blood flow imaging with maximized speckle contrast," Journal of biomedical optics **15**, 016003-016003-016005 (2010).
29. D. M. de Bruin, R. H. Bremmer, V. M. Kodach, R. de Kinkelder, J. van Marle, T. G. van Leeuwen, and D. J. Faber, "Optical phantoms of varying geometry based on thin building blocks with controlled optical properties," Journal of biomedical optics **15**, 025001 (2010).
30. T. L. Alexander, J. E. Harvey, and A. R. Weeks, "Average speckle size as a function of intensity threshold level: comparisonof experimental measurements with theory," Applied optics **33**, 8240-8250 (1994).
31. S. J. Kirkpatrick, D. D. Duncan, and E. M. Wells-Gray, "Detrimental effects of speckle-pixel size matching in laser speckle contrast imaging," Opt. Lett. **33**, 2886-2888 (2008).
32. O. Thompson, M. Andrews, and E. Hirst, "Correction for spatial averaging in laser speckle contrast analysis," Biomedical optics express **2**, 1021-1029 (2011).
33. J. M. Brown and A. J. Giaccia, "The unique physiology of solid tumors: opportunities (and problems) for cancer therapy," Cancer research **58**, 1408-1416 (1998).
34. C. W. Song, "Effect of local hyperthermia on blood flow and microenvironment: a review," Cancer research **44**, 4721s-4730s (1984).
35. V. Kodach, D. Faber, J. van Marle, T. van Leeuwen, and J. Kalkman, "Determination of the scattering anisotropy with optical coherence tomography," Opt. Express **19**, 6131-6140 (2011).
36. H. Ullah, A. Mariampillai, M. Ikram, and I. Vitkin, "Can temporal analysis of optical coherence tomography statistics report on dextrorotatory-glucose levels in blood?," Laser Physics **21**, 1962-1971 (2011).

4

Quantitative Blood Flow Velocity Imaging using Laser Speckle Flowmetry

Adapted from:

A. Nadort, K. Kalkman, T. G. van Leeuwen, and D. J. Faber, "Quantitative blood flow velocity imaging using laser speckle flowmetry" (in submission).

My contribution to this manuscript:
Concept, design and realization of all experiments, performing part of the experiments, supervising K. Kalkman, data analysis, paper writing

ABSTRACT Laser speckle flowmetry suffers from a debated quantitative relationship with blood flow, velocity or tissue perfusion and a lack of calibration of the inverse relationship $1/\tau_c = \alpha V$ between decorrelation time (τ_c) and flow velocity (V). Using a modified microcirculation imager, we experimentally investigate the influence of the optical properties of scatterers on α *in vitro* and *in vivo*. We found good agreement with theoretical predictions based on the scattering phase function, within certain limits on scatterer size and multiple scattering. We present a practical model-based scaling factor to correct for multiple scattering in microcirculatory vessels. Our results show that laser speckle flowmetry offers a quantitative measure of flow velocity in addition to vessel morphology, providing the quantification of local blood flow, velocity and tissue perfusion for clinically relevant applications.

4.1 INTRODUCTION

Quantification of microcirculatory blood supply to tissues is of paramount importance for diagnosis, therapy planning and monitoring, e.g. of metabolic, vascular and critical diseases [1, 2]. Quantifying cerebral blood flow gives insight into brain metabolism [3], while visualizing angiogenic vasculature can aid in localizing tumours [4, 5] and monitoring their development and oxygen metabolism [6-8]. Important clinical microcirculation parameters are blood flow (volume of blood per unit time in the vasculature) and perfusion (volume of blood per volume tissue, per unit time). Both are intimately related to (local) blood flow velocity through the morphology of the vasculature itself (e.g. local vessel diameters and vessel density). Laser speckle flowmetry [9] has become a widely available vascular imaging tool with the potential to be used at the bedside or during operations due to its technological simplicity, and high spatial and temporal resolution [10-14]. Direct quantification of blood flow velocity through imaging has the additional advantage of acquiring vessel morphology, leading to the quantification of local blood flow and perfusion. However, a true quantitative representation of blood flow velocity by laser speckle flowmetry techniques was hindered by multiple scattering inside the vessels and lack of calibration of the flow velocity and speckle dynamics [15, 16], which are both addressed in the following pages. We present a practical guideline to quantitative blood flow velocity measurements through laser speckle contrast imaging (LSCI), thereby enabling the quantitative estimation of functional microcirculatory parameters real time and non-invasively.

LSCI provides a measure for blood flow by quantifying the decrease in speckle contrast as a result of 'blurring' of dynamic speckles within a finite camera exposure time [9, 17]. When scatterers, e.g. red blood cells (RBCs), move the speckle contrast K, defined as the ratio of the standard deviation (σ_i) to the mean ($\langle I \rangle$) of the pixel intensity, decreases with increasing ratio of the camera exposure time T and the characteristic timescale of the speckle dynamics τ_c [18, 19]. The interpretation of τ_c as a measure of blood flow, velocity or tissue is confounded [15, 20], but represents a clinically relevant question. We investigate this matter and show that the parameter τ_c can be quantitatively related to blood flow velocity.

Contributing to this quest we recently integrated sidestream dark field (SDF) microscopy [21, 22] with LSCI [19]. SDF-LSCI enabled us to simultaneously obtain speckle decorrelation times and flow velocities in microcirculatory vessels or phantom flow channels. We have shown that in biological tissue the speckle pattern decorrelates due to both desired and undesired dynamics and a first correction of τ_c for decorrelation sources other than blood flow (such as muscle movements) is needed. We will further validate LSCI by investigating on the relationship between τ_c and flow velocity (V). Albeit that the relation is verified to be of the form $1/\tau_c = \alpha V$ in flow phantom experiments, the exact value of the proportionality constant α is debated and has not been verified *in vivo* [16, 23]. Suggestions for α ranged from a dependence on system parameters [16, 24, 25] to a dependence on the optical properties of the scatterers [26] and dependence on multiple scattering [16, 26]. These predictions differ 1-2 orders of magnitude [23]. In spite of this controversy speckle flowmetry has shown great clinical potential for visualizing vasculature and measuring relative flow velocities [10-13, 27-30], however, to become a true quantitative tool the assessment of α beyond speculation is a necessity. In this work, we quantify the $1/\tau_c = \alpha V$ relationship *in vivo*, which was suggested to depend on scatterer size through the scatterer phase function [26] and

multiple scattering through the number of dynamic scattering events [16, 26]. To this end we investigate the influence of scatterer size and volume fraction on α, using an *in vitro* flow phantom and solutions of polystyrene spheres. We place our results in theoretical context taking into account the optical properties and experimental geometry, resulting in a practical relation $1/\tau_c = \alpha' A(N) \times V$ where α' is the proportionality constant for single scattering events and $A(N)$ scales with the average number of dynamic scattering events N. Applying this theoretical framework to chick embryo and human microcirculation beds demonstrates the feasibility of LSCI for quantitative mapping of blood flow velocities (V) *in vivo*. As a guideline for the reader a flow chart presenting the sequential steps, which will be described in this Chapter, is shown in Fig. 4.1.

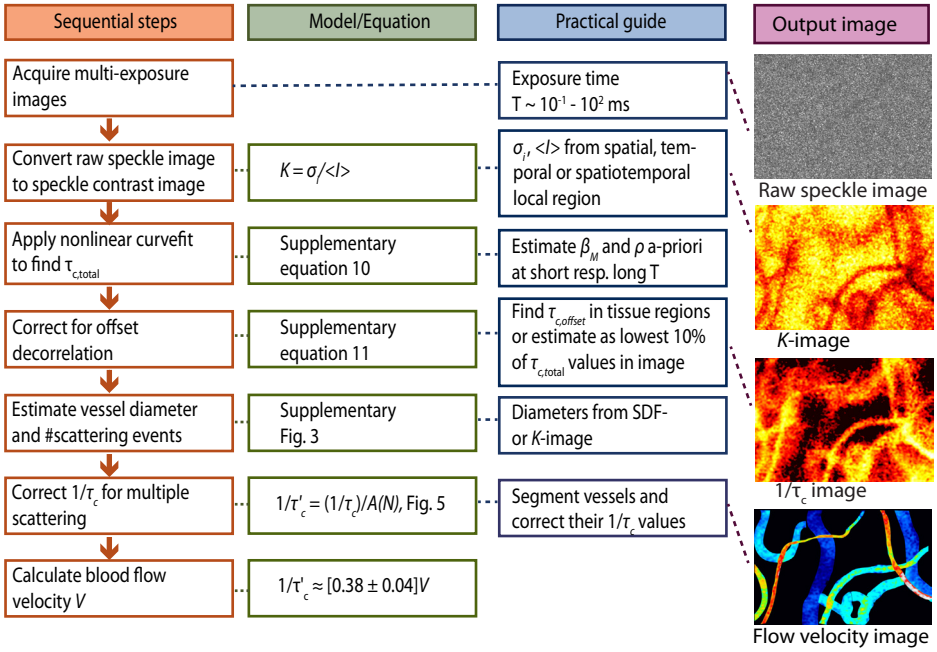

Figure 4.1 | Flow chart for quantitative laser speckle flowmetry. *This paper discusses the sequential steps, theoretical model and practical guide to quantifying blood flow velocities in vivo using laser speckle contrast imaging (LSCI).*

4.2 THEORETICAL FRAMEWORK

When coherent light backscattered from different positions in biological tissue is imaged on a camera, the ensemble of phase differences gives rise to a randomly varying spatial intensity distribution (speckle). Movement of scatterers results in a temporally fluctuating speckle pattern. The characteristic timescale τ_c of the fluctuation can be used to quantify the motion of scattering particles. However, τ_c also depends on optical and physical properties of the tissue, e.g. the scattering phase function and scattering from more than one moving particle causing faster decorrelation of the speckle pattern (shorter τ_c). We review the optical properties relevant to our application and their relationship with τ_C in Supplementary section 4.1a and 4.1b, respectively. The parameter τ_C parameterizes the temporal electric field autocorrelation function (ACF) $g_1(\tau)$ describing the sample dynamics. This approach builds upon the theoretical foundation of Laser Doppler Flowmetry (LDF) [26, 31], Diffusing Wave Spectroscopy (DWS) [32, 33] and using recent advances in the modelling of optical scattering of whole blood [34]. Because for large concentrations of scatterers, as in blood, the scattering is not linear with their concentration, the inter-particle correlation ("dependent scattering") has to be taken into account to estimate the real scattering coefficient. This correlation is implemented by modelling flowing blood as a discrete random medium of hard spheres which is characterized by the local density and pair correlation function. The latter is calculated using Percus-

Yevick (PY) equations [35, 36] as before [34, 37]. Next the number of scattering events in the vessel has to be determined. The probability density for the number of scattering events per unit volume $p(n)$ is Poissonian only for low volume fractions of scatterers [26]. For RBCs in whole blood (volume fraction or hematocrit (Hct) 30 - 50%) we use a normal distribution for $p(n)$, where the relation between mean (N) and variance (σ_n^2) is determined by the pair correlation function [38, 39] (Supplementary section 4.1c). Here, N is estimated from Monte Carlo simulations of our measurement geometry (Supplementary section 4.2 and 4.3).

Temporal speckle dynamics can be derived from spatial intensity statistics of an imaged speckle pattern (Supplementary section 4.1d). After the initial derivation [9] essential improvements were included [40, 41], for example a correction for a static component in the speckle pattern. When a Gaussian form of $g_1(\tau)$ is appropriate [40] an analytical expression for speckle contrast $K(T/\tau_c)$ can be derived for curve fitting, where T is the camera exposure time. Next to the sought τ_c, the model incorporates the parameters β_M [19, 42, 43] (the measurement geometric calibration constant) and ρ (the fraction of dynamically scattered light where $\rho = I_f / (I_f + I_s)$, with I_f the detected intensity of the fluctuating scattered light and I_s the detected intensity of the light scattered by static components) that can both be measured. The resulting expression is Supplementary Eq. (4.10), from which τ_c can be reliably estimated by applying a multi-exposure acquisition scheme and subsequent nonlinear curve fit [28, 44].

4.4 METHODS

4.3.1 Data acquisition

To enable SDF-LSCI, a clinical microcirculation imager based on SDF microscopy (Microscan, Microvision Medical, The Netherlands) was modified to provide illumination with laser light (HeNe, 632.8 nm) guided through four optical multimode fibres surrounding a central imaging pathway with 5x magnification (Supplementary Fig. S4.1) [19] , and an Airy disk of 4.2 µm. Light that is back reflected forms a speckle pattern on an 8-bit monochrome camera (IEEE 1394, Guppy F-080B, Allied Vision Technologies, Germany) with a field of view of 1 x 0.7 mm on 1024 x 768 pixels and 30 frames per second. The minimal speckle diameter was 2.2 pixels ≈ 10.2 µm [45]. For conventional SDF imaging broad band green light (530 ± 20 nm) was coupled into the fibres to provide contrast between flowing RBCs and surrounding tissue to enable RBC flow measurement [46]. During *in vivo* data acquisition the SDF and SDF-LSCI modes were alternated to measure the flow velocity and decorrelation time of the same region [19].

4.3.2 *In vitro* flow phantom

We designed a tissue simulating flow phantom consisting of a polymer tube (diameter 0.2 ± 0.03 mm; depth 0.3 mm ± 0.03 mm, verified with OCT measurements [19]) embedded in silicone elastomer (Sylgard® 184 Silicone Elastomer DOW/Corning, US) mixed with titanium dioxide (TiO_2, anatase form, Sigma Aldrich, US) in the concentration [TiO_2] = 1 mg/ml to mimic tissue scattering [47]. The tube was connected to a 0.5 ml syringe, slowly pressed by a syringe pump (Harvard model PHD2000, US) which resulted in a flow range of 0.1 - 20 mm/s. The flowing media consisted of polystyrene spheres with diameters D = 0.6, 1, 2, 5, 7 and 10 µm (Kisker-Biotech, Germany) with stock volume fraction of 2.5 vol%. For 1, 2 and 5 µm particles we prepared different volume fractions in the range 0.6 - 7 vol%. The range of scattering coefficients μ_s as calculated using Mie and Percus-Yevick theory [37] was 7 - 150

mm^{-1} as specified in Supplementary table S4.2. The range of scattering coefficients μs of the dynamic polystyrene spheres as calculated using Mie and Percus-Yevick theory [37] was 7 - 150 mm^{-1} as specified in Supplementary table S4.2. This range adequately covers the μs for full blood, which is around 42 mm^{-1} for chick embryo blood and 93 mm^{-1} for human blood. A complete flow series was repeated 2 or 3 times per sample, however, we note that for large spheres the low flows (<1 mm/s) were excluded due to precipitation of scatterers.

4.3.3 *In vivo* microcirculation

We recorded multimodal *in vivo* SDF-LSCI image frames from the readily accessible microcirculation of a chick embryo at embryonic day 9, grown *ex ovo* [48]. The imaging tip of the integrated SDF-LSCI device was gently put in contact with the chorioallantoic membrane tissue to prevent disruption of blood flow. The human sublingual microcirculation SDF-LSCI dataset was previously obtained [19] and analyzed using the current model. For the sublingual microcirculation the device was hand-held, while it was secured in a stand for chick embryo microcirculation imaging.

4.3.4 Data analysis

In vitro: Speckle contrast *K* was calculated from the raw speckle images according to Supplementary Section S4.1d, Eq. (4.8) over a local region of 10 x 10 pixels. To obtain a multi-exposure curve, we applied an exposure time range of 0.3 - 30 ms using neutral density filters to prevent overexposure (Supplementary Fig. S4.4). For each *T* minimally 200 *K*-values were selected in the centre of the tube (standard deviation in $K < 5\%$). β_M and ρ were a-priori estimated at $T << \tau_c$ (static phantom) and at $T >> \tau_c$ (flow > 15 mm/s and T > 10 ms) respectively, leaving τ_c the only fit parameter in Supplementary Eq. (4.10). Specifically, ρ was individually estimated for each scatterer size and volume fraction and kept constant for all other flow velocities in the same size/volume fraction series, while β_M is expected to be constant and was found to be 0.40 ± 0.02. The goodness of nonlinear fit $<R_{adj}^2>$ averaged over all fits of *K(T)* vs. *T* was 0.98 ± 0.02.

In vivo: To calculate *K* a spatiotemporal local region of 7 x 7 x 20 pixels was applied to optimize the *in vivo* spatiotemporal resolution and minimize the uncertainty in *K* [19], and minimally 25 *K* values were obtained per vessel and *T* (standard deviation in $K < 7\%$). The exposure time range was extended to longer T [0.5 - 100 ms] and ρ and β_M were a-priori estimated at long and short *T* respectively. In the subsequent curve fit both were constraint within 5% of their estimated value, and τ_c was unconstraint. The goodness of nonlinear fit $<R_{adj}^2>$ averaged over all fits was 0.99 ± 0.01. The *in vivo* decorrelation times ($\tau_{c,total}$) were corrected for statistically independent sources of decorrelation (flow and muscle movement) via the 'offset' $\tau_{c,offset}$ measured from adjacent tissue as described in Supplementary Eq. (4.11) [19]. Absolute flow measurements (maximal measurable flow < 2 mm/s) were obtained from videos acquired in conventional SDF-mode using commercially available software (AVA3.0, Microvision Medical, The Netherlands) [46]. To correct the decorrelation times for multiple scattering the number of scattering events *N* in the vessel were estimated using Monte Carlo simulations as described in Supplementary Section 4.3. Next, we calculated an *in vivo* scaling factor $A(N) = \alpha(N)/\alpha'$, where $\alpha(N)$ was theoretically derived using the optical properties of blood (Supplementary table S4.1) for *N* scattering events, and α' for single scattering. Finally, $1/\tau_c$ was rescaled according to $1/\tau'_c = (1/\tau_c)/A(N)$.

4.4 RESULTS

4.4.1 Influence of size and volume fraction of scatterers

Experimental LSCI data was acquired using an integrated SDF-LSCI device (Supplementary Fig. S4.1). Multi-exposure SDF-LSCI frames were recorded for 9 flow velocities [0.1 - 20 mm/s] and 6 differently sized microspheres [diameter D = 0.6 - 10 µm; all 2.5 vol%] and τ_c was estimated by fitting Supplementary Eq. (4.10) to the measured speckle contrast (a typical example is shown in Supplementary Fig. S4.4). In Fig. 4.2a, $1/\tau_c$ vs. V is plotted for the different sphere sizes, where the slope defines α. For large scatterers (5, 7 and 10 µm) α increases with decreasing size. For small scatterers (0.6, 1 and 2 µm) however, α is approximately constant. The theoretical predictions for α follow from Supplementary Section 4.1 using the optical and physical properties listed in Supplementary Table S4.2 and Monte Carlo simulations for this geometry. Fig. 4.2b shows α plotted (data points) for all scatterer sizes, together with predictions (solid line). The shaded area represents the uncertainty in the calculation due to variations in size and refractive index of the scatterers.

In order to determine the effect of concentration, we prepared different volume fractions of solutions of 1, 2 and 5 µm spheres (Supplementary table S4.2) and determined α shown in Fig. 4.3a together with α from 2.5 vol% solutions of 0.6, 7 and 10 µm. In Fig. 4.3b the same data points are plotted as a function of optical properties, scattering coefficient μ_s and N, which results in a more uniform increase of α with increasing μ_s resp. N, until α remains constant. Fig. 4.3c shows measured values vs. prediction yielding good correspondence for small α (low μ_s and N), however for higher α theory overestimates the experimental measurement.

4.4.2 Quantitative flowmetry *in vivo*

We assessed *in vivo* decorrelation times by imaging the readily available microcirculation of the chorioallantoic membrane of a chick embryo grown ex ovo. Multi-exposure SDF-LSCI and conventional SDF frames were recorded for 35 unique vessels for which RBC tracking was possible, to independently estimate τ_c (by

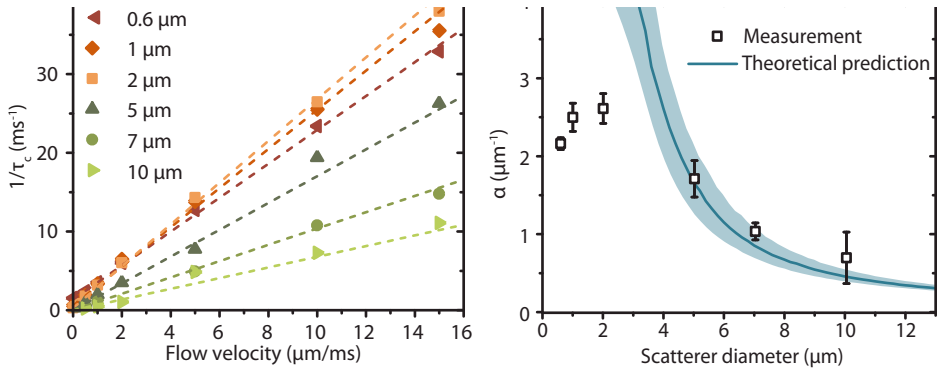

Figure 4.2 | Influence of size on α. (a) *$1/\tau_c$ plotted against V for 6 different diameters of scatterers (polystyrene microspheres [0.6 - 10 µm]), together with a linear fit (dotted lines) to the data points with weights τ_c. The slope of the linear fit is α. No error bars are plotted for clarity, the average standard error on τ_c was 4% ± 2% (max. error 12%).* ***(b)*** *α versus scatterer diameter, error bars are 95% CI intervals from linear fit in (a). Also plotted is the theoretically derived α (solid line) using Mie-Percus-Yevick scattering approximations and the number of scattering events N in the flow tube (diameter d 0.2 ± 0.03 mm) as obtained from Monte Carlo simulations ($N = 1.2\mu_s d$). The shaded area represents the uncertainty in α due to error margins in optical properties of the scatterers.*

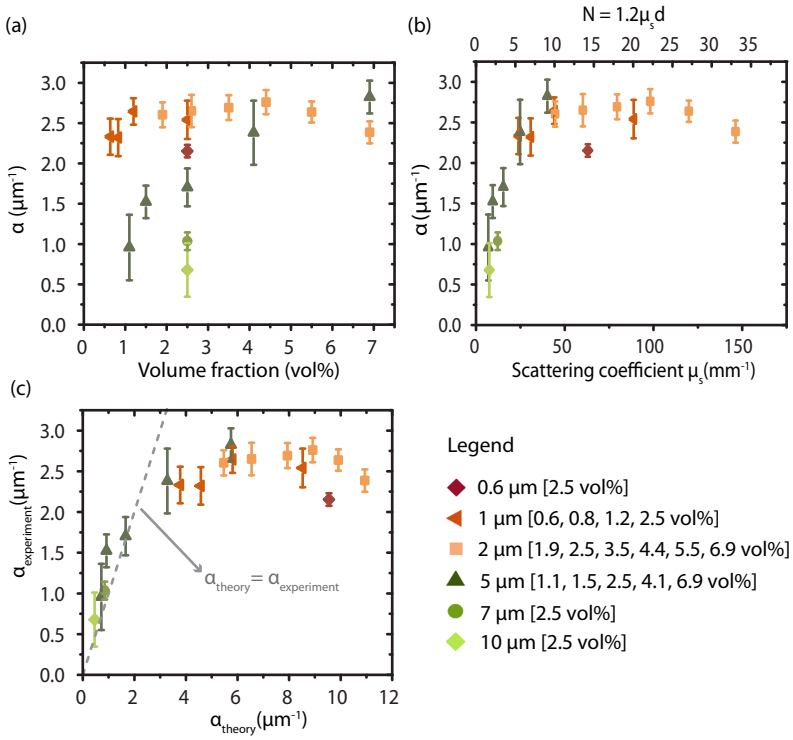

Figure 4.3 | Influence of volume fraction on α. *Experimentally measured α versus* ***(a)*** *scatterer volume fraction,* ***(b)*** *scattering properties (μ_s and N in the flow tube with diameter d 0.2 ± 0.03 mm, $N = 1.2\mu_s d$) and* ***(c)*** *theoretically derived α for differently sized polystyrene spheres in varying volume fractions. Error bars are 95% CI intervals from linear fit on $1/\tau_c$ vs. V.*

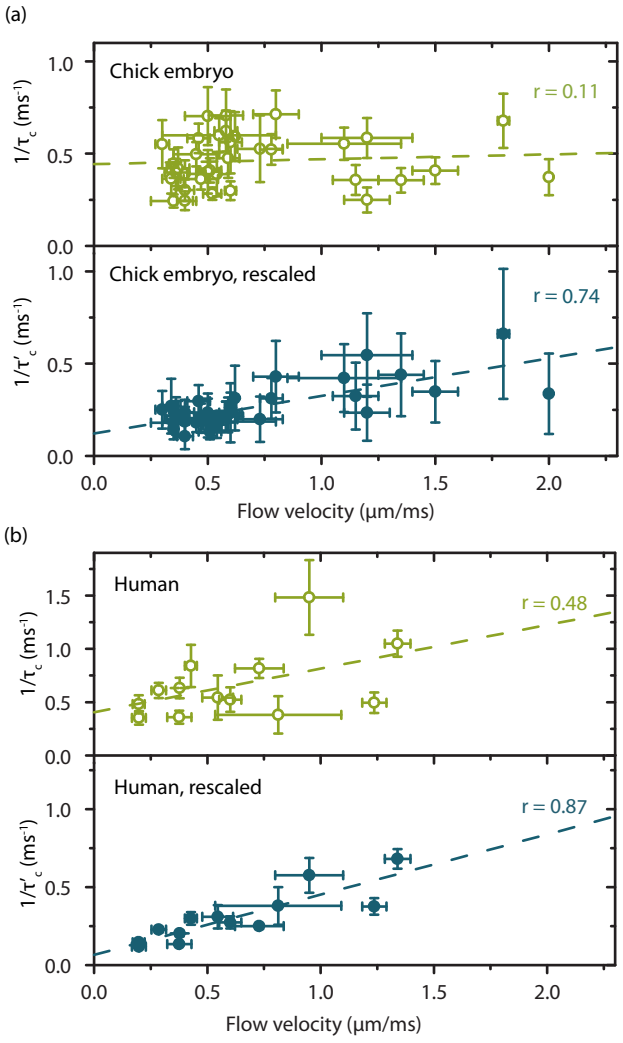

Figure 4.4 | In vivo determination of α. *$1/\tau_c$ versus V for RBCs in vivo, for* ***(a)*** *chick embryo and* ***(b)*** *human microcirculation. The top panels (green open circles) show $1/\tau_c$ estimated by a multi-exposure curve fit (Supplementary section Id, Eq. 4.10) and $\tau_{c,offset}$ correction (Supplementary Eq. (4.11) [19]). The bottom panels show $1/\tau'_c$ rescaled for multiple scattering (see text). In both (a) and b) one data point was excluded as an outlier (not shown). Vertical error bars represent 95% CI of the multi-exposure curve fit and horizontal error bars represent the standard deviation in flow velocity measurements. The slope, or α', is 0.20 ± 0.07 (95% CI) and 0.39 ± 0.15 for chick embryo respectively human RBCs, and the theoretical prediction for α' is 0.27 respectively 0.38.*

LSCI) and V (by SDF) of the same vessels. Compared to controlled phantom experiments, first it is essential to account for 'offset' decorrelation due to dynamic scattering of photons outside the focal plane [19]. Second, the average number of scattering events varies per vessel diameter, estimated from Monte Carlo simulations (Supplementary Section 4.3). Therefore, for each vessel a unique $\alpha(N, \mu_s, p(\boldsymbol{q}))$ can be found. We assume that for the microcirculation μ_s and $p(\boldsymbol{q})$ are invariant and we can write $\alpha(N)$. This allows rescaling of each τ_c to $N = 1$ by a model-based *in vivo* scaling factor $A(N)=\alpha(N)/\alpha'$, denoting the parameters rescaled for single scattering α' and τ'_c. In Fig. 4.4a $1/\tau_c$ (top panel) and $1/\tau'_c$ (bottom panel) are plotted versus blood flow velocity. The correlation coefficient of the linear fit of $1/\tau_c$ and $1/\tau'_c$ vs. V improved after rescaling from r = 0.11 to r = 0.74, respectively. The slope of the rescaled linear fit gave $\alpha' = 0.20 \pm 0.07$ (95% CI), close to theoretical $\alpha' = 0.27$ with an uncertainty range of [0.24 - 0.30] calculated by varying the size ±5% and refractive index n_{RBC} ±1% (Supplementary table S4.1). The scaling factor $A(N)$ for chick embryo blood vessels is shown in Supplementary Fig. S4.5. Next, we reassessed the human sublingual microcirculation measurements acquired previously (14 unique vessels with known flow velocities) [19] by model-based rescaling of τ_c. The correlation coefficient increased from r = 0.48 to r = 0.87 between $1/\tau_c$ (Fig. 4.4b, top panel) and $1/\tau'_c$ data (Fig. 4.4b, bottom panel), respectively, vs. flow velocity. The *in vivo* α (human) was 0.41 ± 0.50 (95% CI) for the original data and α' was 0.39 ± 0.15 (95% CI) for the rescaled data, near identical to the prediction for α' of 0.38 with an uncertainty range of [0.34 - 0.41] calculated by varying the size ±5% and n_{RBC} ±1%. The quantity $1/\tau_c$ is essentially related to both flow velocity and vessel diameter, therefore a strong correlation with V is not expected, however, by correcting for volume fraction of RBCs the correlation is much improved as also evidenced by the reduction in 95% CI range for α'.

To illustrate the quantitative imaging ability of laser speckle flowmetry we constructed a $1/\tau_c$ map and a blood flow velocity map as shown in Fig. 4.5 and Supplementary Movie 1 (human) and Supplementary Movie 2 (chick embryo)[§], following the practical steps outlined in Fig. 4.1 and Supplementary Section 4.7. The scaling factor $A(N)$ for human blood vessels is shown in Fig. 4.6 for values of hematocrit corresponding to whole blood (Hct = 45 %) and the microcirculation (Hct = 30 %) [49].

4.5 DISCUSSION

In this Chapter we demonstrate non-invasive quantitative blood flow velocity measurements *in vivo*, using a relatively simple and available technique based on LSCI. LSCI suffers from a debated quantitative relationship with blood flow, velocity or tissue perfusion [15, 20] and a lack of calibration of the inverse relationship between τ_c and flow velocity quantified by the proportionality constant α [23]. Several predictions for α have been suggested in literature, but disagree in their absolute value and physical dependence [24-26, 50]. The results of our study confirm that scatterer size and volume fraction influence the relationship between $1/\tau_c$ and V [26]. To quantitatively understand this relation we employed a theoretical model based on optical and physical properties of the scatterers, where α is particularly influenced by the scattering phase function and multiple scattering effects . The assumption that the scattering properties of RBCs in the microcirculation are invariant implies that rescaling for the number of scattering events is

§ Movie 1 can be downloaded at
https://www.dropbox.com/s/rswrysdxkuhfoh0/Movie%201%20Human.avi?dl=0 and Movie 2 at
https://www.dropbox.com/s/kl1ctnxxtraokbw/Movie%202%20Chick%20embryo.avi?dl=0

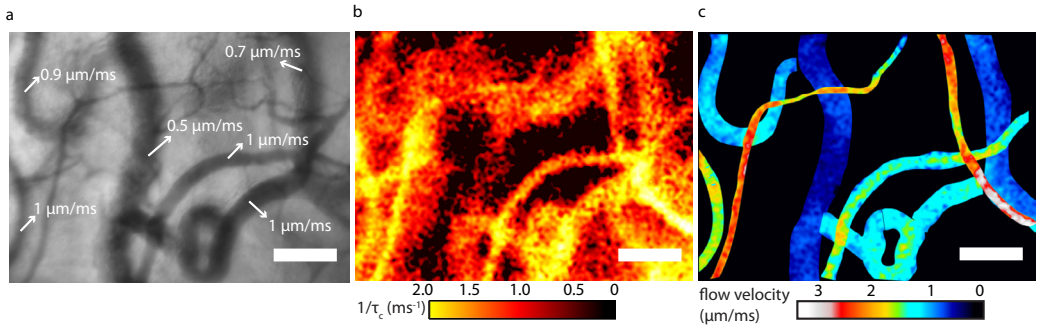

Figure 4.5 | Microcirculatory flow velocity mapping. (a) *Conventional SDF image where the contrast is based on absorption differences between RBCs and tissue. Flows below 2 mm/s can be measured by RBC tracking.* ***(b)*** $1/\tau_c$ *map of the same microcirculation region obtained with multi-exposure SDF-LSCI after correction for* $\tau_{c,offset}$*, contrast is obtained by perfusion dynamics.* **(c)** *Map of actual blood flow velocities after correction for* $\tau_{c,offset}$ *and A(N), and masking of selected blood vessel contours. The scale bar is 100 µm.*

required for quantitative *in vivo* flowmetry. This has previously been implemented empirically by rescaling τ_c by a weighting term that is proportional to the vessel diameter [28]. We estimated the average number of scattering events with Monte Carlo simulations and related its distribution to the Mie-Percus-Yevick scattering model of whole blood. This approach resulted in an excellent agreement between theory and experiment, validating α *in vivo* for microcirculatory blood flow velocities and confirming the quantitative measure of flow velocity by LSCI. Conveniently, vessel diameters and vessel density can be estimated from the images, allowing quantitative mapping of both blood flow and velocity and estimating tissue perfusion using laser speckle flowmetry.

In Figs. 4.2 and 4.3 we systematically varied the size and volume fraction of flowing polystyrene spheres and compared the experimental and theoretical results. In Fig. 4.2b α for 5, 7 and 10 µm diameter particles (2.5 vol%) is in good agreement with our predictions, but for smaller scatterers (red colour shades) α is overestimated by theory. For the small scatterers (0.6, 1 and 2 µm), which are below the resolution limit of the system, α seems to saturate to a value of 2 - 2.5 μm^{-1} in our system. A similar value for α was found in our previous report, using 2.5 vol% Intralipid® as flowing fat emulsion with sub-resolution effective scatterer size [19]. Supplementary Fig. S4.7 shows that saturation of α is expected for small scatterers, albeit at much higher values. Moreover, α does not show dependence on volume fraction for these small spheres (Fig 4.2), suggesting that α in this case is predominantly determined by system properties rather than sample properties [16, 24]. On the other hand, from Supplementary table S4.1, all experiments with small particles involve a high μ_s and thus a large number of dynamic scattering events so that an alternative explanation is that our theory overestimates decorrelation by multiple scattering when the number of events becomes large. A satisfactory theoretical explanation for either possibility has hitherto not been found.

In our *in vivo* SDF-LSCI geometry, RBCs are above the resolution limit and in whole blood (high μ_s) multiple scattering is present in most vessels (our data set: d = [10 - 55 µm], N = [1 - 5]) and N was low (<5) saturation of α is unlikely. Simulating N *in vivo* and applying the theoretical model to the optical properties of blood allowed to rescale the obtained τ_c for multiple scattering resulting in a high linear correlation between $1/\tau'_c$ and flow velocity. In addition, the measured α' is in perfect agreement with the theoretical prediction. Introducing the offset-decorrelation correction to conventional LSCI analysis yields a quantita-

tive decorrelation map (Fig. 4.5b) and subsequently applying the model-based scaling factor yields a quantitative blood velocity map (Fig. 4.5c). Though *in vivo* α' could only be validated against low flow velocities (< 2 mm/s) measured by conventional SDF flowmetry, the *in vitro* experiments verified α' up to 15 mm/s indicating that LSCI is capable of measuring high microcirculatory flow velocities as well. The small discrepancies between Fig. 4.5a and Fig. 4.5c in terms of flow velocity values are due to the image processing algorithm as described in Supplementary Section S4.7. These algorithms should be refined in order to more precisely correct for the local 'offset' decorrelation and vessel diameters. In Supplementary Section 4.7 we identified improvements for post-processing of the images to increase the LSCI accuracy. In addition, it is important to realize that the microcirculation is a dynamic, biological environment and flow velocities are not constant both in time and in space, within one vessel. Although the RBC-tracking algorithms applied in the commercial software accompanying SDF imaging have a high accuracy, they measure the flow at a specific instant and location. By combining the results from the same vessel over a several time points we increase the accuracy for comparison to τc's derived using LSCI. Nevertheless the underlying biological variation ultimately limits this comparison, and agreements within 20-30% (as found in Fig. 4.5) are satisfactory. Besides physiological variation in flow velocities, the appearance of RBCs is disc-shaped, like a filled-in doughnut, which can deform when RBSs are flowing through small capillaries. These aspects influence the scattering properties and are unfeasible to implement in the MPY scattering theory, and could therefore additionally reduce the accuracy of our model. Finally, extending the multi-exposure regime to lower exposure times will increase the maximum flow velocity limit further.

The variance in the estimation of N with Monte Carlo simulations is due to uncertainties in the included optical properties and fidelity of the simulated measurement geometry. Our phantom experiment offers an alternative way to validate N as described in Supplementary Section 4.9 and Supplementary Fig. S4.8. The latter also illustrates the importance of including the parameter ρ to obtain τ_c from the speckle contrast K. Naturally, different geometries result in different ρ (e.g. due to different static/dynamic medium properties, tube diameter, etc.) thus ρ needs appropriate estimation/calibration. *In vivo*, ρ is influenced by geometry, vessel diameter, vessel depth and Hct values and can be estimated using long exposure times. When neglecting to appropriately estimate ρ the resulting value for τ_c can deviate majorly [28, 44]. Estimation of N *in vivo* using Monte Carlo simulations depends on the geometrical and optical properties such as vessel depth, diameter and $\mu_{s,blood'}$. Varying the vessel depth between 0.1 and 0.4 mm and the Hct between 30% and 45% resulted in comparable values for N (Supplementary Fig. S4.3), indicating that the estimation of N is robust. In addition, calculating α' using these varying N values influenced α' by less than ± 0.02 for microcirculatory vessel diameters. Alternatively, low-coherence interferometric set-ups allow path-length resolved speckle signals to be acquired [50-52], providing better estimation of N albeit without the simplicity of the LSCI approach.

To make our results more widely applicable we performed Monte Carlo simulations for a conventional speckle imaging set-up where wide field laser light illuminates tissue at an angle and the backscattered light is captured by a camera directly above the tissue [10, 13, 14, 27, 28, 53]. In this geometry very similar N values for dynamic detected photons were found for both *in vitro* and *in vivo* optical properties (Supplementary Fig. S4.3), which generalizes our multiple scattering correction. As a practical guideline we therefore plotted the *in vivo* scaling factor $A(N)$ for two Hct values in Fig. 4.6, solid lines. For compari-

son to conventional LSCI approaches we also plotted $A(N)$ for Gaussian and Lorentzian shape of $g_{1,}(\tau)$ (dashed lines), calculated using a normal distribution for $p(n)$. Rescaling for multiple scattering is thus highly model dependent, where the Lorentzian ($A(N) \sim N$) and the Gaussian ($A(N) \sim \sqrt{N}$) model result in an underestimation or overestimation of V, respectively. Thus, the practical realization of quantitative laser speckle flowmetry necessitates the estimation of N from the geometry of blood vessels. Then, τ'_c is calculated according to $1/\tau'_c = (1/\tau_c)/A(N)$ and the flow velocity estimated from $1/\tau'_c \approx [0.38 \pm 0.04]V$. We emphasize that τ_c *in vivo* is subject to additive decorrelation sources along the photon path through tissue [19], which should be estimated and corrected accordingly.

We use the analytical model of Supplementary Eq. (4.10) to fit experimental $K(T)$ vs. T curves, based on the *ansatz* that this model accurately retrieves the actual decorrelation time τ_c, even though our derived $g_1(\tau)$ is not necessarily purely Gaussian. We verified the validity of this approach by calculation (Supplementary Section S4.10). It is shown that the current model and the Gaussian model approximate each other sufficiently, especially for $N > 1$, by examining the final $K(T)$ curve. We therefore conclude that assuming a Gaussian ACF, thereby making the model analytical and practical, results in an acceptably small error in τ_c. This result does not imply that scaling factors $A(N)$ should be based on Gaussian approximations to $g_1(\tau)$ as evidenced by Fig. 4.6. We therefore scale our *in vivo* measured τ_c to the value τ'_c (for single scattering) using the model-based factor $A(N)$.

The approach to calculate g_1 for multiple scattering has been recognized in literature [50, 52, 54], explicitly in the LDF [26] and DWS [33] field. The differences in the treatment of multiple scattering and modelling g_1 between LDF, DWS and our approach are discussed in Supplementary Section S4.11. Key challenges are to find a valid model for g_1 and a valid expression for $p(n)$ in the specific geometry. Here we have shown that our experimental α' (and estimation of $p(n)$) matches brilliantly with theory ($\alpha' = 0.38$) and falls in between predictions from the LDF framework ($\alpha'_{LDF} = 0.36$) and DWS framework ($\alpha'_{DWS} = 0.54$).

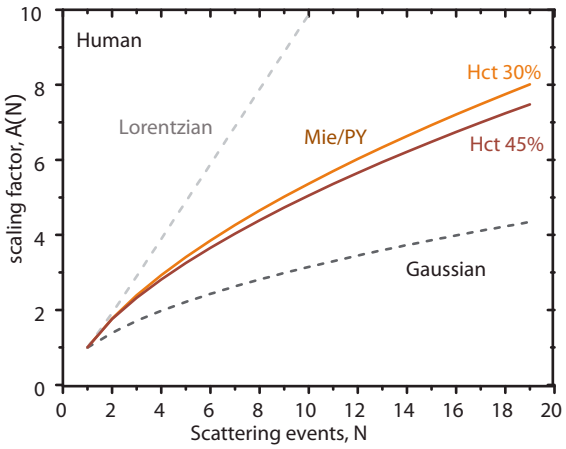

Figure 4.6 | Multiple scattering scaling factor. *Scaling factor $A(N)$ for α is calculated using our model based on Mie/PY scattering in human blood for Hct = 30% (orange line) and Hct = 45% (red line). Dashed lines represent $A(N)$ for Lorentzian (grey) and Gaussian (black) models for g_1. All scaling factors are calculated using a normal distribution for $p(n)$.*

The experimental and theoretical findings in this study improve the quantitative flowmetry capabilities of LSCI and show that the clinically relevant parameters blood flow, velocity and tissue perfusion, can be

quantitatively represented in SDF-LSCI microcirculation images, escaping the doctrine of qualitative and relative flow measures. This enables SDF-LSCI to quantitatively study microcirculation within and between organs and organisms and during the course of disease and therapy. In essence, for quantitative *in vivo* speckle flowmetry reliable calculation of τ_c, correction for 'offset' decorrelation [19], and estimation of vessel diameter to correct for multiple scattering are key ingredients. We recommend to consider the influence of system resolution on α, for example when choosing flowing scattering solutions in phantom experiments. The highly vascularized chorioallantoic membrane of the chick embryo can be a practical calibration model as an intermediate between *in vitro* and *in vivo* validation.

4.6 ACKNOWLEDGMENTS

The authors kindly thank Microscan B.V. (Amsterdam) for providing a modified Microscan and financial support. A.N. gratefully acknowledges the financial support from the Gerbrand de Jong Fonds (the Netherlands). Part of this work was sponsored by Technology Foundation STW under the *i*MIT programme

4.7 REFERENCES

1. B. Fagrell and M. Intaglietta, "Microcirculation: its significance in clinical and molecular medicine," J. Intern. Med. **241**, 349-362 (1997).
2. C. Ince, "The microcirculation is the motor of sepsis," Critical Care **9**, S13 (2005).
3. A. Villringer and U. Dirnagl, "Coupling of brain activity and cerebral blood flow: basis of functional neuroimaging," Cerebrovasc. Brain Metab. Rev. **7**, 240-276 (1994).
4. K. R. Mathura, G. J. Bouma, and C. Ince, "Abnormal microcirculation in brain tumours during surgery," The Lancet **358**, 1698-1699 (2001).
5. J. A. Lindeboom, K. R. Mathura, and C. Ince, "Orthogonal polarization spectral (OPS) imaging and topographical characteristics of oral squamous cell carcinoma," Oral oncology **42**, 581-585 (2006).
6. K. E. Emblem, K. Mouridsen, A. Bjornerud, C. T. Farrar, D. Jennings, R. J. Borra, P. Y. Wen, P. Ivy, T. T. Batchelor, and B. R. Rosen, "Vessel architectural imaging identifies cancer patient responders to anti-angiogenic therapy," Nature medicine **19**, 1178-1183 (2013).
7. J. Folkman, "Angiogenesis in cancer, vascular, rheumatoid and other disease," Nature medicine **1**, 27-30 (1995).
8. P. Carmeliet and R. K. Jain, "Angiogenesis in cancer and other diseases," Nature **407**, 249-257 (2000).
9. A. Fercher and J. Briers, "Flow visualization by means of single-exposure speckle photography," Opt. Commun. **37**, 326-330 (1981).
10. A. K. Dunn, H. Bolay, M. A. Moskowitz, and D. A. Boas, "Dynamic imaging of cerebral blood flow using laser speckle," Journal of Cerebral Blood Flow & Metabolism **21**, 195-201 (2001).
11. A. B. Parthasarathy, E. L. Weber, L. M. Richards, D. J. Fox, and A. K. Dunn, "Laser speckle contrast imaging of cerebral blood flow in humans during neurosurgery: a pilot clinical study," Journal of biomedical optics **15**(2010).
12. H. Knotzer and W. R. Hasibeder, "Microcirculatory function monitoring at the bedside—a view from the intensive care," Physiol. Meas. **28**, R65 (2007).
13. P. Li, S. Ni, L. Zhang, S. Zeng, and Q. Luo, "Imaging cerebral blood flow through the intact rat skull with temporal laser speckle imaging," Opt. Lett. **31**, 1824-1826 (2006).
14. C. Ayata, A. K. Dunn, Y. Gursoy-Özdemir, Z. Huang, D. A. Boas, and M. A. Moskowitz, "Laser speckle flowmetry for the study of cerebrovascular physiology in normal and ischemic mouse cortex," Journal of Cerebral Blood Flow & Metabolism **24**, 744-755 (2004).
15. D. Briers, D. D. Duncan, E. Hirst, S. J. Kirkpatrick, M. Larsson, W. Steenbergen, T. Stromberg, and O. B. Thompson, "Laser speckle contrast imaging: theoretical and practical limitations," Journal of biomedical optics **18**, 066018-066018 (2013).
16. D. D. Duncan and S. J. Kirkpatrick, "Can laser speckle flowmetry be made a quantitative tool?," JOSA A **25**, 2088-2094 (2008).
17. J. D. Briers and S. Webster, "Laser speckle contrast analysis (LASCA): a nonscanning, full-field technique for monitoring capillary blood flow," Journal of biomedical optics **1**, 174-179 (1996).
18. J. W. Goodman, *Speckle phenomena in optics: theory and applications* (Roberts and Company Publishers, Greenwood Village, CO, 2007).
19. A. Nadort, R. G. Woolthuis, T. G. van Leeuwen, and D. J. Faber, "Quantitative laser speckle flowmetry of the *in vivo* microcirculation using sidestream dark field microscopy," Biomedical optics express **4**, 2347-2361 (2013).
20. O. B. Thompson and M. K. Andrews, "Tissue perfusion measurements: multiple-exposure laser speckle analysis generates laser Doppler–like spectra," Journal of biomedical optics **15**, 027015-027015-027017 (2010).
21. P. Goedhart, M. Khalilzada, R. Bezemer, J. Merza, and C. Ince, "Sidestream Dark Field (SDF) imaging: a novel stroboscopic LED ring-based imaging modality for clinical assessment of the microcirculation," Opt. Express **15**, 15101-15114 (2007).
22. W. Groner, J. W. Winkelman, A. G. Harris, C. Ince, G. J. Bouma, K. Messmer, and R. G. Nadeau, "Orthogonal polarization spectral imaging: a new method for study of the microcirculation," Nature medicine **5**, 1209-1213 (1999).
23. M. Draijer, E. Hondebrink, T. Van Leeuwen, and W. Steenbergen, "Review of laser speckle contrast techniques for visualizing tissue perfusion," Lasers in medical science **24**, 639-651 (2009).
24. T. Yoshimura, "Statistical properties of dynamic speckles," JOSA A **3**, 1032-1054 (1986).
25. J. D. Briers, G. Richards, and X. W. He, "Capillary blood flow monitoring using laser speckle contrast analysis (LASCA)," Journal of biomedical optics **4**, 164-175 (1999).
26. R. Bonner and R. Nossal, "Model for laser Doppler mea-

surements of blood flow in tissue," Applied optics **20**, 2097-2107 (1981).
27. T. Durduran, M. G. Burnett, G. Yu, C. Zhou, D. Furuya, A. G. Yodh, J. A. Detre, and J. H. Greenberg, "Spatiotemporal quantification of cerebral blood flow during functional activation in rat somatosensory cortex using laser-speckle flowmetry," Journal of Cerebral Blood Flow & Metabolism **24**, 518-525 (2004).
28. S. M. S. Kazmi, A. B. Parthasarthy, N. E. Song, T. A. Jones, and A. K. Dunn, "Chronic imaging of cortical blood flow using Multi-Exposure Speckle Imaging," Journal of Cerebral Blood Flow & Metabolism **33**, 798-808 (2013).
29. G. A. Armitage, K. G. Todd, A. Shuaib, and I. R. Winship, "Laser speckle contrast imaging of collateral blood flow during acute ischemic stroke," Journal of Cerebral Blood Flow & Metabolism **30**, 1432-1436 (2010).
30. M. Roustit, C. Millet, S. Blaise, B. Dufournet, and J. Cracowski, "Excellent reproducibility of laser speckle contrast imaging to assess skin microvascular reactivity," Microvascular Research **80**, 505-511 (2010).
31. M. Stern, "*In vivo* evaluation of microcirculation by coherent light scattering," Nature **254**, 56-58 (1975).
32. D. Pine, D. Weitz, P. Chaikin, and E. Herbolzheimer, "Diffusing wave spectroscopy," Physical Review Letters **60**, 1134 (1988).
33. D. Weitz, J. Zhu, D. Durian, H. Gang, and D. Pine, "Diffusing-wave spectroscopy: The technique and some applications," Physica Scripta **1993**, 610 (1993).
34. N. Bosschaart, G. J. Edelman, M. C. Aalders, T. G. van Leeuwen, and D. J. Faber, "A literature review and novel theoretical approach on the optical properties of whole blood," Lasers in medical science **29**, 453-479 (2014).
35. J. K. Percus and G. J. Yevick, "Analysis of classical statistical mechanics by means of collective coordinates," Physical Review **110**, 1 (1958).
36. M. Wertheim, "Exact solution of the Percus-Yevick integral equation for hard spheres," Physical Review Letters **10**, 321-323 (1963).
37. V. D. Nguyen, D. Faber, E. van der Pol, T. van Leeuwen, and J. Kalkman, "Dependent and multiple scattering in transmission and backscattering optical coherence tomography," Opt. Express **21**, 29145-29156 (2013).
38. J.-P. Hansen and I. R. McDonald, *Theory of Simple Liquids* (Elsevier, Amsterdam, 1990).
39. L. Tsang, J. A. Kong, and K.-H. Ding, *Scattering of Electromagnetic Waves, Theories and Applications* (John Wiley & Sons, New York, 2004), Vol. 27.
40. R. Bandyopadhyay, A. Gittings, S. Suh, P. Dixon, and D. Durian, "Speckle-visibility spectroscopy: A tool to study time-varying dynamics," Review of scientific instruments **76**, 093110-093110-093111 (2005).
41. P. Zakharov, A. Völker, A. Buck, B. Weber, and F. Scheffold, "Quantitative modeling of laser speckle imaging," Opt. Lett. **31**, 3465-3467 (2006).
42. D. A. Boas and A. K. Dunn, "Laser speckle contrast imaging in biomedical optics," Journal of biomedical optics **15**(2010).
43. O. Thompson, M. Andrews, and E. Hirst, "Correction for spatial averaging in laser speckle contrast analysis," Biomedical optics express **2**, 1021-1029 (2011).
44. A. B. Parthasarathy, W. J. Tom, A. Gopal, X. Zhang, and A. K. Dunn, "Robust flow measurement with multi-exposure speckle imaging," Opt. Express **16**, 1975-1989 (2008).
45. S. J. Kirkpatrick, D. D. Duncan, and E. M. Wells-Gray, "Detrimental effects of speckle-pixel size matching in laser speckle contrast imaging," Opt. Lett. **33**, 2886-2888 (2008).
46. J. G. G. Dobbe, G. J. Streekstra, B. Atasever, R. Van Zijderveld, and C. Ince, "Measurement of functional microcirculatory geometry and velocity distributions using automated image analysis," Medical and Biological Engineering and Computing **46**, 659-670 (2008).
47. D. M. de Bruin, R. H. Bremmer, V. M. Kodach, R. de Kinkelder, J. van Marle, T. G. van Leeuwen, and D. J. Faber, "Optical phantoms of varying geometry based on thin building blocks with controlled optical properties," Journal of biomedical optics **15**, 025001 (2010).
48. D. S. Dohle, S. D. Pasa, S. Gustmann, M. Laub, J. H. Wissler, H. P. Jennissen, and N. Dünker, "Chick ex ovo culture and ex ovo CAM assay: how it really works," Journal of visualized experiments: JoVE (2009).
49. A. R. Pries, T. W. Secomb, P. Gaehtgens, and J. Gross, "Blood flow in microvascular networks. Experiments and simulation," Circul. Res. **67**, 826-834 (1990).
50. A. Wax, C. Yang, R. R. Dasari, and M. S. Feld, "Path-length-resolved dynamic light scattering: modeling the transition from single to diffusive scattering," Applied optics **40**, 4222-4227 (2001).
51. J. Kalkman, R. Sprik, and T. van Leeuwen, "Path-length-resolved diffusive particle dynamics in spectral-domain optical coherence tomography," Physical Review Letters **105**, 198302 (2010).
52. K. K. Bizheva, A. M. Siegel, and D. A. Boas, "Path-length-resolved dynamic light scattering in highly scattering random media: The transition to diffusing wave spectroscopy," Physical Review E **58**, 7664 (1998).
53. B. Choi, N. M. Kang, and J. S. Nelson, "Laser speckle imaging for monitoring blood flow dynamics in the *in vivo* rodent dorsal skin fold model," Microvascular Research **68**, 143-146 (2004).
54. T. B. Rice, E. Kwan, C. K. Hayakawa, A. J. Durkin, B. Choi, and B. J. Tromberg, "Quantitative, depth-resolved determination of particle motion using multi-exposure, spatial frequency domain laser speckle imaging," Biomedical optics express **4**, 2880-2892 (2013).

SUPPLEMENTARY INFORMATION

S4.1 THEORY

S4.1a Optical and physical properties of the dynamic medium

We briefly review the optical properties relevant to our application. We model our phantom and tissue as a discrete random medium of hard spheres (i.e. occupying non-overlapping volumes). The differential scattering cross section $\sigma_{sca}(\boldsymbol{q})$ describing the angular distribution of scattered light by a single sphere, is calculated using Mie (M) theory [1]. Here $\boldsymbol{q} = \boldsymbol{k}_{scat} - \boldsymbol{k}_{in}$ is the scattering vector with magnitude $|\boldsymbol{q}| = 2k\sin(\theta/2)$; k is the wavenumber $2\pi/\lambda$ and θ is the scattering angle. To account for inter-particle correlation effects ("dependent scattering"), we calculate the structure factor $S(\boldsymbol{q})$ using the Percus-Yevick (PY) equation [2] for hard spheres [3]. The scattering coefficient μ_s, cross section σ_{sca} and scattering phase function $p(\boldsymbol{q})$ are then found, respectively, as:

$$\mu_{s,MPY} = \eta\sigma_{sca,MPY} = \eta 2\pi \int_0^{2k} \sigma_{sca,MIE}(\boldsymbol{q}) S_{PY}(\boldsymbol{q}, f_v) \boldsymbol{q} d\boldsymbol{q} \qquad (4.1a)$$

$$p_{MPY}(\boldsymbol{q}) = \frac{\sigma_{sca,MIE}(\boldsymbol{q}) S_{PY}(\boldsymbol{q}, f_v)}{\sigma_{sca,MPY}} \qquad (4.1a)$$

Here $\eta = f_v/V_p$ is the particle number density in the medium; with f_v the volume fractions of particles with volume V_p. The structure factor is given by the Fourier transform of the pair correlation function PCF(r) which is interpreted as the distribution of distances r between particle pairs. For dilute solutions of hard spheres of diameter D, PCF(r) = 0 when $r < D$ and unity otherwise. For higher volume fractions PCF(r) shows damped oscillatory behaviour, with increased probability of finding pair separations at multiples of D and decreased probability in between. In the limit $r \to \infty$; PCF(r) goes to unity. The structure factor $S(\boldsymbol{q})$ is approximately constant at unity for low volume fractions. Non-unity $S(\boldsymbol{q})$ at higher values of f_v cause an angular redistribution of scattered light (Eq. (4.1b)) as well as non-linear scaling of the scattering coefficient.

S4.1b Dependence of τ_c on the optical properties of the dynamic medium

Consider an ensemble of scatterers (indexed i) each moving with velocity $\boldsymbol{V}_i$ in a vessel within an otherwise static, scattering medium. The velocity distribution is given by $p(\boldsymbol{V})$. The normalized electric field autocorrelation (ACF) function $g_1(\tau) = \langle E^*(t+\tau)E(t)\rangle_t / \langle E(t)E^*(t)\rangle_t$, for a single scattering event from moving particles is [4]:

$$g_{1,single}(\boldsymbol{q}, \tau) = \left\langle \sum_i \exp\left(-i\boldsymbol{q} \cdot \boldsymbol{V}_i \tau\right) \right\rangle \qquad (4.2)$$

When light undergoes many scattering events before reaching the vessel, the propagation direction becomes isotropic. Consequently, the direction of the scattering vector $\boldsymbol{q}$ with respect to the velocity vector $\boldsymbol{V}$ also becomes isotropic, and the velocity distribution depends only on the magnitude $|\boldsymbol{V}| = V$. We assume

a Gaussian-shaped speed distribution $p(V) = \sqrt{(2/\pi)}\,(3/V_0)^{3/2}\exp(-3V^2/2V_0^2)$; where V_0 is the average flow velocity. Averaging over $p(V)$ yields [4-6]:

$$g_{1,\text{single}}(\boldsymbol{q},\tau) = \exp\left(-\boldsymbol{q}^2 V_0^2 \tau^2 / 6\right) \tag{4.3}$$

In the following, we drop the subscript '0' on velocity. The average over $\boldsymbol{q}$ is calculated as:

$$g_{1,\text{single}}(\tau) = \int_0^{2k} p_{MPY}(\boldsymbol{q}) \exp\left(-\boldsymbol{q}^2 V^2 \tau^2 / 6\right) \boldsymbol{q}\, d\boldsymbol{q} \tag{4.4}$$

The angular weighting by the phase function of Supplementary Eq. (4.1b), introduces dependence on the optical and physical properties in g_1 (and thus in τ_C).

S4.1c Multiple scattering

Eq. (4.4) describes the electric field decorrelation due to single scattering events. If subsequent scattering events are assumed to be statistically independent, the ACF becomes $[g_1(\tau)]^n$ where n is the number of scattering events from moving scatterers. The total correlation function follows after weighting with the appropriate distribution of n:

$$g_1(\tau) = \sum_{n=1}^{\infty} p(n)\left[g_{1,\text{single}}(\tau)\right]^n \tag{4.5}$$

Because the scattering events take place at the particles, the distribution $p(n)$ in the measurement volume follows the microscopic distribution of the number of particles $p(\eta_{micr})$ in the dynamic medium. If the particles positions are independent of each other, $p(\eta_{micr})$ and $p(n)$ are given by the Poisson distribution [7], with equal mean and variance of $\langle\eta_{micr}\rangle = \sigma^2\eta_{micr} = \eta$ (the global average density); and of $\langle n\rangle = \sigma^2{}_n = N$, respectively. When correlations between the particle positions are present, e.g. when PCF(r)≠1, the Poissonian distribution model is no longer valid. Although the exact distribution is unknown, the relation between mean (N) and variance (σ_n^2) is determined by the PCF as [8, 9]:

$$\frac{\sigma_n^2}{N} = 1 + \eta\int\left[PCF_{PY}(r) - 1\right]dr = \frac{(1-f_v)^4}{(1+2f_v)^2} \tag{4.6}$$

Where the right-hand side is valid for the PY equation of PCF(r) for hard spheres. In our present analysis, we assume $p(n)$ follows a normal distribution where the relation between mean and variance is given by Eq. (4.6). Parameter N is estimated from Monte Carlo simulation of our experimental geometry (Supplementary Section 4.3) The ACF $g_1(\tau)$ is an exponentially decaying function of time, parameterized by the characteristic timescale τ_c (decorrelation time) which is evaluated from [4, 7]:

$$\tau_c = \int_0^{\infty} g_1(\tau)\, d\tau \tag{4.7}$$

Following the above outlined exercise, g_1 can be plotted according to the set of optical and physical properties (including N) and the proportionality constant α can be derived as $1/\tau_c$ at $V = 1$. The ACF

calculated using the above formulae is of Gaussian form (because all involved functionals, i.e. phase function, velocity distribution and distribution of the number of scattering events, are of (near) Gaussian shape). In the following, we therefore assume that $g_1(\tau) = \exp(-0.25\pi(\tau/\tau_c)^2)$ for mathematical convenience of the procedure to extract τ_c from spatial speckle contrast measurements (Supplementary Section 4.1d). The validity of this approximation is discussed in Supplementary Section S4.10.

S4.1d Spatial assessment of temporal speckle dynamics

Laser Speckle Contrast Imaging (LSCI) assesses sample dynamics from spatial measurement of speckle contrast, defined as the ratio of the standard deviation (σ_i) to the mean ($\langle I \rangle$) of the intensity:

$$K = \frac{\sigma_i}{\langle I \rangle} \tag{4.8}$$

This quantity is related to sample dynamics through temporal integration of the ACF $g_1(\tau)$ as obtained from Supplementary Eq. (4.5) [7]:

$$K(T) = \beta_M^{1/2}\left[\frac{2}{T}\int_0^T\left(1-\frac{\tau}{T}\right)\left|g_1(\tau)\right|^2 d\tau\right]^{1/2} \tag{4.9}$$

Here, T is the exposure time of the camera and β_M is a measurement-geometry specific constant that can be calibrated [10]. In the general case of flow in a single vessel or channel, $g_1(\tau)$ is assumed to have a Gaussian form $g_1(\tau) = \exp(-0.25\pi(\tau/\tau_c)^2)$ as described in Supplementary Section 4.1c. For Brownian motion, $g_1(\tau)$ takes a Lorentzian form: $g_1(\tau) = \exp(-(\tau/\tau_c))$. A sampled biological tissue volume likely consist of both static and dynamic scatterers. The influence of the static component on $g_1(\tau)$ can be taken into account [11-13] by introducing a dependence on , with I_f the detected intensity of the fluctuating scattered light and I_s the detected intensity of the light scattered by static components. The speckle contrast Supplementary Eq. (4.9) can be solved analytically for the Gaussian form of $g_1(\tau)$ to give [11, 12]:

$$K(x) = \beta^{1/2}\left[\rho^2\frac{\exp\left(-2(x)^2\right)-1+\sqrt{2\pi}x\,erf(\sqrt{2}x)}{2(x)^2} + 2\rho(1-\rho)\frac{\exp\left(-(x)^2\right)-1+\sqrt{\pi}x\,erf(x)}{(x)^2} + (1-\rho)^2\right]^{1/2} + C_{noise} \tag{4.10}$$

where $x = \sqrt{\pi}T/2\tau_{c,total}$ and C_{noise} an added noise term for measurement noise. For our determination of $\tau_{c,total}$, we fit the model of Supplementary Eq. (4.10) to measurements of K obtained with different exposure times as detailed in Methods. The definition of x differs by a factor $\sqrt{\pi}/2$ from other publications and Chapter 3 [10, 14, 15] in which $g_1(\tau) = \exp(-(\tau/\tau_c)^2)$ is used – a form that is not compliant with our Supplementary Eq. (4.7). In biological tissue $\tau_{c,total}$ represents the total decorrelation due to contributions from 'offset' (e.g. muscle movements) and the desired flow dynamics.

S4.2 SIDESTREAM DARK FIELD AND LASER SPECKLE CONTRAST IMAGING (SDF-LSCI) SET UP

To enable absolute blood flow measurements and estimation of τ_c of the same *in vivo* vessels we modified a clinical microcirculation imager (Microscan, Microvision Medical, The Netherlands) to allow illumination by different light sources [10]. The conventional system provides illumination by six green LEDs at the tip of the lens tube, which were replaced by four optical fibres (POF ESKA, fibre core 980 µm, NA 0.5). The fibres are directed through the imager alongside the lens tube, which is covered with a sterile cap and can be brought into contact with the tissue of interest. In SDF-LSCI mode, as is shown in Supplementary Fig. S4.1, laser light (632.8 nm, He/Ne, Spectra Physics, US) is split into four beams by three 50:50 beam splitters and coupled into the four multimode fibres. Raw speckle frames with different exposure times are captured by a monochrome camera at 30 frames per second (IEEE 1394, Guppy F-080B, Allied Vision Technologies, Germany), controlled by self-written software (LabVIEW, National Instruments, US). For exposure times above 33 ms obviously the frame rate is less. Overexposure is prevented by a neutral density filter wheel in front of the laser. In conventional SDF mode the fibres are illuminated by four LEDs (530 ± 20 nm). Conventional SDF images show good contrast between tissue and highly absorbing red blood cells (RBCs). Conventional and SDF-LSCI mode were consecutively employed to image the same microcirculation area. The focal plane can be translated between tissue surface and 0.4 mm depth and the optical magnification is 5x.

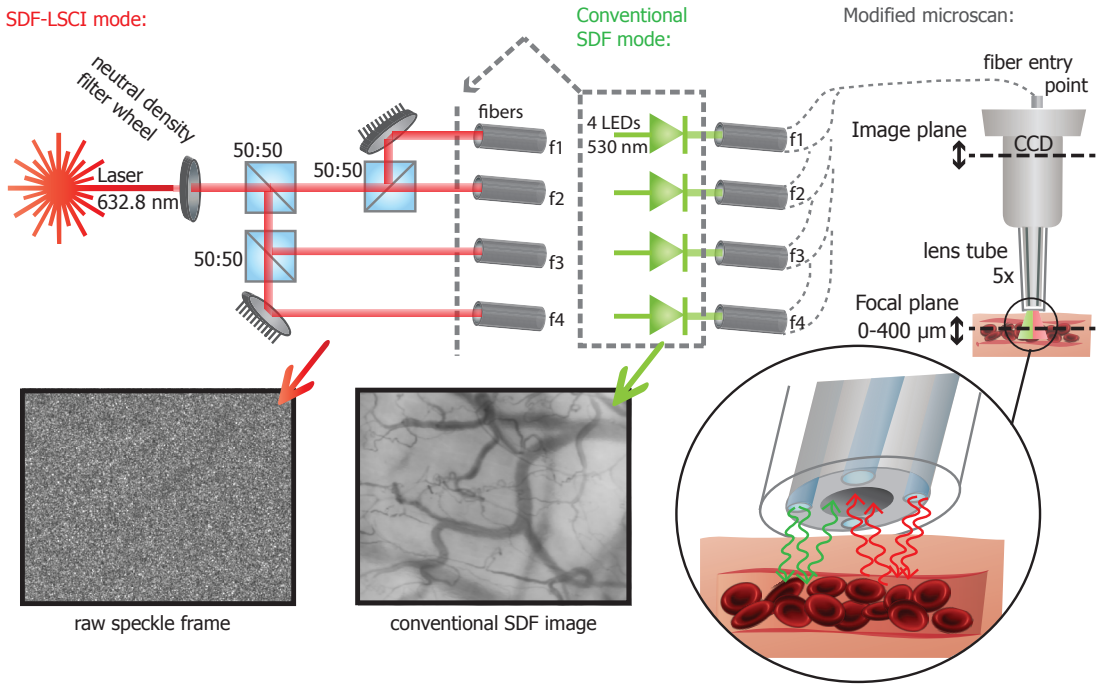

Supplementary Figure S4.1 | Dual-mode non-invasive microcirculation imaging set-up. *SDF-LSCI mode: speckle contrast due to reflection of coherent laser light by flowing RBCs and 'static' tissue. Conventional SDF mode: contrast due to absorption of green light by flowing RBCs. See text left for more details.*

S4.3 MONTE CARLO SIMULATIONS TO ESTIMATE *N*

To get a reliable estimate for the number of dynamic scattering events, *N*, we built the geometry in Monte Carlo simulation freeware [16, 17], and included the scattering coefficients of the static phantom and dynamic polystyrene spheres for all sizes and volume fractions (see Supplementary table S4.2), as shown in Supplementary Fig. S4.2. Photon transport was simulated for one fibre, and the results were rotated 90, 180 and 270 degrees to mimic 1 fibre in each corner. In this set-up the optical absorption is low and can be ignored. The number of Doppler events are stored per detected photon. We simulated 5000 dynamic photons (thus photons with at least 1 scattering event in the flow tube) detected at the centre of the tube/vessel region in the field of view and calculated the average number or Doppler scattering events, *N*, per dynamic photon. The relationship between μ_s and *N* could be linearly fitted by $N = 1.2\mu_s d$, (r^2 = 0.99) for 15 different simulations with μ_s ranging from 20 - 150 mm^{-1} and *d* the tube diameter of 0.2 mm (see Supplementary Fig. S4.2b). The factor F = 1.2 [95% upper CI - lower CI: 1.21 - 1.26, CI confidence interval] is likely due to an increased effective optical path length as a result of scattering, photons crossing the tube with a longitudinal component, and photons crossing the tube more than once. For low μ_s (< 20 mm^{-1}) the factor was slightly higher (< 1.9), due to a low number of scattering events in the tube (*N* < 5) and subsequent overestimation of the photon path through the tube. We therefore fixed the factor at 1.2 for all μ_s and this specific *d* of 0.2 mm.

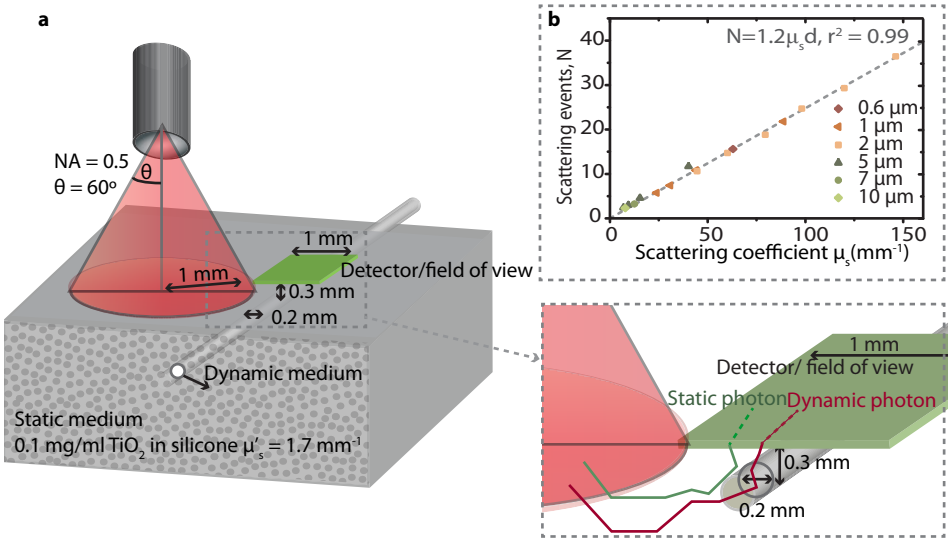

Supplementary Figure S4.2 | Monte Carlo geometry and simulation in vitro. (a) *To mimic the SDF geometry a diverging beam is located at ~1 mm distance from the detector field representing a high NA fibre and photons are launched into the static medium (TiO_2 in silicone). The flow tube with optical properties for polystyrene spheres is placed in the medium (diameter 0.2 ± 0.03 mm; depth 0.3 mm ± 0.03 mm). The simulation results are rotated to represent a fibre in each corner. For each photon detected at the centre of the tube (in the detector plane) the number of Doppler scattering events N is counted, and the average N per detected photon is plotted versus scattering coefficient in* ***(b)****, as well as a linear fit to the data (dashed line).*

The number of scattering events in the *in vivo* vessels was also estimated using Monte Carlo simulations with the same geometry as shown in Supplementary Fig. S4.2 adapted to the scattering properties of blood. The optical properties of human blood are reviewed by Bosschaart et al.[18]. We calculated the optical properties accordingly, taking into account a reduced microcirculatory hematocrit (Hct) as a result of the Fahraeus effect [19] (average microcirculatory Hct = 30%, see Supplementary table S4.1), for a range of vessel diameters [0.02 - 0.4 mm]. The resulting *N* can be described by $N = (0.92d+0.92)\mu_s d$, with *d* in mm and μ_s = 95 mm^{-1}. For chick embryo whole blood no experimentally validated optical properties

were found, therefore, we estimated the optical properties using the known red blood cell volume [20] and hematocrit [21] calculated using Mie scattering and Pervus-Yevick theories [1, 3], see Supplementary table S4.1. Inserting these value into the Monte Carlo geometry resulted in $N = (0.68d+0.92)\mu_s d$, with $\mu_s = 86$ mm^{-1}. To find N the *in vivo* vessel diameters can be estimated from conventional SDF images.

To generalize our results, we simulated two other scenarios: 1. N for vessels with full hematocrit (Hct = 45%) and 2. N for a common LSCI system geometry. In most LSCI systems, the laser light illuminates the tissue at a 45° angle and the detector is placed perpendicularly above the tissue. For all situations similar values for N were found, as is plotted in Supplementary Fig. S4.3 below.

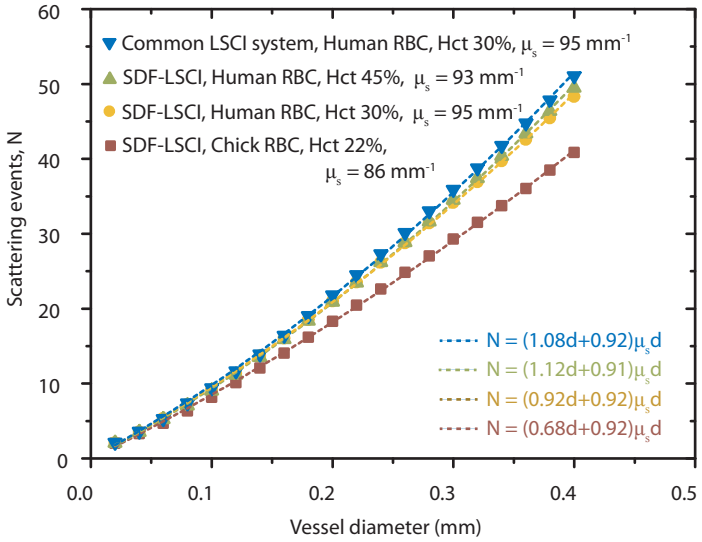

Supplementary Figure S4.3 | In vivo scattering events from Monte Carlo simulations. *The average N per detected dynamic photon for a range of vessel diameters was obtained from Monte Carlo simulations using in vivo optical properties for human (Hct 30% (yellow circles) and Hct 45% (green triangles)) and chick embryo (Hct 22% (red squares)) blood, see Supplementary table 1. In addition, N was simulated for a common LSCI system where the laser beam is directly illuminating the tissue at a 45° angle and the camera is placed perpendicularly above the tissue (blue upside down triangles). Polynomial curve fits are plotted as dashed lines and the fit coefficients are displayed (all $r^2 > 0.99$).*

S4.4 MULTI-EXPOSURE CURVES AND FITS

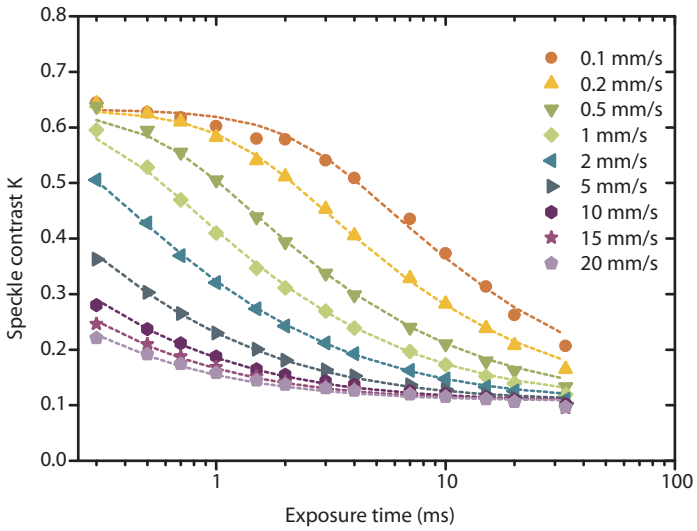

Supplementary Figure S4.4 | Multi-exposure curves and fits. *Multi-exposure speckle contrast values (data points) and corresponding fit of Supplementary Eq. (4.10) (dashed lines) for 9 different flow velocities for 2 μm polystyrene spheres (2.5 vol%). Speckle contrast K is calculated according to Supplementary Eq. (4.8), for a local region of 10 x 10 spatial pixels. No error bars are shown for clarity. At least 200 K-values in the centre of the tube were selected and the standard deviation in was K less than 5%.*

S4.5 OPTICAL PROPERTIES OF SCATTERERS

Supplementary table S4.1 and S4.2 list the optical properties of scatterers used in the *in vivo* and *in vitro* experiments. To estimate the error in theoretical α we varied the size of the polystyrene spheres by ±10% and the refractive index by ±5%, as this variation was reported for the purchased polystyrene spheres (Kisker-Biotech, Germany) [22]. For the red blood cells (RBCs) we varied the size by ±5% and refractive index by ±1%.

Table S4.1. Optical properties of scatterers at 632.8 nm[a]

	Refractive index particle	Refractive index medium	Scatterer diameter	Vol %	Scattering coefficient	g[b]
Human blood, microcirculation	n_{RBC} = 1.3937[c]	n_{plasma} = 1.345[c]	5.6 µm[d]	30%	$\mu_{s,blood}$ = 95 mm^{-1}	0.991
Human blood	n_{RBC} = 1.3937[c]	n_{plasma} = 1.345[c]	5.6 µm[d]	45%	$\mu_{s,blood}$ = 93 mm^{-1}	0.986
Chick blood, microcirculation	n_{RBC} = 1.3937[c]	n_{plasma} = 1.345[c]	7.1 µm[d]	22%[e]	$\mu_{s,blood,chick}$ = 42 mm^{-1}	0.993
TiO_2 in silicone	n_{TIO2} = 2.49[f]	$n_{silicone}$ = 1.4225[f]	~0.2 µm[f]	0.0265% (1 mg/ml)	$\mu_{s,phantom}$ = 4.1 mm^{-1}	0.58
Polystyrene spheres	n_{sphere} = 1.5872	n_{water} = 1.332	see Suppl. table 2	see Suppl. table 2	see Suppl. table 2	see Suppl. table 2

[a] Calculated using Mie and Percus-Yevick theory [23]. [b] Anisotropy (g) is the average cosine of the scattering angle. [c] See ref [18]. [d] Calculated for an equivolumetric sphere with the same volume as an human/chick RBC [18,20] [e] See ref [21] [f] See ref [24].

Table S4.2. Optical properties of polystyrene sphere solutions in water at 632.8 nm[a]

Size series			Volume fraction series								
2.5 vol%			1 µm			2 µm			5 µm		
D[b]	μ_s[c]	g[d]	vol%	μ_s[c]	g[d]	vol%	μ_s[c]	g[d]	vol%	μ_s[c]	g[d]
0.6	63	0.848	0.64	24	0.917	1.9	45	0.912	1.1	6.9	0.864
1	89	0.914	0.83	31	0.917	2.5	58	0.911	1.5	9.4	0.864
2	58	0.911	1.2	44	0.916	3.5	80	0.909	2.5	15	0.862
5	15	0.862	2.5	89	0.914	4.4	98	0.908	4.1	25	0.859
7	13	0.918				5.5	120	0.906	6.9	40	0.854
10	7.5	0.899				6.9	147	0.903			

[a]Calculated using Mie and Percus-Yevick theory [23]. [b]*D* is diameter in µm. [c] μ_s in mm-1.
[d]Anisotropy (*g*) is the average cosine of the scattering angle.

S4.6 MULTIPLE SCATTERING SCALING FACTOR FOR CHICK EMBRYO BLOOD

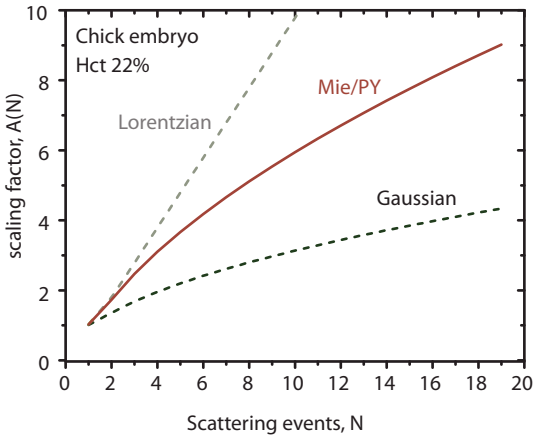

Supplementary Figure S4.5 | Multiple scattering scaling factor for α, A(N) for chick embryo blood. *A(N) is plotted versus multiple scattering events, N, in chick embryo blood calculated using our model based on Mie/PY scattering (red line). Dashed lines represent A, for Lorentzian (grey) and Gaussian (black) models for g_1. All scaling factors are calculated using a normal distribution for p(n) for Hct = 22%.*

S4.7 MICROCIRCULATORY FLOW MAPPING

With conventional-SDF and SDF-LSCI images at multiple exposure times at hand, a quantitative blood flow map can be constructed. We applied the following steps:

1. Raw speckle images were converted to *K*-images by calculating the ratio of standard deviation and mean intensity at each pixel from a local neighbourhood using a spatiotemporal local region of 7 x 7 (spatial) x 20 (temporal) pixels.
2. For each pixel in the *K*-image a multi-exposure curve fit is performed (with a priori estimated β_M and ρ as fixed parameters, as described in Methods and Supplementary Section Id) to estimate $\tau_{c,total}$.
3. To correct for offset decorrelation $\tau_{c,offset}$ is estimated as the average of the lowest 10% of pixels in the $1/\tau_{c,total}$ map and τ_c is calculated per pixel according to [10]:

$$\tau_c = \tau_{c,offset} \cdot \tau_{c,total} \Big/ \left(\tau_{c,offset}^{\,2} - \tau_{c,total}^{\,2} \right)^{1/2} \qquad (4.11)$$

   An example of such $1/\tau_c$ map (perfusion map) in false colour is shown in Fig. 4.5b (human, main paper) and Supplementary Fig. 4.6b (chick embryo).
4. For selected vessels the diameter is estimated from the conventional-SDF images and *N* is estimated following Supplementary Fig. S4.3 based on Monte Carlo simulations of our measurement geometry.
5. Selected vessels are manually masked based on conventional SDF images and $1/\tau_c$ is corrected for multiple scattering according to $1/\tau'_c = (1/\tau_c)/A(N)$, see Fig. 4.6 (human, main Chapter 4) and Supplementary Fig. S4.5 (chick embryo)
6. The resulting map is represented in false colour to visualize the blood flow (Fig. 4.5c, main Chapter 4 and Supplementary Fig. S4.6c), using $1/\tau'_c \approx [0.39 \pm 0.15]V$

This practical guide shows the feasibility of quantitative flowmetry. We identified the following revisions for enhanced performance. Step 3: The offset decorrelation correction would be improved if a site adjacent to each vessel is selected to estimate $\tau_{c,offset}$. Step 4: The vessel diameter can vary along a vessel and at intersections, therefore an improved estimate of N can be obtained by measuring the diameter dynamically along the vessels. Step 5: Vessel masking is done manually for selected vessels, automatic masking will be more complete and efficient.

In Supplementary Movie 2§ a video representation of Supplementary Fig. S4.6 is shown for the chick embryo microcirculation.

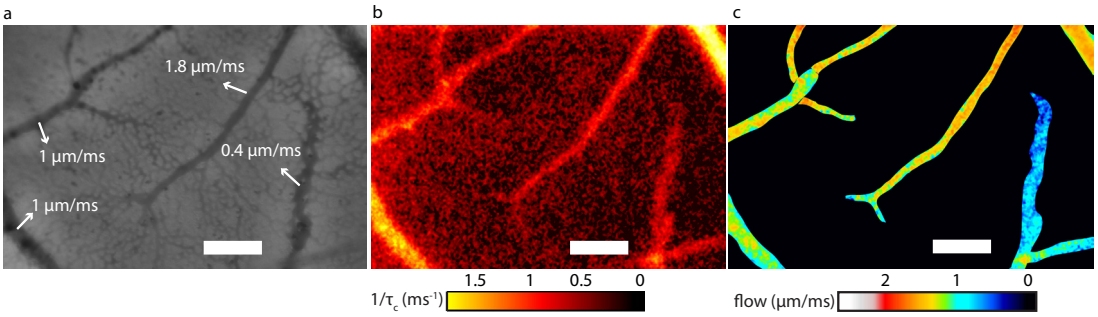

Supplementary Figure S4.6 | Blood flow mapping of chick embryo chorioallantoic membrane. ***(a)*** *Conventional SDF image with contrast due to higher absorption of (green) light by RBCs than by tissue. Flows below 2 mm/s can be measured by RBC tracking.* ***(b)*** *$1/\tau_c$ map of the same microcirculation region obtained with multi-exposure SDF-LSCI with contrast due to flow dynamics* ***(c)*** *Map of actual blood flow velocity after correction for $\tau_{c,offset}$ and A(N) (See Supplementary Fig. S4.5), and masking of selected blood vessel contours. The scale bar is 100 µm.*

S4.8 THEORETICAL PREDICTION FOR α VERSUS SCATTERER DIAMETER (POLYSTYRENE SPHERES)

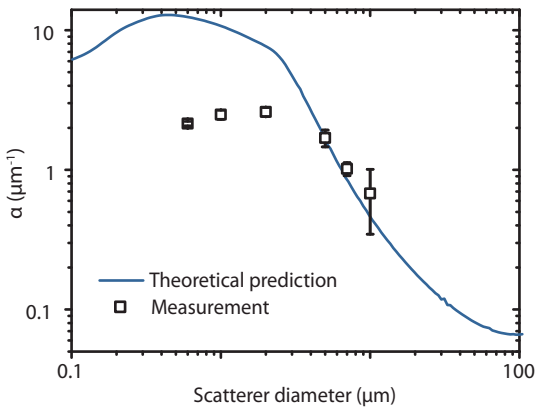

Supplementary Figure S4.7 | α versus size. *Measurement and theoretical prediction for α versus scatterer diameter (polystyrene spheres) in logarithmic scale showing the saturation of α for small diameters. Error bars are 95% CI intervals. Theoretical α is derived using Mie-Percus-Yevick scattering approximations and the number of scattering events N as obtained from Monte Carlo simulations ($N = 1.2\mu_s d$) for the in vitro flow phantom set-up.*

§ Movie 2 can be downloaded at
https://www.dropbox.com/s/kl1ctnxxtraokbw/Movie%202%20Chick%20embryo.avi?dl=0

S4.9 Experimental validation of Monte Carlo simulations

The number of scattering events N in the tube (phantom experiment) was estimated with Monte Carlo simulations (Supplementary Section 4.3), and yielded: $N = F\mu_s d$, with $F = 1.2$. We validate this estimation using experimental values of ρ (the fraction of detected photons that have been dynamically scattered). The probability of photons reaching the vessel is denoted c_1. The probability of crossing the vessel with path length l without scattering events follows from Beer's law as $\exp(-\mu_s l)$, where μ_s is the scattering coefficient. Normalizing the path length on vessel diameter d using $l=F{\cdot}d$ we obtain the probability for passing the vessel under the condition of one or more scattering events as $[1-\exp(-\mu_s F{\cdot}d)]$ so that ρ can be estimated as $\rho=c_1[1-\exp(-\mu_s F{\cdot}d)]$. In Supplementary Fig. S4.8 ρ is plotted for all *in vitro* measurements. The best fit yielded $c_1 = 0.83$ and $F = 0.95$ [95% upper CI - lower CI: 0.81 - 1.1], $r^2 = 0.83$. Fixing $F = 1.2$ to match the Monte Carlo estimation resulted in $r^2 = 0.74$. Both fits are plotted in Supplementary Fig. S4.8 and resemble the data. This analysis confirms our simulated estimate for N.

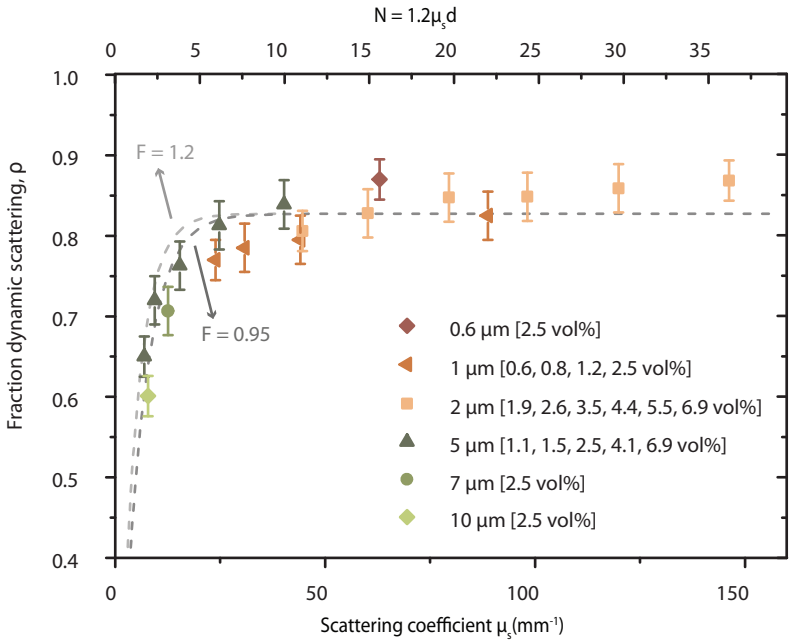

Supplementary Figure S4.8 | Fraction dynamically scattered light (ρ) versus scattering properties. *The dashed line represents a curve fit (see text above) of $\rho=c_1[1-\exp(-\mu_s F{\cdot}d)]$ with fit parameters $c_1 = 0.83$ and $F = 0.95$ ($r^2 = 0.83$), or $F = 1.2$ ($r^2 = 0.74$)*

S4.10 INFLUENCE OF GAUSSIAN APPROXIMATION ON $K(T)$

The decorrelation time τ_C is derived from the measurement of spatial speckle contrast K vs. integration time T by fitting an analytical model to the measurements. The model in Supplementary equation (4.10) assumes a Gaussian form of the autocorrelation function $g_1(\tau)$ which we justify by the approximately Gaussian form of all distributions in the model:

- The velocity distribution $P(V)$ is assumed to Gaussian because of the randomization of the scattering vector $\boldsymbol{q}$ with respect to the flow velocity vector $\boldsymbol{V}$. This assumption is not expected to hold all experimental geometries; e.g. for collimated incident light on a laminar flow profile.
- The phase function $p(\boldsymbol{q})$ is approximately Gaussian for particles with little refractive index difference from their suspended medium. For large particles with high refractive index contrast this assumption has limited accuracy.
- The distribution of the number of scattering events is Poissonian for highly diluted samples. We assume a Gaussian distribution of n which will be less valid for small number of scattering events.

We calculated $g_1(\tau)$ and $K(T)$ using our model for RBCs, and N = 1, 5 and 50 scattering events, respectively, yielding $\tau_c(1)$=2.66 ms; $\tau_c(5)$=0.78 ms and $\tau_c(50)$=0.18 ms. Supplementary Fig. S4.9 shows both groups of curves simulated for a flow velocity V = 1 μm/ms. We then calculate $g_1(\tau)$ and $K(T)$ for the Gaussian ACF using the respective values for τ_c (Supplementary equation (4.7)). Subsequent scaling of the time-axes on τ_c causes these latter curves to overlap. For reference, $g_1(\tau)$ and $K(T)$ based on the Lorentzian model (appropriate when Brownian motion is considered) are also provided. From the close resemblance of $K(T)$ curves using our model of $g_1(\tau)$ and that obtained from a Gaussian form with the same τ_c, we conclude that τ_c can be retrieved adequately using Supplementary equation (4.10). We note that this result does not imply that $g_{1,single}(\tau)$ is Gaussian nor that the scaling factor based on this assumption should be used ($A(N) \sim \sqrt{N}$, reference curve in Supplementary Fig. S4.5 and main Chapter Fig. 4.6. Rather, the $K(T)$ curve at any number of scattering events can be fitted with Supplementary Eq. (4.10) to yield τ_c and model based rescaling to τ'_c follows from the Mie/PY curve in Supplementary Fig. S4.5 and main Chapter Fig. 4.6.

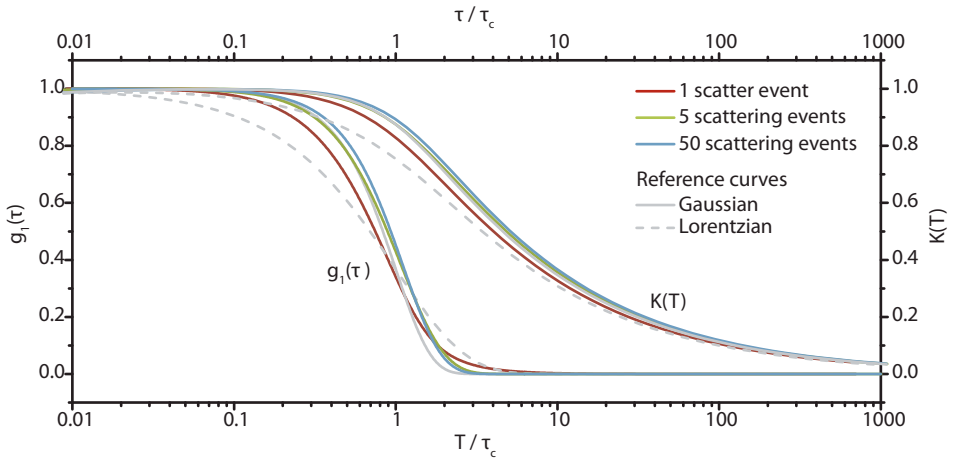

Supplementary Figure S4.9 | Theoretical modelling of $g_1(\tau)$ and K(T) in the multiple scattering regime. *$g_1(\tau)$ and $K(T)$ are theoretically calculated for the optical and geometrical properties of RBCs, for N = 1 (red), 5 (green) and 50 (blue) scattering events, yielding τ_c = 2.66 ms, τ_c = 0.78 ms and τ_c = 0.18 ms for N = 1, 5, 50 respectively. Gaussian (solid line) and Lorentzian (dashed line) models with the same τ_c are also plotted. A flow velocity of V = 1 μm/ms was used in the calculation.*

S4.11 RELATION TO DIFFUSING WAVE SPECTROSCOPY AND LASER DOPPLER FLOWMETRY

The model presented in Supplementary Section 4.1 is of similar form and origin as the theory for Diffusive Wave Spectroscopy (DWS) [23, 24] and for Laser Doppler flowmetry (LDF) [6]. Our model differs in two key areas with both. The first area covers the different approaches in deriving the ACF for single scattering events $g_{1,single}$. Rather than carrying out the integration over the velocity distribution, leading from Supplementary Eq. (4.2) to Supplementary Eq. (4.3), DWS uses a cumulant expansion for short times τ to bring the ensemble average into the exponential:

$$g_{1,\text{single}}(\tau) = \begin{cases} \left\langle \exp\left(-\boldsymbol{q}^2 V^2 \tau^2 / 6\right)\right\rangle_{\boldsymbol{q}} & \text{This work, Supplementary equation (4)} \\ \exp\left(-\left\langle \boldsymbol{q}^2 \right\rangle_{\boldsymbol{q}} V^2 \tau^2 / 6\right) & \text{Diffusive Wave Spectroscopy, ref [21]} \end{cases} \quad (4.12)$$

Where the $\langle \ldots \rangle_{\boldsymbol{q}}$ represents integration over the phase function. For DWS, $\langle \mathbf{q}^2 \rangle_{\boldsymbol{q}}$, evaluates to $2k_0^2(1\text{-}g)$ where g is the average cosine of the scattering angle. Then, the scaling factor α' between the inverse of the decorrelation time and flow velocity, $1/\tau_C = \alpha' V$ becomes:

$$\alpha'_{\text{DWS}} = k_0 \sqrt{\frac{1}{3}(1-g)} \quad (4.13)$$

We note that the dependence on particle diameter and volume fraction is included in g. Using Supplementary Table S4.1 we find $\alpha'_{\text{DWS}} \approx 0.54$ in the human microcirculation. The LDF framework proceeds to integrate Supplementary Eq. (4.12) over $\boldsymbol{q}$, weighted by the form factor, which is equivalent to our weighting with the phase function. However, LDF uses the Rayleigh-Gans (RG) approximation to estimate the angular distribution of scattered light, whereas we use the more generically applicable Mie theory combined with Percus-Yevick equation to account for volume fraction effects. LDF [6] proceeds to approximate the RG phase function by a Gaussian form leading to

$$\alpha'_{LDF} \approx \frac{1}{1.35r} \quad (4.14)$$

Where r is the particle radius. Our definition of τ_c in Supplementary Eq. (4.7) differs from the definition by Bonner and Nossal [6] who use $\tau_{1/2}$, which is related to τ_c by $\tau_{1/2} = \tau_c\sqrt{(4\ln 2/\pi)}$. For comparison reasons we adhere to our definition which explains the difference of the factor 1.35 with the factor 1.27 that is often cited in literature. For human blood we find $\alpha'_{\text{LDF}} \approx 0.26$.

The second key difference concerns how multiple scattering is treated. Our summation over the number of scattering events n is replaced by integration over the path length distribution $p(l)$. The two quantities are related through $l=n/\mu_s$:

$$g_1(\tau)=\begin{cases}\sum_n p(n)\left\langle \exp\left(-n\boldsymbol{q}^2V^2\tau^2/6\right)\right\rangle_{\boldsymbol{q}} & \text{This work, Supplementary equation (5)}\\ \int p(l)\exp\left(-2k_0^2(1-g)V^2\tau^2 l/6\right) & \text{Diffusive Wave Spectroscopy, ref [21]}\end{cases} \quad (4.15)$$

Expressions for *p(l)* can then be derived from e.g. the radiative transport equation [24], or, similar to our approach, approximated from Monte Carlo simulations [25]. LDF assumes the Poissonian form of *p*(*n*) to carry out the summation, thereby essentially limiting the range of validity to low volume fractions. Contrary to the coherent techniques discussed here, low coherence interferometry allows control over *p*(*l*), either coercing the experiment to single scattering [26] or low-order scattering [27]. The latter work proposes an empirical correction to the assumed Poissonian form of *p(l)*. Part of the correction is related to instrumental factors, part is attributed to volume fraction-dependent effects on the optical properties (correctly so in our opinion for the reasons given in Supplementary section 4.1c). The choice of *p*(*n*) becomes of lesser influence as the mean number of scattering events *N* increases, because all forms of *p*(*n*) eventually become Gaussian as per the Central Limit Theorem.

S4.12 References for Supplementary Information to Chapter 4

1. H. C. Hulst, *Light scattering by small particles* (Courier Dover Publications, 1957).
2. J. K. Percus and G. J. Yevick, "Analysis of classical statistical mechanics by means of collective coordinates," Physical Review **110**, 1 (1958).
3. M. Wertheim, "Exact solution of the Percus-Yevick integral equation for hard spheres," Phys. Rev. Lett. **10**, 321-323 (1963).
4. B. J. Berne and R. Pecora, *Dynamic light scattering: with applications to chemistry, biology, and physics* (Courier Dover Publications, 2000).
5. D. Boas and A. Yodh, "Spatially varying dynamical properties of turbid media probed with diffusing temporal light correlation," JOSA A **14**, 192-215 (1997).
6. R. Bonner and R. Nossal, "Model for laser Doppler measurements of blood flow in tissue," Applied optics **20**, 2097-2107 (1981).
7. J. W. Goodman, *Speckle phenomena in optics: theory and applications* (Roberts and Company Publishers, Greenwood Village, CO, 2007).
8. J.-P. Hansen and I. R. McDonald, *Theory of simple liquids* (Elsevier, Amsterdam, 1990).
9. L. Tsang, J. A. Kong, and K.-H. Ding, *Scattering of Electromagnetic Waves, Theories and Applications* (John Wiley & Sons, New York, 2004), Vol. 27.
10. A. Nadort, R. G. Woolthuis, T. G. van Leeuwen, and D. J. Faber, "Quantitative laser speckle flowmetry of the *in vivo* microcirculation using sidestream dark field microscopy," Biomedical optics express **4**, 2347-2361 (2013).
11. D. A. Boas and A. K. Dunn, "Laser speckle contrast imaging in biomedical optics," Journal of biomedical optics **15**(2010).
12. A. B. Parthasarathy, W. J. Tom, A. Gopal, X. Zhang, and A. K. Dunn, "Robust flow measurement with multi-exposure speckle imaging," Opt. Express **16**, 1975-1989 (2008).
13. P. Zakharov, A. Völker, A. Buck, B. Weber, and F. Scheffold, "Quantitative modeling of laser speckle imaging," Opt. Lett. **31**, 3465-3467 (2006).
14. D. D. Duncan and S. J. Kirkpatrick, "Can laser speckle flowmetry be made a quantitative tool?," JOSA A **25**, 2088-2094 (2008).
15. A. B. Parthasarathy, S. Kazmi, and A. K. Dunn, "Quantitative imaging of ischemic stroke through thinned skull in mice with Multi Exposure Speckle Imaging," Biomedical optics express **1**, 246-259 (2010).
16. F. F. M. de Mul, " Monte-Carlo simulation of Light transport in Turbid Media," in *Handbook of Coherent Domain Optical Methods, Biomedical Diagnostics, Environment and Material Science*, V. V. Tuchin, ed. (Kluwer Publishers, 2004), pp. 465-533.
17. F. F. M. de Mul, M. H. Koelink, M. L. Kok, P. J. Harmsma, J. Greve, R. Graaff, and J. G. Aarnoudse, "Laser Doppler velocimetry and Monte Carlo simulations on models for blood perfusion in tissue," Appl. Opt. **34** (1995).
18. N. Bosschaart, G. J. Edelman, M. C. Aalders, T. G. van Leeuwen, and D. J. Faber, "A literature review and novel theoretical approach on the optical properties of whole blood," Lasers Med. Sci. **29**, 453-479 (2014).
19. A. R. Pries, T. W. Secomb, P. Gaehtgens, and J. Gross, "Blood flow in microvascular networks. Experiments and simulation," Circ. Res. **67**, 826-834 (1990).
20. L. Chan, "Changes in the composition of plasma membrane proteins during differentiation of embryonic chick erythroid cell," Proceedings of the National Academy of Sciences **74**, 1062-1066 (1977).
21. P. M. Johnston, *Hematocrit Values for the Chick Embryo at Various Ages* (1955), Vol. 180, pp. 361-362.
22. A. Nicolet and F. Meli, "Report on the needs, specifications and commercial sources of microvesicle reference materials," (EMRP JRP HLT02 MetVes, 2012).
23. D. Pine, D. Weitz, P. Chaikin, and E. Herbolzheimer, "Diffusing wave spectroscopy," Phys. Rev. Lett. **60**, 1134 (1988).
24. D. Weitz, J. Zhu, D. Durian, H. Gang, and D. Pine, "Diffusing-wave spectroscopy: The technique and some applications," Phys. Scr. **1993**, 610 (1993).
25. T. B. Rice, E. Kwan, C. K. Hayakawa, A. J. Durkin, B. Choi, and B. J. Tromberg, "Quantitative, depth-resolved determination of particle motion using multi-exposure, spatial frequency domain laser speckle imaging," Biomedical optics express **4**, 2880-2892 (2013).
26. J. Kalkman, R. Sprik, and T. van Leeuwen, "Path-length-resolved diffusive particle dynamics in spectral-domain optical coherence tomography," Phys. Rev. Lett. **105**, 198302 (2010).
27. A. Wax, C. Yang, R. R. Dasari, and M. S. Feld, "Path-length-resolved dynamic light scattering: modeling the transition from single to diffusive scattering," Appl. Opt. **40**, 4222-4227 (2001).

5

Upconversion Nanoparticles

Parts in this chapter are adapted from co-authored publications:

Ref. 9.

A. V. Zvyagin, Z. Song, **A. Nadort**, V. K. A. Sreenivasan, and S. M. Deyev, "Luminescent Nanomaterials for Molecular-Specific Cellular Imaging," in Handbook of Nano-Optics and Nanophotonics (Springer, 2013), pp. 563-596.

My contribution to this book chapter: *Literature review on optical properties of UCNPs*

Ref. 12

Z. Song, Y. G. Anissimov, J. Zhao, A. V. Nechaev, **A. Nadort**, D. Jin, T. W. Prow, M. S. Roberts, and A. V. Zvyagin, "Background free imaging of upconversion nanoparticle distribution in human skin," Journal of biomedical optics 18, 061215-061215 (2013).

My contribution to this paper: *Design of quantitative imaging experiment and experimental quantification of microscope parameters.*

Ref. 34

K. Liu, J. A. Holz, Y. Ding, X. Liu, Y. Zhang, T. Langping, X. Kong, B. Priem, **A. Nadort**, S. A. G. Lambrechts, M. C. G. Aalders, W. J. Buma, P. D. Y. Liu, and H. Zhang, "Targeted labeling of early-stage tumor spheroid in chorioallantoic membrane model with upconversion nanoparticles," Nanoscale (2014).

My contribution to this paper: P*art of design, realization and performance of chick embryo CAM tumour model and intravital imaging system*.

Ref. 36

A. E. Guller, A. N. Generalova, E.V. Petersen, A.V. Nechaev, I.A. Trusova, N.N. Landyshev, **A. Nadort**, E.A. Grebenik, S.M. Deyev, A.B. Shekhter and A.V. Zvyagin, "Cytotoxicity and non-specific cellular uptake of bare and surface-modified upconversion nanoparticles in human skin cells, " Nano Research (2014).

My contribution to this paper: *Design and realization of quantitative imaging experiment, performing UCNP optical characterization and cellular uptake imaging experiment and confocal imaging, including data analysis and paper writing (relevant parts)*.

Abstract This chapter introduces optical techniques to assess biological tissues based on photoluminescent probes, as well as the relevant tissue optical properties and the desirable characteristics of the luminophores. Upconversion nanoparticles represent a class of luminophores that are particularly interesting for molecular imaging in the biomedical context. Therefore, their optical properties, the upconversion process and an introduction on bioconjugation of these nanomaterials is included.

5.1 INTRODUCTION

The results of the previous chapters on laser speckle flowmetry are promising for functional monitoring of the microvasculature in the clinic. As elucidated in Chapter 1, the microcirculation plays an important role in tumour development but can also be effective in tumour therapy and delivery of drugs and contrast agents, for example mediated by the enhanced permeability and retention (EPR) effect and targeted delivery. Although the EPR effect and its applicability in tumour detection and therapy were described almost 30 years ago [1], therapies exploiting the tumour vessel hyperpermeability are still limited in clinical use and need further investigation [2, 3]. Underlying this apparently moderate progress is the complexity of tumour development, in particular the structural features and biochemical processes, which can vary both spatially and temporally within one tumour but also between tumour types, location and patient specific characteristics [4, 5]. Therefore, imaging the tumour microvasculature is instrumental but not sufficient for a thorough understanding of tumour development. In addition, tumour detection by increased microvasculature is only possible in the case of hyper-vascularised tumours, which are characteristic for advanced stages of cancer and imply reduced patient survival [6]. Therefore, more sensitive detection approaches at the early stages of cancer are needed.

The increased focus on nanotechnology in cancer research can potentially accelerate the progress in tumour detection and therapy [7]. Controlling the size, shape and surface properties of nanoparticles allows controlling their interaction with normal versus cancer cells and tissue [2]. Therefore, nano-engineering can provide solutions for cancer therapy. Visualizing the interaction of nanoparticles with tumour vasculature or tumour cells is an important capability for cancer research, where a high imaging contrast is essential. In this chapter, I will discuss the desirable characteristics of nanoparticles that result in a high imaging contrast and introduce a novel class of nanoparticles, called upconversion nanoparticles (UCNPs), as promising photoluminescent nanomaterials.

5.2 PHOTOLUMINESCENT IMAGING OF BIOTISSUE

The ideal luminophore for biomedical imaging has excellent optical properties, as well as chemical and physical stability in biological environments [8, 9]. These optical properties include a high absorption coefficient and quantum yield for brightness, a large Stokes shift for minimal interference between excitation and emission light, and preferably no photoluminescence intermittency (blinking) and irreversible light-induced transitions to the dark states (photobleaching). In addition, the excitation and emission radiation should substantially penetrate into biological tissue. This last property is determined by the optical absorption and scattering properties of biological tissue, where the absorption is mainly due to the three tissue constituents water, oxygenated and deoxygenated haemoglobin. In Fig. 5.1a the absorption due to blood and water in skin tissue is plotted for the visible (VIS) and near infrared (NIR) wavelength range. In skin the pigment melanin is also responsible for absorption of light, although this is highly dependent on skin type (e.g. Caucasian, Mediterranean, Negroid) [10] and therefore excluded from this graph. For Caucasian skin the absorption by melanin (0.4%) is less than the absorption by blood for wavelengths >400 nm [11]. The total effective attenuation coefficient in skin including the effects of scattering is also calculated and plotted [12]. In Fig. 5.1b the tissue penetration depth of light in skin is visualized for the

UV-VIS-NIR spectrum. The tissue transparency window (650 - 1300 nm) is marked by the low effective attenuation and deep tissue penetration depth of light. Luminophores whose excitation and emission fall in this window can be detected at greater depths in tissue. In addition, unwanted tissue autofluorescence is much lower compared to exciting in the shorter wavelength range.

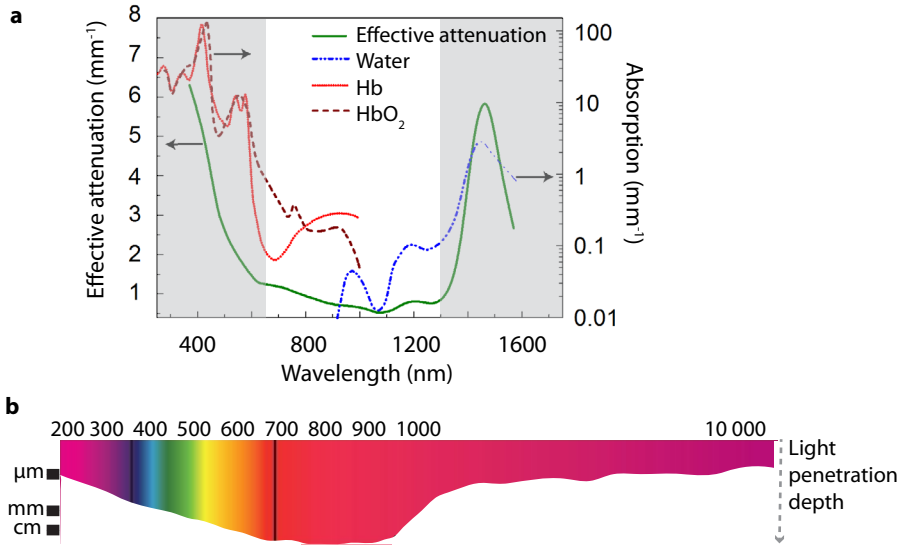

Figure 5.1 | Optical properties of skin. (a) *Optical effective attenuation spectrum of skin (green solid line), dominated by absorption spectra of water (blue -..-), deoxygenized haemoglobin (Hb, brown - -), oxygenized haemoglobin (HbO_2, red solid) and scattering of skin. The biological tissue transparency window is the unshaded area (650 - 1300 nm). Adapted from ref. [12].* ***(b)*** *Light penetration depth in skin tissue for the UV-VIS-NIR wavelength range, calculated as the depth where 37% of the incident light ($e^{-1} = 0.37$) is not diffused or absorbed (the depth scale is a logarithmic scale).*

Near infrared dyes are a group of organic fluorescent dyes whose excitation and emission properties fall in the tissue transparency window and are therefore attractive for cancer targeting and imaging [8, 13]. However, conventional NIR dyes have a poor hydrophilicity and stability in biological media, a low quantum yield and low photostability due to bleaching, although recent developments of NIR dyes have improved these characteristics to some extent [8, 14]. An alternative way to use NIR excitation light is the use of 2-photon imaging where luminophores absorb two NIR photons simultaneously and subsequently emit one photon of higher energy (shorter wavelength) than each of the excitation photons [15, 16]. This technique has delivered high-quality images and has optical sectioning capability enabling tomography. However, the chance for the simultaneous absorption of two photons is low and excitation intensities of the order 10^6 -10^9 W/cm^2 are needed for sufficient signal detection [16], acquired with expensive short pulsed lasers. Yet another process that involves the generation of anti-Stokes shifted light is photon upconversion, based on the sequential absorption and energy transfer steps involving real metastable states of the luminophore as detailed in the next section. This process occurs at excitation intensities of 1 - 10^3 W/cm^2 [17], attainable with low-cost continuous-wave lasers. Similar to dynamic light scattering techniques, the utility and production of upconversion materials depended highly on the introduction of the laser more than 50 years ago [17, 18]. However, the synthesis of nanosized upconversion materials that can be dispersed in a solution was a challenging task, which was achieved only ten years ago in the early 2000's. [19, 20]. Since then, the study of upconversion nanoparticles (UCNPs) in the biomedical sciences expanded majorly due to their key photophysical advantages: excitation in the NIR and emission in the VIS/NIR region at modest excitation intensity also characterised by a long emission lifetimes (~milliseconds) compared to conventional fluorophores (~nanoseconds). There are no endogenous molecules

known that are capable of this conversion, therefore emission of UCNPs can be discriminated from that of autofluorescence, leading to strong suppression of the background, as for example is shown in Fig. 5.2. The large anti-Stokes shift of UCNPs enables optical filters to completely reject any Stokes-shifted autofluorescence that might be induced, as opposed to NIR-dyes that exhibit a Stokes-shift which cannot be distinguished from the autofluorescence induced by NIR excitation wavelengths [12] In addition, the long lifetimes allow for time-gated detection, which can eliminate the residual background signals due to the excitation beam and autofluorescence. UCNPs have other advantageous optical properties such as nonblinking, nonphotobleaching, sharp emission bands and a large anti-Stokes shift [21].

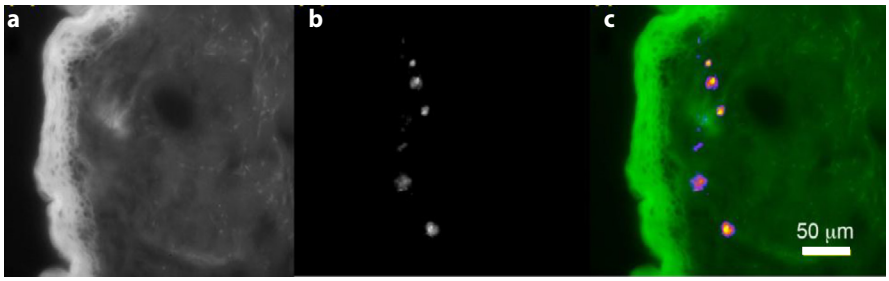

Figure 5.2. | UCNPs (NaYF4:Yb,Tm) distribution in excised skin. (a) *UV (365 nm) excited autofluorescence image of skin tissue slice treated with UCNPs* ***(b)*** *NIR (980 nm) excited upconversion image of same skin tissue slice showing only UCNP signal and no background of autofluorescence and* ***(c)*** *pseudo-colour overlay of (a) and (b) showing UCNPs (purple) in skin furrow and dermis (green), respectively. Adapted from ref. [12].*

5.3 THE UPCONVERSION PROCESS

UCNPs are dopant-host systems where trivalent lanthanide ions are dispersed in an inorganic nanocrystal matrix. The lanthanide ions are optically active centres, which can absorb photons and emit photoluminescence. Generally, the photoluminescence arises from electronic transitions in the 4f-4f orbital within a single lanthanide ion. The 4f electrons are shielded by the complete outer 5s and 5p shells resulting in sharp emission bands. The electronic transmission within the 4f shell are forbidden by quantum mechanical selection rules, but can happen due to local crystal field-induced relaxation, resulting in long lifetimes of the higher energy levels of the 4f electrons (~ milliseconds). This metastable excited state enables the occurrence of sequential excitation to a second energy level, and the exchange of energy by ion-ion interactions [17, 21]. There are five basic mechanisms for upconversion identified: excited-state absorption, energy transfer upconversion, cooperative sensitization upconversion, cross relaxation and photon avalanche [21, 22].

Most photoluminescence by UCNPs relies on the energy transfer upconversion process, which is schematically shown in Figs. 5.3 and 5.4. A detailed energy diagram of the transitions in two often used dopant pairs, Ytterbium (Yb^{3+}) - Erbium (Er^{3+}) and Ytterbium - Thulium (Tm^{3+}), is shown in Fig. 5.3a [9]. A two-level Yb^{3+} ion serves as the donor (also known as the sensitiser) which has a high absorption cross-section for the NIR excitation photons via the $^2F_{7/2} \rightarrow {}^2F_{5/2}$ transition path. Then, it non-radiatively transfers the excitation energy to a neighbouring Yb^{3+} ion, or a neighbouring Er^{3+} (or Tm^{3+}) ion (also known as the activator). As a result, the ensemble of the excited Yb^{3+} ions forms a delocalised quasi-exciton across the entire nanocrystal matrix maintained by the non-radiative energy exchange process. This excitation energy is continuously transferred to the network of activators, Er^{3+} or Tm^{3+}, a fast process at a rate of 1000

s^{-1} for the representative crystal matrix $Cs_3Lu_2Br_9$ [23]. The activated ion, for example, Er^{3+} in the $^4I_{11/2}$ metastable state can coalesce with the metastable Yb^{3+} ($^2F_{5/2}$) via the collective pair-wise process called energy transfer upconversion. As a result, the Er^{3+} ($^4I_{11/2}$) makes a transition to the next-level excited state Er^{3+} ($^4F_{7/2}$), followed by a rapid non-radiative transition to Er^{3+} ($^4S_{3/2}$) at the expense of the Yb^{3+} ($^2F_{5/2}$) → Yb^{3+} ($^2F_{7/2}$) falling back to the ground state. The Er^{3+} ($^4S_{3/2}$) emits in a multiplet green spectral band, and also in a multiplet red spectral band, following the non-radiative phonon-assisted transition Er^{3+} ($^4S_{3/2}$) → Er^{3+} ($^4F_{9/2}$), as one can see in the emission spectral bands in Fig. 5.3b. The Er^{3+} ($^4F_{9/2}$) population is also built up via an alternative excitation path: non-radiative transition Er^{3+} ($^4I_{11/2}$) → Er^{3+} ($^4I_{13/2}$), followed by the energy transfer upconversion Er^{3+} ($^4I_{13/2}$) → Er^{3+} ($^4F_{9/2}$) and Yb^{3+} ($^2F_{5/2}$) → Yb^{3+} ($^2F_{7/2}$) back to the ground state. Other energy transfer paths involve the absorption and exchange of 3 excitation photons resulting in a blue emission band (Fig. 5.3b). The energy diagram of the Tm^{3+} activator ion results in two main emission bands at the NIR and blue wavelengths (Fig. 5.3c).

Fig. 5.4 presents a simplified schematic diagram of energy transfer upconversion. At low (sub-saturation, ~100 W/cm^2) excitation intensity I_{ex} the emitted upconversion signal depends on the population of the second energy level which depends on $I_{ex}^{\ 2}$ for a 2-photon process, generally $I_{ex}^{\ n}$ for an *n*-photon process (although competitive energy transfer processes and size-dependent nonradiative decay result in a value somewhat deviating from *n* [24-27]). Due to this nonlinearity, the upconversion efficiency η_{uc} decreases when I_{ex} decreases. This poses a challenge to tissue imaging, since tissue scattering decreases I_{ex} with imaging depth resulting in a quick reduction of the photoluminescence signal with depth. A relatively high upconversion efficiency is observed for the Yb,Er and Yb,Tm dopant pairs in a host matrix consisting of $NaYF_4$ [25], typically around 1% for nanosized materials [28]. The η_{uc} also depends on the synthesized crystal purity, phase and size and is therefore an important parameter to measure for feedback on the design and synthesis of UCNPs. In comparison, NIR-dyes and NIR-QD's possess higher conversion efficiencies of 5-25% and 20-70% respectively [9], however, QD's fluorescence is intermittent ('blinking'), while NIR dyes have a poor photochemical stability ('bleaching'). The advantages of UCNPs such as a high photochemical and thermal stability, a large anti-Stokes shift, favourable excitation and emission properties in the context of biological tissue optical properties and stable optical properties in biological environments, motivate to further investigate and improve the conversion efficiency of UCNPs. In Chapter 6 a quantitative measurement system for the determination of the absolute η_{uc} is designed using an integrating sphere set up. Since the background signal is virtually absent detection of UCNPs with a high contrast is achievable in spite of the low η_{uc}. In Chapter 6 the UCNP imaging limits are explored both experimentally and theoretically by imaging of a single particle in the context of biological tissue. The imaging systems deployed in Chapters 6 and 7 are wide-field luminescence imaging systems. In the context of this, the long emission lifetimes of UCNPs can be utilized for time-gated detection and complete suppression of the excitation light which is a big advantage in comparison to short-lived fluorescence from organic dyes and QD's. However, it should be noted that the long emission lifetimes pose a disadvantage to other imaging set-ups that are based on the scanning of a small illumination spot, such as scanning confocal systems. This optical property is important to keep in mind when designing detection systems for UCNP-guided imaging applications. Besides the assessment of optical properties and imaging systems, for UCNP-based biomedical applications biocompatible particles are required to uncover information about living cells and tissues.

5.4 BIOCONJUGATION

Generally, living systems treat exogenous material as an unwelcome intruder and engage in disposal protocols. For a more meaningful communication with cells, an ideal optically bright luminophore exhibits excellent biochemical properties, such as a good dispersibility in buffers and suitable chemical functionality allowing strong attachment of biomolecules – a process termed bioconjugation. Bioconjugation is a critical step in building biomolecular nanoparticle assemblies, serving two main functions in the context of cancer research: facilitating prolonged circulation times in the bloodstream and tumour targeting purposes.

The biochemical properties of UCNPs provide a challenge in this regard. Firstly, as-synthesized UCNPs are hydrophobic due to surface oleic groups and would rapidly aggregate when dispersed in water or buffer, making them useless for further biomedical interactions. Secondly, the most popular inorganic host of UCNP, $NaYF_4$ does not provide adequate surface anchoring points for firm docking of biomolecules. And thirdly, the η_{uc} is highly susceptible to surface functionalization, where high-energy vibronic modes

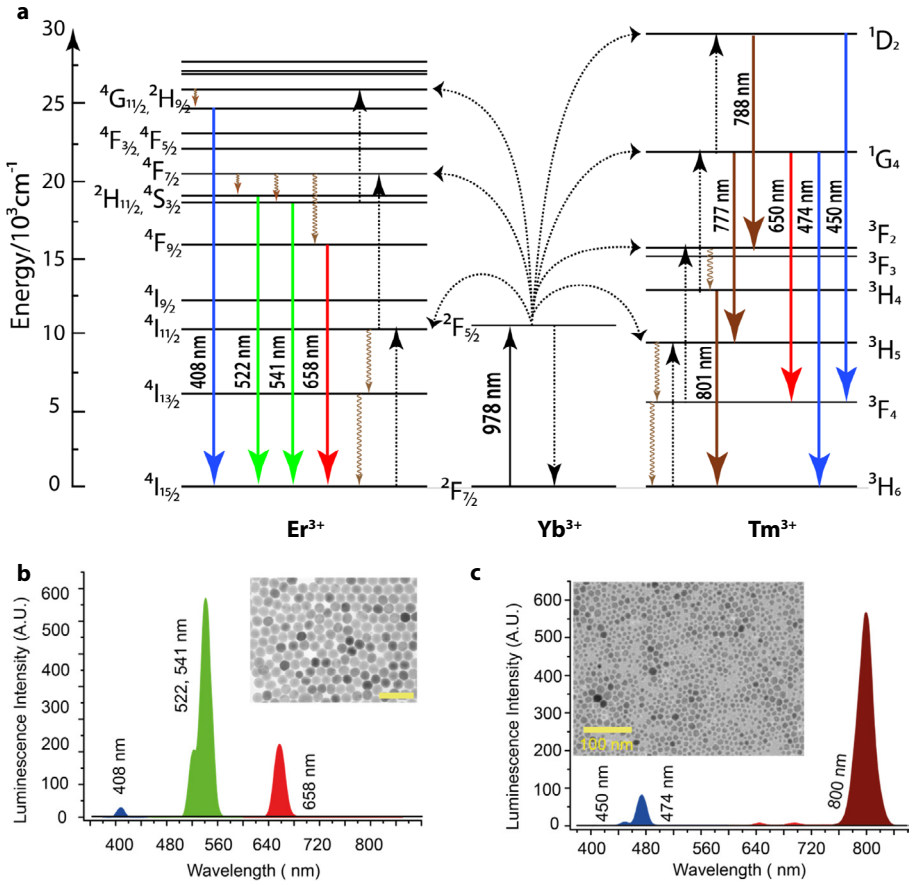

Figure 5.3 | Energy levels in photon upconversion. ***(a)*** *Schematic energy level diagram of Yb^{3+} sensitizer ions with participating Erbium (Er^{3+}) or Thulium (Tm^{3+}) activator ions. The upconversion process results in specific emission spectra for NaYF4:Yb,Er* ***(b)*** *and NaYF4:Yb,Tm* ***(c)*** *nanomaterials. The insets show their corresponding transmission electron microscopy images. Adapted from ref. [12] and ref. [9].*

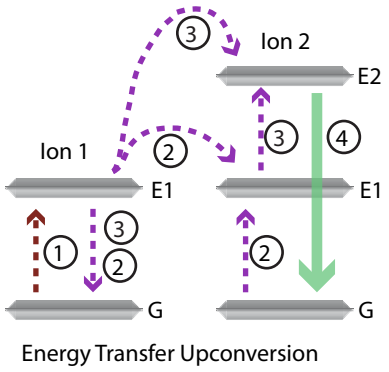

Figure 5.4 | Schematic diagram of energy transfer upconversion process in UCNPs. *The following consecutive steps can be identified: 1. photon excitation of ion 1 to energy level E1; 2. energy transfer to energy level E1 (ion 2) and remission to ground state G (ion 1); 3. energy transfer to energy level E2 (ion 3) and remission to ground state G (ion 1) and 4. emission of one higher energy photon and remission to ground state G (ion 2).*

of some functional groups provide non-radiative depletion of the excited states of the activator ions [29]. A common solution is to cover the surface of nanoparticles by polyethylene-glycol (PEG). These groups prevent nanoparticle merging and aggregation via the mechanism of steric hindrance [30]. Also, PEGylation represents the core of the so-called stealth functionalization preventing PEGylated nanoparticles intravenously injected into the blood stream from rapid immune-mediated removal [31]. However, PEG groups have their disadvantages associated with poorly-controlled polymer chains, and PEG chemistry is expensive [9]. Another methodology to improve the UCNP surface anchoring properties is to coat the particles with an additional layer that is suitable for subsequent bioconjugation. Coating the UCNP with a silica shell represents an attractive approach due to the shell stability in the biological range of pH, and maturity of the silica surface coating technology [32]. A different coating method makes use of amphiphilic polymers that represent molecules with hydrophobic and hydrophilic terminals. This approach has been successfully demonstrated for the surface activation of several inorganic nanocrystals [33]. An amphiphilic polymer can intercalate the hydrophobic surface groups with their hydrophobic portion and their extending hydrophilic portion ensures water solubility. Addition of bis(6-aminohexyl)amine resulted in cross-linking of the polymer chains around each nanoparticle and a successful and robust transfer of hydrophobically capped nanocrystals from organic to aqueous solution [33]. Suitable amphiphilic polymers for UCNPs are for example poly(maleic anhydride-alt-1-octadecene) (UCNP-PMAO), polyethylenimine (UCNP-PEI), poly (D,L-lactide) (UCNP-PLa), and poly(lactide-co-glycolide) (UCNP-PLG). A layer-by-layer approach can be applied to control the coating thickness. These surface modifications are illustrated in Fig. 5.5. An additional advantage of the amphiphilic polymer coating is the shielding of the surface from environmental interaction to prevent quenching processes. In Chapter 7, the amphiphilic polymer coating is successfully applied to UCNPs, showing prolonged stability in water and buffer solutions. A last modification strategy is based on ligand exchange, where surface oleates are first removed to obtain ligand-free UCNPs, which are subsequently treated with hydrophilic surface groups such as poly acrylic acid (UCNP-PAA) making them water soluble (referred to in Chapter 8 [34]).

Amphiphilic polymer coated UCNPs with exposed COOH functional groups are suitable for further functionalization. Using a universal bioconjugation protocol, i.e. EDC/sNHS reaction, subsequent attachment of proteins (e.g. antibodies), or applying the modular approach using streptavidin:biotin or barstar:barnase

protocols is straightforward [35]. In Chapter 7, this latter protocol is utilized to biofunctionalize UCNPs with antibodies targeting human breast cancer. This shows that UCNPs not only possess unique optical advantages for imaging in living tissues, they also serve as a docking platform that can be engineered for targeted detection and imaging of tumours.

In the next chapters, UCNP photophysical and biochemical properties are put to the experimental test, specifically imaging of single UCNPs (Chapter 6) and the detection of a small cluster of UCNP-targeted breast cancer cells (Chapter 7). In both chapters, the results are interpreted in the theoretical framework of UCNP detection in tissue, which allows projection onto imaging scenarios using UCNPs and predict their performance. This helps to identify feasible applications of UCNPs in the biomedical context.

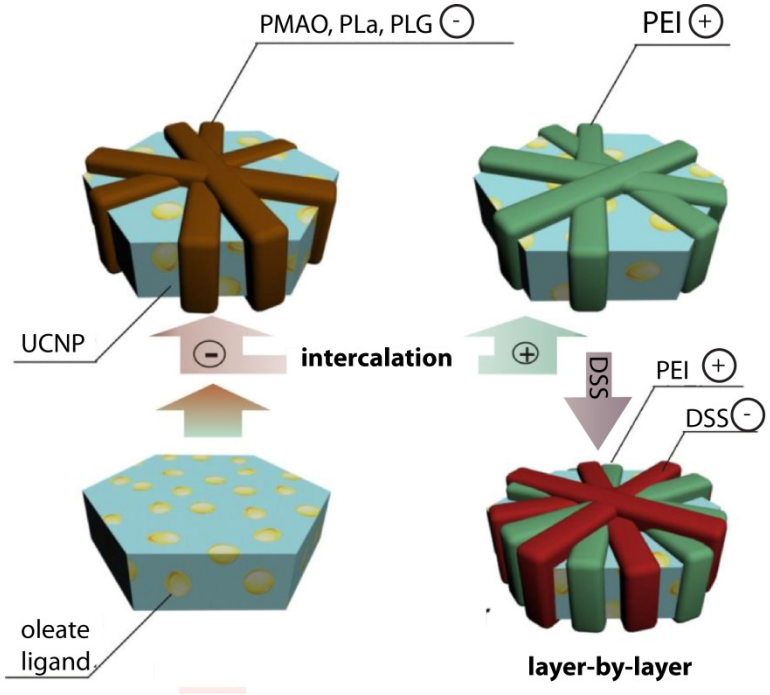

Figure 5.5 | Surface modification of UCNPs. *As-synthesized UCNP (NaYF4: Yb,Er) surface modified with amphiphilic polymers (negatively-charged PMAO, PLa and PLG; and positively-charged PEI) performed by intercalation. The resultant particles were colloidally stable UCNP-PMAO, UCNP-PLa, UCNP-PLG (negative) and UCNP-PEI (positive). Bilayer modification of UCNP-PEI with DSS was performed by the layer-by-layer assembly method and resulted in UCNP-PEI-DSS. Adapted from ref. [36]*

5.5 References

1. Y. Matsumura and H. Maeda, "A new concept for macromolecular therapeutics in cancer chemotherapy: mechanism of tumoritropic accumulation of proteins and the antitumor agent smancs," Cancer Res. **46**, 6387-6392 (1986).
2. S. D. Perrault, C. Walkey, T. Jennings, H. C. Fischer, and W. C. Chan, "Mediating tumor targeting efficiency of nanoparticles through design," Nano Lett. **9**, 1909-1915 (2009).
3. A. Z. Wang, R. Langer, and O. C. Farokhzad, "Nanoparticle delivery of cancer drugs," Annu. Rev. Med. **63**, 185-198 (2012).
4. P. Carmeliet and R. K. Jain, "Angiogenesis in cancer and other diseases," Nature **407**, 249-257 (2000).
5. U. Prabhakar, H. Maeda, R. K. Jain, E. M. Sevick-Muraca, W. Zamboni, O. C. Farokhzad, S. T. Barry, A. Gabizon, P. Grodzinski, and D. C. Blakey, "Challenges and key considerations of the enhanced permeability and retention effect for nanomedicine drug delivery in oncology," Cancer Res. **73**, 2412-2417 (2013).
6. M. Sant, T. Aareleid, F. Berrino, M. B. Lasota, P. Carli, J. Faivre, P. Grosclaude, G. Hedelin, T. Matsuda, and H. Møller, "EUROCARE-3: survival of cancer patients diagnosed 1990–94—results and commentary," Ann. Oncol. **14**, v61-v118 (2003).
7. M. Wang and M. Thanou, "Targeting nanoparticles to cancer," Pharmacol. Res. **62**, 90-99 (2010).
8. S. Luo, E. Zhang, Y. Su, T. Cheng, and C. Shi, "A review of NIR dyes in cancer targeting and imaging," Biomaterials **32**, 7127-7138 (2011).
9. A. V. Zvyagin, Z. Song, A. Nadort, V. K. A. Sreenivasan, and S. M. Deyev, "Luminescent Nanomaterials for Molecular-Specific Cellular Imaging," in *Handbook of Nano-Optics and Nanophotonics* (Springer, 2013), pp. 563-596.
10. N. Bosschaart, R. Mentink, J. H. Kok, T. G. Van Leeuwen, and M. C. Aalders, "Optical properties of neonatal skin measured *in vivo* as a function of age and skin pigmentation," J. Biomed. Opt. **16**, 097003-097003-097010 (2011).
11. N. Bosschaart, "Quantitative and localized spectroscopy for non-invasive bilirubinometry in neonates," (University of Amsterdam, Amsterdam, 2012).
12. Z. Song, Y. G. Anissimov, J. Zhao, A. V. Nechaev, A. Nadort, D. Jin, T. W. Prow, M. S. Roberts, and A. V. Zvyagin, "Background free imaging of upconversion nanoparticle distribution in human skin," J. Biomed. Opt. **18**, 061215-061215 (2013).
13. S. A. Hilderbrand and R. Weissleder, "Near-infrared fluorescence: application to< i> *in vivo*</i> molecular imaging," Curr. Opin. Chem. Biol. **14**, 71-79 (2010).
14. U. Resch-Genger, M. Grabolle, S. Cavaliere-Jaricot, R. Nitschke, and T. Nann, "Quantum dots versus organic dyes as fluorescent labels," Nat. Meth. **5**, 763-775 (2008).
15. W. Denk, J. H. Strickler, and W. W. Webb, "Two-photon laser scanning fluorescence microscopy," Science **248**, 73-76 (1990).
16. C. Buehler, K. H. Kim, C. Y. Dong, B. R. Masters, and P. T. So, "Innovations in two-photon deep tissue microscopy," Engineering in Medicine and Biology Magazine, IEEE **18**, 23-30 (1999).
17. F. Auzel, "Upconversion and anti-stokes processes with f and d ions in solids," Chem. Rev. **104**, 139-174 (2004).
18. J. Hecht, "Short history of laser development," Optical Engineering **49**, 091002-091002-091023 (2010).
19. S. Heer, K. Kömpe, H. U. Güdel, and M. Haase, "Highly Efficient Multicolour Upconversion Emission in Transparent Colloids of Lanthanide-Doped $NaYF_4$ Nanocrystals," Adv. Mater. **16**, 2102-2105 (2004).
20. S. Heer, O. Lehmann, M. Haase, and H. U. Güdel, "Blue, Green, and Red Upconversion Emission from Lanthanide-Doped LuPO4 and YbPO4 Nanocrystals in a Transparent Colloidal Solution," Angewandte Chemie International Edition **42**, 3179-3182 (2003).
21. G. Chen, H. Qiu, P. N. Prasad, and X. Chen, "Upconversion Nanoparticles: Design, Nanochemistry, and Applications in Theranostics," Chem. Rev. (2014).
22. G. Chen, G. Somesfalean, Y. Liu, Z. Zhang, Q. Sun, and F. Wang, "Upconversion mechanism for two-color emission in rare-earth-ion-doped Zr O 2 nanocrystals," Physical Review B **75**, 195204 (2007).
23. M. P. Hehlen, G. Frei, and H. U. Güdel, "Dynamics of infrared-to-visible upconversion in Cs 3 Lu 2 Br 9: 1% Er 3+," Physical Review B **50**, 16264 (1994).
24. J. Suyver, A. Aebischer, D. Biner, P. Gerner, J. Grimm, S. Heer, K. Krämer, C. Reinhard, and H. Güdel, "Novel materials doped with trivalent lanthanides and transition metal ions showing near-infrared to visible photon upconversion," Optical Materials **27**, 1111-1130 (2005).
25. K. W. Krämer, D. Biner, G. Frei, H. U. Güdel, M. P. Hehlen, and S. R. Lüthi, "Hexagonal sodium yttrium fluoride based green and blue emitting upconversion phosphors," Chem. Mater. **16**, 1244-1251 (2004).
26. M. Pollnau, D. Gamelin, S. Lüthi, H. Güdel, and M. Hehlen, "Power dependence of upconversion luminescence in lanthanide and transition-metal-ion systems," Physical Review B **61**, 3337 (2000).
27. Y. Wang, S. Smolarek, X. Kong, W. J. Buma, A. M. Brouwer, and H. Zhang, "Effect of surface related organic vibrational modes in luminescent upconversion dynamics of rare earth ions doped nanoparticles," J. Nanosci. Nanotechnol. **10**, 7149-7153 (2010).
28. J.-C. Boyer and F. C. Van Veggel, "Absolute quantum yield measurements of colloidal NaYF 4: Er3+, Yb3+ upconverting nanoparticles," Nanoscale **2**, 1417-1419 (2010).
29. F. Wang, J. Wang, and X. Liu, "Direct Evidence of a Surface Quenching Effect on Size-Dependent Luminescence of Upconversion Nanoparticles," Angew. Chem. **122**, 7618-7622 (2010).
30. J.-C. Boyer, M.-P. Manseau, J. I. Murray, and F. C. van Veggel, "Surface modification of upconverting NaYF4 nanoparticles with PEG– phosphate ligands for NIR (800 nm) biolabeling within the biological window," Langmuir **26**, 1157-1164 (2009).
31. R. Gref, M. Lück, P. Quellec, M. Marchand, E. Dellacherie, S. Harnisch, T. Blunk, and R. Müller, "'Stealth'corona-core nanoparticles surface modified by polyethylene glycol (PEG): influences of the corona (PEG chain length and surface density) and of the core composition on phagocytic uptake and plasma protein adsorption," Colloids and Surfaces B: Biointerfaces **18**, 301-313 (2000).
32. R. S. Niedbala, H. Feindt, K. Kardos, T. Vail, J. Burton, B. Bielska, S. Li, D. Milunic, P. Bourdelle, and R. Vallejo, "Detection of analytes by immunoassay using up-converting phosphor technology," Anal. Biochem. **293**, 22-30 (2001).
33. T. Pellegrino, L. Manna, S. Kudera, T. Liedl, D. Koktysh, A. L. Rogach, S. Keller, J. Rädler, G. Natile, and W. J. Parak, "Hydrophobic nanocrystals coated with an amphiphilic polymer shell: a general route to water soluble nanocrystals," Nano Lett. **4**, 703-707 (2004).
34. K. Liu, J. A. Holz, Y. Ding, X. Liu, Y. Zhang, T. Langping, X. Kong, B. Priem, A. Nadort, S. A. G. Lambrechts, M. C. G. Aalders, W. J. Buma, P. D. Y. Liu, and H. Zhang, "Targeted labeling of early-stage tumor spheroid in chorioallantoic membrane model with upconversion nanoparticles," Nanoscale (2014).
35. V. K. Sreenivasan, A. V. Zvyagin, and E. M. Goldys, "Luminescent nanoparticles and their applications in the life

sciences," J. Phys.: Condens. Matter **25**, 194101 (2013).
36. A. E. Guller, A. N. Generalova, E. V. Petersen, A. V. Nechaev, I. A. Trusova, N. N. Landyshev, A. Nadort, E. A. Grebenik, S. M. Deyev, A. B. Shekhter, and A. V. Zvyagin, "Cytotoxicity and non-specific cellular uptake of bare and surface-modified upconversion nanoparticles in human skin cells," Nano Research (in press) (2014).

6

Quantitative Imaging of Single Upconversion Nanoparticles in Biological Tissue

Adapted from:

A. Nadort, V. K. Sreenivasan, Z. Song, E. A. Grebenik, A. V. Nechaev, V. A. Semchishen, V. Y. Panchenko, and A. V. Zvyagin, "Quantitative imaging of single upconversion nanoparticles in biological tissue," PLoS One 8, e63292 (2013).

My contribution to this paper:
Design and realization of all imaging, modelling and optical characterization experiments, performing the experiments, data analysis, paper writing (I have not contributed to: synthesis of the nanoparticles)

Abstract The unique luminescent properties of new-generation synthetic nanomaterials, upconversion nanoparticles (UCNPs), enable high-contrast optical biomedical imaging by suppressing the background of biological tissue autofluorescence and evading high tissue absorption. This raised high expectations on the UCNP utilities for intracellular and deep tissue imaging, such as whole animal imaging. At the same time, the critical nonlinear dependence of the UCNP luminescence on the excitation intensity results in dramatic signal reduction at (~1 cm) depth in biological tissue. Here, we report on the experimental and theoretical investigation of this trade-off aiming at the identification of optimal application niches of UCNPs e.g. biological liquids and subsurface tissue layers. As an example of such applications, we report on single UCNP imaging through a layer of haemolysed blood. To extend this result towards in vivo applications, we quantified the optical properties of single UCNPs and theoretically analyzed the prospects of single-particle detectability in scattering and absorbing bio-tissue using a human skin model. The model predicts that a single 70-nm UCNP would be detectable at skin depths up to 400 μm, unlike a hardly detectable single fluorescent (fluorescein) dye molecule. UCNP-assisted imaging in the ballistic regime thus allows for excellent applications niches, where high sensitivity is the key requirement.

6.1 INTRODUCTION

Optical imaging of biological tissues provides highly informative, non-invasive and inexpensive means to assess the tissue physiological status and functionality, especially for diagnosis of pathological sites. Labelling these tissue sites with luminescent biocomplexes, often referred to as molecular probes, improves localization accuracy and sensitivity. Deployment of a new class of molecular probes whose excitation/ emission falls into the so-called biological tissue transparency window (650 nm – 1300 nm), allows deeper imaging in virtue of the minimized absorption and scattering of biotissue in this near-infra-red (NIR) wavelength range [1, 2]. For example, specific labelling of cancerous lesions with a molecular probe based on indocyanine green (the only NIR organic dye approved for routine clinical procedures) provided up to a 4-fold increase in the tumour imaging contrast in comparison with that achieved using the intrinsic haemoglobin spectral signature and tissue scattering [3, 4].

The development of NIR-emitting probes is traditionally directed towards organic dyes, but more recent studies have demonstrated considerable promise of inorganic nanoparticle-based probes, such as quantum dots (QDs) and most novel upconversion nanoparticles (UCNPs) [5, 6]. Organic NIR-dyes are favourably small, easily dispersed in an aqueous environment and can be functionalized using established bioconjugation protocols. However, their poor thermal and photochemical stability (photobleaching) and a low fluorescence quantum yield (QY) (5-25% in NIR, with propensity to deteriorate in biological environments) are inferior in comparison with QDs whose attractive optical properties include size-tuneable optical absorption and emission, high photochemical stability and high QY (20-70% in NIR), in addition to high thermal stability [7]. On the other hand, QD fluorescence is intermittent ('blinking') hindering applications such as single molecule tracking, while QD intrinsic toxicity largely precludes their use *in vivo* [8]. UCNPs share the high photochemical and thermal stability of QDs and other inorganic nanomaterials, complemented with non-blinking emission and demonstrated biocompatibility. In addition, UCNPs can be employed as a docking platform for large drug payloads for targeted delivery [9]. The key advantage of UCNPs is their unique photochemical structure that enables "upconversion" of NIR excitation light (980 nm) of modest intensity (100 W/cm^2) to the higher energy visible emission (450 - 850 nm) [10]. Since no known biological molecule is capable of such conversion [1, 11], the intrinsic tissue fluorescence, termed autofluorescence, can be eliminated in the detection path by conventional optical short-pass filtering. In addition, the exceptionally long (sub-milliseconds) luminescence lifetimes of UCNPs allow realization of time-gated detection schemes that can completely suppress the residual back-scattered excitation light bleeding through the (interference) spectral filters [12]. Since *in vivo* imaging performance is crucially dependent on the contrast provided by the molecular probe [1], background-free detection of UCNPs is very promising, as has been shown by the autofluorescence-free trans-illumination imaging in mice using biocompatible UCNPs [13, 14].

The unique upconversion property of UCNPs is a result of the sequential photon absorption and energy transfer processes within an inorganic host matrix, where hexagonalphase β-$NaYF_4$ co-doped with trivalent lanthanide ions reported to be the most efficient [15, 16]. These dopant ions are classified as sensitizers and activators considering their respective roles in the UCNP absorption and emission. The sensitizer, typically Ytterbium ion (Yb^{3+}), absorbs the NIR-radiation energy and transfers it non-radiatively to the closely spaced neighbouring Yb^{3+}, forming a network of excited Yb^{3+} (referred to as delocalized quasi-

exciton [17]) until the energy is seized by activator ions, usually Erbium (Er^{3+}), or Thulium (Tm^{3+}). The activator makes a transition to a metastable excited state, from where it can coalesce with a nearby excited Yb^{3+}-ion and transfer to the next energy level (a process called energy transfer upconversion) at the expense of the participating Yb^{3+} decaying to the ground state. Multiple-step energy transfer upconversion is also possible. The activator can return to the ground state by radiating a photon in the visible or NIR wavelength range. The upconversion emission results from the absorption of 2 or more NIR photons, and hence is supralinear versus the excitation intensity, I_{ex}, as quantified by the conversion efficiency (η_{uc}) addressed in Section 6.2.2. In contrast with other anti-Stokes processes occurring at $I_{ex} \sim \times 10^5$ W/cm^2 [18] the energy transfer upconversion occurs via real metastable excited state(s) at rather modest $I_{ex} \sim 1 \times 10^2$ W/cm^2 that is readily achievable by focusing a continuous-wave excitation beam.

The specific photophysical properties of upconversion nanoparticles entail several challenges for optical biomedical imaging. Firstly, the quasi-excitonic nature of UCNP excitation renders the emission size dependent and susceptible to surface quenching [19] and (biological) environment, which causes reduction of η_{uc} values that are generally small compared to those of QDs or organic fluorescent dyes. Values of η_{uc} are typically around 1% for nanoparticle diameters of ~50 nm, shown to be the optimal size for cellular receptor-mediated internalization [20]. Secondly, η_{uc} is dependent on the excitation intensity and increases to a plateau value, for which the I_{ex} is referred to as saturation intensity, I_{sat} ($I_{sat} \cong 1 \times 10^2$ W/cm^2). Keeping I_{ex} close to I_{sat} is preferable for biomedical imaging.

This dependency of η_{uc} on I_{ex} poses the main challenge for UCNP-assisted optical imaging in deep (live) tissue layers exceeding centimetre(s). Indeed, the realization of I_{sat} by focusing is hardly possible in turbid biotissue, while the laser power is limited by the allowed maximum permissible exposures (MPEs). The UCNP luminescence signal is therefore diminished with depth as was demonstrated in tissue phantom experiments [14]. In another recent study, the critical dependence of η_{uc} versus depth was manifested by the considerable deterioration of axial and lateral resolution of full-field upconversion microscopy at depths of ~300-400 μm [21]. These results urge identification of practical application niches for UCNPs that will benefit from the aforementioned advantages of UCNPs, while not being restricted by their limitations. Promising scenarios include imaging in biological fluids, thick slices and subsurface tissue layers, where the UCNP-based molecular probe contrast is expected to be superior to that of existing molecular probes, including organic fluorescent dyes.

This work aims to explore the cutting-edge optical imaging scenario represented by a single UCNP buried in an absorbing biological environment, which was demonstrated by single-UCNP imaging through a layer of haemolysed blood. We believe this result has not been reported before [22-25]. We report on absolute conversion efficiency and spectral properties of single UCNPs. The subsequent thorough characterization of the UCNP emission signal and excitation/detection parameters allowed projection of the experimental results onto a theoretical model, generalized to biomedical imaging applications of extreme sensitivity in challenging *in vivo* environments. Single-UCNP imaging was modelled to be feasible in skin depths of a few hundred micrometers, with superior contrast compared to a conventional fluorescent dye molecule. The results show that imaging in the ballistic regime allows for excellent applications of UCNP-guided imaging in life sciences where high sensitivity is a key requirement.

6.2 MATERIALS AND METHODS

6.2.1 Synthesis

Synthesis reagents

Y_2O_3, Yb_2O_3, Er_2O_3, sodium trifluoroacetate 99%, trifluoroacetic acid 98%, oleic acid 90%, 1-octadecene 90% (all purchased from Sigma-Aldrich).

Synthesis protocol of β-$NaYF_4$

Yb,Er nanophosphors: The mixture of Y_2O_3 (0.78 mmol), Yb_2O_3 (0.20 mmol), Er_2O_3 (0.02 mmol) was suspended in 70% trifluoroacetic acid (20 ml) and gently refluxed until a clear solution was obtained (≈ 6 h), then cooled to room temperature. After the solution was evaporated, the formed residue was dried in vacuum (0.1 torr, 3h). The resulting slurry was thoroughly grinded in agate mortar into a fine homogenous powder. This rare-earth trifluoroacetate mixture and sodium trifluoroacetate (1 mmol) were added to oleic acid (6 ml) and 1-octadecene (6 ml) in a three-neck flask, with a thermometer, septum stopper and glass magnetic stirrer. The solution was heated to 100 °C and stirred under vacuum for 30 min for degassing and removal of water. The mixture was subsequently gradually heated at a rate of 8 °C/min to 290 °C, and kept at this temperature for 45 min under argon atmosphere. A solution of sodium trifluoroacetate (1 mmol) in oleic acid (2 ml) and 1-octadecene (2 ml), heated to 85°C, was added to the reaction, after which the reaction temperature was raised to 330°C and stirred for 15 min under argon. Next, isopropanol (130 ml) was added to the cooled solution and the mixture was centrifuged at 6000 rpm for 30 min. The resultant nanoparticles were washed with absolute ethanol (4 times), dried, dissolved in chloroform (10 ml), precipitated with isopropanol (50 ml) and centrifuged at 4000 rpm for 10 min. The last procedure was repeated 2 times. The residue was dried at room temperature.

6.2.2 Imaging

Transmission electron microscopy

The UCNPs were dissolved in hexane, drop-casted on Formav©-coated TEM grids and dried in a desiccator at room temperature. The grids were imaged with a Philips CM10 TEM and analysed using ImageJ free-ware to obtain the UCNP size distributions. For single-UCNP imaging, the hexane solutions were diluted and drop-casted on Formav©-coated TEM nickel finder grids for easy navigation. The thinly coated finder grids can be imaged using TEM and optical epi-luminescence systems. In order to find single nanoparticles, low-magnification TEM imaging was carried out gradually zooming into areas of interest to track the UCNP location precisely.

Laser-illuminated inverted epi-luminescence microscope

A wide-field inverted epi-luminescence microscope (Olympus IX70) equipped with a water-immersion objective (40×, NA 1.15, Olympus) was modified to allow external laser illumination at the sample plane (fibre-coupled diode laser at wavelength 978 nm, LD980-01CW CXCH-Photonics). In order to achieve uniform illumination of the size-controllable field-of-view at the sample plane, a modified Köhler illumination scheme was designed and built in-house, as shown in Fig. 6.1, with detailed description and ray diagram provided in Fig. S6.1 (Supplementary Information, SI). In brief, an image of the field diaphragm placed in the excitation beam path was formed at the sample plane (conjugate planes FD and

SP, Fig. 6.1), while the excitation beam was homogenized and collimated (owing to the conjugate planes LS and BFP, Fig. 6.1). In order to reduce laser speckle induced sample illumination non-uniformity, the laser-coupling fibre was mechanically dithered at a frequency > 5 KHz. A zero-aperture adjustable iris diaphragm served as the field diaphragm allowing tailoring of the field-of-view at the sample plane, to a diameter as small as 20 µm that contained only several UCNPs. The sample image was captured by an electron-multiplying CCD (EMCCD) camera (Andor iXon DU-885) mounted to the microscope detection port. An acousto-optic tuneable filter (AOTF) (LSi-300 Hyperspectral Imaging System, Gooch and Housego) was integrated into the detection path of the epi-luminescence microscope for hyperspectral imaging. The employed spectral range was 500 - 700 nm with 3-nm increments and a bandwidth of 3.7 nm. The spectral filter module (filter cube) contained a high-pass absorbance filter (cut-off 850 nm, Thorlabs) placed in the excitation beam path to remove the 978-nm laser side lobs. A dichroic beam-splitter (cut-off, 511 nm, Semrock) reflected the excitation light toward the sample, while passing the emitted light to the detection path. Two additional short-pass filters (cut-off, 842 nm, Semrock and cut-off, 700 nm, Thorlabs) in the detection channel suppressed the excitation light leakage (see Fig. S6.2, SI). At the sample plane, the TEM finder grid with deposited UCNPs was placed on a microscope glass slide and covered with a standard cover slip.

6.2.3 Emission spectra (ensemble)

The UCNP powder was placed in a custom-designed sample holder that consisted of a thin glass plate (thickness, 0.45 mm) with a 1.5-mm diameter circular hole in the centre sandwiched between two glass cover-slips. The excitation fibre was butted against the UCNP powder glass facing the hole filled with the UCNP powder. The emission spectrum was measured in transmission using a calibrated fibre-coupled diffraction-grating based spectrometer (Ocean Optics) in conjunction with a short-pass emission filter (cut-off, 842 nm).

6.2.4 Conversion efficiency

Absolute conversion efficiency of ensemble UCNPs

The UCNP powder was placed in the custom-designed sample holder (see section 6.2.3) at one of the exit ports of a 4-inch integrating sphere (Labsphere), as described by Page et al. [15]. At the backside of the sample holder, a tilted aluminium-coated glass slide was placed to reflect the light back into the integrating sphere avoiding a double-pass through the sample. A multimode optical illumination fibre (fibre core 400 µm, NA 0.22) was butted against the sample holder at the centre of the hole. This assured precise control and reproducibility of the excitation spot size at the UCNP sample to calculate I_{ex}. Luminescence emitted by the UCNP sample was spatially integrated in the sphere by means of multiple reflections from the walls, and eventually detected using a photodiode (PD) (Thorlabs, PDA-55) at the exit port positioned at 90° with respect to the illumination path. The signal from the PD was connected to a lock-in amplifier (Stanford Research Systems, model SR830) and the excitation laser (LD980-01CW CXCH-Photonics) that was pulsed (pulse generator, Stanford research systems, model DG535), with pulse width of 4 ms and frequency 125 Hz to enable reliable registration of the UCNP luminescence signals as low as 1 µW. The I_{ex} range was controlled by the laser diode current and neutral density filters. The UCNP emission and unabsorbed excitation power were measured by inserting a short-pass (cut-off, 842 nm) and long-pass (cut-off, 830 nm, Semrock) filter, respectively, in the detection channel (in front of the PD).

The performance of the interference filters and the detector channel collection efficiency was increased by positioning a high-power lens in the detection channel. The spectral response of the integrating sphere and PD was calibrated for a broad spectral range (470 – 1050 nm). By definition, η_{uc} was calculated as P_{em}/P_{abs} [W/W]. P_{em} was determined by measuring the luminescence signal corrected for the absolute spectral response of the system and the UCNP spectral emission (see SI, Fig. S6.3a). P_{abs} was determined by measuring the excitation powers unabsorbed by a reference sample (TiO_2), P_{ref}, and the UCNP powder, P_{UCNP}, so that $P_{abs} = P_{ref} - P_{UCNP}$. P_{abs} mainly resulted from the linear absorption of Yb^{3+}-ions. For robust estimation of P_{abs} the measurements were repeated for several excitation intensities and a linear fit was performed to calculate the absorbed fraction of the excitation light ($r^2 > 0.99$).

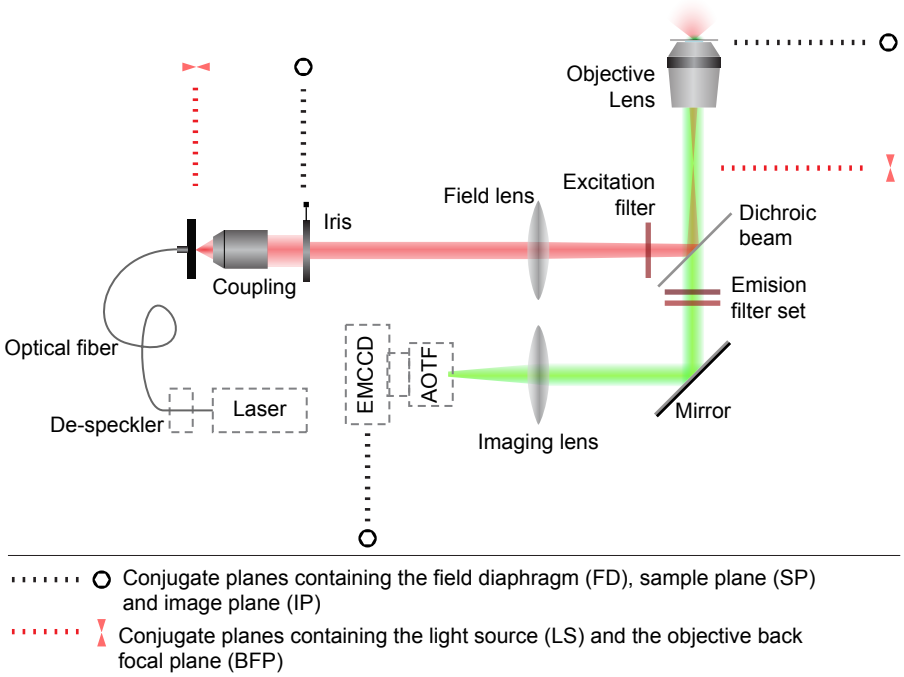

Figure 6.1 | Diagram of the custom-modified epi-luminescence imaging system employed for single-UCNP and spectral imaging. *A wide-field inverted epi-luminescence microscope was modified to allow external fibre-coupled laser illumination. The optical fibre was dithered to average out speckles. The excitation light was configured to uniformly illuminate the field-of-view at the sample plane via a modified Köhler illumination scheme. The sample plane was imaged using an EMCCD camera, optionally mounted with an AOTF for hyperspectral imaging. An adjustable iris diaphragm allowed reduction of the field-of-view to restrict imaging to several single UCNP particles and small clusters.*

Absolute conversion efficiency of single-UCNP

UCNPs sparsely deposited on the TEM finder grid were imaged using the epi-luminescence microscope set-up, as described earlier. The emitted power was determined by reading out the pixel values of the EMCCD image using the camera settings, sensitivity specifications and by calibrating the throughput of the microscope optics from sample plane to image plane. Two aspects of the EMCCD related to the epi-luminescence imaging are important to note: 1. The sensor quantum efficiency, $QE_{CCD}(\lambda)$ [number e^-/ number photons] is wavelength-dependent, so that integration over the relevant wavelength range (400 - 800 nm) was necessary. 2. The camera electron-multiplication gain (EM gain) allowed straightforward multiplication of the pixel read-out values by the EM gain (in virtue of RealGame™ EMCCD feature). The UCNP signal read out by the sensor, S_{UCNP}, depended on the UCNP sample emitted intensity and the spectral calibration coefficient of the imaging system according to:

$$S_{UCNP} = N_{YB}\sigma_{abs}^{Yb} I_{ex}\eta_{uc}\zeta_{total} + N_{el} \quad (6.1)$$

where S_{UCNP} and N_{el} [counts/s] are the signal per UCNP node and electronic noise level, respectively; N_{YB} the number of Ytterbium (Yb^{3+}) ions per node that absorbed the excitation light; σ_{abs} [cm^2] the Yb^{3+} absorption cross-section (neglecting the absorption due to ~10-fold fewer Er^{3+} ions and $\sigma_{Er,abs'} << \sigma_{Yb,abs'}$) [15, 26]; and ζ_{total} [counts/W/s] the calibration coefficient integrated over the UCNP emission spectrum (see Fig. S6.4). S_{UCNP} was the sum of the pixels that sampled an image of the UCNP node. The noise contained shot, dark and read noise components. Optical background was negligible (see Fig. S6.2). The number of Yb^{3+} per UCNP node was estimated using the $NaYF_4$ crystal lattice constants (a = 5.991 Å, c = 3.526 Å) [27], TEM-derived dimensions and numbers, and Na to Yb molar ratio [28]. ζ_{total} was calculated as:

$$\zeta_{total} = \int_{\lambda=400}^{\lambda=800} QE_{CCD}(\lambda)\xi_{optics}(\lambda)N_{ph}(\lambda)\, d\lambda \frac{EMgain}{S_{CCD}} \quad (6.2)$$

where ξ_{optics} is the throughput of the imaging optics, N_{ph} the photon emission rate per wavelength per UCNP emission power [number of photons/W/s], *EMgain* is a linear factor and S_{CCD} is the camera sensitivity [number of e^-/count]. The values of QE_{CCD} and S_{CCD} were provided by the EMCCD manufacturer. The absolute throughput ξ_{optics} was spectrally calibrated by imaging an optical fibre in the sample plane and comparing the known fibre output power to the power detected by the camera at the relevant wavelength range (see Fig. S6.5). In Fig. S6.4 the spectral output and the detector response are shown for UCNP imaging using a water- and blood-immersion objective.

6.3 RESULTS AND DISCUSSION

Realization of the prime goal of ultrahigh-sensitivity imaging of UCNPs in biological tissue is critically dependent on the attainable UCNP contrast, which is defined as the ratio of the detected luminescence signal (*S*) originating from the UCNPs to the background signal (B) stemming from the residual biological tissue autofluorescence and noise. The signal estimation calls for a thorough characterization of the excitation and emission properties of UCNPs, as well as quantification of the excitation/detection paths of the optical microscopy system adapted for ultrahigh-sensitivity imaging, where the adverse effects of the biological tissue on UCNP excitation and detection are taken into account. These effects are greatly exacerbated in the case of most fluorescent organic dyes, as will be shown in our cross-comparison study of optical imaging of a UCNP and fluorescein dye molecule in biological tissue. For the background signal estimation, the tissue optical properties (including scattering, absorption and autofluorescence) need to be considered. We commence by reporting on the measurement of absolute conversion efficiency and emission spectra of UCNPs, using an integrating sphere set-up and calibrated optical microscopy system (Section 6.3.1; ensemble and single-particle measurements). In Section 6.3.2 the quantitative assessment of single-UCNP imaging contrast in biological environment is addressed experimentally and theoretically, using haemolysed blood and skin models, respectively. We combine the physical characteristics of UCNPs, the optical properties of biological tissue and the abilities of advanced imaging systems to provide clear guidance towards intelligent development and a realistic application scope of upconversion nanomaterials.

6.3.1 Quantitative Characterization

Conversion Efficiency. Comments on Conventions

Conversion efficiency, η_{uc}, of UCNPs represents the most important parameter that governs the luminescence properties. It is defined as the emitted power/absorbed power (P_{em}/P_{abs}) expressed in W/W [15]. We note that this important parameter is used inconsistently across the literature. Traditionally, the term "quantum yield" (QY) is defined as the ratio of the number of photons emitted to the number of photons absorbed by the sample [29]. However, during the upconversion process one photon is emitted as a result of the absorption of two or more photons, thus the QY would not exceed 50% following this definition. In order to re-normalize this value, the QY of 2- or 3- photon absorption processes is scaled by a factor 2 or 3 respectively [16, 30], although not consistently in literature [13, 31]. In addition, the emission is the result of a complex, unknown combination of 2- and 3-photon excitation pathways [32, 33], rendering this approach speculative. For these reasons, the term "conversion efficiency" is believed to more adequately represent the net output of the complex upconversion process.

It is worthwhile to comment here on two other issues with UCNP conventions. Firstly, the dependency of η_{uc} on I_{ex} complicates the comparison of η_{uc} or QY measurements taken at different values of I_{ex}. For example, the reported QY values of 0.18% [22] and 0.47% [13] measured at $I_{ex} \sim 10^3$ W/cm^2 and 17.5 W/cm^2 respectively, are hardly comparable due to an unknown functional dependence of η_{uc} on I_{ex}. Secondly, quantitative reports on the absolute η_{uc} or related values are still scarce in literature [15, 31] often replaced by the limited-accuracy comparisons of UCNP emission with that of bulk phosphors or organic dyes [6, 23]. In order to address this lacuna, we present the results of the measurements of absolute η_{uc} of UCNPs synthesized in-house for a large range of excitation intensities up to I_{sat}.

Photophysical Properties of As-Synthesized Upconversion Nanoparticles

We carried out characterization of the key photophysical properties of as-synthesized UCNPs in powder form. The β-$NaYF_4$ nanocrystals were synthesized following the thermal decomposition method, and co-doped with Yb^{3+} and Er^{3+} ions (β-$NaYF_4$:Yb,Er) at the most efficient molar ratio of 20% Yb^{3+} and 2% Er^{3+} [5, 28, 32]. The measurement of η_{uc} versus excitation intensity at the excitation wavelength (λ_{ex}) of 978 nm, was performed using a custom-modified integrating sphere set up. The integrating sphere ensured absolute measurement of the absorption and emission characteristics of UCNP powder independent of scattering by the sample. Size, morphology and η_{uc} results are summarized in Fig. 6.2 and full scale TEM images of variable magnification are provided in SI, Fig. S6.6. The synthesis yielded quasi-spherical UCNPs of diameters measured to be 68 ± 16 nm. The η_{uc} was measured to reach nearly 2% at $I_{ex} \equiv I_{sat} \cong 150$ W/cm^2, a high value in comparison with that of the comparably sized β-$NaYF_4$:Yb,Er sample reported by Boyer et al. [31], (QY ≈ 0.3% at comparable I_{ex}, recalculated using the emission spectrum and photon energies to $\eta_{uc} \approx 0.5\%$), although the sample environment (organic solvent hexane known to quench η_{uc}) might account for this difference. As was expected for the supralinear upconversion process, the η_{uc} dropped dramatically at low I_{ex}, as can be seen in Fig. 6.2a. The UCNP emission spectra versus I_{ex} were acquired using a calibrated spectrometer and presented in Supplementary Information Fig. S6.3. These spectra exhibited two characteristic emission bands grouped in green (510-560 nm) and red (640-680 nm) emission multiplets, as shown in Fig. S6.3a. The red and green emission bands were attributed to the Er atomic transitions induced by the sequential two and three photon energy absorption processes

[10]. The complex multi-step excitation process of the UCNPs is nonlinear, as manifested by the supralinear dependence of the emitted luminescence power, P_{em} on I_{ex}: $P_{em} \sim I_{ex}^{n}$, where the power index n varies versus I_{ex} reaching $n = 1$ at $I_{ex} = I_{sat}$. At low I_{ex}, n would ideally take discrete values of 2 or 3, reflecting the 2 or 3- step excitation process. However, the measured n takes the values of 1.5 and 1.9 for the green and red emission bands respectively (Fig. S6.3c), reflecting more complex processes of the linear decay, exited state absorption, energy transfer upconversion, cross-relaxation and quenching, and their interrelations in the different upconversion pathways [16, 28, 33-35]. It is beyond the scope of this paper to elucidate these mechanisms. However, it is important to account for the spectral and η_{uc} dependence on the excitation intensity in a quantitative analysis of the UCNP imaging *in vivo*.

The complexity of the upconversion excitation/emission process is confounded by ensemble averaging, where the surface-related (non-radiative relaxation) processes can be concealed by inter-particle interactions. Characterization of an isolated individual UCNP is instrumental to remove this uncertainty.

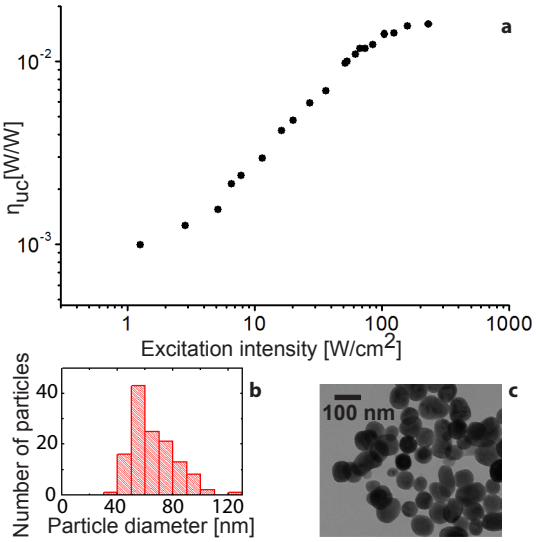

Figure 6.2 | Photophysical properties of UCNPs. ***(a)*** *Plot of the absolute conversion efficiency (η_{uc}) [W/W] of the reported upconversion nanoparticle sample versus the excitation intensity at λ_{ex} = 978 nm measured using a calibrated integrating sphere set-up. η_{uc} is the ratio of the emitted power integrated over the entire emission spectral range (500-700 nm) to the absorbed power.* ***(b)*** *Size histogram obtained by analyzing the transmission electron microscopy (TEM) images of $NaYF_4$:Yb,Er UCNPs (330 particles) synthesized in-house. A typical TEM-image is shown in* ***(c)****.*

Single Particle Spectral Imaging

A single upconversion nanoparticle represents an excellent measurement entity for the quantitative measurements of the emission spectra and η_{uc}, because it is unaffected by inter-particle interactions and has known physical dimensions. In order to establish this single-UCNP experimental model, we modified a wide-field epi-luminescence inverted microscope to allow uniform illumination of the sample plane with an external excitation laser (978 nm). A high-sensitivity EMCCD camera was incorporated in the microscope detection path. This imaging modality has several advantages, including short acquisition times (~1 s) at moderate $I_{ex} \cong 250$ W/cm^2 uniformly distributed across the field-of-view, as compared to scanning configurations that operate at $I_{ex} \cong 10^6$ W/cm^2 and with a pixel dwell time of 10 ms [22, 24], resulting in acquisition times of 40 minutes for a 512×512 pixel image. In order to demonstrate single-UCNP imaging, the as-synthesized powder was dispersed in organic solvent and sparsely deposited on a TEM grid pre-coated with a Formav© monolayer film. This enabled TEM and epi-luminescence imaging of the same sample areas to be matched and individual nanoparticles singled out. An example of this correlative imaging method is shown in Fig. 6.3, where the two top panels display the matched constellation of UCNPs acquired by TEM and epi-luminescence microscopy, respectively, and a single particle (designated "single") is observable.

The utility of this single-UCNP imaging system is demonstrated by comparison of the luminescence spectra of single, clustered, and powder UCNP samples that were obtained using an acousto-optic tuneable filter (AOTF) integrated into the detection path of the epi-luminescence microscope. This enabled acquisition of spectral data from every pixel, converting our microscope into a hyperspectral imaging modality. The spectral responses of "single" and "cluster 2" were examined individually and locally by reading out spectral data from the corresponding pixels (Figures 6.4a and 6.3b). The emission spectra of the other small clusters were similar (data not shown). The ensemble-averaged spectrum of the UCNP powder was also obtained using the hyperspectral imaging mode (Fig. 6.4c) by processing a full-field image of the powder sample. In order to cross-validate the spectral measurements, the UCNP powder emission spectra were additionally acquired with a diffraction-grating based calibrated spectrometer (dashed curves, Fig. 6.4). The dependency of the spectral features on excitation intensity is discussed in Section 6.3.1 and Fig. S6.3. The spectral emissions of the individual, clustered and ensemble UCNPs showed a high resemblance at equivalent I_{ex}. Hence, the UCNP spectral luminescence profile appeared to be primarily dependent on I_{ex} and independent on the inter-particle interactions in air, thus clarifying the speculations made by Wu et al. [24] This enabled accurate characterization of η_{uc} of single UCNPs, as described next.

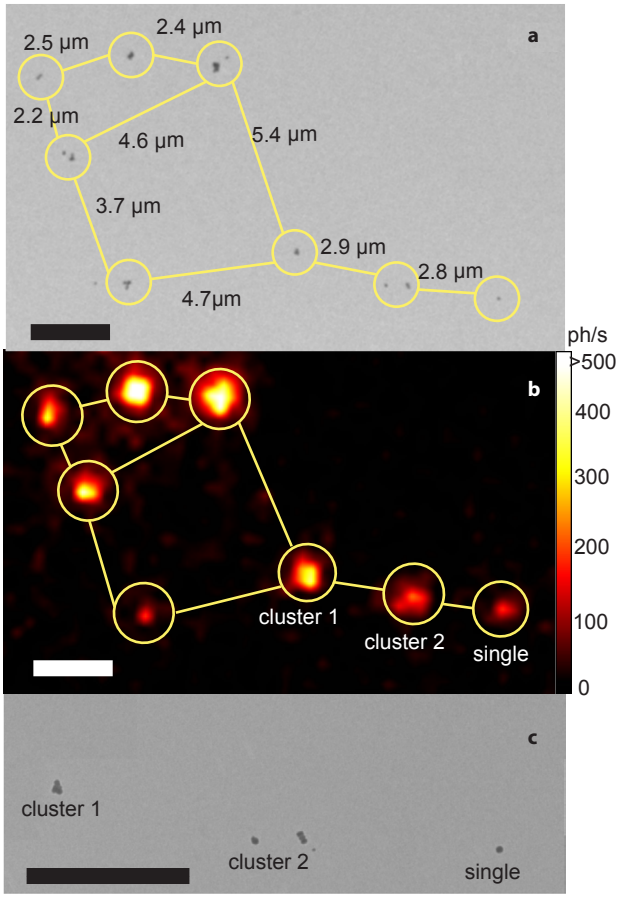

Figure 6.3. Single-UCNP correlative imaging using (a) *TEM and* ***(b)*** *epi-luminescence microscopy images corresponding to the same areas of the sample TEM grid. The distances between the individual (encircled) nanoparticles/clusters, given in (a), were precisely matched to these in (b) to identify the same UCNP constellation.* ***(c)*** *Close-up TEM image of the same area as in (a), where UCNP sites designated 'cluster 1', 'cluster 2', and 'single' correspond to the three sites in (b). The individual UCNPs within 'cluster 1' and 'cluster 2' were optically unresolvable. "Single" designates a single UCNP particle clearly observable, as a diffraction-limited spot in (b). The excitation wavelength, intensity and exposure time were 978 nm, ~250 W/cm² and 0.7 s, respectively. The pixel values were converted to photons/second (ph/s) and color-coded using the look-up color bar in (b).*

Measurement of Single Particle Conversion Efficiency

Each node of the UCNP constellation shown in Fig. 6.3 can be characterized in terms of the number/dimension of nanoparticles per node and corresponding photon detection rate (encoded in false colour in Fig. 6.3b) that can be converted to photon emission rate (P_{em}) per excitation intensity, which suffices to determine the UCNP conversion efficiency, $\eta_{uc} = P_{em}/P_{abs}$. The photon emission rate integrated over the node was obtained by reading out and converting the corresponding image pixels, since the epi-luminescence detection channel throughput, and the EMCCD spectral quantum efficiency versus the camera settings

were calibrated (see Eqs. 6.1 and 6.2, Figs. S6.5 and S6.4, SI). The conversion efficiency was found by:

$$\eta_{uc} = \frac{P_{em}}{P_{abs}} = \frac{(S_{UCNP} - N_{el})/\zeta_{total}}{N_{YB}\sigma_{abs}I_{ex}} \qquad (6.3)$$

where the quantities are explained in section 6.2.4.

The calculated η_{uc} of the single UCNP and two clusters (as identified in Fig. 6.3) obtained by processing the image data is presented in Table 6.1 along with the relevant parameters. The excitation intensity corresponded to the saturation regime where the ensemble-averaged η_{uc} measured with the integrating sphere was nearly 2%. The calculated values of η_{uc} of the individual UCNP constellation nodes ranged between 1.2 and 2.0%, due to the variability in the host crystal composition and impurities. The independent η_{uc} measurements for the isolated and ensemble UCNPs exhibited excellent agreement, which indicates that the η_{uc} dependence on I_{ex} and emission peak ratios hold for single UCNPs. Although the absolute η_{uc} of the single-UCNP was marginally lower than that of the ensemble-averaged UCNPs, it was adequately high to enable ultrasensitive imaging at the single-particle sensitivity level in biological scenarios, as addressed in the following section.

6

6.3.2 Biomedical Imaging Applications

Single Particle Imaging Through Haemolysed Blood

The feasibility of single-UCNP imaging in a biological environment was explored by obscuring the UCNP sample with a highly absorbing biological fluid, such as blood, with results presented in Fig. 6.5. Whole blood (1 ml) was haemolysed by replacing plasma with distilled water. After centrifuging the supernatant

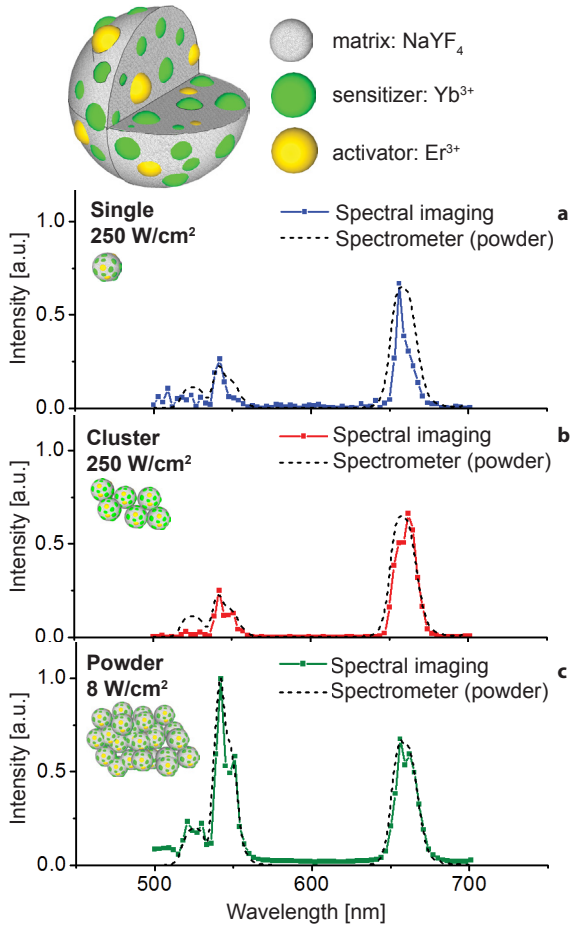

Figure 6.4 | Spectral imaging of UCNPs. *Emission spectra of UCNPs in* ***(a)*** *single,* ***(b)*** *small cluster (designated 'cluster 2' in Figure 6.3) and* ***(c)*** *powder form (data points joined by solid lines) captured using hyperspectral epi-luminescence microscopy, overlaid with the ensemble-averaged spectra of UCNP powder captured by a calibrated spectrometer (dashed lines). The corresponding exposure times and EMCCD camera electron-multiplication (EM) gains were (a) 4 sec and 255; (b) 1.5 sec and 44; and (c) 0.014 sec and 9. Since the samples (a) and (b) contained considerably less emitters than the powder sample (c), the excitation intensities at λ_{ex} = 978 nm were varied, respectively, from 250 W/cm² to 8 W/cm² to accommodate for the large disparity in the emission signals that would otherwise exceed the dynamic range of the EMCCD. The decreased Iex resulted in an increased green-to-red emission ratio in (c) due to the varied upconversion energy redistribution between the green and red multiplets. Top panel, schematic diagram of $NaYF_4$:Yb,Er UCNP.*

was used to replace the water between the objective and sample plane to create a "blood-immersion objective", as shown in Fig. 6.5a. Heamolisation of the full blood was necessary as the wide-field configuration was not efficient in suppressing out-of-focus signals, which precludes the use of whole blood due to scattering. The blood layer thickness was ~250 um, and the resulting absorption coefficient of the haemoglobin solution is shown in Fig. 6.5b. The UCNP emission spectrum is superimposed on the blood absorption spectrum to emphasize the high absorption in the green emission band and low absorption in the red emission band. This differential absorption by the blood altered the sample coloration, as shown in Fig. 6.5c. A low-magnification image of the UCNP sample illuminated by the 978-nm laser was captured by a digital colour camera through the eyepiece port of the epi-luminescence microscope, which reproduced the colour perception by the human eye. The UCNP sample appeared green (Fig. 6.5c, top panel), when using the standard water-immersion configuration of the objective lens, despite the prominent red band in the UCNP emission spectrum. This is explained by the higher spectral sensitivity of the eye to green colour compared to that of red colour (~20 times [36]). In case of the haemolysed "blood-immersion objective", however (Fig. 6.5c, bottom panel), the green emitted light was largely absorbed by the haemoglobin,

Table 6.1. *Determination of the absolute η_{uc} using data from the calibrated epi-luminescence imaging of single and small clusters of UCNPs.*

	P_{em} [W] (25%)	N_{Yb} (10%)	$\sigma_{Yb,abs}$ [cm^2] [b)]	I_{ex} [W/cm^2] (10%)	η_{uc} [%]
Cluster 1 [a)]	2.6×10^{-14}	5.5×10^{5}	1.0×10^{-20}	2.6×10^{2}	2.0±0.5
Cluster 2 [a)]	2.2×10^{-14}	6.1×10^{5}	1.0×10^{-20}	2.6×10^{2}	1.3±0.3
Single [a)]	4.9×10^{-15}	2.3×10^{5}	1.0×10^{-20}	2.6×10^{2}	1.2±0.3

[a)]As identified in Figures 6.3b and 6.3c. [b)]The Yb^{3+} absorption cross-section, as in Refs [14, 34]. Unites are given in square brackets, percentage standard deviations are given in brackets, except for η_{uc}.

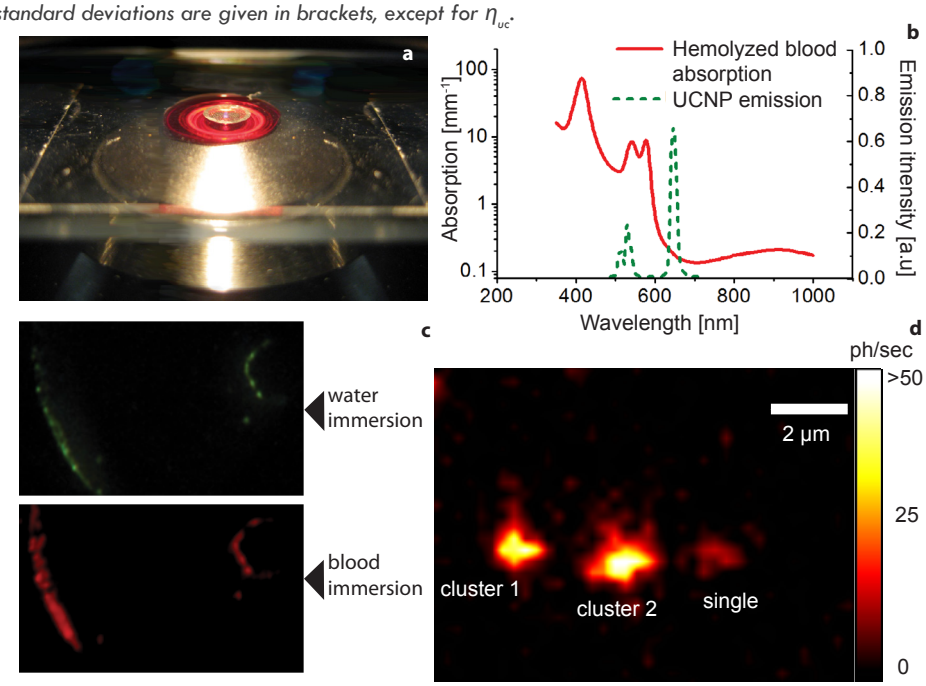

Figure 6.5 | Epi-luminescence imaging of a single UCNP using the "blood-immersion" objective. (a) *A photograph of the haemolysed blood layer between the objective and cover slip.* ***(b)*** *Absorption spectrum of the haemolysed blood (red solid curve) and UCNP emission spectrum (green dashed curve).* ***(c)*** *Low-magnification images of the UCNP sample recorded through the eyepiece port using the water- (top) and blood- (bottom) immersion objective. The dried UCNP colloid rims appeared green (top) and red (bottom) due to the green light absorption by blood.* ***(d)*** *Epi-luminescence microscopy image of the UCNP constellation identified in Fig. 6.2c, imaged using the blood-immersion objective. The single UCNP is clearly observable, although blurred. The EMCCD camera settings and excitation parameters were equivalent to these of Fig. 6.2. The pixel values were converted to photons/second (ph/s) and colour-coded using the look-up bar in (d).*

and the UCNP sample appeared red to the human eye and in the digital colour image. Hence, the UCNP red emission and NIR excitation passed with small losses through the biological fluid, suggesting the feasibility of imaging single UCNPs. This ultrahigh-sensitivity imaging through an obscuring biological fluid was demonstrated, as shown in Fig. 6.5d, where the previously identified single UCNP was clearly observable. Single-UCNP imaging has been reported using scanning [22, 24] and wide-field [23, 25] set ups, for exposed particles. To the best of our knowledge, this is the first demonstration of single-UCNP imaging in a biological medium, using a moderate excitation intensity (250 W/cm^2) approaching the laser safety limits in a biological sample of realistic thickness. The demonstrated imaging through a 250-μm thick haemolysed blood layer is, for example, favourably comparable with the diameters of blood vessels in the microcirculation, which can be found in proximity to organ surfaces [37].

These experimental results show the feasibility of optical imaging of single upconversion nanoparticles in biological fluids, in accordance with the assessment of the photophysical properties. These results constitute an experimental platform from which the detection limits of single-particle imaging in live skin is assessed theoretically, as presented in the next section.

Modelling of Single Particle Imaging in Skin

In comparison with conventional *in vivo* fluorescence-assisted imaging, UCNP-assisted imaging offers the advantage of reduced excitation/emission light losses and complete suppression of the optical background due to tissue autofluorescence [11]. The implication of this improvement is demonstrated by a simplified quantitative comparison of imaging in skin using fluorescein (FL) and UCNPs at the single-particle level. The choice for this representative visible organic fluorescent dye is dictated by its broad acceptance in the field of experimental skin research *in vivo* in animals and humans [38], as well as in diagnostic procedures in skin [39] and other organs [40]. In our model, a single emitter (FL and UCNP) is considered buried in skin at a depth z. The calculated single-emitter signal (S) and background (B) values were compared in terms of their contrast (S/B) at different z. A confocal imaging setting is assumed in this model to reduce the adverse obscuring effect of out-of-focus signals that burden fluorescence-assisted imaging. The confocal imaging is known to improve the signal discrimination, such that the signals primarily originated from the focal volume at z.

The excitation power, $P_{0,ex}$ at the focal volume is attenuated according to Beer-Lambert's law: $P_{ex}(z)=P_{0,ex}e^{-\mu_{tr}z}$, where μ_{tr} is the transport attenuation coefficient [mm^{-1}] defined as a sum of the absorption, μ_a and reduced scattering coefficient, $\mu_s'=(1-g)\mu_s$, μ_s being the scattering coefficient, and g – the anisotropy factor. The attenuation is due to photon removal from the focusing path by absorption (μ_a) and isotropic scattering (μ_s'). μ_{tr} was computed in the visible and NIR spectral range using the reported values of μ_a and μ_s' for fresh Caucasian adult skin samples *in vitro*; while assuming a layered skin structure of epidermis, dermis and subcutaneous fat of corresponding thicknesses 80 μm, 400 μm and 520 μm, respectively [41]. The emitted power was calculated using $P_{em,UCNP} = N_{Yb}\sigma_{Yb,abs}I_{ex}\eta_{uc}$ and $P_{em,FL}=1\cdot\sigma_{FL,abs}I_{ex}\Phi_{FL}$ where I_{ex} – the excitation intensity at depth z calculated by dividing $P_{ex}(z)$ by the excitation area. Φ_{FL} – the FL conversion efficiency was taken as 0.9 and $\sigma_{FL,abs}= 3.5\times10^{-16}$ cm^2 at λ_{ex} = 500 nm, [7] and 1 signifies a single FL emitter. $N_{Yb}\approx1.1\cdot10^5$ was calculated using the $NaYF_4$ crystal lattice constants [27] and Na to Yb molar ratio [28] for a 70 nm particle, η_{uc} was obtained using the data plotted in Fig. 6.2a at the corresponding

values of I_{ex}, and with $\sigma_{Yb,abs}$ as listed in Table 6.1. The maximum permissible exposure (MPE) for skin is tabulated as 200 W/cm^2 at 500 nm (FL) and 700 W/cm^2 at 978 nm (UCNP) for a 1-ms exposure time [42]. The UCNP emission is attenuated along the return path through skin, which was accounted for using μ_{tr} of skin at the UCNP and FL emission wavelengths. The isotropic emission collection efficiency was determined by the objective lens acceptance angle (NA = 0.8). The collected emission photo conversion by the EMCCD camera (moderate EM gain, ×100) was computed using the calibration protocol presented earlier (Eqs. 6.1 - 6.3).

The single-UCNP imaging contrast was estimated using the background level set by the electronic noise, with dark and read noise components specified by the camera manufacturer (Andor), and shot noise calculated as $\sqrt{N_e}$- (N_e- the photoelectron number before the EM-gain). The total noise was multiplied by the EM-characteristic multiplicative noise factor $\sqrt{2}$ [43]. The FL imaging background (B), however, had an additional autofluorescence-induced component. At λ_{ex} = 500 nm, the autofluorescence was mainly due to the abundant endogenous fluorophore in skin, flavin adenine dinucleotide (FAD), whose concentration in skin was reported to be ~1 µg/mg [44]. ~750 FAD molecules were situated in a 1-µm^3 focal volume and contributed to B. In addition, the out-of-focus FAD-induced background signal was estimated following the model of confocal imaging by Magnor et al. for scattering media, assuming a homogeneous distribution of FAD in skin [45]. $\sigma_{FAD,abs}$ and Φ_{FAD} were taken as 6.0×10^{-18} cm^2 at 500 nm and 0.033, respectively [46]. The FAD-induced electronic signal at the EMCCD camera was computed analogously to that of FL and UCNP, corrected for the spectral filtering of the FAD emission profile extending beyond the FL emission spectrum.

Fig. 6.6 shows a plot of the calculated imaging contrast of a single emitter versus depth in skin tissue. The absolute luminescence signal S from FL is high at the shallow imaging depths (< 300 µm) in comparison with that of UCNP, and so is B due to the autofluorescence by FAD (Fig. 6.6, inset). The resultant contrast provided by FL is therefore very modest, with the highest value of 2 at the skin surface. Taking into consideration the non-uniformity of autofluorescence across the skin sample, single-FL imaging is at best problematic, if at all possible, particularly given the serious issue of the short lifetime of FL before undergoing photobleaching. In regard to S/B of the single UCNP, the relatively low S was compensated by the extremely small B, almost invariable versus depth. The contrast is therefore, much higher, moderately decreasing from a value of 10 down to 3 over the 200-µm depth, which allows reliable detection of a single UCNP particle. Based on our model S/B reached a value of 1 at 400-µm depth in skin, however, due to a number of the simplifying assumptions made this is likely to be the best-case-scenario.

Feasibility of Single Particle Imaging in Biotissue

The remarkable progress in the synthesis of upconversion nanomaterials and demonstration of their unique luminescence properties have led to new possibilities in optical biomedical imaging using UCNPs. However, an uptake of this luminescent nanotechnology into cellular imaging is tempered by the existence of competitive luminescent nanomaterials that exhibit a high contrast against the dim autofluorescence background of cells (e.g. europium complexes, quantum dots). Nam et al. reported the imaging of UCNP-labelled live HeLa cells for 6 h using 980 nm excitation at I_{ex} = 3 kW/cm^2, which allowed high-sensitivity intracellular imaging [47]. At these excitation intensities, *in vitro* single UCNP imaging in cells is feasible, as our results suggest. The scope of *in vivo* UCNP applications for optical deep tissue imaging of small

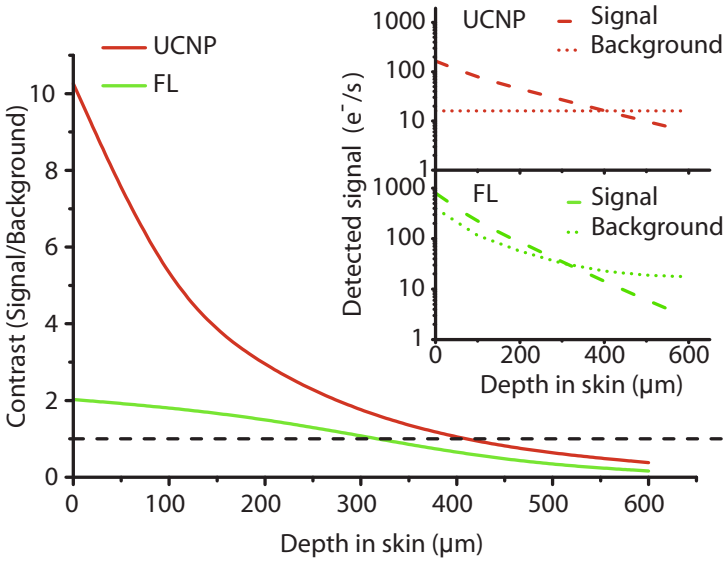

Figure 6.6 | Theoretical estimation of single-emitter detection sensitivity in skin. *A plot of the optical (confocal) detection contrasts of a single upconversion nanoparticle (UCNP, brown) and organic fluorescence dye (fluorescein, FC, green) versus their depth in skin, as modelled theoretically. The inset shows more detailed quantitative plots of the imaging signal (dashed) and background (dotted) of UCNP and FL versus depth in skin expressed in electrons per second (e^-/s). The black dotted line demarcates the contrast value of 1. See text for details.*

lesions appears to be limited by the supralinear dependence of the upconversion luminescence on the excitation intensity, which is greatly diminished at $I_{ex} << I_{sat}$ in deep (> 1 cm) tissue layers. This confines the application niche of UCNP-based molecular probes to optical luminescent imaging in biological fluids, subsurface tissue layers and thick biological tissue slices. Within these domains, the UCNP-based molecular probes have the potential to exhibit outstanding performance and provide unparalleled imaging capabilities, as was demonstrated and modelled in this paper (Fig.'s 6.5 and 6.6). Such exceptional performance is achieved due to the unique photophysical properties of UCNP that allows evading the adverse effects of high absorption and autofluorescence of biological tissue, as long as the high excitation intensity is attainable by focusing.

The theoretical analysis highlights great promise for imaging single nanoparticles embedded in biological tissue, and provides a useful guidance to luminescent nanoparticle design (not necessarily limited to UCNPs) and optical imaging modality. For example, an improved photochemical design of UCNPs, e.g. co-doping $NaYF_4$ with Ytterbium and Thulium featuring an emission peak at 800 nm should further reduce the absorption by blood (Fig. 6.5) and result in an increased imaging depth [48]. A promising recent result was the synthesis of 42-nm UCNPs with an exceptional high conversion efficiency at 800 nm (3.5%) [49], using core-shell synthesis to reduce surface quenching [50]. The maximum imaging depth (SNR > 1) for the reported UCNP sample, with mean size 42 nm and the highest reported value of η_{uc} = 3.5%, was found to be 450 μm (see SI, Fig. S6.7). There are several reports demonstrating UCNP-assisted imaging depths of 2 cm [13] and 3.2 cm [51] in live mice and fat tissue respectively for ensemble particles. In this paper, the absolute detection sensitivity of single UCNP imaging *in vivo* is addressed, which can readily be extended to an ensemble of UCNPs.

At the same time, our presented optical imaging model was oversimplified. The confocal scanning modality is impractically slow due the long (sub-milliseconds) UCNP luminescence lifetime, which requires to the

dwell time to be set to ~500 µs per pixel to avoid smearing of the emission light onto adjacent pixels due to the UCNP after-glow [21]. On the other hand, the wide-field epi-luminescence modality suffers from the overshadowing of small single-UCNP signals by large UCNP clusters, so that on some occasions, we had to reduce the field diaphragm of the epi-luminescence microscope to collapse the field-of-view to a diameter of ~20 µm. The wide-field configuration was not efficient in suppressing out-of-focus signals, which precluded the use of whole blood due to scattering, and required blood haemolysis. This could possibly be prevented by optical clearing mechanisms that result in a reduced attenuation coefficient of whole blood [52]. Lastly, the NIR irradiation dose (250 W/cm^2 CW) still exceeded the maximum permissible exposure for skin. Although excitation at 980 nm at a ten-fold greater intensity has been shown to be tolerable to live cells for 6 h *in vitro* [47], continuous *in vivo* imaging at the excitation intensity as low as 0.5 W/cm^2 caused significant skin damage to mice [53], due to high water absorption in the live animal. Shifting the excitation wavelength from 980 to 915 nm was suggested to reduce water absorption. A pulsed laser excitation regime delivering high energy per pulse at a low repetition rate represents another possible solution to maintain acceptable imaging contrast within the laser safety limits. Therefore, advanced optical imaging – possibly, a hybrid of the wide-field epi-luminescence and confocal modalities – is required to harness the UCNP specificity and uniqueness.

There are a number of interesting prospects to employ UCNPs as molecular probes in tissues sites accessible to ballistic photons including skin, the superficial microcirculation and sub-surface lesions for luminescence-guided surgery. Recent reports demonstrate that imaging of low amounts of UCNP-labelled stem cells is feasible: as few as ~10 labelled cells were subcutaneously detected in nude mice and *in vivo* detection limits for UCNP-based imaging were an order of magnitude lower in comparison with QDs [54, 55]. UCNPs conjugated to a cancer-targeting peptide, for example somatostatin [56, 57] can facilitate the diagnosis of skin cancer [58]; detection of circulating tumour cells in subcutaneous blood vessels, or the sensitive guidance to tumour sites by receptor-targeted optical imaging [59]. Recently, we have successfully conjugated UCNPs with scFv4D5 mini-antibodies raised against the human epidermal growth factor receptor (HER2/neu) overexpressed in e.g. breast adenocarcinoma cells and demonstrated high-specific binding *in vitro* (Chapter 7). Delivery of conjugated UCNPs to tumours *in vivo* poses new challenges. The primary delivery mechanism of intravenous injected nanoparticles is thought to be the enhanced permeability and retention effect, caused by leaky blood vessel walls in tumour tissue. Subsequent nanoparticle diffusion into the tumour core occurs via intercellular or intracellular routes, where the latter mediated by endocytosis is more likely than the former due to the large nanoparticle size compared to the intercellular space [47, 60]. As a last example, UCNP-facilitated ion sensing by combining the optical properties of ion sensing chromophores/fluorophores with UCNP optical characteristics seems to be promising [61].

6.4. CONCLUSION

The adoption of upconversion nanomaterials in optical biomedical imaging demands specification of application areas where the UCNP merits are critical while the limitations are tolerable, and where the cutting-edge sensitivity required for UCNP-assisted imaging performance is achievable. We examined this ultrahigh-sensitivity optical imaging scenario by performing imaging and characterization of a single UCNP in a biological environment represented by haemolysed blood. In particular, the key UCNP param-

eters of absolute conversion efficiency and spectral emission were measured in individual and ensemble particles and found comparable. These experimental results were utilized in an idealized theoretical model, which was believed to aid identification of application areas of extreme sensitivity in challenging *in vivo* environments, including biological liquids, subsurface layers and thick tissue slices. Specifically, our theoretical skin imaging model suggests that UCNP imaging had superior contrast over that of conventional fluorescent dyes. The background-free imaging of single upconversion nanoparticles at depths up to 400 μm in skin was found feasible. Therefore, the application scope of carefully tailored UCNP-based molecular probes is significant, including luminescence-guided surgery and ultrahigh-sensitivity bioassays in unprocessed biological fluids.

6.5 Acknowledgements

This work was performed in part at the OptoFab node of the Australian National Fabrication Facility, a company established under the National Collaborative Research Infrastructure Strategy to provide nano and microfabrication facilities for Australia's researchers.

6.6 References

1. S. A. Hilderbrand and R. Weissleder, "Near-Infrared Fluorescence: Application to *In vivo* Molecular Imaging," Curr. Opin. Chem. Biol. 14, 9-71 (2009).
2. M. S. Patterson, B. Chance, and B. C. Wilson, "Time Resolved Reflectance and Transmittance for the Non-Invasive Measurement of Tissue Optical Properties," Appl. Opt. 28, 2331-2336 (1989).
3. A. Corlu, R. Choe, T. Durduran, M. A. Rosen, M. Schweiger, S. R. Arridge, M. D. Schnall, and A. G. Yodh, "Three-Dimensional *In vivo* Fluorescence Diffuse Optical Tomography of Breast Cancer in Humans," Opt. Express 15, 6696-6716 (2007).
4. B. E. Schaafsma, J. S. D. Mieog, M. Hutteman, J. R. van der Vorst, P. J. K. Kuppen, C. W. G. M. Löwik, J. V. Frangioni, C. J. H. van de Velde, and A. L. Vahrmeijer, "The clinical use of indocyanine green as a near-infrared fluorescent contrast agent for image-guided oncologic surgery," J. Surg. Oncol. 104, 323-332 (2011).
5. S. Heer, K. Kömpe, H. U. Güdel, and M. Haase, "Highly Efficient Multicolour Upconversion Emission in Transparent Colloids of Lanthanide-Doped NaYF4 Nanocrystals," Adv. Mater. 16, 2102-2105 (2004).
6. G. Yi, H. Lu, S. Zhao, Y. Ge, W. Yang, D. Chen, and L. H. Guo, "Synthesis, Characterization, and Biological Application of Size-controlled Nanocrystalline NaYF4: Yb, Er Infrared-to-Visible Up-Conversion Phosphors," Nano Lett. 4, 2191-2196 (2004).
7. U. Resch-Genger, M. Grabolle, S. Cavaliere-Jaricot, R. Nitschke, and T. Nann, "Quantum Dots Versus Organic Dyes as Fluorescent Labels," Nat. Methods 5, 763-775 (2008).
8. M. C. Mancini, B. A. Kairdolf, A. M. Smith, and S. Nie, "Oxidative Quenching and Degradation of Polymer-encapsulated Quantum Dots: New Insights Into the Long-Term Fate and Toxicity of Nanocrystals *In vivo*," J. Am. Chem. Soc. 130, 10836-10837 (2008).
9. K. Liu, X. Liu, Q. Zeng, Y. Zhang, L. Tu, T. Liu, X. Kong, Y. Wang, F. Cao, S. A. G. Lambrechts, M. C. G. Aalders, and H. Zhang, "Covalently Assembled NIR Nanoplatform for Simultaneous Fluorescence Imaging and Photodynamic Therapy of Cancer Cells," ACS nano 6, 4054-4062 (2012).
10. F. Auzel, "Upconversion and Anti-Stokes Processes With f and d Ions in Solids," Chem. Rev. 104, 139-174 (2004).
11. C. T. Xu, N. Svensson, J. Axelsson, P. Svenmarker, G. Somesfalean, G. Chen, H. Liang, H. Liu, Z. Zhang, and S. Andersson-Engels, "Autofluorescence Insensitive Imaging Using Upconverting Nanocrystals in Scattering Media," Appl. Phys. Lett. 93, 171103 (2008).
12. F. Leblond, S. C. Davis, P. A. Valdés, and B. W. Pogue, "Pre-Clinical Whole-Body Fluorescence Imaging: Review of Instruments, Methods and Applications," J. Photochem. Photobiol., B. 98, 77-94 (2010).
13. Q. Liu, Y. Sun, T. Yang, W. Feng, C. Li, and F. Li, "Sub-10 nm Hexagonal Lanthanide-Doped NaLuF4 Upconversion Nanocrystals for Sensitive Bioimaging *in vivo*," J. Am. Chem. Soc. 133, 17122-17125 (2011).
14. C. Vinegoni, D. Razansky, S. A. Hilderbrand, F. Shao, V. Ntziachristos, and R. Weissleder, "Transillumination Fluorescence Imaging in Mice Using Biocompatible Upconverting Nanoparticles," Opt. Lett. 34, 2566-2568 (2009).
15. R. H. Page, K. I. Schaffers, P. A. Waide, J. B. Tassano, S. A. Payne, W. F. Krupke, and W. K. Bischel, "Upconversion-pumped Luminescence Efficiency of Rare-Earth-doped Hosts Sensitized With Trivalent Ytterbium," JOSA B 15, 996-1008 (1998).
16. J. Suyver, A. Aebischer, D. Biner, P. Gerner, J. Grimm, S. Heer, K. Krämer, C. Reinhard, and H. Güdel, "Novel Materials Doped With Trivalent Lanthanides and Transition Metal Ions Showing Near-Infrared to Visible Photon Upconversion," Opt. Mater. 27, 1111-1130 (2005).
17. M. P. Hehlen, G. Frei, and H. U. Güdel, "Dynamics of infrared-to-visible upconversion in Cs3Lu2Br9: 1% Er3+," Phys. Rev. B. 50, 16264 (1994).
18. W. R. Zipfel, R. M. Williams, R. Christie, A. Y. Nikitin, B. T. Hyman, and W. W. Webb, "Live Tissue Intrinsic Emission Microscopy Using Multiphoton-excited Native Fluorescence and Second Harmonic Generation," Proc. Natl. Acad. Sci. U. S. A. 100, 7075 (2003).
19. F. Wang, J. Wang, and X. Liu, "Direct Evidence of a Surface Quenching Effect on Size-Dependent Luminescence of Upconversion Nanoparticles," Angew. Chem. Int. Ed. 122, 7618-7622 (2010).
20. T. Kelf, V. Sreenivasan, J. Sun, E. Kim, E. Goldys, and A. Zvyagin, "Non-Specific Cellular Uptake of Surface-Functionalized Quantum Dots," Nanotechnology 21, 285105 (2010).
21. J. Pichaandi, J. C. Boyer, K. R. Delaney, and F. C. J. M. van Veggel, "Two-Photon Upconversion Laser (Scanning

and Wide Field) Microscopy using Ln3+-Doped NaYF4 Upconverting Nanocrystals A Critical Evaluation of their Performance and Potential in Bio-imaging," J. Phys. Chem. C., 19054–19064 (2011).
22. A. D. Ostrowski, E. M. Chan, D. J. Gargas, E. M. Katz, G. Han, P. J. Schuck, D. J. Milliron, and B. E. Cohen, "Controlled Synthesis and Single Particle Imaging of Bright, Sub-10 nm Lanthanide-Doped Upconverting Nanocrystals," ACS nano 6, 2686-2692 (2012).
23. G. Mialon, S. Türkcan, G. Dantelle, D. P. Collins, M. Hadjipanayi, R. A. Taylor, T. Gacoin, A. Alexandrou, and J. P. Boilot, "High Up-Conversion Efficiency of YVO4: Yb, Er Nanoparticles in Water Down to the Single-Particle Level," J. Phys. Chem. C., 22449–22454 (2010).
24. S. Wu, G. Han, D. J. Milliron, S. Aloni, V. Altoe, D. V. Talapin, B. E. Cohen, and P. J. Schuck, "Non-blinking and Photostable Upconverted Luminescence from Single Lanthanide-Doped Nanocrystals," Proc. Natl. Acad. Sci. U. S. A. 106, 10917-10921 (2009).
25. Y. I. Park, J. H. Kim, K. T. Lee, K. S. Jeon, H. B. Na, J. H. Yu, H. M. Kim, N. Lee, S. H. Choi, and S. I. Baik, "Nonblinking and nonbleaching upconverting nanoparticles as an optical imaging nanoprobe and T1 magnetic resonance imaging contrast agent," Adv. Mater. 21, 4467-4471 (2009).
26. G. Lakshminarayana, J. Ruan, and J. Qiu, "NIR Luminescence From Er-Yb, Bi-Yb and Bi-Nd Codoped Germanate Glasses for Optical Amplification," J. Alloys Compd. 476, 878, (2009).
27. H. X. Mai, Y. W. Zhang, R. Si, Z. G. Yan, L. Sun, L. P. You, and C. H. Yan, "High-Quality sodium rare-earth fluoride nanocrystals: controlled synthesis and optical properties," J. Am. Chem. Soc. 128, 6426-6436 (2006).
28. K. W. Krämer, D. Biner, G. Frei, H. U. Güdel, M. P. Hehlen, and S. R. Luethi, "Hexagonal Sodium Yttrium Fluoride Based Green and Blue Emitting Upconversion Phosphors," Chem. Mater. 16, 1244-1251 (2004).
29. W. Melhuish and M. Zander, "Nomenclature, Symbols, Units and Their Usage in Spectrochemical Analysis-VII. Molecular Absorption Spectroscopy, Ultraviolet and Visible (UV/VIS) " Pure Appl. Chem 56, 231-245 (1984).
30. V. Tikhomirov, G. Adamo, A. Nikolaenko, V. Rodriguez, P. Gredin, M. Mortier, N. Zheludev, and V. Moshchalkov, "Cathodo-and photoluminescence in Yb3+ Er3+ Co-Doped PbF2 Nanoparticles," Opt. Express 18, 8836-8846 (2010).
31. J. C. Boyer and F. C. J. M. Van Veggel, "Absolute Quantum Yield Measurements of Colloidal NaYF4: Er3+, Yb3+ Upconverting Nanoparticles," Nanoscale 2, 1417-1419 (2010).
32. H. X. Mai, Y. W. Zhang, L. D. Sun, and C. H. Yan, "Highly Efficient Multicolor Up-conversion Emissions and Their Mechanisms of Monodisperse NaYF4: Yb, Er Core and Core/Shell-Structured Nanocrystals," J. Phys. Chem. C. 111, 13721-13729 (2007).
33. Y. Wang, L. Tu, J. Zhao, Y. Sun, X. Kong, and H. Zhang, "Upconversion Luminescence of β-NaYF4: Yb3+, Er3+@ β-NaYF4 Core/Shell Nanoparticles: Excitation Power Density and Surface Dependence," J. Phys. Chem. C. 113, 7164-7169 (2009).
34. M. Pollnau, D. Gamelin, S. Lüthi, H. Güdel, and M. Hehlen, "Power Dependence of Upconversion Luminescence in Lanthanide and Transition-Metal-Ion Systems," Phys. Rev. B. 61, 3337 (2000).
35. J. Shan, M. Uddi, R. Wei, N. Yao, and Y. Ju, "The Hidden Effects of Particle Shape and Criteria for Evaluating the Upconversion Luminescence of the Lanthanide Doped Nanophosphors," J. Phys. Chem. C. 114, 2452-2461 (2010).
36. Commission Internationale de l'Eclairage Proceedings, Commission Internationale de l'Eclairage Proceedings (Cambridge University Press, Cambridge, United Kingdom, 1931).
37. E. C. Boerma, K. Mathura, P. van der Voort, P. Spronk, and C. Ince, "Quantifying Bedside-derived Imaging of Microcirculatory Abnormalities in Septic Patients: A Prospective Validation Study," Crit. Care 9, R601-R606 (2005).
38. A. Bollinger, J. Frey, K. Jäger, J. Furrer, J. Seglias, and W. Siegenthaler, "Patterns of Diffusion Through Skin Capillaries in Patients With Long-Term Diabetes," N. Engl. J. Med. 307, 1305-1310 (1982).
39. S. Dietterle, J. Lademann, H. J. Röwert- Huber, E. Stockfleth, C. Antoniou, W. Sterry, and S. Astner, "In-Vivo Diagnosis and Non-Inasive Monitoring of Imiquimod 5% Cream for Non-Melanoma Skin Cancer Using Confocal Laser Scanning Microscopy," Laser Phys. Lett. 5, 752-759 (2008).
40. P. L. Hsiung, J. Hardy, S. Friedland, R. Soetikno, C. B. Du, A. P. Wu, P. Sahbaie, J. M. Crawford, A. W. Lowe, and C. H. Contag, "Detection of colonic dysplasia *in vivo* using a targeted heptapeptide and confocal microendoscopy," Nat. Med. 14, 454-458 (2008).
41. E. Salomatina, B. Jiang, J. Novak, and A. N. Yaroslavsky, "Optical properties of normal and cancerous human skin in the visible and near-infrared spectral range," J. Biomed. Opt. 11, 064026 (2006).
42. Standards Australia Limited/Standards New Zealand, AS/NZS 60825 (SAI Global Limited, Sydney, AU and Wellington, NZ, 2012), 1-48.
43. M. S. Robbins and B. J. Hadwen, "The noise performance of electron multiplying charge-coupled devices," IEEE Transactions on Electronic Devices 50, 1227-1232 (2003).
44. O. A. Bessey, O. H. Lowry, and R. H. Love, "The Fluorimetric Measurement of the Nucleotides or Riboflavind and Their Concentration in Tissues," J. Biol. Chem. 180, 755-769 (1949).
45. M. Magnor, P. Dorn, and W. Rudolph, "Simulation of confocal microscopy through scattering media with and without time gating," JOSA B 18, 1695-1700 (2001).
46. S. D. M. Islam, T. Susdorf, A. Penzkofer, and P. Hegemann, "Fluorescence quenching of flavin adenine dinucleotide in aqueous solution by pH dependent isomerisation and photo-induced electron transfer," Chem. Phys. 295, 137-149 (2003).
47. S. H. Nam, Y. M. Bae, Y. I. Park, J. H. Kim, H. M. Kim, J. S. Choi, K. T. Lee, T. Hyeon, and Y. D. Suh, "Long-Term Real-Time Tracking of Lanthanide Ion Doped Upconverting Nanoparticles in Living Cells," Angew. Chem. 123, 6217-6221 (2011).
48. N. Dong, M. Pedroni, F. Piccinelli, G. Conti, A. Sbarbati, J. R. Hernandez, L. M. Maestro, M. C. Iglesias de la Cruz, F. Sanz-Rodriguez, and A. Juarranz, "NIR-to-NIR Two-Photon Excited CaF2: Tm3+, Yb3+ Nanoparticles: Multifunctional Nanoprobes for Highly Penetrating Fluorescence Bio-Imaging," ACS nano 5, 8665-8671 (2011).
49. C. T. Xu, P. Svenmarker, H. Liu, X. Wu, M. E. Messing, L. R. Wallenberg, and S. Andersson-Engels, "High-Resolution Fluorescence Diffuse Optical Tomography Developed with Nonlinear Upconverting Nanoparticles," ACS nano (2012).
50. G. S. Yi and G. M. Chow, "Water-soluble NaYF4: Yb, Er (Tm)/NaYF4/polymer core/shell/shell nanoparticles with significant enhancement of upconversion fluorescence," Chem. Mater. 19, 341-343 (2007).
51. G. Chen, J. Shen, T. Y. Ohulchanskyy, N. J. Patel, A. Kutikov, Z. Li, J. Song, R. K. Pandey, H. Ågren, and P. N. Prasad, "(*a*-NaYbF4: Tm3+)/CaF2 Core/Shell Nanoparticles with Efficient Near-Infrared to Near-Infrared Upconversion for High-Contrast Deep Tissue Bioimaging," ACS nano, 8280–8287 (2012).
52. V. V. Tuchin, X. Xu, and R. K. Wang, "Dynamic optical coherence tomography in studies of optical clearing, sedimenta-

tion, and aggregation of immersed blood," Appl. Opt. 41, 258-271 (2002).
53. Q. Zhan, J. Qian, H. Liang, G. Somesfalean, D. Wang, S. He, Z. Zhang, and S. Andersson-Engels, "Using 915-nm Laser Excited Tm3+/Er3+/Ho3+ Doped NaYbF4 Upconversion Nanoparticles for *In vitro* and Deeper *In vivo* Bioimaging Without Overheating Irradiation," ACS nano, 3744–3757 (2011).
54. C. Wang, L. Cheng, H. Xu, and Z. Liu, "Towards whole-body imaging at the single cell level using ultra-sensitive stem cell labeling with oligo-arginine modified upconversion nanoparticles," Biomaterials (2012).
55. L. Cheng, K. Yang, S. Zhang, M. Shao, S. Lee, and Z. Liu, "Highly-sensitive multiplexed *in vivo* imaging using PEGylated upconversion nanoparticles," Nano Res 3, 722-732 (2010).
56. V. K. A. Sreenivasan, E. J. Kim, A. K. Goodchild, M. Connor, and A. V. Zvyagin, "Targeting somatostatin receptors using in situ-bioconjugated fluorescent nanoparticles," Nanomedicine (2012).
57. V. K. A. Sreenivasan, O. A. Stremovskiy, T. A. Kelf, M. Heblinski, A. K. Goodchild, M. Connor, S. M. Deyev, and A. V. Zvyagin, "Pharmacological Characterization of a Recombinant, Fluorescent Somatostatin Receptor Agonist," Bioconjugate Chem. 22, 1768-1775 (2011).
58. B. D. Nguyen and A. E. McCullough, "Imaging of Merkel Cell Carcinoma1," Radiographics 22, 367-376 (2002).
59. A. Becker, C. Hessenius, K. Licha, B. Ebert, U. Sukowski, W. Semmler, B. Wiedenmann, and C. Grözinger, "Receptor-targeted Optical Imaging of Tumors With Near-Infrared Fluorescent Ligands," Nat. Biotechnol. 19, 327-331 (2001).
60. H. R. Kim, K. Andrieux, S. Gil, M. Taverna, H. Chacun, D. Desmaële, F. Taran, D. Georgin, and P. Couvreur, "Translocation of poly (ethylene glycol-co-hexadecyl) cyanoacrylate nanoparticles into rat brain endothelial cells: role of apolipoproteins in receptor-mediated endocytosis," Biomacromolecules 8, 793-799 (2007).
61. L. Xie, Y. Qin, and H.-Y. Chen, "Direct Fluorescent Measurement of Blood Potassium with Polymeric Optical Sensors Based on Upconverting Nanomaterials," Anal. Chem. (2013).

SUPPLEMENTARY INFORMATION

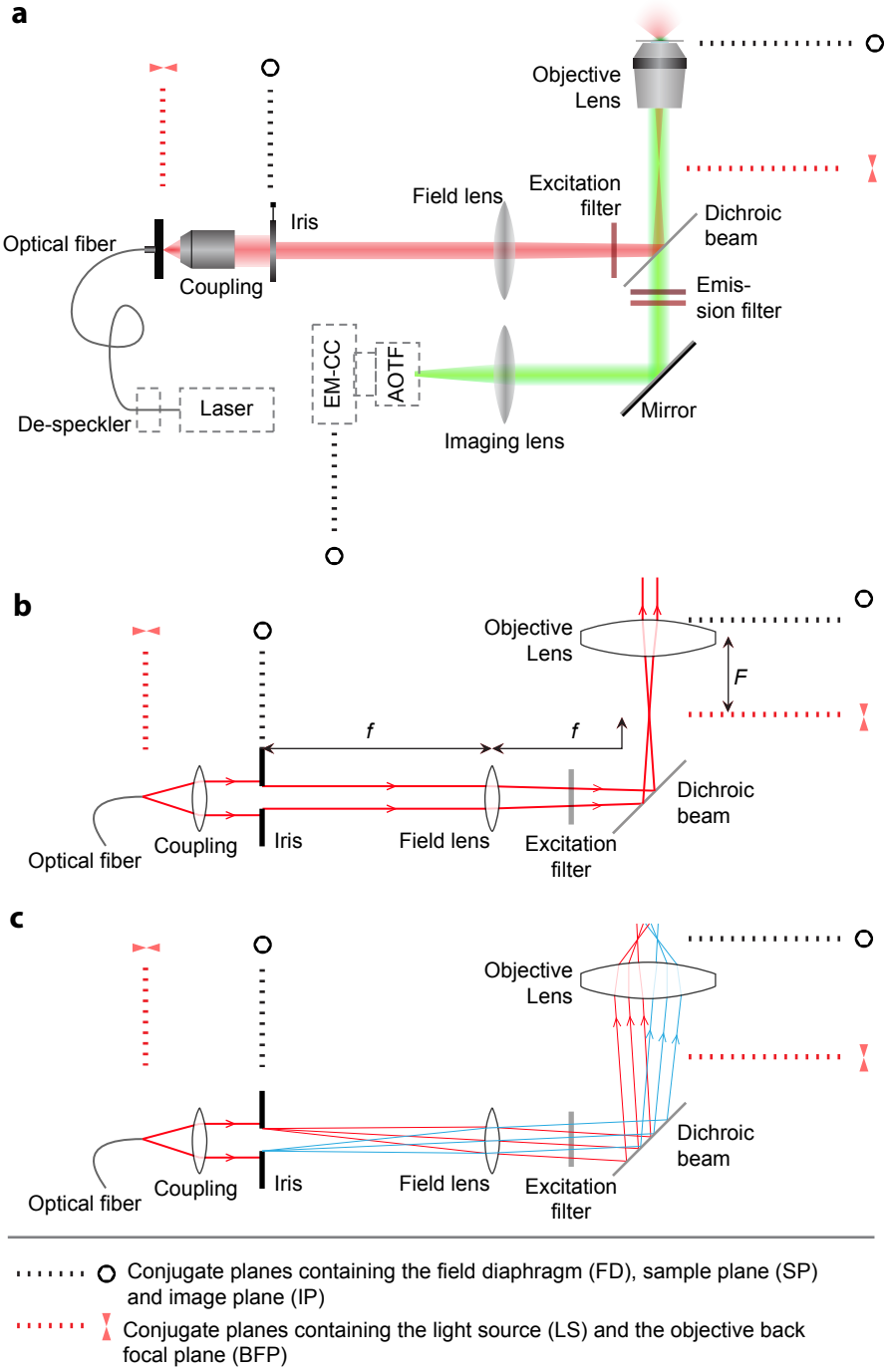

Figure S6.1 | Set-up and Köhler ray diagram. *The set-up consisted of a wide-field inverted epi-fluorescence microscope (Olympus IX70) equipped with a water-immersion objective (40x, NA 1.15, Olympus). The laser illumination was guided to the sample plane using a modified illumination path replacing the default Mercury/Xenon arc lamp housing. To achieve homogeneous illumination at the sample plane and to have precise control over the field-of-view, a modified Köhler illumination scheme was built as is shown in panel* **(a)**. *The two Köhler illumination ray diagrams illustrating the homogeneous illumination light ray path and the image forming light ray path are shown in panels* **(b)** *and* **(c)** *respectively. The conjugate planes are explained in the legend. In* **(b)** *a collimated laser beam filled the adjustable iris located at the back focal plane of the field lens, which was, in turn, one focal distance away from the back focal plane of the objective resulting in even and collimated sample illumination. In* **(c)** *the image forming function of the Köhler scheme is depicted: the image of the iris located at the focal point of the field lens resulted in the formation of its image at the objective focal plane. The magnification of the iris image was the ratio between the focal lengths of the objective and the field lens (~28x in this setup). A zero-aperture iris was used to control the illumination area. The other components of the set-up are an electron-multiplying CCD (EMCCD) camera (Andor iXon DU-885) and an acousto-optic tunable filter (AOTF) (LSi-300 Hyperspectral Imaging System, Gooch and Housego) mounted to the left side port of the microscope; excitation and emission filters; a 978 nm laser (LD980-01CW, CXCH-Photonics) and an mechanical dither to average out speckles. These components are further discussed in the main paper.*

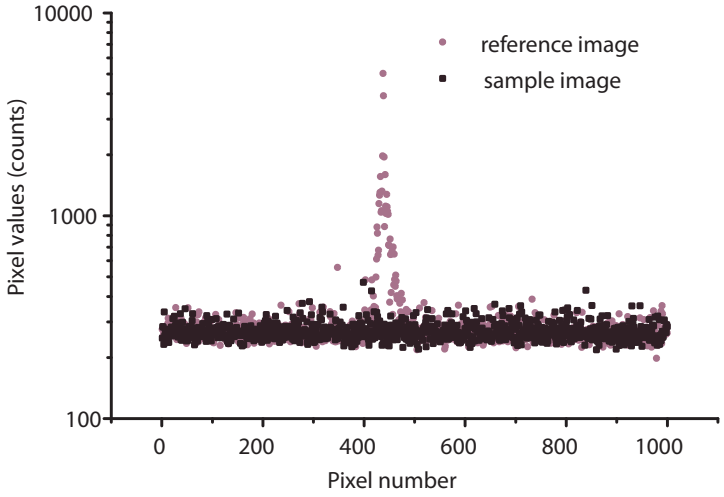

Figure S6.2 | Reference and sample image intensity. *To estimate the amount of excitation light bleeding through the emission filter set and reaching the EMCCD camera, we imaged a TEM-grid with reference material (TiO_2) and obtained the pixel values on a line through the field-of-view on the image. The graph shows the pixel values in counts for each pixel along the line (pixel number) for the reference TEM-grid and for a TEM-grid with UCNP sample deposited. As can be seen no elevation of pixel value was observed for the reference image at the field-of-view, whereas the sample image pixel values increased at the focus spot due to detection of upconverted light. The detected signal was nonzero due to addition of a pixel base level and (low) values for read and dark noise. We can conclude that virtually no excitation light reached the detector.*

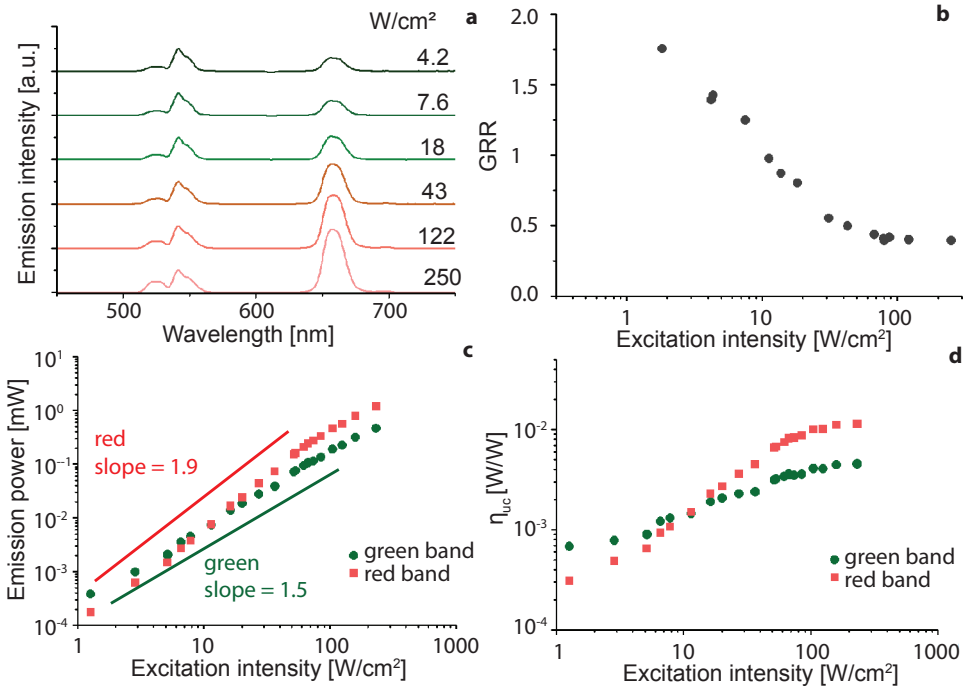

Figure S6.3 | Excitation intensity dependence of the green and red emission bands. (a) *Ensemble emission spectra of UCNP powder were measured in transmission using a customized glass sample holder and calibrated spectrometer for several excitation intensities at excitation wavelength 978 nm (see section 6.2.3). The spectra were normalized at the 540 nm peak and are presented with an offset for clarity.* ***(b)*** *Integrating the spectra of (a) over the green and red emission band resulted in a green-to-red-ratio (GRR) dependence on excitation intensity. In* ***(c)****, the emitted power dependence on excitation intensity in the green and red emission band is plotted on a double-logarithmic scale that showed a linear slope until emission saturation is reached around 150 W/cm². The slope is 1.9 for red emission and 1.5 for green emission, confirming a nonlinear emission process that involves at least 2 photons. Panel* ***(d)*** *shows the conversion efficiency (η_{uc}) dependence of the green and the red emission bands on excitation intensity.*

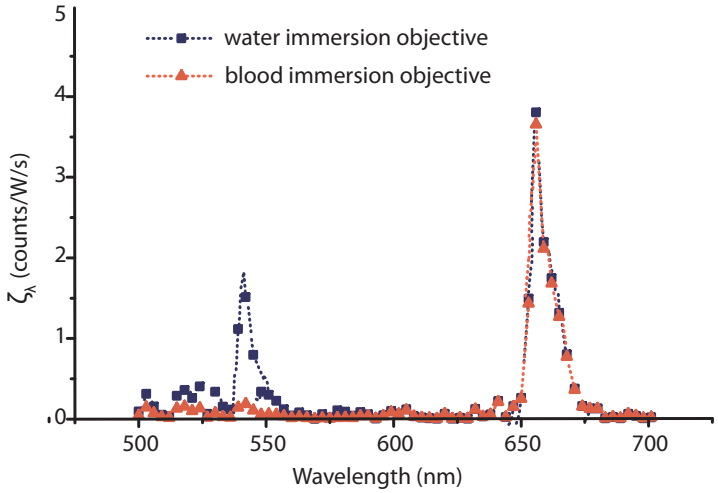

Figure S6.4 | Calibrated detector response for single UCNP immersed in water or blood. *Using the emission spectrum of the single UCNP (Fig. 6.4a) and Eq. 6.2 the spectral calibration coefficient for each wavelength can be calculated using EMgain = 1, S_{ccd} = 0.89 [e^-/count], N_{ph} the number of photons per second per UCNP emission power of 1 W per wavelength [photons/W/s] and QE_{CCD} the detector quantum efficiency [e-/photon] per wavelength. Data points are connected by a dotted line as guide to the eye. In case of the haemolysed blood-immersion objective the signal is reduced due to absorption by haemoglobin. Integrating over all wavelengths (using spline interpolation) results in total counts/W/s for UCNP emission, referred to as ζ_{total}.*

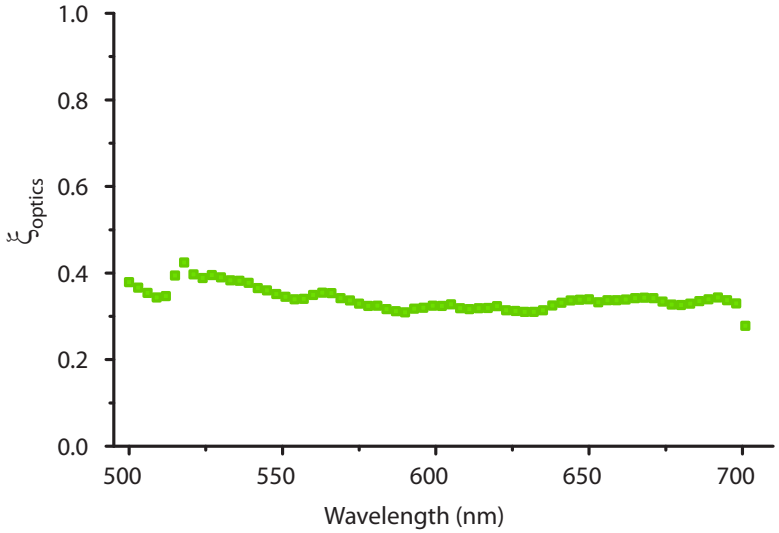

Figure S6.5 | Spectral throughput of inverted epi-luminescence microscopy system. *The absolute throughput, ξ_{optics}, defined as $Signal_{sensor\text{-}plane}$ / $Signal_{sample\text{-}plane,}$ of the microscope imaging system was obtained by imaging an optical fibre (multimode, 100 µm core, NA 0.22) placed at the sample plane of the microscope. The output power of the fibre was measured using a calibrated power meter (Thorlabs). Using the camera settings and sensitivity specifications the power detected by the sensor can be calculated from the image pixel values, and subsequently the throughput can be obtained. This was done for several wavelengths and spectrally interpolated using a white light source (Ocean Optics LS-1, tungsten halogen), as plotted in the graph. The discontinuity around 510 nm was due to the dichroic beam splitter with a cut-off wavelength at 511 nm. Assuming isotropic emission of upconverted light by the UCNPs, the actual throughput of the system needed to be corrected for the acceptance angle of the microscope objective, a factor 1/3 for NA = 1.15 (not shown).*

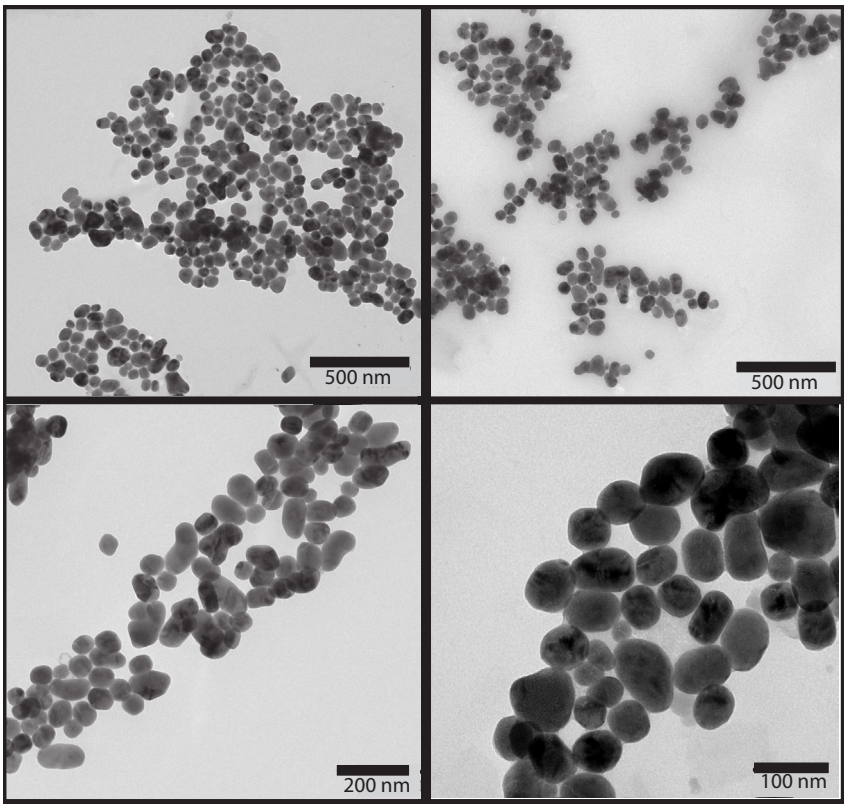

Figure S6.6 | TEM images with different magnifications of in-house synthesized UCNPs.

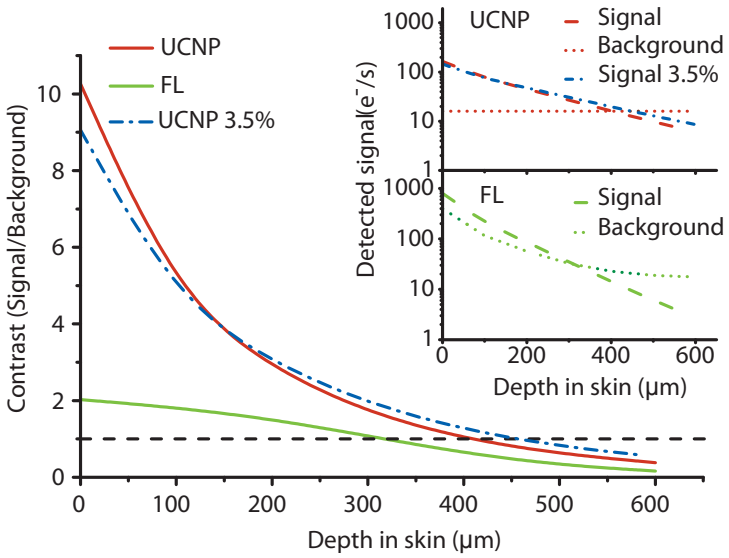

Figure S6.7. Theoretical estimation of single UCNP detection sensitivity in skin, a comparison between in-house synthesized and state-of-the-art UCNPs *(Yb,Tm-co-doped core-shell UCNPs, ref 49), possessing the highest reported conversion efficiency 3.5%. Using our model described in Section 6.3.2, we calculated the imaging signal contrast and plotted the result (blue dot-dashed line) together with the previous results for fluorescein and the 70-nm UCNP. The 42-nm 3.5%-UCNP has a reduced absorption of excitation light due to the smaller size of the particle which reduced the imaging contrast, but the higher η_{uc} and the reduced transport attenuation coefficient of skin for the luminescence signal resulted in a higher contrast at increasing depth. The maximum imaging depth in skin is 450 μm, with contrast 1.*

7

Feasibility Study of the Optical Imaging of a Breast Cancer Lesion Labeled with Upconversion Nanoparticle Biocomplexes

Adapted from:

E. A. Grebenik, **A. Nadort**, A. N. Generalova, A. V. Nechaev, V. K. Sreenivasan, E. V. Khaydukov, V. A. Semchishen, A. P. Popov, V. I. Sokolov, A. S. Akhmanov, V. P. Zubov, D. V. Klinov, V. Y. Panchenko, S. M. Deyev, and A. V. Zvyagin, "Feasibility study of the optical imaging of a breast cancer lesion labeled with upconversion nanoparticle biocomplexes," J. Biomed. Opt. 18, 076004-076004 (2013).

My contribution to this paper:
Concept, design and realization of optical imaging and UCNP characterization and optical phantom experiments, performing these experiments, data analysis, paper writing. A. Nadort has not been involved in UCNP biofunctionalization and cell labelling experiments.

Abstract Innovative luminescent nanomaterials, termed upconversion nanoparticles (UCNPs), have demonstrated considerable promise as molecular probes for high-contrast optical imaging in cells and small animals. The feasibility study of optical diagnostics in humans is reported here based on experimental and theoretical modelling of optical imaging of an UCNP-labelled breast cancer lesion. UCNPs synthesized in-house were surface-capped with an amphiphilic polymer to achieve good colloidal stability in aqueous buffer solutions. The scFv4D5 mini-antibodies were grafted onto the UCNPs via a high-affinity molecular linker barstar:barnase (Bs:Bn) to allow their specific binding to the human epidermal growth factor receptor HER2/neu, which is overexpressed in human breast adenocarcinoma cells SK-BR-3. UCNP-Bs:Bn-scFv4D5 biocomplexes exhibited high-specific immobilization on the SK-BR-3 cells with the optical contrast as high as 10:1 benchmarked against a negative control cell line. Breast cancer optical diagnostics was experimentally modelled by means of epi-luminescence imaging of a monolayer of the UCNP-labelled SK-BR-3 cells buried under a breast tissue mimicking optical phantom. The experimental results were analysed theoretically and projected to in vivo detection of early-stage breast cancer. The model predicts that the UCNP-assisted cancer detection is feasible up to 4 mm in tissue depth, showing considerable potential for diagnostic and image-guided surgery applications.

7.1 INTRODUCTION

Discrimination between healthy and pathological tissue is at the heart of medical diagnostics, where optical imaging can offer non-invasive affordable solutions for accessible organs, such as the skin and hollow organs [1,2]. For example, diffuse optical tomography localizes a pathological lesion through the altered light scattering and absorption properties resulting from abnormal physiological conditions (manifested through e.g. blood oxygenation, bilirubin concentration, etc.), achievable in the centimetre-range surface depths [1]. This is a non-invasive and patient friendly technique. However, the poor spatial resolution and non-specificity represent shortfalls of this technique [3], although recent advances have been made.

Labelling pathological lesions with molecular probes overcomes these shortfalls by enhancing the molecular contrast, as has been recently demonstrated in a number of studies [4,5]. Such a molecular probe comprises two functional modules: a targeting vector and a contrast agent. The targeting vector's functionality requires high affinity and specificity for the targeted tissue site, such as cell receptors in the case of a cancerous lesion, and often employs peptide ligands or antibodies [3]. One of the accepted targets for cancer diagnostics is the human epidermal growth factor receptor 2 (HER2/neu), which is overexpressed in a number of cancers and often accompanied by high drug resistance [6]. Identification and precise localization of a cancerous lesion using minimally invasive optical means can aid diagnostic and therapeutic decisions. A recombinant scFv4D5 mini-antibody is an example of a high-efficiency HER2/neu-targeting vector that represents a single chain variable fragment of immunoglobulin (Ig) and exhibits lower cross-reactivity and immunogenicity in comparison with the corresponding full-size antibody [7].

The use of contrast agents, exploiting their fluorescent or, more generally, luminescent properties, is widespread in biomedical optical imaging. These luminescent molecular probes allow high-sensitivity and high-resolution imaging, since the absorbed excitation light is re-emitted as luminescence in a different spectral band, which can be spectrally discriminated from the excitation light. Despite a number of successful applications of these molecular probes in many areas of the life sciences, several challenges limit their application scope in e.g. *in vivo* biomedical optical imaging. First, the vast majority of luminescent molecular probes is excited by light in the ultraviolet (UV) or visible spectral ranges, while the emitted luminescence signal is detectable in the visible spectral range, where both excitation and emission light are strongly absorbed and scattered by biological tissues. Second, the exposure of live biological tissue to light in this spectral range induces intrinsic fluorescence, termed autofluorescence, due to its constituent endogenous (intrinsic) fluorophores. Both the luminescence of the exogenous (extraneously introduced) molecular probes and biotissue autofluorescence are shifted to longer wavelength (Stokes shift). Although signals generated by the luminescent molecular probe and the autofluorescence background are separable using spectral methods, the practical efficiency of these approaches is limited [8]. Several other shortfalls that impede the widespread implementation of luminescent agents include toxic effects (quantum dots) and poor thermal and photochemical stability (green fluorescent protein, red fluorescent protein, luciferase-mediated bioluminescence) [9,10]. Moreover, long-term excitation radiation of the luminescent probes in UV or visible spectral ranges can cause tissue photodamage [9].

A recent breakthrough in synthetic chemistry has resulted in an increased efficiency for luminescent

nanomaterials termed upconversion nanoparticles (UCNPs) [11]. The most popular type of UCNPs is an $NaYF_4$ nanocrystal codoped with ytterbium (Yb^{3+}) and erbium (Er^{3+}) lanthanide ions (short-hand notation, $NaYF_4$:Yb,Er) [12]. The absorbed photon energy conversion in UCNPs occurs through complex multistage processes that include conversion of two or more near infrared (NIR) excitation photons (typically, at wavelength 980 nm) to higher energy emission in the visible and NIR spectral range, as detailed previously in Chapters 5 and 6. To recall, the main advantages of the UCNPs in the context of optical biomedical imaging applications are as follows. The spectral bands of the excitation light (980 nm) and part of the emitted luminescence response, fall into the so-called biological tissue "transparency window" (650 to 1300 nm), where light penetration in tissue takes place with minimal absorption and scattering. The autofluorescence response of live biological tissue at this excitation wavelength is insignificant and very often undetectable. Furthermore, UCNP emission is spectrally shifted toward shorter wavelength (anti-Stokes shift), making spectral separation of the luminescence and autofluorescence signals easy and efficient [13]. Moreover, the exceptionally long luminescence lifetime of UCNPs (sub-milliseconds), enables the implementation of an optical time-gated scheme that is capable of completely suppressing the short-lifetime autofluorescence background and scattered excitation light [14].

The promise of UCNPs has recently been demonstrated by imaging UCNP-based biocomplexes in cell cultures and small animal models, which showed that the autofluorescence background was suppressed [15–19]. For example, Zhan et al. have demonstrated labelling a HeLa cancer cell line with noncovalent conjugates of UCNP and anti-carcinoembryonic antigen (CEA)8 antibody followed by *in vitro* cell imaging. The anti-CEA8 is commonly used to immunologically detect the CEA, a cancer biomarker expressed on the surface of HeLa cells [18]. *In vivo* optical imaging of U87MG human glioblastoma tumors in living nude mice was reported by Xiong et al., where an arginine–glycine–asparatic peptide served as the targeting vector capable of specifically bind to αvβ3 integrin receptor overexpressed in the case of tumour angiogenesis [17].

However, the feasibility of optical imaging in live human tissue assisted by UCNP-based molecular probes under the biologically safe laser excitation conditions remains largely unexplored. The evaluation of the possibility of UCNP-assisted optical imaging in the context of early-stage cancer diagnostics is the key goal of this study. To this end, we report on UCNP synthesis and characterization in-house, followed by surface polymer coating which stabilizes the particles in aqueous buffer colloids. A flexible modular design using a high-affinity molecular linker barstar:barnase (Bs:Bn) was instrumental to achieve bioconjugation of the UCNP to the targeting vector, resulting in the assembly of UCNP-scFv4D5 mini-antibody biocomplexes [6,20]. Human breast adenocarcinoma cells SK-BR-3 overexpressing HER2/ neu were target-labelled with the UCNP biocomplexes and imaged using epi-luminescence microscopy. Optical imaging of a compact cancer cell cluster (pertinent to cancer stage I) was simulated using our breast cancer cell model covered with an optical phantom that reproduced breast tissue properties. The experimental imaging data enabled the theoretical evaluation of the feasibility of UCNP-assisted optical diagnostic imaging of a cancerous site in human breast tissue.

The key advance of our work is quantitative modelling of the optical imaging of early-stage breast cancer, where all integral parts of our model, including nanoparticle specific immobilization on the can-

cer cells, optical tissue phantom and optical imaging system, are well-controlled and characterized. This allows realistic evaluation of the feasibility of the optical imaging of an UCNP-labelled cancer lesion *in vivo*, albeit not in clinical, but in laboratory settings.

7.2 MATERIALS AND METHODS

7.2.1 Synthesis of β-$NaY_{0.78}Yb_{0.2}Er_{0.02}F_4$ UCNPs

All chemicals were purchased from Sigma–Aldrich (Germany). Nanoparticles of programmable size and crystal phase were grown from a solution of sodium metal salts and oleic acid in an oxygen-free atmosphere at elevated temperatures. The mixture of Y_2O_3 (0.78 mmol), Yb_2O_3 (0.2 mmol), and Er_2O_3 (0.02 mmol) was refluxed in 70% trifluoroacetic acid (20 ml) for ca. 6 h. The resulting clear solution was cooled to room temperature and the solvent was evaporated. The obtained residue was dried under vacuum at 0.1 torr for 3 h and thoroughly ground in an agate mortar until a fine homogeneous powder was produced. This powder was mixed with sodium trifluoroacetate (2 mmol), oleic acid (6 ml), and 1-octadecene (6 ml) in a three-necked flask equipped with a thermometer and magnetic stirrer, and stirred at 100°C under vacuum for 30 min. The degassed and water-free mixture was gradually heated to 290°C at a rate of 6 °C/min and kept at this temperature for 45 min under an argon atmosphere. The temperature was then raised to 310°C for 70 min. Next, the solution was cooled, suspended in propanol-2 (130 ml), and centrifuged at 6000 rpm for 30 min (Z206A centrifuge, Hermle, Germany). The as-synthesized particles were washed with absolute ethanol four times and dried. The particles were then dissolved in chloroform (10 ml), precipitated with propanol-2 (50 ml), and centrifuged at 4000 rpm for twice 10 min. The final product was dried at room temperature [11].

7.2.2 Protein Production and Characterization

We isolated and purified the Bn-scFv4D5 fusion protein, as described by Deyev et al. [20] with slight modifications. *Escherichia coli* strain SB536 [F^-, WG1, ΔfhuA (ton Δ), ΔhhoAB (SacII), *shh*] was transformed with the pSD4D5BnHis5 plasmid with the inserted Bs-coding moiety protecting bacterial cells from Bn cytotoxic effect. The transformants were then grown in YTPS broth (1% yeast extract, 1% trypton, 150 mM NaCl, 40 mM K_2HPO_4, 10 mM KH_2PO_4, 2 mM $MgCl_2$, 0.1 g/l ampicillin, pH 7.5) at 37°C until the optical density at 560 nm wavelength (OD_{560}) reached 0.6, and supplied with isopropyl β-D-1-thiogalactopyranoside (1 mM) for 5-h *lac* promoter induction. The obtained biomass was harvested by centrifugation (Allegra 21R Centrifuge, Beckman Coulter, USA) and disintegrated on ice by sonication in a lysis buffer [5 mM tris(hydroxymethyl)aminomethane– hydrochloride (Tris–HCl), 40 mM K_2HPO_4, 500 mM NaCl, pH 8.2]. The extract was clarified by centrifugation and filtration through a membrane filter (220-nm pore size) and loaded onto a HiTrap nickel-nitrilotriacetic acid 1-ml column (GE Healthcare Worldwide). In order to remove the Bs inhibitor, the column was washed with urea solution (8 M), with subsequent refolding of the fusion protein by a linear urea concentration gradient (8–0 M). The refolded protein was then eluted by a 225-mM imidazole solution and transferred to a phosphate buffer (20 mM NaCl, 6.5 mM NaH_2PO_4, 41 mM Na_2HPO_4, pH 6.5) using a PD-10 desalting column (GE Healthcare Worldwide), and finally purified in a HiTrap SP-Sepharose Fast Flow 1-ml column (GE Healthcare Worldwide). Electrophoretic analysis of eluted fractions in polyacrylamide gel (12.5%) showed the Bn-scFv4D5 elution at 275 mM NaCl.

The Bs C40A protein was produced using *E. coli* strain HB101 [F^- Δ(*gpt-proA)62 leu B6 glnV44 ara-14 galK2 lacY1* Δ*(mcrC-mrr) rpsL20* (Str^r) *xyl-5 mtl-1recA13*], carrying pMT641 plasmid [6]. The cells were cultivated in YTPS broth until the stationary growth phase, and then centrifuged, followed by re-suspension in cold lysis buffer [0.05 M Tris–HCl, 0.1 M NaCl, 10 mM ethylenediaminetetraacetic acid (EDTA), 10 mM dithiothreitol (DTT), pH 8.0]. The obtained solution was sonicated on ice with a 30% ammonium sulfate saturation for cell disruption followed by nucleic acid precipitation with poly (ethyleneimine). Further, the cell extract was clarified by centrifugation and Bs content was precipitated by 70% ammonium sulfate saturation. The resulting precipitate was dissolved in TD buffer (0.1 M Tris–HCl, 10 mM EDTA, 10 mM DTT, pH 8.0) and fractionated according to protein size in a Sephadex G-100 SuperFine column (C16/100) equilibrated with TSDT buffer (0.02 M Tris–HCl, 0.02 M NaCl, 2 mM EDTA, 2 mM DTT, 0.05% Tween-20, pH 8.0). Finally, Bs was purified in a HiTrap Q-Sepharose Fast Flow 1-ml column (GE Healthcare Worldwide) equilibrated with TDG buffer (0.2 M Tris–HCl, 2 mM DTT, 10% glycerol, pH 8.0). Elution was performed with a NaCl concentration gradient. The Bs was identified by polyacrylamide gel (17%) electrophoresis.

Ribonucleic activity of the recombinant protein, BnscFv4D5 was determined by the acid-insoluble ribonucleic acid (RNA) precipitation assay [21]. 40-µl dilutions (from 30 to 0.015 nM) of the analysed protein in Tris–HCl buffer (0.125 M Tris–HCl, pH 8.5) were mixed with 160 µl yeast RNA aliquots (2 mg/ml) and allowed enzymatic RNA splitting at 37°C. After 15 min, the reaction was stopped by adding 6% chloric acid (200 µl) to the mixture at +2°C for 15 min. Non-reacted RNA substrate was removed by centrifugation (Eppendorf 5415D Centrifuge, Germany) and supernatants were analysed for released nucleotide concentrations, which determine the OD_{260}. To estimate the Bs:Bn affinity, different Bs dilutions were added to a solution of Bn at a constant saturation concentration followed by the same measurements. In the last case, Bs concentration was inversely proportional to the OD_{260}.

ScFv4D5-HER2/neu affinity was evaluated by using antihuman polyclonal antibodies. A 96-well flat-bottomed polystyrene plate was coated with a recombinant $p185^{HER2–EDC}$ antigen prepared in coating buffer (0.1 M Na_2CO_3, 0.1 M $NaHCO_3$, pH 9.2) at amounts of 8 and 16 ng/well. After 1 h antigen absorption, the plate was washed with phosphate-buffered saline (PBS) and unsaturated surface-binding sites were blocked with a blocking solution [5% milk (Tesco, UK) in PBS, pH 7.4]. The Bn-scFv4D5 solved in PBS with Tween-20 (0.1%) was then added at different dilutions with a starting concentration of 5 nM. After 1 h of incubation with constant shaking in a rocker shaker, the plate was washed. To detect the immobilized Bn-scFv4D5, first, polyclonal rabbit-anti-human antibody and second, peroxidase-conjugated goat-anti-rabbit IgG were used with washing between the steps. For subsequent colourimetrical measurement 1,2-diaminobenzene (Sigma–Aldrich, Germany) (0.04%) with hydrogen peroxide (0.06%) in citric buffer (7.3 g/l citric acid, 11.86 g/l $Na_2HPO_4 \cdot 2H2O$, pH 5) were added to the wells. The reaction was stopped by adding 2 M sulfuric acid (50 µl). The OD_{450} was read using a plate spectrophotometer (StatFax-2100, Awareness Technology, USA). The affinity constant (K_{aff}) was calculated, as described by Beatty et al. [22] with consideration of antibody monovalency using the following equation:

$$K_{aff} = \frac{(n-1)}{n\left[Ab'\right]_t - \left[Ab\right]_t} \qquad (7.1)$$

where $[Ab']_t$ and $[Ab]_t$ are the total antibody concentrations, in the wells at OD-50′ and OD-50 for plates coated with total antigen concentrations of $[Ag']_t$ (8 ng) and $[Ag]_t$ (16 ng), respectively, and

$$n = \frac{[Ag]_t}{[Ag']_t} \tag{7.2}$$

7.2.3 Bioconjugation of UCNPs

The as-synthesized UCNPs were coated with poly(maleic anhydride-*alt*-1-octadecene) amphiphilic polymer [PMAO (Sigma–Aldrich, Germany)], as described by Pellegrino et al. [23] with slight modifications. 1,6-Diaminohexane (Serva, Germany) was added to cross-link the PMAO chains around the particles. In order to link the biomolecules to the UCNPs, the surface carboxylic groups of the PMAO shell were activated in a cold buffered aqueous solution with an excess of 1-ethyl-3- (3-dimethylaminopropyl)carbodiimide (EDC) and N-hydroxysulfosuccinimide (sulfo-NHS) cross-linkers (Sigma–Aldrich, Germany) under sonication. The nanoparticles were then washed from unreacted cross-linkers by centrifugation at 4°C, redispersed in cold Bs solution, and allowed to bind to Bs overnight. The unbound Bs molecules were removed from the solution by three centrifugation–re-suspension cycles, and the resultant product was stored in PBS.

7.2.4 Transmission Electron Microscopy (TEM)

The UCNP and PMAO–UCNP solutions were diluted by *n*-hexane and water, respectively, then sonicated and dropcasted onto a thin bar 300-mesh copper TEM grids, coated with 0.3% pioloform. After overnight drying in a desiccator at room temperature, the grids were imaged using a Philips CM10 TEM (Philips, Eindhoven, The Netherlands). ImageJ freeware was used for UCNP size distribution analysis.

7.2.5 Fourier Transform Infrared (FTIR) Spectroscopy

Pure PMAO was thoroughly ground and then pressed with KBr to form a tablet. The UCNP modified with PMAO was dried using a Savant SpeedVac Concentrator (France), then ground and pressed with KBr to form a tablet. FTIR spectra were recorded using an FTIR spectrophotometer (Varian 3100, USA).

7.2.6 PMAO–UCNP Emission Spectra

The PMAO–UCNP powder was placed in a custom-designed sample holder and illuminated with a 978-nm laser coupled to a multimode fibre that was butted against the sample. The emitted signal was recorded in transmission by a calibrated spectrometer (Ocean Optics, USA) filtered with a short-pass emission filter, wavelength cut-off 842 nm (Semrock, USA).

7.2.7 PMAO–UCNP Absolute Conversion Efficiency (η_{uc}) Measurements

The η_{uc} measurements were performed in a calibrated integrating sphere setup as described previously [24, Chapter 6]. In short, an integrating sphere spatially integrates all radiant flux, thus absolute absorption and emission can be measured independent of scattering by the particles. The PMAO–UCNP in powder form was placed in a custom-made sample holder at one exit port of the integrating sphere and excited by 978-nm laser light delivered by a multimode optical fibre. Using appropriate filters and a photodiode placed at the perpendicular exit port of the sphere, both emitted power (P_{em}) and absorbed power (P_{abs}) were measured over a large range of excitation intensities. η_{uc} was calculated according to the definition, P_{em}/P_{abs} [W/W].

7.2.8 Cell Labelling

Human breast adenocarcinoma cells SK-BR-3 and Chinese hamster ovary cells CHO-K1 were purchased from American Type Culture Collection and cultured in RPMI 1640 medium (HyClone, USA) supplied with $_{L}$-glutamine and 10% fetal bovine serum (HyClone, USA). The cells were seeded on 8-well glass slides at a concentration of ca. 3×10^4 cells/ml. After 24-h cultivation at 37 °C in a CO_2-incubator (with 5% CO_2), the cells were inactivated by 1% formaldehyde to prevent nonspecific UCNP internalization. Nonspecific binding of the particles to the glass slide was also eliminated by incubating the sample with a blocking agent [1% bovine serum albumin (Bio-Rad, USA) in PBS] for 1 h. The Bn-scFv4D5 solution (in PBS with 0.1% bovine serum albumin and 0.1% Tween-20) was then applied for targeting Bn through the scFv4D5-HER2/neu interaction. After 1 h of the incubation, the cells were rinsed with PBS and treated with the UCNP-Bs (100 µg/ml) colloid for 20 min. This time was considered to be sufficient to complete the formation of the UCNP-Bs:Bn-scFv4D5 complexes due to extremely high Bs:Bn affinity (Kd~10^{-14} M). Next, the cells were washed several times to remove unbound UCNP-Bs. Finally, the cells were fixed in 4% formaldehyde in PBS and mounted between a microscope slide and a coverslip. The negative control cell line was used to prove that the binding of UCNPs to the cancer cells was not a result of physical adsorption of the Bn-scFv4D5.

7.2.9 Laser-Illuminated Inverted Epi-Luminescence Microscopy

Laser (978 nm, LD980-01CW, CXCH-Photonics, China) excitation was delivered to the sample plane of a wide-field inverted epi-luminescence microscope (Olympus IX70, Japan) via a Köhler illumination scheme. An oil-immersion objective (100×, NA 1.30, Olympus, Japan) was used for bright-field cell imaging. A long-working distance dry objective (50×, NA 0.45, Olympus, Japan) was employed for UCNP-assisted imaging through the phantom layers to simulate an *in vivo* imaging procedure. The sample plane was imaged using an electron-multiplying CCD [EMCCD (iXon DU-885, Andor, Northern Ireland)] camera.

7.2.10 Phantom Fabrication

Melted agarose–water solution (1.5%) (Promega, Spain) was mixed with absorbing dyes [Magenta (Royal Talens, Holland) and black Indian ink (Winsor & Newton, UK)] and TiO_2 submicron particles [1 mg/ml (Sigma–Aldrich, Germany)] to model the scattering properties of breast tissue [25]. Uniformly thin and flat phantom layers were prepared by setting the warm agarose mixture between two glass plates spaced 0.4, 0.8, and 1.4 mm apart.

7.3 Results and Discussion

7.3.1 Synthesis and Characterization of UCNP-Based Molecular Probe

We designed, synthesized, and characterized a new molecular probe for cancer cell imaging. This comprised a contrast agent — an UCNP coated with an amphiphilic polymer — and a targeting vector — a mini-antibody raised against HER2/neu receptors.

UCNP synthesis and surface functionalization

The UCNPs composed of $NaYF_4$:Yb,Er were synthesized by performing a modified coordinate stabilization reaction. As-synthesized UCNPs were re-dispersed in *n*-hexane by sonication and then imaged by

TEM. The results of TEM imaging showed particles 120 ±20 nm in size and predominantly hexagonal in shape, as presented in Fig. 7.1(a), left panel. The hexagonal shape of the particles indicates the beta-phase of the host crystallite $NaYF_4$, which is the most favourable for the energy transfer upconversion process [26]. The as-synthesized UCNPs coordinated with oleic acid hydrophobic moieties were surface-capped with PMAO [23]. Carboxylic groups of the PMAO that appeared as a result of the hydrolysis of anhydride functional groups became exposed outwards, producing hydrophilic UCNPs, i.e. stable in aqueous solutions. In addition, the hydrophilic terminals allowed covalent binding to biomolecules through the carboxylic groups. PMAO surface-capped nanoparticles were dispersed in water, sonicated, and imaged by TEM. As seen in Fig. 7.1(a), right panel, there was negligible change in the particle size during the surface capping procedure, as expected. The polymer coating is imaged as a supramolecular network of amphiphilic molecules juxtaposed on the core material and as thin layer fragments of low electron density (Fig. 7.1(a), right panel).

We also determined the mean hydrodynamic diameters of the PMAO-UCNP particles by means of dynamic light scattering (DLS), yielding 130 ± 20 nm (Fig. 7.1(b)], which corroborated the TEM size measurement, considering a ±10% size overestimation by DLS measurements). The produced aqueous colloid remained stable for at least 2 months, as confirmed by DLS measurements. The PMAO surface capping of UCNP altered its surface charge. Its zeta-potential was measured in water as −53 mV in comparison to that of −5 mV for the as-synthesized particles. The abundant surface carboxyl groups of the polymer layer were believed to build up this highly negative surface charge.

FTIR spectroscopy of the PMAO surface-capped particles further confirmed the successful surface modification of the UCNP sample. The results of the comparative analysis of PMAO-UCNP and pure PMAO are presented in Fig. 7.1(c). C–H stretching of CH_2 polymer groups at 2919 and 2851 cm^{-1} appeared in both UCNP and PMAO-UCNP samples. The maleic anhydride ring spectral signature is of particular note. It featured two peaks at 1858 and 1781 cm^{-1} in pure PMAO, which disappeared as a result of the hydrolysis upon the PMAO-UCNP transfer to water, with the corresponding anhydride ring opening and production of free carboxylic groups presented at 1734 and 1560 cm^{-1} [27,28]. The hydrolysis of a certain number of anhydride groups in pure PMAO is known to display an FTIR peak at 1710 cm^{-1}, which is present in Fig. 7.1(c) [28].

Photophysical properties of PMAO-UCNP

Optical characterization of the excitation and emission properties of UCNP and, in particular, PMAO-UCNP was performed. The choice of PMAO-UCNP was primarily dictated by its improved η_{uc} in comparison with the as-synthesized UCNP. Additionally, the PMAO-UCNP exhibited excellent immunity to environmental and surface conditions, so that its emission properties measured in powder form remained the same both in solution and after bioconjugation. The emission spectrum of PMAO-UCNP powder was acquired using a calibrated spectrometer with excitation by a 978-nm laser [excitation intensity (I_{ex}), 28 W/cm^2], and is shown in Fig. 7.2(a). The spectrum featured three emission bands, which are known to result from the Er emission multiplets [11]. These multiplets can be grouped into two (green and red) wavelength bands, as respectively colour coded in Fig. 7.2(a). The optical absorption of the NIR excitation light at 978 nm and the η_{uc} of UCNP determine the intensity of the emitted signal. The η_{uc} is defined as the ratio

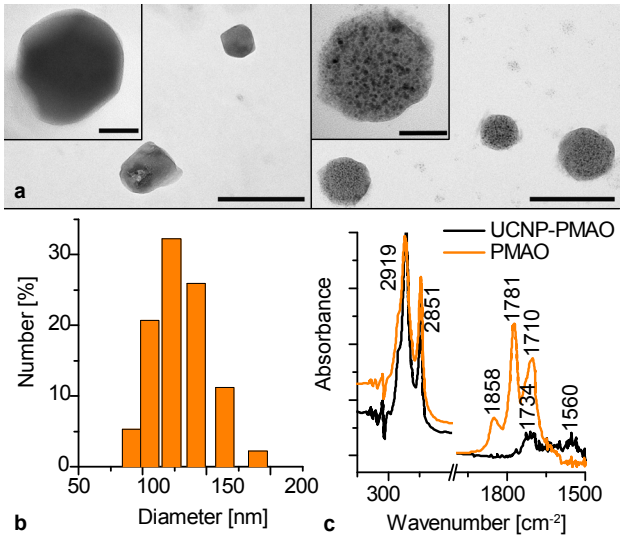

Fig. 7.1 | Characterization of upconversion nanoparticles surface-capped with amphiphilic polymer, PMAO. ***(a)*** *Transmission electron microscopy imaging of as-synthesized (left panel) and PMAO-capped (right panel) UCNPs. Scale bar, 200 nm. Zoomed-in images of the UCNPs are shown in insets in the left top corners. Scale bar, 50 nm. Right panel, a PMAO polymer layer on an UCNP crystal is visualized as a granular structure that represents a supramolecular network of amphiphilic molecules.* ***(b)*** *Histogram of the hydrodynamic size distribution of PMAO–UCNP obtained by dynamic light scattering measurements. This distribution remained unchanged for at least 2 months.* ***(c)*** *Fourier-transform infrared spectra of PMAO-UCNP and pure PMAO. The peak analysis points to the formation of the PMAO shell around the particles. See text for more details.*

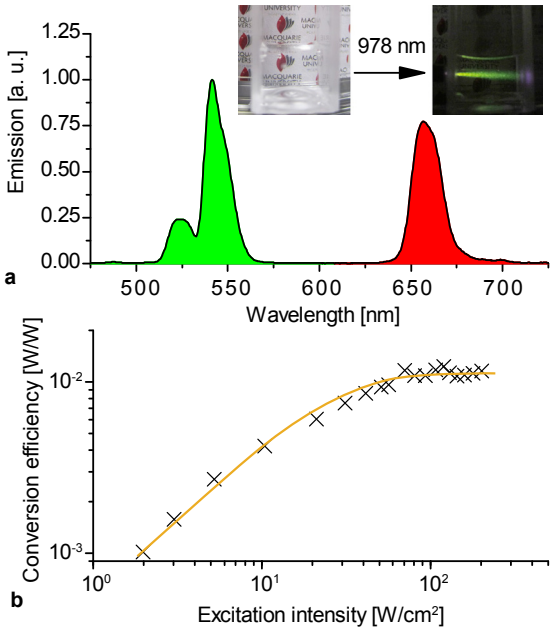

Fig. 7.2 | Photophysical characteristics of the PMAO-UCNP. ***(a)*** *Emission spectrum of the PMAO-UCNP powder featuring three (unresolved) emission multiplets grouped in green and red wavelength regions. Inset, left panel, a cuvette with UCNP aqueous colloid exhibiting high transparency; right panel, green-colour emission along the 978-nm laser beam path captured under low ambient light condition.* ***(b)*** *Absolute conversion efficiency of PMAO-UCNP as a function of the excitation intensity at 978 nm, measured using a calibrated integrating sphere setup. The orange line is a guide to the eye, and saturation is reached at ~60 W/cm².*

of the emitted power to the absorbed power measured in W/W. The emitted power depends nonlinearly on the I_{ex} since each emitted photon is a result of the absorption of two or more photons followed by non-radiative relaxation processes. At high values of I_{ex} approaching saturation, η_{uc} reaches a plateau. Measurement of η_{uc} versus I_{ex} is essential for the evaluation of UCNP-assisted imaging performance. In Fig. 7.2(b), η_{uc} of PMAO-UCNP integrated over the entire emission spectrum is plotted versus I_{ex}. We note that the green-to-red emission ratio decreases as the I_{ex} is increased. η_{uc} of the PMAO-UCNP sample starts

to saturate at I_{ex} = 60 W/cm^2 (I_{sat}) and reaches a maximum value of 1.2%. It is clear that the passivating surface coating affects η_{uc} and makes the coated UCNP much less susceptible to the environment and additional surface coating [29]. Hence, bioconjugation of PMAO-UCNP, as described in the next section, was of only minor influence to the η_{uc} of the polymer-coated UCNPs.

7.3.2 Design, Production and Target Delivery of UCNP-Bioconjugates

Bioconjugation

The PMAO-UCNP was grafted with mini-antibodies, scFv4D5, designed for targeted delivery to cancer cells that overexpress specific receptors HER2/neu. PMAO-UCNP and scFv4D5 were linked using a high-affinity molecular pair Bs:Bn.20,30 Bacterial ribonuclease Bn, and its inhibitor Bs, are small (12.4 and 10.2 kDa, respectively) proteins that are stable over a wide range of pH (from 2 to 12) and temperatures (50°C and 70°C, respectively), and have terminal groups accessible for covalent modifications and genetic fusion. A PMAO-UCNP bioconjugate was realized by its surface coating with Bs, thus forming the first submodule, while Bn was a part of the other submodule, which included an anti-HER2/neu scFv4D5 mini-antibody (Fig. 7.3(a) and 7.3(b)). The Bs-binding ability of the Bn-scFv4D5 was proved by measurement of the Bn ribonucleic activity inhibition by Bs (Fig. 7.4(a)) and the Bn-scFv4D5-HER2/ neu affinity constant was calculated from Fig. 7.4(b) to be 1.62 × 10^9 M^{-1} (Eqs. (7.1) and (7.2)). The PMAO-UCNP conjugation with Bs was implemented using a reaction with EDC and sulfo-NHS relying on the covalent linkage of the PMAO-UCNP carboxyl groups and Bs amino groups (Fig. 7.3(b)). The negatively charged Bs (pI 4.6) was favoured over the positively charged Bn (pI 8.9) for the conjugation reaction to avoid undesirable electrostatic adsorption due to the negative zeta-potential of the PMAO-UCNP [30].

Specific Labelling of Cancer Cells with the UCNP-Bs: Bn-scFv4D5 Complexes

Experimental confirmation of the bioconjugation reaction and the functionality of the UCNP-Bs:Bn-scFv4D5 biocomplexes was performed by specific immobilization of these biocomplexes on cancer cells, more specifically, human breast adenocarcinoma cells SK-BR-3 known to overexpress HER2/neu, and fixed in 1% paraformaldehyde [31]. Chinese hamster ovary cells CHO-K1 devoid of HER2/neu were used as a negative control. Both cell lines were incubated with recombinant mini-antibody submodules Bn-scFv4D5 to bind to HER2/neu through the antibody- receptor interaction, so that Bn was immobilized on the targeted cells. At the second incubation stage, UCNP-Bs was attached to the cell-immobilized Bn via high-affinity binding to Bs (Fig. 7.3(b)). Imaging of the UCNP biocomplex-treated cells using modified epi-luminescence microscopy under the 978-nm excitation showed that UCNP-Bs:BnscFv4D5 biocomplexes were immobilized on the SK-BR-3 cells with a 10-fold higher signal compared to the control CHO-K1 cells (Fig. 7.3(c)). The UCNP labelling level was estimated by image analysis of the luminescent signal integrated over the cell surface area using MATLAB software (Fig. 7.3(d)). The SK-BR-3 cells exhibited high overall UCNP labelling level with several discrete signals from UCNP clusters.

7.3.3 Evaluation of the Feasibility of UCNP-Assisted Optical Imaging in Human Breast Tissue

Breast tissue phantom

Since adenocarcinoma cells are hosted in human breast tissue, imaging contrast of these cells can be modelled experimentally, provided a human breast tissue model is available. To this end, we designed an agarose-based phantom that mimicked the optical absorption properties of live human breast tissue

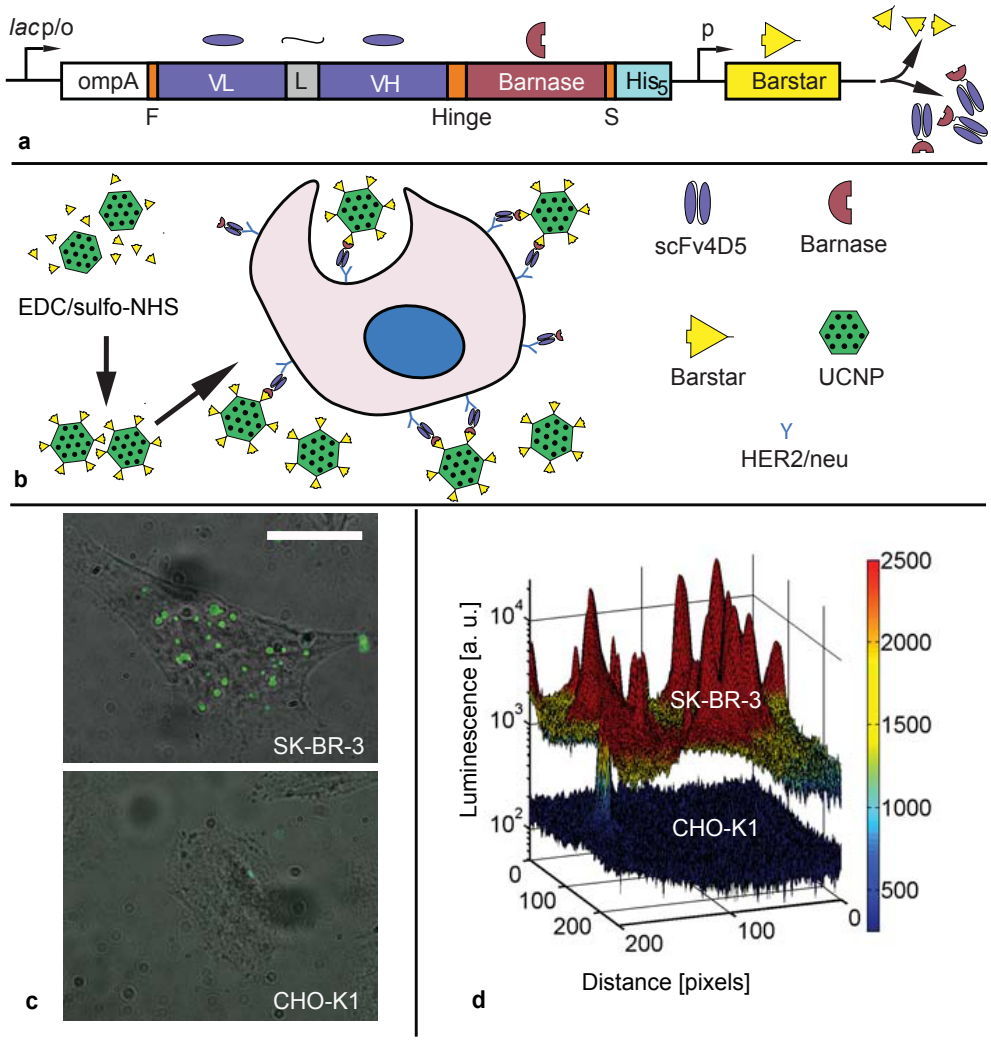

Fig. 7.3 | Cell labelling with UCNP-Bs:Bn-scFv4D5 biocomplexes. ***(a)*** *Targeting vector, Bn-scFv4D5 gene construction. The gene is under the control of a lac promoter (lac p/o) and the ompA signal peptide, and includes the N-terminal FLAG tag (F), VL-linker-VH oriented scFv4D5 mini-antibody, hinge linker (16 amino acids), Bn, short spacer S (Gly-Ala-Pro), and C-terminal His5-tag, localized sequentially. Bs coexpression is under the control of its own constitutive promoter (p) and required to suppress the Bn cytotoxicity.* ***(b)*** *The concept of cell labeling with self-assembled UCNP biocomplexes UCNPBs: Bn-scFv4D5.* ***(c)*** *Epi-luminescence microscopy of the HER2/neu overexpressing SK-BR-3 cell labeled with UCNP-Bs:Bn-scFv4D5, and control and CHO-K1 cell. Scale bar, 20 μm.* ***(d)*** *Three-dimensional surface plot of the luminescence signal acquired from the CHO-K1 and SK-BR-3 cells incubated with UCNP-Bs: Bn-scFv4D5. Although the labelled SK-BR-3 cells exhibited several discrete peaks due to UCNP biocomplex clusters, many more single and small clustered UCNP biocomplexes were also attached to these cells, resulting in higher overall signal level in between these peaks.*

in the spectral ranges of the UCNP excitation and emission (Fig. 7.5(a)), and scattering in NIR region. The absorption of breast tissue was calculated, considering absorption of haemoglobin (0.002 mM) and oxy-haemoglobin (0.011 mM) in the green range and NIR light absorption of water [32]. The spectrum of breast tissue absorption in the red spectral range was obtained from *in vivo* measurements [33]. Agarose was chosen as the matrix, as its water content (about 99%) is similar to that of live breast tissue (10% to 60%), and resulted in slightly higher absorption of the excitation light compared to live tissue, i.e. by 0.2 cm^{-1}. The phantom and breast tissue absorption coefficients (μ_a) integrated over the relevant wavelength bands were similar (green: $\mu_{a,breast}$ = 1.35 cm^{-1}, $\mu_{a,phantom}$ = 1.50 cm^{-1}, red: $\mu_{a,breast}$ = 0.06 cm^{-1}, $\mu_{a,phantom}$ = 0.06 cm^{-1} and 978 nm: $\mu_{a,breast}$ = 0.3 cm^{-1}, $\mu_{a,phantom}$ = 0.5 cm^{-1}), see Fig. 7.5(a). The reduced scattering coefficient of breast tissue *in vivo* was simulated by adding TiO_2 submicron particles to the phantom [34]. The scattering coefficient and average cosine of scattering (*g*-value) in our phantom were defined by Mie calculations of 1 mg/ml TiO_2 particles in water. Matching the reduced scattering coefficient μ'_s

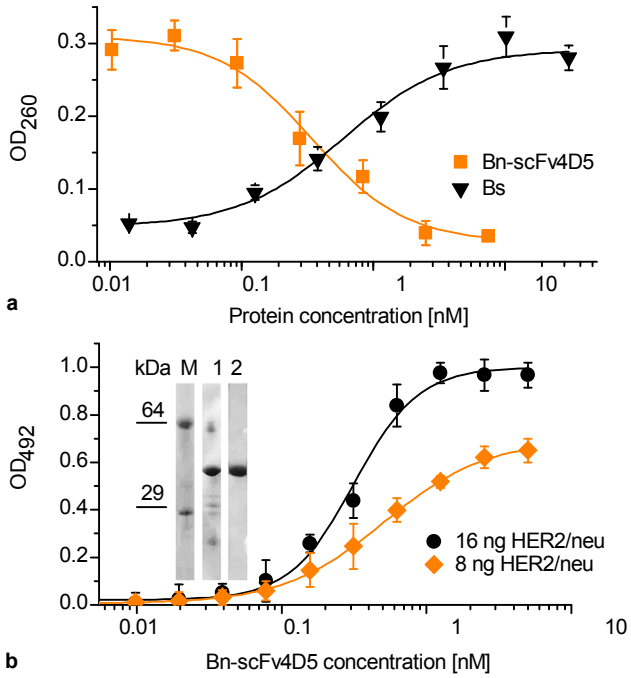

Fig. 7.4 | Functional characterization of the scFv4D5-Bn protein. *(a) Assaying of Bn-scFv4D5 affinity to Bs through measurements of ribonucleic activity inhibition.* ***(b)*** *Determination of the Bn-scFv4D5 recombinant protein affinity to HER2/neu by enzyme-linked immunoassay (K_{aff} 1.62 × 10^9 M^{-1}). Inset, electrophoresis gel profile of the Bn-scFv4D5 after two steps of the purification procedure: M, protein marker; 1, Ni^{2+} affinity chromatography; and 2, ion-exchange chromatography*

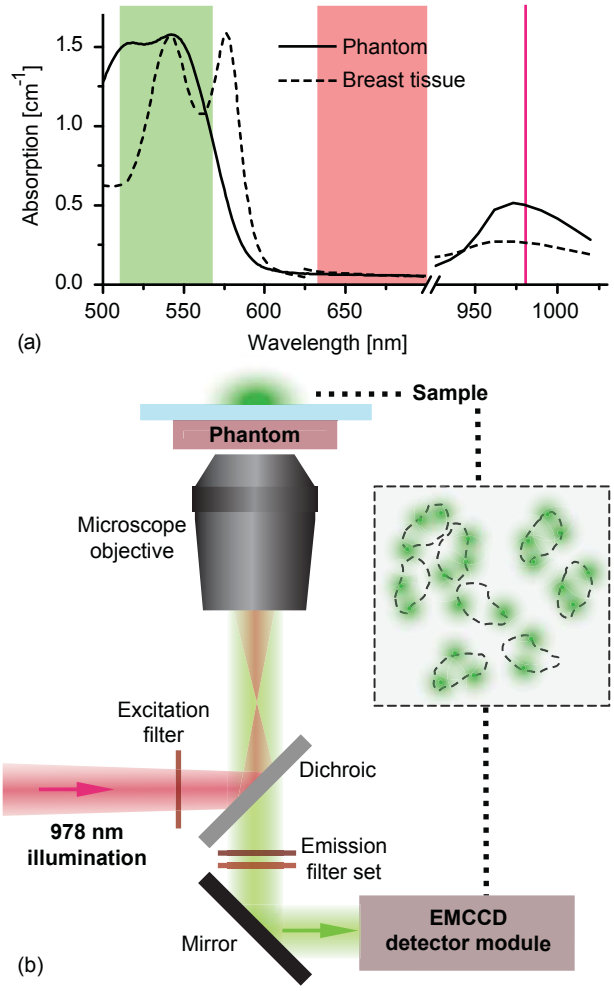

Fig. 7.5 | Experimental modelling of UCNP-assisted optical imaging. *(a) Optical absorption spectrum of the tissue simulating phantom designed to reproduce the key optical properties of breast tissue in the UCNP excitation and emission spectral ranges (solid line). The tissue absorption spectrum (dashed line) is obtained from the literature. The UCNP emission in green and red bands and excitation in the NIR region are shown as shaded areas.* ***(b)*** *Schematic diagram of the optical imaging setup; UCNP-labelled cancer cells are imaged through the phantom mimicking absorption and scattering properties of breast tissue.*

(with $\mu'_s = (1-g)\mu_s$, μ_s being the scattering coefficient, and g is the anisotropy factor) at 978 nm with values recorded *in vivo* (978 nm: $\mu'_{s,breast}$ = 8 to 12 cm^{-1}, $\mu'_{s,phantom}$ = 10 cm^{-1}) resulted in a decreased scattering coefficient of the phantom compared to live tissue for the green and red wavelength bands (red: $\mu'_{s,breast}$ = 13 to 20 cm^{-1}, $\mu'_{s,phantom}$ = 6.9 cm^{-1} and green: $\mu'_{s,breast}$ = 15 to 22 cm^{-1}, $\mu'_{s,phantom}$ = 6.6 cm^{-1}) [33]. Matching μ'_s of live tissue and phantom material at 978 nm was crucial and hence prioritized in our modelling, since the scattering of 978-nm light primarily determined the luminescence

signal decay with depth due to the nonlinear UCNP η_{uc}. As is seen from Fig. 7.5(a), UCNP excitation at 980 nm is suboptimal for bioimaging due to the onset of the water absorption, and the use of the excitation at 915 nm is sometime preferable, although the excitation efficiency is lower. The use of a commercially available 915-nm semiconductor laser as an excitation source for an UCNP luminescence can considerably increase the imaging depth as was reported by Zhan et al. [18].

Experimental modelling of UCNP-assisted cancerous lesion imaging

An optical phantom simulating breast tissue optical properties provides an excellent model to assess the prospects of *in vivo* UCNP-targeted imaging of breast cancer lesions. The cancer cells labelled with UCNP-Bs:Bn-scFv4D5 biocomplexes were covered with a stack of phantom layers (0.4 to 2.0 mm) and imaged using a modified epi-luminescence microscope, see Fig. 7.5(b). A long-working distance objective lens allowed stacking thin phantom layers on top of the sample, while re-adjusting the objective lens distance to the sample. The signal-to-noise ratio (SNR) was defined as a ratio of the luminescence signal to the standard deviation of the signal, where the signal was estimated as a sum of the pixel values over the sample area with the background subtracted. The sample area was a cellular region outlined as inferred from the bright-field microscopy (Fig. 7.5(b), dashed lines). The background level was estimated as the mean pixel value outside the illumination spot in the same image. The total noise level (N_{total}) was defined as:

$$N_{total} = \sqrt{N_{shot}^2 + N_{dark}^2 + N_{read}^2 + N_{rest}^2} \qquad (7.3)$$

where N_{shot}, N_{dark}, N_{read}, and N_{rest} are signal shot noise multiplied by the EM-characteristic multiplicative noise factor 1.4, dark noise, read noise, and rest noise, respectively, all measured in number of electrons [e^-] [35,36]. For the experimental image data, the dark, read, and rest noises were estimated as the standard deviation of the dark background. The signal shot noise was derived from the acquired upconversion signal (*signal*):

$$N_{shot} = \sqrt{signal} \qquad (7.4)$$

The SNR of the same sample area is plotted versus phantom thickness in Fig. 7.6. According to the SNR estimation and observed image contrast, the signals from the UCNP-labelled SK-BR-3 cells were clearly observable through the phantom up to 1.6-mm thick (SNR = 4.5, Fig. 7.6).

We note that the excitation intensity at 978 nm, I_{ex}, decreases with the phantom thickness, and at a depth greater than 0.4 mm it is below I_{sat} as found using the Lambert–Beer law:

$$P(z) = P(0)e^{-\mu_{tr} z} \qquad (7.5)$$

where μ_{tr} is the transport attenuation coefficient (mm^{-1}) defined as a sum of the absorption, μ_a and reduced scattering coefficients μ'_s [24]. The decrease in I_{ex} below I_{sat} yields lower η_{uc} that contributes to SNR loss, in addition to increased attenuation of the emitted light with the phantom thickness.

In Eq. 7.5 the attenuation in tissue is based on a hybrid model between Lambert-Beer, and Diffusion theory based on the Radiative Transfer Equation. In essence, it calculates the attenuation in tissue due to photon removal from the focussing path by absorption and isotropic scattering. The classical Lambert-Beer model uses the attenuation coefficient (μa + μs) while here we use the transport attenuation co efficient ($\mu_a + \mu'_s$). The diffusion approximation of the Radiative Transfer Equation is valid when the tissue scattering coefficient is higher as compared with the absorption coefficient at the UCNP excitation and emission wavelengths and for depths beyond 1 mm. It uses ($\sqrt{(3\mu_a(\mu_a + \mu'_s))}$) for tissue attenuation. We have compared our experimental phantom results of signal versus depth to all three models, and found that the hybrid Lambert-Beer model is best-fitting, also for depths beyond 1 mm. A possible explanation for the non-applicability of the diffusion model is the high-NA objective used for imaging, effectively rejecting out of focus (diffuse) photons in the set-up. A possible explanation for the non-applicability of the classical Lambert-Beer model are the high anisotropy values (g) for tissue, which means that many photons are scattered at such small angels that they stay in the focal beam. In this regime of moderate depth, focused beams and high g-values, the hybrid Lambert-Beer model is thus most appropriate.

Quantitative imaging of the UCNP-labelled SK-BR-3 cells allowed estimation of the total number of UCNP biocomplexes per cell, using the following equation:

$$S_{UCNP} = N_{UCNP} N_{YB} \sigma_{abs,YB} I_{ex} \eta_{UC} \zeta_{total} \qquad (7.6)$$

where S_{UCNP} is the detected luminescent signal (counts/s); N_{UCNP} is the number of UCNP biocomplexes per cell; N_{Yb} is the total number of Yb ions per UCNP crystal; $\sigma_{abs,Yb}$ is the Yb absorption cross section (1×10^{-20} cm^2); I_{ex} (W/cm^2); η_{uc} according to Fig. 7.2(b); and ζ_{total} (counts/W/s) is the spectral calibration coefficient of the detection path in the microscope system calculated as described in Chapter 6 [24], Eq. 6.2.

The total number of UCNP biocomplexes per SK-BR-3 cell *in vitro* was calculated to be [2.8 ± 0.5]×10^4 using Eq. (7.6). In order to put this estimation in the context of an *in vivo* imaging scenario, we made use of the cross-comparison between the *in vivo* and *in vitro* labelling efficiency reported to be ca. 10-fold less for the *in vivo* case [37,38]. Therefore, the number of UCNPs in one breast cancer cell *in vivo* was estimated to be ~3000.

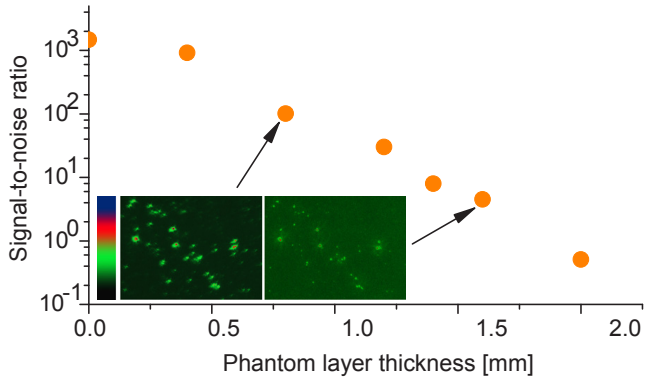

Fig. 7.6 | UCNP-labelled SK-BR-3 cell imaging *through a breast tissue simulating phantom at excitation intensity 100 W/cm^2. The signal-to-noise ratio was estimated as the total signal from one SK-BR-3 cell divided by the total noise (see text for details), and plotted versus the phantom thickness. Inset shows a false colour image of the UCNP-labelled SK-BR-3 cells through 0.8 and 1.6-mm phantom layers, arrows point to the corresponding data points in the graph; left panel, colour bar.*

Theoretical modelling of** in vivo **imaging

The experimental data of the UCNP-assisted imaging sets the framework for the estimation of limits of *in vivo* detection of UCNP-labelled breast cancer lesions versus depth in breast tissue. Equation (7.5) was used to calculate the attenuation of the excitation and emission power, P at depth z due to absorption and scattering in tissue. This power relationship holds for both the excitation light travelling into the tissue toward the UCNP sample and the emitted light travelling backward.

Initially, we calculated the UCNP signal versus the phantom thickness and compared it with that acquired experimentally (cf. Fig. 7.6). The experimental data were obtained by adding up all pixels from the area occupied by the SK-BR-3 cells, subtracting the background, and normalizing for the EM gain, exposure time, microscope throughput, and camera sensitivity. The UCNP signal *in vitro* for one SK-BR-3 cell versus the phantom thickness is shown in Fig. 7.7 plotted as separate data points (triangles). The UCNP signal *in vitro* was also modelled using Eqs. (7.5) and (7.6), with the optical properties of the phantom and I_{ex} = 100 W/cm^2 as parameters. As is shown in Fig. 7.7 (orange solid line), the modelled signal dependency on phantom thickness fits the data points very well for the entire depth range down to 2 mm. Therefore, extrapolation of the signal to the greater depths pertinent for *in vivo* optical imaging is feasible. The UCNP-assisted imaging limit was theoretically estimated considering early-stage cancer tumour diagnostics under the maximum permissible laser exposure condition. A total number of ~160 breast cancer cells localized in the imaging volume ~260 × 260 × 10 μm^3 were estimated, considering the EMCCD sensor optically conjugated with the imaging plane via a 50× objective lens. A pulse energy of 0.7 J/cm^2 (I_{ex} = 710 W/cm^2) of the excitation beam for a 1 ms pulse duration was calculated as the maximum permissible exposure for skin [39]. The camera acquisition parameters were exposure time 1 ms and EM gain 300×. We assumed an optimized imaging system with the background completely suppressed [14]. The calculated UCNP signal intensity versus depth in tissue is shown in Fig. 7.7 (black solid line). As can be seen, the modelled *in* vivo signal of a tumour cluster is higher than that of the experimental in vitro signal. This is attributed to the higher number of cells in the sample volume, normalized to the reduced scattering coefficient in the green and red regions and the increased I_{ex}, even though the lower labelling efficiency was taken into account (Eqs. (7.5) and (7.6)). The slope change of this curve at ca. 2 mm is explained by noting that I_{ex} is above the saturation intensity level within 2 mm from the surface in tissue yielding a nearly constant η_{uc} (see Fig. 7.2(b)). As the depth increases, I_{ex} and consequently η_{uc} decrease, thus contributing to the negative slope. The standard deviation of the signal was estimated to be less than 20%, with the main components due to the labelling variation from cell to cell, and noise. The UCNP-signal can be reliably measured only when it is well above the noise level. The in vitro noise was estimated as described above, and plotted in Fig. 7.7 as data points (×). The relatively high noise level due to the excitation light at 978 nm bleeding through the filters can be completely suppressed, e.g. by employing time-gated detection [14] as plotted in Fig. 7.7 (black dashed line), where the dark and read noise were specified by the manufacturer, and the rest noise was zero. As one can see, the UCNP signal approaches the noise level beyond 4-mm depth in tissue, which represents a significant range for a number of applications, including early-stage breast cancer tumour diagnostics and image-guided surgery [4].

7.4 CONCLUSION

Optical imaging of an early-stage human breast cancer lesion labelled with luminescent UCNPs was modelled using cell cultures and optical phantoms. Human breast adenocarcinoma cells SK-BR-3 that overexpress epidermal growth factor receptor HER2/neu were targeted by polymer-capped UCNPs grafted with an anti-HER2/neu targeting vector via a high-affinity molecular pair Bs:Bn. Selective binding of the UCNP-Bs:Bn-scFv4D5 biocomplexes to the SK-BR-3 cells (the ratio 10:1 as compared to a negative control) was demonstrated. The luminescence signal of the UCNPs was detectable even through a 1.6-mm thick agarose phantom mimicking breast tissue optical properties. A theoretical model based on the experimental data predicted the feasibility of *in vivo* optical imaging at a depth of up to 4 mm in live breast tissue, under the reasonable assumption of complete suppression of background signals due to excitation light scattering and biological tissue autofluorescence, which is feasible given the UCNP luminescence properties. We believe this study demonstrates considerable potential for UCNP-assisted optical imaging for early-stage cancer diagnostic and image-guided surgery applications.

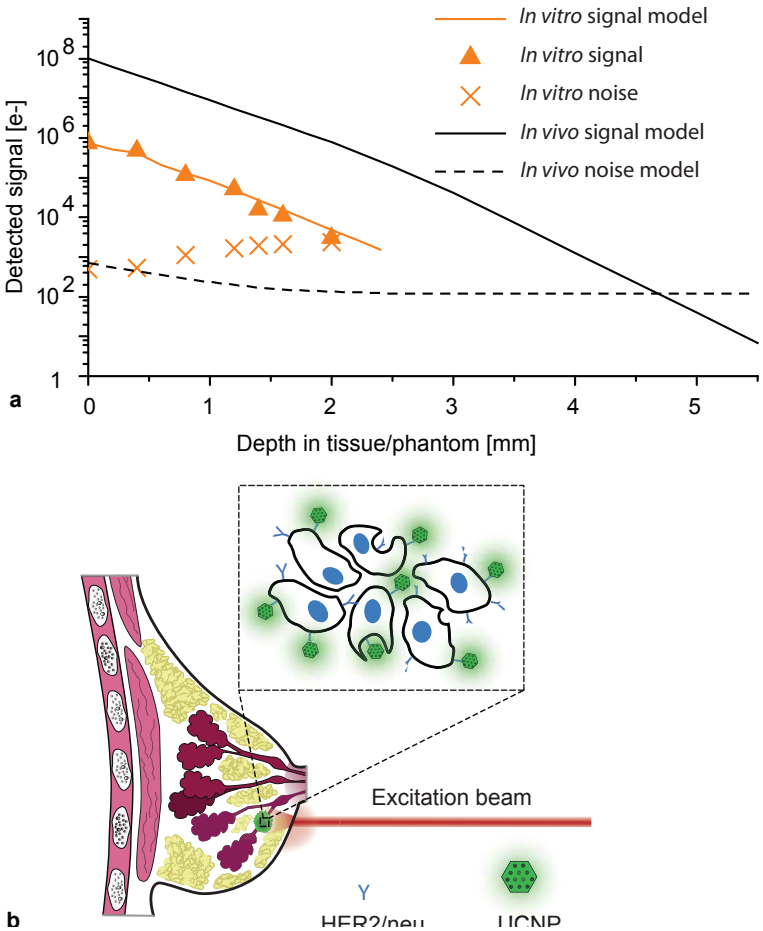

***Fig. 7.7 | Theoretical estimation of UCNP-assisted** in vivo **optical imaging sensitivity**: signal intensity and noise level versus the depth in tissue. **(a)** The theoretically modelled UCNP signal in vitro from one cell (orange solid line) is plotted as a function of the phantom thickness, which fits the experimental SK-BR-3 cell imaging data (triangles). In vivo UCNP signal (– , black solid line), in vitro (×, orange crosses) and in vivo (- -, black dashed line) noise levels are plotted versus depth in tissue/phantom. ~160 (SK-BR-3) breast cancer cells localized within an imaging volume of ~260 × 260 × 10 μm3 were modelled, considering ~3000 UCNP-Bs:Bn-scFv4D5 biocomplexes immobilized on each cell by HER2/neu, as schematically drawn in **(b)**.*

7.5 Acknowledgments

We would like to thank Dr. A.N. Bykov for stimulating discussion on the theoretical aspects of modelling biological tissue phantoms. We wish to acknowledge support of the Russian Foundation of Basic Research, Grant Nos. 11-04-12113, 12-04- 01258-a, and 13-02-01138.

7.6 REFERENCES

1. H. Soliman et al., "Functional imaging using diffuse optical spectroscopy of neoadjuvant chemotherapy response in women with locally advanced breast cancer," Clin. Cancer Res. 16(9), 2605–2614 (2010).
2. L. V. Wang, "Multiscale photoacoustic microscopy and computed tomography," Nat. Photonics 3(9), 503–509 (2009).
3. R. Weissleder, "A clearer vision for *in vivo* imaging," Nat. Biotechnol. 19(4), 316–317 (2001).
4. S. Achilefu, "Lighting up tumors with receptor-specific optical molecular probes," Technol. Cancer Res. Treat. 3(4), 393–409 (2004).
5. Y. Ye et al., "Design, synthesis, and evaluation of near infrared fluorescent multimeric RGD peptides for targeting tumors," J. Med. Chem. 49(7), 2268–2275 (2006).
6. T. A. Zdobnova et al., "Fluorescent immunolabeling of cancer cells by quantum dots and antibody scFv fragment," J. Biomed. Opt. 14(2), 021004 (2009).
7. S. M. Deyev and E. N. Lebedenko, "Multivalency: the hallmark of antibodies used for optimization of tumor targeting by design," Bioessays 30(9), 904–918 (2008).
8. F. Leblond et al., "Pre-clinical whole-body fluorescence imaging: review of instruments, methods and applications," J. Photochem. Photobiol. B 98(1), 77–94 (2010).
9. N. M. Idris et al., "Tracking transplanted cells in live animal using upconversion fluorescent nanoparticles," Biomaterials 30(28), 5104–5113 (2009).
10. T. W. Prow et al., "Quantum dot penetration into viable human skin," Nanotoxicology 6(2), 173–185 (2012).
11. H. X. Mai et al., "Highly efficient multicolor up-conversion emissions and their mechanisms of monodisperse NaYF4:Yb, Er core and core/ shell-structured nanocrystals," J. Phys. Chem. C 111(37), 13721–13729 (2007).
12. R. H. Page et al., "Upconversion-pumped luminescence efficiency of rare-earth-doped hosts sensitized with trivalent ytterbium," J. Opt. Soc. Am. B 15(3), 996–1008 (1998).
13. C. Vinegoni et al., "Transillumination fluorescence imaging in mice using biocompatible upconverting nanoparticles," Opt. Lett. 34(17), 2566–2568 (2009).
14. K. Hanaoka et al., "Time-resolved long-lived luminescence imaging method employing luminescent lanthanide probes with a new microscopy system," J. Am. Chem. Soc. 129(44), 13502–13509 (2007).
15. T. Cao et al., "High-quality water-soluble and surface-functionalized upconversion nanocrystals as luminescent probes for bioimaging," Biomaterials 32(11), 2959–2968 (2011).
16. Q. Liu et al., "Sub-10 nm hexagonal lanthanide-doped NaLuF4 upconversion nanocyrstals for sensitive bioimaging *in vivo*," J. Am. Chem. Soc. 133(43), 17122–17125 (2011).
17. L. Xiong et al., "High contrast upconversion luminescence targeted imaging *in vivo* using peptide-labeled nanophosphors," Anal. Chem. 81(21), 8687–8694 (2009).
18. Q. Q. Zhan et al., "Using 915-nm laser excited Tm3þ/Er3þ/Ho3þ doped NaYbF4 upconversion nanoparticles for *in vitro* and deeper *in vivo* bioimaging without overheating irradiation," ACS Nano 5(5), 3744–3757 (2011).
19. C. Wang, L. Cheng, and Z. Liu, "Research spotlight: upconversion nanoparticles for potential cancer theranostics," Ther. Delivery 2(10), 1235–1239 (2011).
20. S. M. Deyev et al., "Design of multivalent complexes using the barnase ·barstar module," Nat. Biotechnol. 21(12), 1486–1492 (2003).
21. G. W. Rushizky et al., "Studies on B. subtilis ribonuclease. I. Characterization of enzymatic specificity," Biochemistry 2(4), 787–793 (1963).
22. J. D. Beatty, B. G. Beatty, and W. G. Vlahos, "Measurement of monoclonal antibody affinity by non-competitive enzyme immunoassay," J. Immunol. Methods 100(1–2), 173–179 (1987).
23. T. Pellegrino et al., "Hydrophobic nanocrystals coated with an amphiphilic polymer shell: a general route to water soluble nanocrystals," Nano Lett. 4(4), 703–707 (2004).
24. A. Nadort et al., "Quantitative imaging of single upconversion nanoparticles in biological tissue," PLoS One 8(5), e63292 (2013).
25 A. V. Bykov et al., "Skin phantoms with realistic vessel structure for OCT measurements," Proc. SPIE 7376, 73760F (2010).
26. F. Wang et al., "Synthesis of polyethylenimine/NaYF4 nanoparticles with upconversion fluorescence," Nanotechnology 17(23), 5786–5791 (2006).
27. L. S. Li et al., "Studies of nanoparticulate cadmium sulfide in amphiphilic polymaleic acid octadecanol ester Langmuir–Blodgett films," Supramol. Sci. 5(5–6), 475–478 (1998).
28. S. Song, L. Liu, and J. Zhang, "Annealing improves tribological property of poly (octadecene-alt-maleic anhydride) self-assembled film," Appl. Surf. Sci. 257(23), 10254–10260 (2011).
29. G. S. Yi and G. M. Chow, "Water-soluble NaYF4:Yb; Er (Tm)/NaYF4/ polymer core/shell/shell nanoparticles with significant enhancement of upconversion fluorescence," Chem. Mater. 19(3), 341–343 (2007).
30. V. K. A. Sreenivasan et al., "Barstar:barnase—a versatile platform for colloidal diamond bioconjugation," J. Mater. Chem. 21(1), 65–68 (2011).
31. N. E. Hynes et al., "Overexpression of the c-erbB-2 protein in human breast tumor cell lines," J. Cell. Biochem. 39(2), 167–173 (1989).
32. H. Heusmann, J. G. Koelzer, and G. Mitic, "Characterization of female breasts *in vivo* by time-resolved and spectroscopic measurements in the near infrared spectroscopy," J. Biomed. Opt. 1(4), 425–434 (1996).
33. A. Pifferi et al., "Spectroscopic time-resolved diffuse reflectance and transmittance measurements of the female breast at different interfiber distances," J. Biomed. Opt. 9(6), 1143–1151 (2004).
34. A. V. Bykov et al., "Multilayer tissue phantoms with embedded capillary system for OCT and DOCT imaging," Proc. SPIE 8091, 80911R (2011).
35. M. S. Robbins and B. J. Hadwen, "The noise performance of electron multiplying charge-coupled devices," IEEE Trans. Electron. Devices 50(5), 1227–1232 (2003).
36. J. C. Waters, "Accuracy and precision in quantitative fluorescence microscopy," J. Cell Biol. 185(7), 1135–1148 (2009).
37. S. R. Benhabbour et al.," *In vitro* and *in vivo* assessment of targeting lipid-based nanoparticles to the epidermal growth factor-receptor (EGFR) using a novel heptameric ZEGFR domain," J. Controlled Release 158(1), 63–71 (2011).
38. J. A. Khan et al., "Designing nanoconjugates to effectively target pancreatic cancer cells *in vitro* and *in vivo*," PLoS One 6(6), e20347 (2011).
39. Standards Australia/Standards New Zealand, AS/NZS 60825, pp. 1–48, SAI Global Limited, Sydney, AU and Wellington, NZ (2012).

8

Discussion and Conclusion

Parts in this chapter are from the following co-authored publications:

Ref. 63

K. Liu, J. A. Holz, Y. Ding, X. Liu, Y. Zhang, T. Langping, X. Kong, B. Priem, **A. Nadort**, S. A. G. Lambrechts, M. C. G. Aalders, W. J. Buma, P. D. Y. Liu, and H. Zhang, "Targeted labeling of early-stage tumor spheroid in chorioallantoic membrane model with upconversion nanoparticles," Nanoscale (2014).

My contribution to this paper: P*art of design, realization and performance of chick embryo CAM tumour model and intravital imaging system.*

Ref. 66

A. E. Guller, A. N. Generalova, E.V. Petersen, A.V. Nechaev, I.A. Trusova, N.N. Landyshev, **A. Nadort**, E.A. Grebenik, S.M. Deyev, A.B. Shekhter and A.V. Zvyagin, "Cytotoxicity and non-specific cellular uptake of bare and surface-modified upconversion nanoparticles in human skin cells, " Nano Research (2014).

My contribution to this paper: *Design and realization of quantitative imaging experiment, performing UCNP optical characterization and cellular uptake imaging experiment and confocal imaging, including data analysis and paper writing (relevant parts).*

ABSTRACT This Chapter reflects on the two main research lines of this thesis that focus on optical techniques to assess biological tissues based on (1) laser speckle flowmetry and (2) photoluminescent signals from upconversion nanoparticles. The results presented in this thesis are summarized and their contributions to clinically relevant applications are discussed. Additional results obtained during this PhD project are included, as well as possibilities for further improvements of the techniques.

8.1 INTRODUCTION

Optical techniques to assess microcirculation functionality are indispensible for the diagnosis, monitoring, therapy guidance and understanding of many diseases ranging from the onset of septic shock to the delivery of drugs to tumours. This thesis contributes to the development of optical techniques to improve the assessment of microcirculation pathology and drug delivery in a minimally invasive way. The first part of this thesis aims to develop a non-invasive and quantitative technique to assess the microcirculatory blood flow based on laser speckle flowmetry. The second part is devoted to the quantification of optical signals arising from photoluminescent upconversion nanoparticles (UCNPs) in the context of sensitive detection in biomedical tissues, in particular vascularised tumour tissue. In this discussion chapter, I will review the two main research lines individually, including the contribution to clinically relevant applications of the results presented in this thesis, additional results and future improvements. In the final Chapter 9, I will present a general conclusion and outlook on how the techniques can be brought together to serve in the context of cancer diagnosis and treatment monitoring and contribute to the clinical understanding of tumour development.

8.2 LASER SPECKLE FLOWMETRY: A QUANTITATIVE TOOL?

8.2.1 Key results on laser speckle flowmetry

Chapters 2 through 4 address several theoretical aspects underlying laser speckle flowmetry which contribute to an increased accuracy in determining blood flow velocity from speckle decorrelation times, accompanied by experimental validation. Chapter 2 starts with the basic expression on speckle statistics given by Goodman [1] and subsequent derivation presented by Fercher and Briers [2], relating the time-varying speckle fluctuations to the imaged speckle contrast (Eq. 2.8). An important input requirement for correct interpretation is a model describing the temporal autocorrelation function (ACF) of the speckle fluctuations, referred to as $g_1(\tau)$ which is parameterized by the characteristic decorrelation time τ_c. Usually a Lorentzian or Gaussian form of $g_1(\tau)$ is assumed [3-5], resulting in the speckle contrast Eq. 3.6 (Lorentzian) or 3.7/4.10 (Gaussian) through which τ_c can be found from speckle contrast K (provided that β_M and ρ are well estimated, for example using a multi-exposure acquisition and subsequent nonlinear curve fit) [6, 7].

The first gap in the speckle literature addressed in this thesis is the relationship between τ_c and blood flow velocity V in tissues *in vivo*. The relationship is often verified to be of the form $1/\tau_c \sim V$ using flow phantom set-ups [7-9], but a lack of knowledge of actual blood flow velocity limited the verification *in vivo*. The integration of sidestream dark field (SDF) microscopy and laser speckle contrast imaging (LSCI) opened up the possibility to compare both (Chapter 3). Flow phantom experiments confirmed that the SDF-LSCI geometry adequately produces and detects speckle patterns, and that the linear relationship of $1/\tau_c$ with V is reproduced. K was reliably estimated by sufficient sampling of speckles in a spatiotemporal local region of the image pixels, while maintaining a useful spatial and temporal resolution *in vivo*. We found a considerable speckle decorrelation for tissue regions without flow when analyzing *in vivo* speckle contrast images and corresponding SDF images of the microcirculation, with a high correlation between tissue decorrelation times and adjacent vessel decorrelation times. Reasonably, this 'offset' decorrelation

is due to additional decorrelation sources such as muscle movements and dynamic scattering events with red blood cells (RBCs) along the photon path to the focal plane. We hypothesized that the total ACF can be regarded as the product of the two (statistically-independent) ACF's describing the offset and flow dynamics [10, 11], and the actual flow τ_c can be derived from a simple equation (Eq. 3.9) that can be practically solved by selecting τ_c's from the vessel and adjacent tissue regions defined from conventional SDF-images. The offset-corrected $1/\tau_c$ vs flow relationship (Fig. 3.7) exhibited a higher linear correlation ($r^2 = 0.95$) as compared to the uncorrected relationship ($r^2 = 0.4$), substantiating our hypothesis. The offset-correction provides a method to find the τ_c belonging to the desired RBC dynamics only and can be regarded as a first step towards quantitative laser speckle flowmetry.

Chapter 3 also revealed that the slope of the graph of $1/\tau_c$ vs. *V in vitro* was much steeper compared to $1/\tau_c$ vs. *V in vivo,* possibly caused by the smaller scatterer size and increase in number of dynamic scattering events *in vitro*. These findings were a motivation to perform a flow phantom experiment with varying size and concentration of flowing scatterers to assess the influence on the slope, designated as the proportionality factor α in the relationship $1/\tau_c = \alpha V$. The outcome of this experiment forms the basis of Chapter 4. The experiment confirmed that α changes with both size and concentration of flowing scatterers which is thus important to take into account for quantitative flowmetry. To generalize these results we modelled the experiment following the theoretical frameworks of DWS and Laser Doppler Flowmetry (LDF), modified to LSCI and our measurement geometry and optical properties. In this model, the scattering phase function of the flowing scatterers and the number of scattering events in the flow tube or blood vessel influence α. The scattering phase function can be predicted using our recent advances in the modelling of optical scattering of whole blood using Mie and Percus-Yevick theories [12-15], and the number of scattering events by Monte Carlo simulations [16, 17]. Under certain conditions, which are met in SDF-LSCI of the *in-vivo* microcirculation, the theory and experiment match perfectly. In Chapter 4 we have thus further quantified laser speckle flowmetry by modelling and validating the relationship between τ_c and flow velocity for the *in vivo* microcirculation.

Together, chapters 3 and 4 provide practical guidelines towards quantitative *in vivo* flowmetry which can be summarized as: a multi-exposure acquisition scheme to reliably estimate τ_c; a correction for additive decorrelation sources by measuring the $\tau_{c,offset}$ from tissue regions; model-based scaling of τ_c for multiple scattering where the number of scattering events in the vessel (N) can be estimated from the vessel diameter; and relating this final τ_c to the actual flow velocity through the proportionality constant α. With the flow velocities at hand further quantitative assessment of the vessel blood flow (blood volume/time) and tissue perfusion (blood volume/tissue volume/time) can be made, since vessel diameters and vessel density can be found from the images. Though intuitively it may seem that the conventionally measured uncorrected decorrelation time relates to tissue perfusion (since it is a measure of multiple dynamic scattering events in tissue and flow velocity), important to keep in mind is that flow velocity and multiple scattering are not linearly related ($1/\tau_c \neq \alpha' VN$ but $1/\tau_c = \alpha' VA(N)$, where α' denotes α for single scattering and $A(N)$ is a model-based scaling factor, Chapter 4) and N is not linearly related to vessel diameter. Furthermore, our approach differentiates between measurement dynamics (due to blood flow, muscle movements, laser stability, etc.) and the clinically relevant vessel dynamics (due to blood flow). In addition, an estimate of V and vessel diameter distribution are clinically relevant parameters for microcirculation

functionality as well. Therefore, our model represents an improvement compared to previous reports on tissue dynamics using LDF, LSCI or DWS where this differentiation is not made, and creates new opportunities for the assessment of the microcirculation in studies within and between organs and organisms or during the course of disease and therapy.

8.2.2 Feasibility of LSCI for clinical microcirculation imaging

The initial motivation to integrate SDF with LSCI as clinical microcirculation imager was the inability of SDF to measure microcirculatory perfusion automatically. The sequential steps for quantitative flowmetry using SDF-LSCI as summarized in the previous paragraph can straightforwardly be automated to enable instantaneous measurements at the bedside or during operations. In addition, SDF-LSCI is sensitive to higher flow velocities than conventional SDF imaging. Flow velocities as high as 20 mm/s were validated in this thesis (compared to <2 mm/s for SDF). Higher flows will be clearly visible in speckle contrast images and if their quantification is desirable the multi-exposure speckle acquisition should be extended towards shorter exposure times. Lastly, SDF-LSCI utilizes wavelengths where the absorption by blood is low (red to NIR range) resulting in deeper light penetration and the potential to image through scattering layers such as the skin. In this case, the vessel diameters can only be estimated from SDF-LSCI images instead of conventional-SDF images. The latter is also important in view of conventional LSCI set-ups, where no absorption-based SDF images of blood vessel can be captured. Vessel and tissue regions can still be identified from the speckle contrast (or decorrelation time) images, although the contrast decreases in the case of low flows. Monte Carlo simulations verified that the number of scattering events in the vessels is similar in both geometries. The results on quantitative SDF-LSCI from chapters 3 and 4 are thus generally applicable to laser speckle flowmetry, and, by the analogy explained in chapter 2, also to LDF imaging systems.

The function of the microcirculation is to supply the tissue with oxygen and nutrients according to its metabolic needs. An impaired microcirculation is an important pathological marker for various diseases and is the cause and the consequence of clinical pathologies, as outlined in Chapter 1 [18]. The improved quantitative performance of the LSCI technique facilitates the comparison of blood flow, velocity and tissue perfusion between different spatial locations or time points, where previously semi-quantitative measures of flow [19, 20], or relative changes in blood flow velocity necessitating a baseline measurement [4, 21], were reported. Quantitative LSCI enables the monitoring of the chronic changes of cerebral perfusion after ischemic stroke [22, 23], vascular remodelling during the healing process in burn wounds [24, 25], or the comparison of microcirculatory perfusion in several organs during septic shock models [26]. The sensitivity to higher flows is instrumental for studying brain metabolism, since blood flow velocities in rat cerebral capillaries were reported up to 2.8 mm/s (venules and venous capillaries) and 21 mm/s (arterioles and arterial capillaries) measured using incident light microscopy and transit time photometry [27]. The control mechanisms of cerebral capillary flow are subject to controversy [28]. A current hypothesis suggesting that neurological signals regulate the capillary flow by triggering the precapillary arterioles, would benefit from quantitative LSCI as a simple non-invasive technique to visualize capillary flow velocity *in vivo*. Cerebral capillary flow control is clinically relevant for e.g. research on functional brain activation, epilepsy, migraine, head trauma, ischemia and hypoxia [28]. The ability to quantify microcirculatory flows through skin has potential applications in neonatal care, where the correlation between baseline

microvascular blood flow as measured with LDF on the lower limb, exhibits significant relationships with clinical illness severity and cardiovascular function in the immediate postnatal period [29, 30]. The application of quantitative LSCI may increase the clinical relevancy by providing information on microcirculation geometry and blood flow velocity non-invasively for this vulnerable group of patients in the neonatal intensive care unit.

8.2.3 Sensitivity to low flows

A current shortcoming of LSCI is the low sensitivity to low flows, for which the offset and flow decorrelation times are very similar and there is hardly any contrast between vessel and tissue. This is aggravated in 'active' tissue such as the tongue measured using a hand-held device. In our *in vivo* experiments flows as low as 0.3 mm/s were quantified by SDF-LSCI. In sepsis, sluggish (< 0.3 mm/s) and interrupted blood flows are indicated as important parameters [31, 32]. Fortunately, the integration of SDF with LSCI allows for an improvement in the analysis that can potentially enhance the sensitivity to lower blood flows: regions belonging to one vessel (same flow velocity) can be outlined according to the conventional-SDF images to serve as the local region to calculate *K*, if needed extended temporally as well. This image-based determination of local region results in a larger local region, thus a more reliable estimation of *K* while also providing a higher spatial and temporal resolution. Since all pixels in the local region represent the same flow, the accuracy and sensitivity to lower flows is likely improved.

8.2.4 Multiple populations of dynamic photons

The offset-correction as presented in this thesis assumes that the photons detected at the vessel region have been subject to offset decorrelation events and subsequently to at least one dynamic scattering event in the vessel, justifying Eq. 3.8: $g_{1,total}(\tau) = g_{1,flow}(\tau) \cdot g_{1,offset}(\tau)$. Consequently, multi-exposure speckle contrast curves representing the total decorrelation would always show faster decorrelation than the flow-only decorrelation curve. To test this, we designed a phantom set-up where a nylon thread with a roughened surface was pulled through a tube embedded in a dynamic medium (titanium dioxide in 30% glycerol), and in a static medium (titanium dioxide in silicone) as used in Chapters 3 and 4. Preliminary results are shown in Fig. 8.1a. The multi-exposure *K*-curve for 'flow' in the static medium can be regarded as due to flow only (as the medium is static) and the multi-exposure *K*-curve for 'flow' in the dynamic medium can be regarded as the total decorrelation due to flow and offset decorrelation. The dynamic phantom shows that for the velocity of 10 mm/s ($\tau_{c,flow} < \tau_{c,offset}$) the total decorrelation is *not* faster than the decorrelation due to flow only (square data points), and Eq. 3.8 breaks down. Generally, we saw that for the dynamic phantom the multi-exposure curves for flow and offset regions were mutually influenced by each other's dynamics, which is caused by scattering of photons from the flow region into the offset region and vice versa. This means that at any position in the image the decorrelation is influenced by both 'offset' and 'total' (flow + offset) photons. Therefore, the autocorrelation functions describing both processes cannot be directly multiplied. A possible way to correct for this is to define a third population of photons contributing to the (fluctuating) electric field: $E(t) = E_{t,total}(t) + E_{t,offset}(t) + E_s(t)$. Subsequently the Siegert relation can be modified accordingly and the speckle equation can be derived similar as before (Chapter 2.3). The *K*-curves resulting from two dynamic populations (total and offset) with different τ_c's for flow and offset are plotted in fig. 8.1b (dark and light green lines), together with the *K*-curves resulting from one (flow) population (dark and light red lines), the τ_c's are chosen to reflect the situation in

Fig. 8.1a and the relative population of offset (and total) photons is set to 0.5. The calculated *K*-curves derived from multiple dynamic photon populations in Fig. 8.1b mimic the dynamic phantom experiment, supporting this approach. In practice, fitting the model presented in Fig. 8.1b is complicated because a large (and closely spaced) range of exposure times is required for a reliable fit. The dynamic phantom experiment exaggerates the biological situation by the highly scattering medium covering the tube (μ'_s = 1.7 mm^{-1}, as compared with the low scattering non-keratinized epithelium layer covering the sublingual microcirculation) giving rise to a large population of offset photons detected at the flow (vessel) region. A lower fraction of offset photons for sublingual vessel regions is expected due to the high scattering coefficient of blood and the transparent epithelium top layer. The excellent results of Chapters 3 and 4 based on Eq. 3.8 verify this. However, the presence of multiple populations of dynamic photons is worth exploring further especially when using LSCI through highly scattering layers such as skin. In the context of the presence of multiple populations of dynamic photons, in addition to the inaccuracies in estimating the number of scattering events within a blood vessel, it should be noted that the introduction of low-coherence gating can be advantageous here. Low-coherence interferometric set-ups allow path-length resolved speckle signals to be acquired [32a, b, c], providing better estimation of N and control over the pathlength distribution p(l). On the other hand, these setups do not encompass the simplicity that is inherent to the LSCI approach.

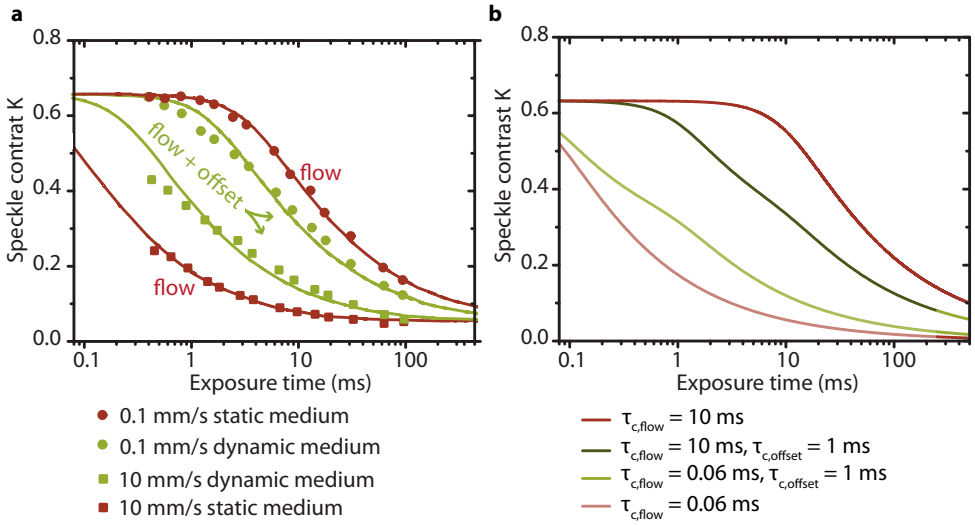

Fig. 8.1 | Dynamic medium flow phantom experiment *(unpublished results).* ***(a)*** *Multi-exposure K-curves and corresponding fit of Eq. 3.7 or 4.10 for a moving thread in static (red curves/data points) and dynamic (green curves/data points) medium* ***(b)*** *Multi-exposure K-curves according to Eq. 3.7/4.10 (β = 0.4, ρ = 1) for 2 different τ_c's (light red [$\tau_{c,flow}$ = 0.06 ms] and dark red [$\tau_{c,flow}$ = 10 ms]) and multi-exposure K-curves resulting from 2 populations of dynamic photons (50% offset, 50% total; light green [$\tau_{c,flow}$ = 0.06 ms, $\tau_{c,offset}$ = 1 ms], dark green [τ_c = 10 ms, $\tau_{c,offset}$ = 1 ms]).*

8.2.5 Conclusions on laser speckle flowmetry

Answering the question: is laser speckle flowmetry a quantitative tool? remains a controversial topic. Using SDF-LSCI as outlined in this thesis can be regarded as considerably quantitative and opportunities for enhancing the accuracy and sensitivity as outlined in Section 8.2.3 are promising. Two bottlenecks in quantitative laser speckle flowmetry, the quantification of α and influence of multiple scattering, have been addressed in this thesis. Both findings can be applied to conventional LSCI set-ups and LDF techniques

as well, thereby contributing to the quantitativeness of many flowmetry applications. The technological simplicity of LSCI set-ups, combined with the potential for automated and quantitative analysis of flow velocities, sensitivity to a large flow range and the ability to measure through scattering layers summarize the advantages of LSCI as clinical microcirculation imager.

8.3 UCNPs for the delivery of contrast enhancing agents to tumours

8.3.1 Key results on imaging Upconversion Nanoparticles in biological tissue

Chapters 5 through 7 show that upconversion nanoparticles (UCNPs) are a valuable addition to the collection of photoluminescent agents in biomedical imaging, where the usefulness greatly depends on the provided signal to background ratio (or contrast). The key optical properties of UCNPs enable autofluorescence-free imaging due to a nonlinear upconversion process at relatively low excitation intensities (close to biological safety limits) with long (sub-millisecond) lifetimes [33]. The remaining background signal consisting of detector noise and excitation light leaking through the filters can be minimized by time-gated detection and scientific grade cooled detectors, advancing towards signal shot noise limited imaging. In view of these optical and detection features, the UCNP imaging contrast is highly dependent on the conversion efficiency. Therefore, we started with designing an integrating sphere set-up to quantify the conversion efficiency versus the excitation intensity, as detailed in Chapter 6. The subsequent assessment of the imaging and detection throughput of the wide-field inverted epi-fluorescent microscope (used in Chapters 6 and 7) operating in continuous wave mode, enabled the quantitative modelling of UCNP-based microscopic imaging. With this system, single particle imaging and hyperspectral imaging confirmed that the ensemble and single UCNP had identical optical properties, which is important to link ensemble measurements [34-37] to discrete particle studies [38, 39]. The experimental detection of a single UCNP through 250 μm haemolysed blood and theoretical estimation of single particle detection in skin-depths up to 400 μm under optimized conditions (pulsed excitation allowing higher excitation intensity and time-gated detection) illustrate the high-sensitivity imaging that is achievable using UCNPs. The long lifetime of the UCNPs is utilized in the modelling in this thesis as an advantage for the complete suppression of excitation light by time-gating the detected signal. On the other hand, long emission lifetimes can be detrimental to the acquisition speeds of scanning confocal imaging systems. Though in the context of the wide-field imaging set-ups explored in this thesis this is not a limitation, it is important to keep in mind for the design of other imaging modalities. Due to the rapid reduction of contrast with imaging depth in tissue, caused by the scattering-induced excitation attenuation and nonlinear UCNP emission, the high-potential applications include UCNP-guided imaging at relatively superficial depths (< a few millimeter) such as *in vitro* thick slices, biological liquids or bioassays, or *in vivo* subsurface structures [40-42]. For these scenarios the detection of small amounts of UCNPs is feasible and opens up possibilities for the detection of a small amount of biomarkers [43, 44] or cells [45, 46], including *in vivo* cell tracking [47].

A promising application is the intraoperative use of UCNPs to guide the surgeon to areas suspect to contain tumour cells. To enhance the tumour-to-tissue contrast, specific labelling of tumour cells is helpful which was addressed in Chapter 7. The UCNPs were biofunctionalized with mini-antibodies that specifically targeted the human epidermal growth factor receptor (HeR2/neu) overexpressed by SK-BR-3 breast cancer cells, resulting in specific labelling of tumour cells in a 10:1 ratio to control cells *in vitro*. The

labelled breast cancer cells were covered with breast tissue simulating optical phantom layers that mimicked the optical scattering and absorption properties of breast tissue. The UCNP signal coming from the monolayer of breast cancer cells was detected through a maximum of 1.6 mm phantom thickness, which was a substantial imaging depth considering the low amount of the labelled cells (< 10 cells) in the image. Using the calibrated imaging and detection properties of the imaging system (such as spectral throughput, detector sensitivity) and UCNP optical signal quantification, the number of UCNPs per cell could be estimated and projected onto an *in vivo* scenario of imaging a small breast cancer lesion embedded in breast tissue. As detailed in Chapter 7, the estimated detection depth of the small lesion was up to 4 mm, which is superior compared to the detection depth estimated using Cy5 (an organic fluorescent NIR dye) as tumour labelling agent being ~2.5 mm [48]. The latter result was estimated from human melanoma bearing mice, and the study additionally revealed an improved long-term survival rate for mice subject to fluorescence guided tumour resection as compared with the control group operated under white light conditions. The improved contrast using upconversion-based photoluminescence would potentially improve the survival rate even further, since a detection depth of several millimetres is clinically relevant e.g. during tumour resections.

Besides the identification and experimental assessment of application niches of UCNPs, chapters 6 and 7 also presented the experimental validation of optical signal modelling in absorbing and scattering media based on Lambert-Beers law. The theoretical model presented in Chapter 6 showed excellent agreement with the experimental results of the phantom study in Chapter 7 (Fig. 7.7, *in vitro* signal data and model), changing only the different model parameters such as objective numerical aperture (NA), optical properties of the tissue (skin in Chapter 6 vs. breast tissue in Chapter 7), number of UCNPs (single in Chapter 6 vs. cluster of labelled cells in Chapter 7) and their optical properties (absorption cross-section and conversion efficiency). The Lambert-Beer model modified using the transport attenuation coefficient (instead of the usual absorption coefficient) was applied to calculate the reduction of excitation intensity with depth in tissue and the reduction of the signal intensity on the return path to the detector. This model implies that photons that have been absorbed or isotropically scattered are removed from the signal calculation, unlike previously reported models based on photon diffusion approximations [49]. Though the higher tissue scattering coefficient as compared with the absorption coefficient at the UCNP excitation and emission wavelengths validate the use of the diffusion approximation, the application of a diffusion-based model did not agree with our results. A possible explanation is the high-NA objective used for imaging, effectively rejecting out of focus (diffuse) photons in the set-up. By changing the model parameters as required, our UCNP tissue imaging model is instrumental for the quantitative assessment of potential UCNP-based imaging scenarios.

8.3.2. *In vivo* application of UCNPs

The evaluation of UCNP properties in the context of *in vivo* situations is crucial for the translation of UCNPs from the lab to clinical applications. An identified purpose in this thesis is the delivery of UCNPs through the leaky tumour vasculature for enhanced detection and/or tumour therapy. In view of this, a versatile model is the chick embryo chorioallantoic membrane (CAM), an extra-embryonic vascularised membrane responsible for the gas exchange of the developing chick embryo. The development of protocols describing *ex ovo* culturing of chick embryos by transferring the embryo into a sterile container,

enabled exposure of the CAM and easy access for intervention and imaging [50, 51]. Since the embryos are immune-deficient (up to embryonic development day 14) foreign cancer cells can be introduced without rejection. Grafting tumour cells on the CAM results in their adoption by the CAM and subsequent tumour-induced angiogenesis enables their growth into proliferating, vascularised tumours [52, 53]. The CAM-based tumour development and their microvascular environment can be studied in detail [54, 55]. The presence of nearly all relevant stroma factors e.g. immune cells (at a later stage), extracellular matrix components, blood and lymphatic vessels make the CAM model highly suited for studying tumour-stroma interactions, tumour metastasis, and therapy-induced changes in tumour development, implying the upcoming role of the CAM model in cancer research [56].

The characteristics of the CAM tumour model are useful to study the delivery of nanoparticles to tumours, as was shown by the delivery of macromolecules like fluorescent dextran [57] and virus-derived fluorescently labelled nanoparticles [58] to the CAM tumour sites through the leaky tumour vasculature. Following the *in vitro* results of Chapters 6 and 7, utilizing the CAM tumour model is an appropriate next step in the assessment of UCNPs for contrast-enhanced tumour detection. As elucidated in Chapter 5, UCNPs should not only exhibit advantageous optical properties but also excellent biochemical properties for effective *in vivo* application, including surface properties that offer a good dispersability in buffers and ensure biocompatible interaction with tissues. Biocompatible surface properties prevent or delay the uptake by the immune system thereby increasing the nanoparticle circulation times. In addition, the biocompatible surface provides functional groups for the binding of molecules (antibodies/ligands) with tumour-specific targeting properties. Long circulation times enhance the probability that the particles will end up in the tumour and facilitate enhanced tumour visibility or induce therapy. Feedback on the UCNP chick embryo circulation time is thus meaningful for UCNP design. Preliminary results on the quantification of UCNP circulation times in chick embryos are presented in Fig. 8.2. The UCNPs were synthesized in-house, coated with a silica shell and subsequently functionalized to produce three different groups: carboxyl (COOH, negatively charged), amine (NH_2, positively charged) and polyethylene-glycol (PEG, neutral) functionalized UCNPs. At several time points after injection of the UCNPs (50 µL of 0.5 mg/ml UCNP solution) a small amount of blood (5 µL) was drawn from the embryos and blood smears were prepared on glass slides as shown in Fig. 8.2c. For each slide the UCNP signal was quantified using the inverted microscope set-up described in Chapter 6. The results (based on 3 different chicks per functional groups) show a decreasing amount of UCNPs in the blood with increasing time, where the PEGylated particles circulate the longest and can still be found after 12 hours of circulating. The quantification of circulation time can tailor the future design of UCNPs with other functional surface groups (e.g. amphiphilic polymers) to optimize biochemistry protocols while maintaining long circulation times.

The next step is the development of vascularised tumours in the chick embryo model. Tumours can be grafted on the CAM by mildly scratching the membrane before placing tumour spheroids [59, 60], tumour cell soaked gelatine-sponges [61], tumour cells resuspended in Matrigel [62], or simply a drop of tumour cells on the affected region of the membrane [57]. We evaluated different tumour cell lines and tumour grafting methods, demonstrating successful tumour growth and vascularisation as shown in Fig. 8.3. In Fig. 8.4 our first published results are shown presenting targeted labelling of small tumours (MCF7 breast cancer cells) by UCNPs functionalized with tumour-specific antibodies [63].

The CAM tumour model represents an interesting method for further development of UCNP-based detection of small tumour lesions, with the proof-of-principle shown in Fig. 8.4. The long exposure time of 2 minutes in spite of the superficial location of the tumour indicates that improved detection of UCNP-labelled tumours is a necessity for practical application of UCNPs, for example for intraoperative diagnosis. On the one hand the UCNP signal could be enhanced by doping the UCNPs with Thulium ions instead of Erbium ions which have a large emission peak at 800 nm (see Figure 5.3), for which tissue attenuation is reduced. In addition, a 70-fold increase of conversion efficiency was shown for UCNPs with a high Tm-dopant concentration (8%) at high excitation intensity [64]. Further improvements include the increase of the absorption cross-section by utilizing 'antenna effects' from dyes, plasmons, quantum dots or other doping elements with a strong absorption to sensitize the UCNPs [42], or shifting the excitation wavelength to 800 nm by adding Nd^{3+} as a second sensitizer [65]. On the other hand the excitation and detection efficiency can be improved by using high power pulsed laser excitation and time-gated detection mechanisms.

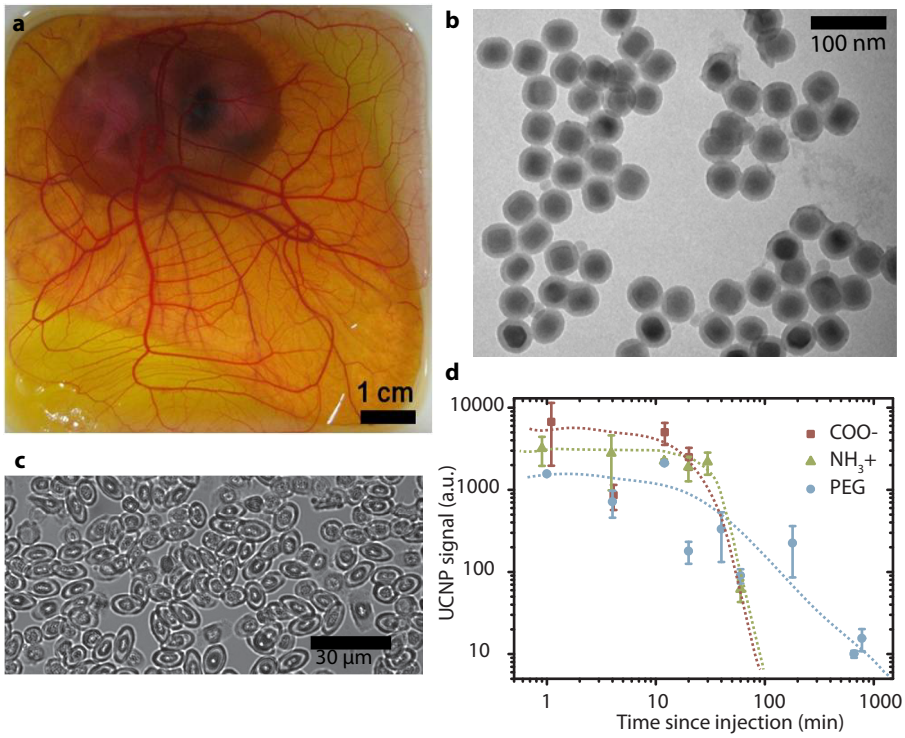

Fig. 8.2 | Chick embryo model for the assessment of UCNP circulation times *(unpublished results).* ***(a)*** *Ex ovo chick embryo at embryonic development day 8.* ***(b)*** *TEM images of UCNPs coated with silica shell before subsequent functionalization.* ***(c)*** *Bright field image of chick embryo blood smear on glass slide.* ***(d)*** *UCNP signal from blood smears sampled at different time points after injection, quantified using epiluminescence microscopy.*

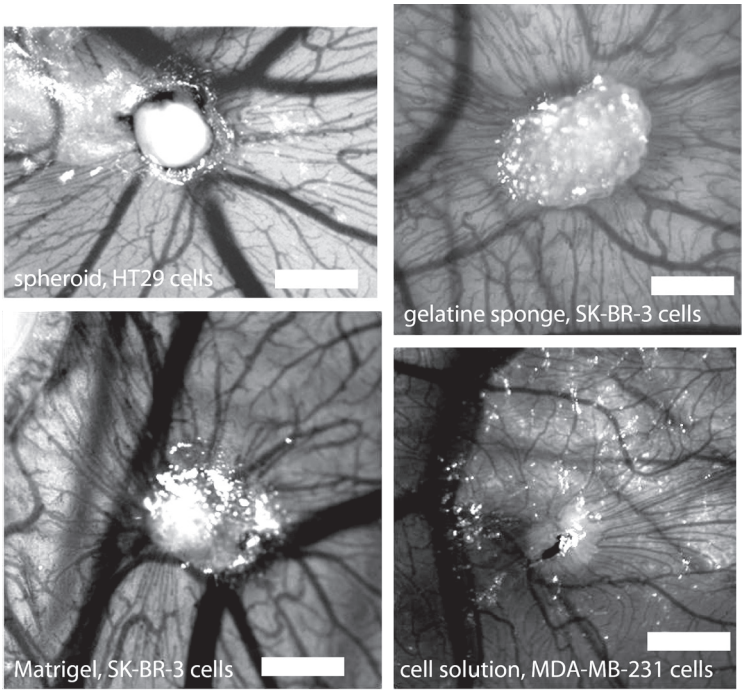

Fig. 8.3 | Chick embryo chorioallantoic membrane (CAM) with tumours. *Growth and vascularisation of tumours, 7 days after grafting of tumour cells on chick embryo CAM using spheroids, gelatine sponges, Matrigel or cell solutions containing HT29 (Human colorectal adenocarcinoma), SK-BR-3 or MDA-MB-231 (human breast cancers) cells. Scale bar represents 250 µm.*

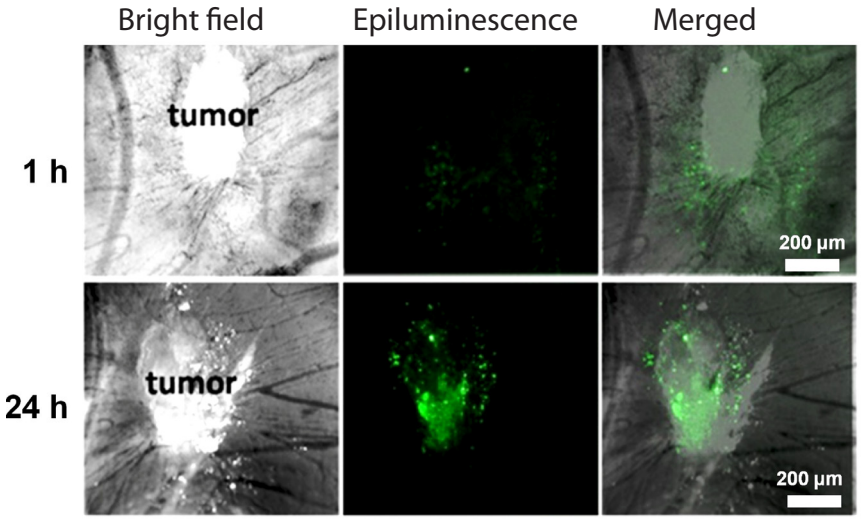

Fig. 8.4 | Targeted labelling of tumour spheroids grafted on the chick embryo CAM. *Antibody-labelled UCNPs were imaged at the tumour region at 1 h (top row) and 24h (bottom row) after injection. From left to right are bright field, epiluminescence (980 nm) and merged intravital microscope images at 4x magnification and 2 minutes exposure time. Adapted from ref. [63]*

8.3.3 Cytotoxicity and non-specific cellular uptake of UCNPs

The previous results demonstrate the potential for UCNP-guided detection of small tumour lesions during operations. A remaining challenge is to ensure the biosafety of UCNPs through preclinical testing of the *in vivo* UCNP biochemical stability, cytotoxicity and systemic toxicity. We assessed the cytotoxicity effects of differently coated UCNPs as well as bare UCNPs on normal human skin cells in a recently published paper [66]. After 24h of incubation of the cells with UCNPs the lowest cytotoxicity was observed for bare and poly-lactide coated UCNPs (see Fig. 8.5a). Using the inverted microscope set-up described in Chapter 6 the non-specific cellular uptake of the UCNPs could also be quantified as presented in Fig.

8.5b. This study shows that cytotoxicity and cellular internalization strongly depend on coating, though the UCNPs do not exhibit intrinsic toxicity. This indicates that ongoing research is needed to design functional UCNP-coatings with increased biocompatibility and reduced cytotoxicity.

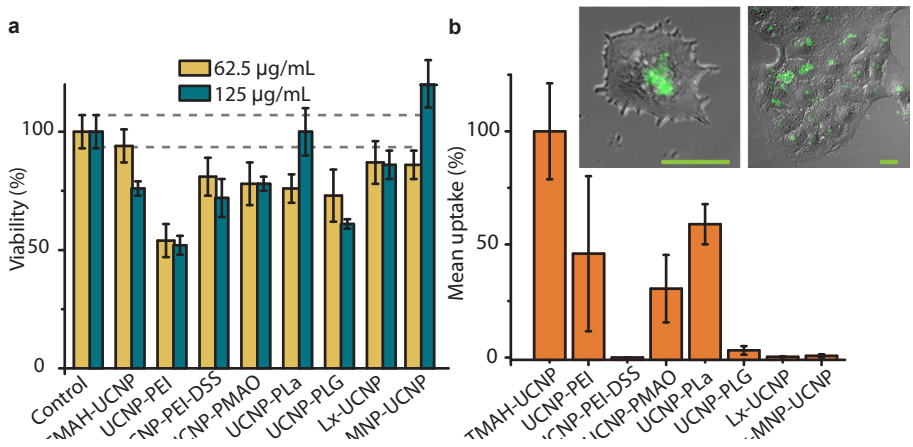

Fig. 8.5 | Viability and cellular uptake of UCNPs *in vitro.* ***(a)*** *Bar plot of the viability of human skin cells (keratinocytes) 24h co-cultured with differently coated UCNPs (concentrations 62 µg/mL yellow and 125 µg/mL green bars). Error bars are 95% confidence interval (CI) of the mean. Control sample viability was set to 100%; grey dashed lines represent the control group's 95% CI. TMAH-UCNP represent bare uncoated particles, and PEI, PEI-DSS, PMAO, PLA and PLG are amphiphilic polymer coatings detailed in Chapter 5.* ***(b)*** *Non-specific cellular uptake of bare and differently coated UCNPs by human skin cells (keratinocytes) after 24h co-culturing (concentration: 125 µg/mL), normalized for the bare UCNP uptake (100%). Inset: merged bright field and luminescence image of a single cell and a monolayer of cells exposed to bare TMAH-UCNPs. Scale bar, 20 µm. Adapted from ref [66].*

8.3.4 Conclusion on upconversion nanoparticles

The group of photoluminescent nanoparticles assessed in this thesis, nominated as upconversion nanoparticles, has considerable advantages for imaging applications in the biomedical context. Particularly the background-free imaging possibility allows imaging of small amounts of particles, expanding the possibilities for imaging of small lesions or minute amounts of biomarkers. Realization of high-sensitivity UCNP-aided imaging warrants further research in two key areas: improving the UCNP brightness and detection sensitivity; and improving the biocompatibility to enhance molecular contrast and provide meaningful sults for clinical applications.

8.4 REFERENCES

1. J. W. Goodman, *Speckle phenomena in optics: theory and applications* (Roberts and Company Publishers, Greenwood Village, CO, 2007).
2. A. Fercher and J. Briers, "Flow visualization by means of single-exposure speckle photography," Opt. Commun. **37**, 326-330 (1981).
3. D. D. Duncan and S. J. Kirkpatrick, "Can laser speckle flowmetry be made a quantitative tool?," JOSA A **25**, 2088-2094 (2008).
4. A. B. Parthasarathy, S. Kazmi, and A. K. Dunn, "Quantitative imaging of ischemic stroke through thinned skull in mice with Multi Exposure Speckle Imaging," Biomedical optics express **1**, 246-259 (2010).
5. J. C. Ramirez-San-Juan, R. Ramos-García, I. Guizar-Iturbide, G. Martínez-Niconoff, and B. Choi, "Impact of velocity distribution assumption on simplified laser speckle imaging equation," Opt. Express **16**, 3197-3203 (2008).
6. D. A. Boas and A. K. Dunn, "Laser speckle contrast imaging in biomedical optics," J. Biomed. Opt. **15**, 011109-011109-011112 (2010).
7. A. B. Parthasarathy, W. J. Tom, A. Gopal, X. Zhang, and A. K. Dunn, "Robust flow measurement with multi-exposure speckle imaging," Opt. Express **16**, 1975-1989 (2008).
8. L. M. Richards, S. Kazmi, J. L. Davis, K. E. Olin, and A. K. Dunn, "Low-cost laser speckle contrast imaging of blood flow using a webcam," Biomedical optics express **4**, 2269-2283 (2013).
9. K. R. Forrester, J. Tulip, C. Leonard, C. Stewart, and R. C. Bray, "A laser speckle imaging technique for measuring tissue perfusion," Biomedical Engineering, IEEE Transactions on **51**, 2074-2084 (2004).
10. D. Bicout and G. Maret, "Multiple light scattering in Taylor-Couette flow," Physica A: Statistical Mechanics and its Applications **210**, 87-112 (1994).
11. D. Durian, "Accuracy of diffusing-wave spectroscopy theories," Physical Review E **51**, 3350 (1995).

12. N. Bosschaart, G. J. Edelman, M. C. Aalders, T. G. van Leeuwen, and D. J. Faber, "A literature review and novel theoretical approach on the optical properties of whole blood," Lasers in medical science **29**, 453-479 (2014).
13. J. K. Percus and G. J. Yevick, "Analysis of classical statistical mechanics by means of collective coordinates," Physical Review **110**, 1 (1958).
14. M. Wertheim, "Exact solution of the Percus-Yevick integral equation for hard spheres," Physical Review Letters **10**, 321-323 (1963).
15. H. C. Hulst, *Light scattering by small particles* (Courier Dover Publications, 1957).
16. F. F. M. de Mul, " Monte-Carlo simulation of Light transport in Turbid Media," in *Handbook of Coherent Domain Optical Methods, Biomedical Diagnostics, Environment and Material Science*, V. V. Tuchin, ed. (Kluwer Publishers, 2004), pp. 465-533.
17. F. F. M. de Mul, M. H. Koelink, M. L. Kok, P. J. Harmsma, J. Greve, R. Graaff, and J. G. Aarnoudse, "Laser Doppler velocimetry and Monte Carlo simulations on models for blood perfusion in tissue," Applied optics **34**, 6595-6611 (1995).
18. B. Fagrell and M. Intaglietta, "Microcirculation: its significance in clinical and molecular medicine," J. Intern. Med. **241**, 349-362 (1997).
19. A. Rege, K. Murari, A. Seifert, A. P. Pathak, and N. V. Thakor, "Multiexposure laser speckle contrast imaging of the angiogenic microenvironment," Journal of biomedical optics **16**, 056006-056006-056010 (2011).
20. R. Bezemer, E. Klijn, M. Khalilzada, A. Lima, M. Heger, J. van Bommel, and C. Ince, "Validation of near-infrared laser speckle imaging for assessing microvascular (re) perfusion," Microvascular Research **79**, 139-143 (2010).
21. A. B. Parthasarathy, E. L. Weber, L. M. Richards, D. J. Fox, and A. K. Dunn, "Laser speckle contrast imaging of cerebral blood flow in humans during neurosurgery: a pilot clinical study," J. Biomed. Opt. **15**, 066030-066030-066038 (2010).
22. S. M. S. Kazmi, A. B. Parthasarthy, N. E. Song, T. A. Jones, and A. K. Dunn, "Chronic imaging of cortical blood flow using Multi-Exposure Speckle Imaging," Journal of Cerebral Blood Flow & Metabolism **33**, 798-808 (2013).
23. A. K. Dunn, H. Bolay, M. A. Moskowitz, and D. A. Boas, "Dynamic imaging of cerebral blood flow using laser speckle," J. Cereb. Blood Flow Metab. **21**, 195-201 (2001).
24. W. K. Stadelmann, A. G. Digenis, and G. R. Tobin, "Physiology and healing dynamics of chronic cutaneous wounds," The American Journal of Surgery **176**, 26S-38S (1998).
25. C. Stewart, R. Frank, K. Forrester, J. Tulip, R. Lindsay, and R. Bray, "A comparison of two laser-based methods for determination of burn scar perfusion: laser Doppler versus laser speckle imaging," Burns **31**, 744-752 (2005).
26. L. B. Hiltebrand, V. Krejci, A. Banic, D. Erni, A. M. Wheatley, and G. H. Sigurdsson, "Dynamic study of the distribution of microcirculatory blood flow in multiple splanchnic organs in septic shock," Crit. Care Med. **28**, 3233-3241 (2000).
27. Y. Ma, A. Koo, H. Kwan, and K. Cheng, "On-line measurement of the dynamic velocity of erythrocytes in the cerebral microvessels in the rat," Microvasc. Res. **8**, 1-13 (1974).
28. Y. Itoh and N. Suzuki, "Control of brain capillary blood flow," J. Cereb. Blood Flow Metab. **32**, 1167-1176 (2012).
29. M. J. Stark, V. L. Clifton, and I. M. Wright, "Microvascular flow, clinical illness severity and cardiovascular function in the preterm infant," Archives of Disease in Childhood-Fetal and Neonatal Edition **93**, F271-F274 (2008).
30. M. J. Stark, V. L. Clifton, and I. M. Wright, "Sex-specific differences in peripheral microvascular blood flow in preterm infants," Pediatr. Res. **63**, 415-419 (2008).
31. D. De Backer, S. Hollenberg, C. Boerma, P. Goedhart, G. Büchele, G. Ospina-Tascon, I. Dobbe, and C. Ince, "How to evaluate the microcirculation: report of a round table conference," Crit. Care **11**, R101 (2007).
32. C. Ince, "The microcirculation is the motor of sepsis," Critical Care **9**, S13 (2005).
32a. A. Wax, C. Yang, R. R. Dasari, and M. S. Feld, "Path-length-resolved dynamic light scattering: modeling the transition from single to diffusive scattering," Applied optics 40, 4222-4227 (2001).
32b. J. Kalkman, R. Sprik, and T. van Leeuwen, "Path-length-resolved diffusive particle dynamics in spectral-domain optical coherence tomography," Physical Review Letters 105, 198302 (2010).
32c. K. K. Bizheva, A. M. Siegel, and D. A. Boas, "Path-length-resolved dynamic light scattering in highly scattering random media: The transition to diffusing wave spectroscopy," Physical Review E 58, 7664 (1998).
33. Z. Song, Y. G. Anissimov, J. Zhao, A. V. Nechaev, A. Nadort, D. Jin, T. W. Prow, M. S. Roberts, and A. V. Zvyagin, "Background free imaging of upconversion nanoparticle distribution in human skin," Journal of biomedical optics **18**, 061215-061215 (2013).
34. J.-C. Boyer and F. C. Van Veggel, "Absolute quantum yield measurements of colloidal NaYF 4: Er3+, Yb3+ upconverting nanoparticles," Nanoscale **2**, 1417-1419 (2010).
35. R. H. Page, K. I. Schaffers, P. A. Waide, J. B. Tassano, S. A. Payne, W. F. Krupke, and W. K. Bischel, "Upconversion-pumped luminescence efficiency of rare-earth-doped hosts sensitized with trivalent ytterbium," JOSA B **15**, 996-1008 (1998).
36. M. Pokhrel and D. K. Sardar, "High upconversion quantum yield at low pump threshold in Er< sup> 3+</sup>/Yb< sup> 3+</sup> doped La< sub> 2</sub> O< sub> 2</sub> S phosphor," Mater. Lett. **99**, 86-89 (2013).
37. F. Wang, R. Deng, J. Wang, Q. Wang, Y. Han, H. Zhu, X. Chen, and X. Liu, "Tuning upconversion through energy migration in core–shell nanoparticles," Nat. Mater. **10**, 968-973 (2011).
38. S. Wu, G. Han, D. J. Milliron, S. Aloni, V. Altoe, D. V. Talapin, B. E. Cohen, and P. J. Schuck, "Non-blinking and photostable upconverted luminescence from single lanthanide-doped nanocrystals," Proceedings of the National Academy of Sciences **106**, 10917-10921 (2009).
39. S. Schietinger, L. d. S. Menezes, B. r. Lauritzen, and O. Benson, "Observation of size dependence in multicolor upconversion in single Yb3+, Er3+ codoped NaYF4 nanocrystals," Nano Lett. **9**, 2477-2481 (2009).
40. Y. Lu, J. Zhao, R. Zhang, Y. Liu, D. Liu, E. M. Goldys, X. Yang, P. Xi, A. Sunna, and J. Lu, "Tunable lifetime multiplexing using luminescent nanocrystals," Nat. Photonics (2013).
41. L. Xiong, Z. Chen, Q. Tian, T. Cao, C. Xu, and F. Li, "High contrast upconversion luminescence targeted imaging *in vivo* using peptide-labeled nanophosphors," Anal. Chem. **81**, 8687-8694 (2009).
42. G. Chen, H. Qiu, P. N. Prasad, and X. Chen, "Upconversion Nanoparticles: Design, Nanochemistry, and Applications in Theranostics," Chem. Rev. (2014).
43. Z. Chen, H. Chen, H. Hu, M. Yu, F. Li, Q. Zhang, Z. Zhou, T. Yi, and C. Huang, "Versatile synthesis strategy for carboxylic acid-functionalized upconverting nanophosphors as biological labels," J. Am. Chem. Soc. **130**, 3023-3029 (2008).
44. Y. Wang, P. Shen, C. Li, Y. Wang, and Z. Liu, "Upconversion fluorescence resonance energy transfer based biosensor for ultrasensitive detection of matrix metalloproteinase-2 in blood," Anal. Chem. **84**, 1466-1473 (2012).
45. Q. Liu, Y. Sun, T. Yang, W. Feng, C. Li, and F. Li, "Sub-10 nm Hexagonal Lanthanide-Doped $NaLuF_4$ Upconversion Nanocrystals for Sensitive Bioimaging *in vivo*," J. Am.

Chem. Soc. **133**, 17122-17125 (2011).
46. M. Wang, C. Mi, Y. Zhang, J. Liu, F. Li, C. Mao, and S. Xu, "NIR-responsive silica-coated NaYbF4: Er/Tm/Ho upconversion fluorescent nanoparticles with tunable emission colors and their applications in immunolabeling and fluorescent imaging of cancer cells," The Journal of Physical Chemistry C **113**, 19021-19027 (2009).
47. N. M. Idris, Z. Li, L. Ye, E. K. Wei Sim, R. Mahendran, P. C.-L. Ho, and Y. Zhang, "Tracking transplanted cells in live animal using upconversion fluorescent nanoparticles," Biomaterials **30**, 5104-5113 (2009).
48. Q. T. Nguyen, E. S. Olson, T. A. Aguilera, T. Jiang, M. Scadeng, L. G. Ellies, and R. Y. Tsien, "Surgery with molecular fluorescence imaging using activatable cell-penetrating peptides decreases residual cancer and improves survival," Proceedings of the National Academy of Sciences **107**, 4317-4322 (2010).
49. C. Vinegoni, D. Razansky, S. A. Hilderbrand, F. Shao, V. Ntziachristos, and R. Weissleder, "Transillumination fluorescence imaging in mice using biocompatible upconverting nanoparticles," Opt. Lett. **34**, 2566-2568 (2009).
50. D. S. Dohle, S. D. Pasa, S. Gustmann, M. Laub, J. H. Wissler, H. P. Jennissen, and N. Dünker, "Chick ex ovo culture and ex ovo CAM assay: how it really works," Journal of visualized experiments: JoVE (2009).
51. H. C. Yalcin, A. Shekhar, A. A. Rane, and J. T. Butcher, "An ex-ovo chicken embryo culture system suitable for imaging and microsurgery applications," Journal of visualized experiments: JoVE (2010).
52. H. Sun, J. Jia, X. Wang, B. Ma, L. Di, G. Song, and J. Ren, "CD44+/CD24– breast cancer cells isolated from MCF-7 cultures exhibit enhanced angiogenic properties," Clin. Transl. Oncol. **15**, 46-54 (2013).
53. D. Ribatti, B. Nico, A. Vacca, L. Roncali, P. H. Burri, and V. Djonov, "Chorioallantoic membrane capillary bed: A useful target for studying angiogenesis and anti-angiogenesis *in vivo*," The Anatomical Record **264**, 317-324 (2001).
54. E. I. Deryugina and J. P. Quigley, "Chick embryo chorioallantoic membrane model systems to study and visualize human tumor cell metastasis," Histochem. Cell Biol. **130**, 1119-1130 (2008).
55. A. Zijlstra, J. Lewis, B. DeGryse, H. Stuhlmann, and J. P. Quigley, "The inhibition of tumor cell intravasation and subsequent metastasis via regulation of *in vivo* tumor cell motility by the tetraspanin CD151," Cancer Cell **13**, 221-234 (2008).
56. M. Klingenberg, J. Becker, S. Eberth, D. Kube, and J. Wilting, "The chick chorioallantoic membrane as an *in vivo* xenograft model for Burkitt lymphoma," BMC Cancer **14**, 339 (2014).
57. D. B. Pink, W. Schulte, M. H. Parseghian, A. Zijlstra, and J. D. Lewis, "Real-time visualization and quantitation of vascular permeability *in vivo*: implications for drug delivery," PloS one **7**, e33760 (2012).
58. C. Choi-Fong, A. Amber, L. Hon-Sing, Z. Andries, and L. John, "Evaluation of nanoparticle uptake in tumors in real time using intravital imaging," Journal of Visualized Experiments (2011).
59. J. Friedrich, C. Seidel, R. Ebner, and L. A. Kunz-Schughart, "Spheroid-based drug screen: considerations and practical approach," Nature protocols **4**, 309-324 (2009).
60. N. De Magalhaes, L.-H. L. Liaw, and M. Berns, "An instruction on the *in vivo* shell-less chorioallantoic membrane 3-dimensional tumor spheroid model," Cytotechnology **62**, 279-283 (2010).
61. D. Ribatti, B. Nico, A. Vacca, and M. Presta, "The gelatin sponge–chorioallantoic membrane assay," Nature protocols **1**, 85-91 (2006).
62. N. A. Lokman, A. S. Elder, C. Ricciardelli, and M. K. Oehler, "Chick chorioallantoic membrane (CAM) assay as an *in vivo* model to study the effect of newly identified molecules on ovarian cancer invasion and metastasis," International journal of molecular sciences **13**, 9959-9970 (2012).
63. K. Liu, J. A. Holz, Y. Ding, X. Liu, Y. Zhang, T. Langping, X. Kong, B. Priem, A. Nadort, S. A. G. Lambrechts, M. C. G. Aalders, W. J. Buma, P. D. Y. Liu, and H. Zhang, "Targeted labeling of early-stage tumor spheroid in chorioallantoic membrane model with upconversion nanoparticles," Nanoscale (2014).
64. J. Zhao, D. Jin, E. P. Schartner, Y. Lu, Y. Liu, A. V. Zvyagin, L. Zhang, J. M. Dawes, P. Xi, and J. A. Piper, "Single-nanocrystal sensitivity achieved by enhanced upconversion luminescence," Nat. Nanotechnol. **8**, 729-734 (2013).
65. J. Shen, G. Chen, A. M. Vu, W. Fan, O. S. Bilsel, C. C. Chang, and G. Han, "Engineering the Upconversion Nanoparticle Excitation Wavelength: Cascade Sensitization of Tri-doped Upconversion Colloidal Nanoparticles at 800 nm," Advanced Optical Materials **1**, 644-650 (2013).
66. A. E. Guller, A. N. Generalova, E. V. Petersen, A. V. Nechaev, I. A. Trusova, N. N. Landyshev, A. Nadort, E. A. Grebenik, S. M. Deyev, A. B. Shekhter, and A. V. Zvyagin, "Cytotoxicity and non-specific cellular uptake of bare and surface-modified upconversion nanoparticles in human skin cells," Nano Research (2014).

9

Outlook

9

Abstract This last chapter reflects shortly on the thesis aims and presented results. The chapter continues with an outlook on the combination of the discussed optical techniques in the context of tumour detection, therapy and monitoring of tumour development.

9.1 INTRODUCTION

The role of the microcirculation in the development of a range of diseases dictates the need for good clinical techniques to assess its functionality. Inadequate tissue perfusion by the microcirculation is often an early indicator of more severe pathologies, for example in diabetes and critical diseases [1-3]. On the other hand, an impaired microcirculation functionality can result from an array of cellular processes and its assessment often lacks specificity or sensitivity for pathological processes. Photoluminescence-assisted imaging can enable enhanced molecular contrast in biological tissues, biological liquids or bioassays [4-6]. The quantification of blood flow and photoluminescent signals in the biomedical context can contribute to clinical information relevant to a wide range of potential clinical applications. Since the acquirement of reliable results is of key importance for the advancement of clinical research, considerable effort has been devoted to improving the quantitative evaluation of optical techniques (all first-authored publications in this thesis start with the word 'quantitative'!). This thesis aimed to give a realistic expectation of the abilities of quantitative flowmetry and photoluminescence-based imaging in tissue by experimental and theoretical modelling of light-tissue interactions. Practical guidelines towards quantitative laser speckle flowmetry are presented together with a detailed theoretical background that elucidates the essential aspects for quantification. Experimental optical characterization of the upconversion nanoparticle (UCNP) photoluminescent properties and modelling of this signal in the biomedical context enables assessment of their detectability in clinically relevant scenarios. The quantification of microcirculatory blood flow and the quantification of the upconversion signal in biological tissues both have their individual clinical application niches. In this last section, I will reflect on their powerful combination for the diagnosis and therapy of tumours, and particularly the monitoring and understanding of tumour development.

9.2 QUANTIFYING BLOOD FLOW AND PHOTOLUMINESCENCE SIGNAL IN TUMOUR TISSUE

Angiogenesis is a hallmark of cancer and facilitates accelerated and uncontrollable tumour growth [7, 8]. Enhanced perfusion as well as enhanced permeability and retention of nanoparticles are complementing indicators for the presence of tumours, which can be measured by the two techniques discussed in this thesis. The complex tumour physiology and structural heterogeneity can be assessed by combining information from blood flow mapping and localizing accumulations of UCNPs. An important property of tumours closely related to angiogenesis, is tumour hypoxia [9, 10]. Tumour hypoxia is associated with resistance to chemo- [11] and radiation therapy [12], and selection for the most resilient tumour cells [13]. Hypoxia stimulates tumour angiogenesis which subsequently relieves the hypoxic region and facilitates prolific growth. As the tumour grows the cells become further separated from the vasculature which induces another state of hypoxia where the tumour is dormant until angiogenesis resumes. Hypoxia is a clinically relevant parameter as it reduces the effects or chemo- and radiotherapy; prevents drug delivery to non-vascularised hypoxic regions and influences cell-cycle specific chemotherapies [14]. The study of hypoxia as a predecessor to angiogenesis provides additional relevant information on tumour heterogeneity and periodicity. UCNPs have been engineered as oxygen sensing complexes [15, 16] and microcirculatory imaging can indicate regions of low perfusion. A detailed reconstruction of physiological processes like hypoxia and angiogenesis will aid in understanding tumour-specific behaviour, and give insight into cellular processes.

The combination of tumour diagnostics and therapy, theranostics, is exemplified by UCNP-mediated photodynamic therapy (PDT). In PDT, cancer cells are destroyed through the generation of cytotoxic singlet oxygen by molecules that act as photosensitizers when excited by optical irradiation. By selecting photosensitizers that absorb in the emission bands of UCNPs, powerful complexes can be generated by loading UCNPs with many photosensitizers. Exciting the UCNP-PDT complexes by 980 nm light results in the generation of singlet oxygen and detectable emission via the green and red UCNP emission bands respectively [17]. Tumour drug delivery of UCNP-PDT nanocomplexes provides novel mechanisms for therapy and diagnostics [18]. The presence of the drug can be confirmed by detection of UCNPs in the tumour, while the effect of therapy on the tumour vasculature post-treatment (assessed by laser speckle flowmetry) is instrumental to evaluate the impact of therapy.

A recognized problem for the delivery of drugs to tumours is the elevated interstitial pressure in the tumour core [19], which dramatically hampers perfusion rates of the core tumour vessels. The perfusion rate and extravasation of nanoparticles are possibly interrelated which can be assessed by the combination of flowmetry and quantification of nanoparticle delivery. In addition, some tumour therapies are aimed at inhibiting uncontrolled angiogenesis in order to normalise the tumour vessels, resulting in a reduced interstitial pressure and an increased delivery of drugs [20]. The combination of both techniques is extremely helpful in monitoring the intended effects of these experimental therapies.

Both techniques described in this thesis have the ability to be performed in microscopic or endoscopic instruments, with feasible modifications to existing lay-outs. Endoscopes can be modified to provide specific illumination properties necessary for the optical techniques described in this thesis, while having the capability to be inserted into the body through existing orifices or key-hole surgery. In most cases, tumours develop inside the body and not on the surface; therefore the adoption of laser speckle flowmetry or upconversion luminescence imaging in endoscopes increases the applicability of both techniques to clinical medicine.

In this last chapter I have described potential collaborations between quantitative perfusion and photoluminescence imaging. The combined application of both techniques can intensify the information on the complex interaction of tumour cellular processes, tumour growth, metastasis and tumour response to therapy.

9.3 REFERENCES

1. C. A. Den Uil, E. Klijn, W. K. Lagrand, J. J. Brugts, C. Ince, P. E. Spronk, and M. L. Simoons, "The microcirculation in health and critical disease," Progress in cardiovascular diseases **51**, 161-170 (2008).
2. B. Fagrell and M. Intaglietta, "Microcirculation: its significance in clinical and molecular medicine," Journal of internal medicine **241**, 349-362 (1997).
3. W. D. Strain, D. D. Adingupu, and A. C. Shore, "Microcirculation on a large scale: techniques, tactics and relevance of studying the microcirculation in larger population samples," Microcirculation **19**, 37-46 (2011).
4. R. Weissleder, "A clearer vision for *in vivo* imaging," Nature biotechnology **19**, 316-316 (2001).
5. G. Chen, H. Qiu, P. N. Prasad, and X. Chen, "Upconversion Nanoparticles: Design, Nanochemistry, and Applications in Theranostics," Chemical reviews (2014).
6. J. V. Frangioni, "*In vivo* near-infrared fluorescence imaging," Current opinion in chemical biology **7**, 626-634 (2003).
7. P. Carmeliet and R. K. Jain, "Angiogenesis in cancer and other diseases," nature **407**, 249-257 (2000).
8. J. Folkman, "Angiogenesis in cancer, vascular, rheumatoid and other disease," Nature medicine **1**, 27-30 (1995).
9. M. Höckel and P. Vaupel, "Tumor hypoxia: definitions and current clinical, biologic, and molecular aspects," Journal of the National Cancer Institute **93**, 266-276 (2001).
10. A. Facciabene, X. Peng, I. S. Hagemann, K. Balint, A. Barchetti, L.-P. Wang, P. A. Gimotty, C. B. Gilks, P. Lal, and L. Zhang, "Tumour hypoxia promotes tolerance and angiogenesis via CCL28 and Treg cells," nature **475**, 226-230 (2011).
11. L. I. Cárdenas-Navia, T. W. Secomb, and M. W. Dewhirst, "Effects of fluctuating oxygenation on tirapazamine efficacy: theoretical predictions," International Journal of Radiation Oncology* Biology* Physics **67**, 581-586 (2007).
12. L. B. Harrison, M. Chadha, R. J. Hill, K. Hu, and D. Shasha, "Impact of tumor hypoxia and anemia on radiation therapy outcomes," The Oncologist **7**, 492-508 (2002).
13. R. Welsh, F. Jensen, N. Cooper, M. Oldstone, B. Banapour, J. Sernatiriger, J. Levy, H. Hoshino, H. Tanaka, and M. Miwa, "Hypoxia-mediated selection of cells with diminished apoptotic potential in solid tumours," nature **379**, 4 (1996).
14. M. A. Shah and G. K. Schwartz, "Cell Cycle-mediated drug resistance an emerging concept in cancer therapy," Clinical Cancer Research **7**, 2168-2181 (2001).
15. L. Liu, B. Li, R. Qin, H. Zhao, X. Ren, and Z. Su, "Synthesis and characterization of new bifunctional nanocomposites possessing upconversion and oxygen-sensing properties," Nanotechnology **21**, 285701 (2010).
16. D. E. Achatz, R. J. Meier, L. H. Fischer, and O. S. Wolfbeis, "Luminescent sensing of oxygen using a quenchable probe and upconverting nanoparticles," Angewandte Chemie International Edition **50**, 260-263 (2011).
17. K. Liu, X. Liu, Q. Zeng, Y. Zhang, L. Tu, T. Liu, X. Kong, Y. Wang, F. Cao, and S. A. Lambrechts, "Covalently assembled NIR nanoplatform for simultaneous fluorescence imaging and photodynamic therapy of cancer cells," Acs Nano **6**, 4054-4062 (2012).
18. N. M. Idris, M. K. Gnanasammandhan, J. Zhang, P. C. Ho, R. Mahendran, and Y. Zhang, "*In vivo* photodynamic therapy using upconversion nanoparticles as remote-controlled nanotransducers," Nature medicine **18**, 1580-1585 (2012).
19. C.-H. Heldin, K. Rubin, K. Pietras, and A. Östman, "High interstitial fluid pressure—an obstacle in cancer therapy," Nature Reviews Cancer **4**, 806-813 (2004).
20. U. Prabhakar, H. Maeda, R. K. Jain, E. M. Sevick-Muraca, W. Zamboni, O. C. Farokhzad, S. T. Barry, A. Gabizon, P. Grodzinski, and D. C. Blakey, "Challenges and key considerations of the enhanced permeability and retention effect for nanomedicine drug delivery in oncology," Cancer research **73**, 2412-2417 (2013).

A

Appendices

A

List of Abbreviations

Ab	antibody
ACF	autocorrelation function
Ag	antigen
AOTF	acousto-optic tuneable filter
Bn	barnase
Bs	barstar
CAM	chorioallantoic membrane
CCD	charge coupled device
CEA	anti-carcinoembryonic antigen
CI	confidence interval
CMOS	complementary metal-oxide semiconductor
CV	coefficient of variation
DLS	dynamic light scattering
DWS	diffusing wave spectroscopy
EMCCD	electron multiplying charge couplde device
EPR	enhanced permeability and retention
FAD	flavin adenine dinucleotide
FL	fluorescein
FTIR	Fourier transform infrared
FWHM	full width at half maximum
GRR	green-to-red-ratio
Hb	haemoglobin
Hct	Haematocrit
He/Ne	Helium/Neon
ICU	intensive care unit
LASCA	laser speckle contrast analysis
sLASCA	spatial laser speckle contrast analysis
tLASCA	temporal laser speckle contrast analysis
LDF	laser Doppler flowmetry
LED	light emitting diode
LSCI	laser speckle contrast imaging
LSI	laser speckle imaging
M	Mie
MESI	multi exposure speckle imaging
MPE	maximum permissable exposure
NA	numerical aperture
NIR	near infrared
OCT	optical coherence tomography
OD	optical density
OPS	orthogonal polarization spectroscopy
PBS	phosphate buffered saline
PCF	pair correlation function
PD	photodiode
PDF	probability density function
PEG	poly-ethylene glycol
PMAO	poly(maleic anhydride-alt-1-octadecene)
POF	plastic optical fibers
PSD	power spectral density
PY	Percus-Yevick
QD	quantum dot
QE	quantum efficiency
QLS	quasi-elastic light scattering
QY	quantum yield
RBC	red blood cell
RNA	ribonucleic acid
S/B	signal/background
SDF	sidestream dark field
SI	supplementary information
SNR	signal-to-noise ratio
SVS	speckle visibility spectroscopy
TEM	transmission electron microscopy
TIO_2	titanium dioxide
UCNP	upconversion nanoparticle
UV	ultraviolet
VIS	visible

A

List of Symbols

Laser speckle flowmetry

$A(N)$	model-based scaling factor for N	$p(n)$	probability distribution for n
c_1	probability constant	$p(\boldsymbol{q})$	scattering phase function
C_{noise}	noise in detected intensity	$p(V)$	velocity probability distribution
C_t	autocovariance of temporal speckle intensity	$p(\eta_{micr})$	microscopic particle distribution
d	diameter (channel/vessel)	$\boldsymbol{q}$	scattering vector
D	scatterer diameter	r	distance between particles in volume
D_b	Brownian motion diffuscion coefficient	R^2	coefficient of determination
E	electric field	R_{adj}^2	adjusted R^2
E^*	complex conjugate of electric field	r_s	speckle size image plane
E_f	fluctuating component electric field	$S(\boldsymbol{q})$	structure factor
E_s	static component electric field	T	camera exposure time
F	vessel/path length factor	t	time
f_v	volume fraction	V	flow velocity
g_1	normalized electric field ACF	$\langle V^2 \rangle$	second moment of velocity distribution
g_2	normalized intensity ACF	V_0	average flow velocity
I	detected intensity	V_p	volume of particle
$\langle I \rangle$	mean detected intensity	α	proportionality constant
I_f	fluctuating component of detected intensity	β_M	measurement-geometry specific constant
I_s	static component detected intensity	Δr	displacement
K	speckle contrast	η	(global) particle number density
K_{max}	maximum attainable speckle contrast	θ	angle
k	wave number	λ	wavelength
l	path length	ρ	fraction dynamically scattered light
M	shape parameter	σ_k	standard deviation in K
M_{opt}	optical magnification	σ_i	standard deviation in I
N	average number dynamic scattering events	σ_n	standard deviation in n
n	number of dynamic scattering events	σ_s	standard deviation in spatial I
N_s	spatial pixels local region	τ	time constant
N_t	temporal pixels local region	τ_c	decorrelation time
		ω	measure of point spread function

Upconversion nanoparticles

$[Ab]$	antibody concentration	P_{abs}	absorbed power
$[Ag]$	antigen concentration	P_{em}	emitted power
Φ	fluorescence conversion efficiency	P_{ex}	excitation power
I_{ex}	excitation intensity	QE_{CCD}	quantum efficiency CCD
I_{sat}	saturation excitation intensity	S_{ccd}	CCD sensitivity
K_{aff}	affinity constant	S_{UCNP}	sensor UCNP-signal intensity
N_e-	number of electrons	T	exposure time
N_{ph}	photon emission rate	z	depth
N_{UCNP}	number of UCNPs	ζ_{total}	system spectral calibration coefficient
N_{YB}	number of Yb ions	η_{uc}	upconversion efficiency
N_{el}, N_{shot}, N_{dark}, N_{read}, N_{rest}	electronic noise level	λ_{ex}	excitation wavelength
σ_{abs}	abs. cross section luminophore	ξ_{optics}	throughput imaging optics

Other symbols

g	anisotropy factor	μ_s'	reduced scattering coefficient
μ_a	absorption coefficient	μ_s	scattering coefficient
n_{RBC}, n_{TIO2}, n_{SPHERE}, n_{plasma}, $n_{silicone}$	refractive index	μ_{tr}	transport attenuation coefficient
		σ_{sca}	scattering cross section

A

A

SAMENVATTING VAN HET PROEFSCHRIFT (SUMMARY IN DUTCH)

Optische technieken hebben een goed perspectief voor toepassing in de gezondheidszorg: ze kunnen niet-invasief zijn, licht is niet-ioniserend, de apparatuur is vaak goedkoop en compact, en optische interacties kunnen zowel structurele als fysiologische informatie over biologisch weefsel geven. De nadelen van optische technieken zijn de gelimiteerde diepte in weefsel tot waar het licht reikt en de verstrooiing door weefsel, waardoor het beeld onscherp wordt. Het deel van de circulatie waar de arteriën en arteriolen zijn vertakt tot capillairen en waar de zuurstof- en nutriëntuitwisseling met cellen in het lichaam plaatsvindt, ligt ten dele vlak onder het weefsel oppervlak. Met optische technieken kunnen we deze microcirculatie daarom in beeld brengen. Een niet goed functionerende microcirculatie kan schade aan weefsel veroorzaken en in het ergste geval leiden tot sterfte, bijvoorbeeld bij septische shock. Er zijn vele andere situaties waar een disfunctionerende microcirculatie het gevolg, de mediator of de aanleiding is van een klinische pathologie. Het monitoren van de microcirculatie kan helpen bij diagnostiek, feedback geven bij therapie, of inzicht geven in fysiologische processen. Een optische techniek die de functionaliteit van de microcirculatie betrouwbaar in beeld kan brengen heeft daarom veel klinische relevantie.

Sidestream dark field (SDF) microscopie is een videomicroscoop-techniek die de microcirculatie onder de tong direct in beeld kan brengen, volgens het principe dat groen licht sterker wordt geabsorbeerd door bloed dan door omliggend weefsel. Uit de beelden waarin de rode bloedcellen als donkere bolletjes door lichtgrijs weefsel bewegen kan de vatdichtheid, de vatgeometrie en de bloedstroomsnelheid van de langzaam stromende capilairen (< 2 mm/s) bepaald worden. In **Hoofdstuk 2** wordt een andere groep van technieken geïntroduceerd die de beweging van rode bloedcellen op basis van een ander principe in beeld brengt: dynamische lichtverstrooiingstechnieken. Coherent laser licht (dezelfde golflengte en fase) dat terug verstrooid wordt uit weefsel heeft een groot aantal verschillende paden door het weefsel afgelegd, waardoor het met een groot aantal verschillende fasen aankomt op de detector en een gerandomiseerd interferentiepatroon ('speckles') veroorzaakt. Als er beweging plaatsvindt in dit weefsel (bijvoorbeeld bloedstroming) zal het interferentiepatroon in de tijd fluctueren. De temporele autocorrelatie functie (ACF) beschrijft deze temporele fluctuaties mathematisch, en hangt af van de optische eigenschappen, de bewegingseigenschappen (bijvoorbeeld random of directioneel) en snelheid. Het speckle patroon kan worden afgebeeld met een camera, waarbij de fluctuaties geïntegreerd worden over de camera sluitertijd. Langzame fluctuaties worden logischerwijs scherper afgebeeld dan snelle fluctuaties, en de scherpte wordt gekwantificeerd als speckle contrast *K*. De mathematische relatie tussen *K* en de ACF is afgeleid in Hoofdstuk 2, met als belangrijke parameter de karakteristieke tijdsconstante de 'decorrelatietijd' τ_c, waarbij τ_c en stroomsnelheid *V* omgekeerd evenredig zijn. De technieken die speckles spatieel afbeelden om een maat voor bloedstroming te vinden vallen onder laser speckle flowmetry technieken. De eenvoudigheid van apparatuur en algoritme, en de gevoeligheid voor een grote range aan stroomsnelheden geven deze techniek veel voordelen als niet-invasieve klinische microcirculatie monitor.

Het nadeel van laser speckle flowmetry technieken is dat de precieze relatie tussen contrast *K* (of τ_c) en bloedstroomsnelheid niet *in vivo* ('in het lichaam') gekwantificeerd is. In **Hoofdstuk 3** combineren we daarom SDF microscopie met laser speckle contrast imaging (LSCI), waarmee zowel de bloedstroomsnelheden (SDF) als de decorrelatie tijden (LSCI) kunnen worden bepaald van dezelfde vaten. In dit

hoofdstuk staat validatie van de geïntegreerde SDF-LSCI techniek centraal. De resultaten laten zien dat *K* betrouwbaar kan worden berekend uit de speckle beelden en dat τ_c nauwkeurig kan worden bepaald door een model te passen aan *K*-waarden bij meerdere sluitertijden. Met optisch weefsel simulerend fantoommateriaal met ingebouwde vloeistof kanaaltjes kan τ_c als functie van *V* systematisch worden geanalyseerd, wat de lineaire relatie tussen $1/\tau_c$ en *V* bevestigde. Vervolgens onderzoeken we de relatie tussen $1/\tau_c$ en *V* voor de microcirculatie onder de tong. De belangrijkste conclusie uit dit eerste *in vivo* experiment is dat τ_c die wordt gemeten voor een vat in het focusvlak sterk afhangt van (onbekende) dynamische verstrooiingen in het weefsel buiten het vat (bijvoorbeeld spierbewegingen of uit-focus bloedvaten). Deze 'offset' decorrelaties kunnen worden gekwantificeerd met *K*-waarden gemeten voor weefsel regio's naast het bloedvat. De offset-gecorrigeerde τ_c waarden *in vivo* geven het verwachte omgekeerd evenredig verband met bloedstroomsnelheid *V*, terwijl de ongecorrigeerde waarden dit verband minder toonden. Dit hoofdstuk presenteert een eerste *in vivo* kwantificatie voor het meten van bloedstroom snelheden met de SDF-LSCI techniek.

A

De autocorrelatie functie is essentieel voor het nauwkeurig bepalen van τ_c (en *V*) uit de *K*-waarden en in **Hoofdstuk 4** gaan we dieper in op het modelleren van de ACF, en de relatie tussen τ_c en *V*. Theorieën op het gebied van dynamische lichtverstrooiingstechnieken voorspellen dat de ACF afhangt van de optische eigenschappen van de stromende verstrooiers: eigenschappen die we kunnen variëren door gebruik te maken van oplossingen van polystyreen bolletjes met verschillende groottes en volume-percentages, en de fantoom opstelling uit Hoofdstuk 3. In specifieke termen: de ACF hangt af van de verstrooiingsfasefunctie (grootte) en meervoudige verstrooiing (volume percentage) en beïnvloedt de relatie tussen $1/\tau_c$. en *V*, beschreven in de parameter α: $1/\tau_c = \alpha V$. De theoretische voorspelling en experimentele uitkomst voor α in het fantoomexperiment komen overeen binnen de randvoorwaarden die worden gehaald in de microcirculatie *in vivo*. Door middel van de theoretische verstrooiingsfasefunctie van rode bloedcellen en het inschatten van het aantal verstrooiingen met stromende rode bloedcellen binnen een bloedvat kan α *in vivo* worden voorspeld. De theoretische en experimentele α in de microcirculatie komen perfect overeen, waardoor *V* nu gekwantificeerd kan worden uit de gemeten τ_c. Samenvattend, de correctie voor offset-decorrelatie (Hoofdstuk 3) en het schalen voor meervoudige verstrooiing (Hoofdstuk 4) leiden tot de kwantitatieve afbeelding van bloedstroomsnelheid in de microcirculatie met de SDF-LSCI techniek. Omdat ook de vat morfologie uit de beelden gehaald kan worden, kunnen de klinisch relevante parameters debiet (volumestroom) en perfusie (volumestroom per weefselvolume) gekwantificeerd worden. De hoofdstukken 2 - 4 vertegenwoordigen theoretische en experimentele inzichten die de potentie voor laser speckle flowmetry technieken als kwantitatitieve klinische microcirculatie monitor onderbouwen.

De microcirculatie levert ook voedingsstoffen en zuurstof aan ongewenste tumorweefsels, en tumoren kunnen via speciale signaalmoleculen de lokale microcirculatie stimuleren om snelle tumorgroei te faciliteren. Het afbeelden van de toename van lokale microcirculatie is niet specifiek genoeg om (kleine) tumoren te detecteren, maar de tumormicrocirculatie kan wel worden gebruikt om medicijnen en andere stoffen aan de tumor te leveren. Daarom richt het tweede deel van dit proefschrift zich op de toepassing van speciale lichtgevende nanodeeltjes die het optische contrast tussen tumor en gezond weefsel kunnen verhogen, waardoor de detectie van (kleine) tumoren verbeterd kan worden. De lichtgevende eigenschappen zoals beschreven in **Hoofdstuk 5** zijn het resultaat van een *upconversion* proces, waarbij licht

van lage energie (lange golflengte, excitatie licht) wordt geabsorbeerd en licht van hoge energie (korte golflengte, emmissie licht) wordt uitgezonden via opeenvolgende energie-uitwisselingen tussen *rare earth ions* in een anorganisch nanokristal, de zogenoemde *upconversion nanoparticles* (UCNPs). Omdat geen enkel (bekend) biologisch molecuul in staat is tot upconversion kan het gewenste optische signaal volledig spectraal gescheiden worden van achtergrond-signaal (zoals autofluorescentie), en omdat upconversion een relatief langzaam proces is (sub-milliseconde) kan het excitatie licht volledig temporeel worden gescheiden van het gewenste upconversion signaal. Beide processen leiden tot de detectie van UCNPs in biologisch weefsel met hoge signaal-ruisverhouding en dus een hoog optisch contrast. Daarnaast valt de excitatie golflengte in het nabij-infrarood dat dieper in het weefsel reikt dan zichtbare golflengtes, en met minder verstrooiing. Deze unieke optische eigenschappen maken UCNPs uitermate geschikt voor biomedische afbeeldingstoepassingen.

Een belangrijke parameter die het contrast van UCNPs in weefsel bepaalt is het rendement van het upconversion proces, dat helaas typisch laag is voor UCNPs (~ 1%). Bovendien heeft het rendement een lineaire relatie met de intensiteit van het excitatie licht: minder excitatie licht levert minder rendement en daarmee veel minder emissie signaal op, vooral in diepe weefsellagen waar de lichtintensiteit afneemt. In **Hoofdstuk 6** evalueren we daarom de optische eigenschappen van UCNPs in de context van biologische weefsels om de optimale toepassingsgebieden voor UCNPs te identificeren. We meten het rendement en het emissie spectrum bij verschillende excitatie intensiteiten met een experimentele opstelling voor UCNP-poeder (*ensemble*) en met een gekwantificeerde optische microscoop voor enkele (*single*) UCNPs. De resultaten laten zien dat de optische eigenschappen van single en ensemble UCNPs gelijk zijn, geven feedback op de kwaliteit van de UCNP-synthese en zijn essentieel voor het modelleren van UCNP-detectie in biologische weefsels. De hoge signaal-ruisverhouding in combinatie met een sterk afnemend signaal bij toenemende diepte van weefsel impliceren dat UCNPs ideaal zijn voor toepassingsgebieden waar de detectie van lage concentraties essentieel is terwijl de diepte van minder belang is. We bevestigen dit experimenteel door één enkele UCNP te detecteren onder een dun laagje (250 micrometer) gehemolyseerd bloed. Met de optisiche eigenschappen van de huid, UCNPs en het detectiesysteem kunnen we het detecteren van één enkele UCNP in de huid theoretisch modelleren, waaruit blijkt dat het contrast van een enkele UCNP veel hoger is in vergelijking met een conventioneel fluorescerend molecuul. De maximale detectie diepte van één enkele UCNP in dit model is ongeveer 0.4 millimeter, wat een klinisch relevante detectie diepte is bijvoorbeeld voor het visualiseren van tumor marges tijdens operaties. Daarnaast kan het detecteren van zeer lage concentraties UCNPs van klinische waarde zijn voor toepassingen in biologische vloeistoffen (bloed, urine), weefsel coupes en weefsel oppervlakten.

De klinische toepassing van UCNPs voor het detecteren van beginnende tumormassa's of tumor marges gedurende operaties wordt verder onderzocht in **Hoofdstuk 7.** Na de synthese zijn UCNPs nog niet geschikt om *in vivo* gebruikt te worden, vanwege het hydrofobe oppervlak dat niet compatibel is met de hydrofiele biologische omgeving. De UCNPs worden daarom verder biochemisch geprepareerd met een mantel van amfifilische polymeren waardoor het oppervlak hydrofiel wordt en moleculaire ankers beschikbaar zijn voor verdere functionalisatie. De eigenschappen van het UCNP-oppervlak spelen een belangrijke rol bij de interactie tussen de nanodeeltjes en cellen. Door speciale eiwitten aan het oppervlak van de UCNPs te bevestigen (functionalisatie) kan worden bereikt dat de concentratie van UCNPs hoger

is bij de ongewenste tumorcellen dan bij gezond weefsel, zodat de tumor kan worden gevisualiseerd met een hoog optisch contrast. Deze eiwitten zijn vaak antilichamen - in Hoofdstuk 7 zijn dit mini-antilichamen die herkend worden door receptoren die overmatig geproduceerd worden door borstkankercellen (Her2/neu receptor, Sk-BR-3 cellen). Het toevoegen van deze gefunctionaliseerde UCNPs aan *in vitro* ('in glas/in het lab') gekweekte tumorcellen en controle cellen (die deze receptor niet overmatig produceren) resulteerde in 10 keer zoveel UCNPs bij de tumorcellen in vergelijking tot de controle cellen. Om de optische detectie van de doelgerichte specifieke levering van UCNPs aan tumorcellen *in vivo* te evalueren hebben we de UCNP-tumorcellen bedekt met dunne laagjes optisch borstweefselsimulerend fantoommateriaal en microscopisch afgebeeld. In dit experiment konden we de cellen tot 1.6 millimeters fantoomdikte nog detecteren. Een optisch model gebaseerd op deze resultaten voorspelt een theoretische detectie diepte in borstweefsel van 4 millimeter voor kleine tumoren ($<< 1$ mm^3). Gerichte levering van UCNPs is dus veelbelovend voor het vroeg ontdekken van beginnende tumoren, waardoor eerder met behandeling kan worden begonnen.

Er is uiteraard nog veel onderzoek nodig voordat UCNPs simpelweg in de bloedbaan geïnjecteerd kunnen worden en met optische technieken de kleinste tumoren gedetecteerd kunnen worden. In **Hoofdstuk 8** zijn de eerste stappen gemaakt om *in vivo* levering van UCNPs te onderzoeken in een kippenembryo experiment. Ook studies naar de toxiciteit van de UCNPs op cellen staan beschreven in dit hoofdstuk. Vooralsnog blijft kanker een complexe, vaak ongeneeslijke ziekte, onder andere vanwege de diversiteit aan verschillende types tumoren, maar ook variatie gedurende de groei van een tumor. Omdat de tumorgroei nauw verbonden is met de faciliterende microcirculatie kan het monitoren van de microcirculatie informatie opleveren over de tumorstructuur. De combinatie van optische technieken zodat zowel de bloedstroming als de levering van nanodeeltjes gedetecteerd kan worden in tumorweefsel (**Hoofdstuk 9**) kan constructief zijn bij onderzoek naar de interactie tussen tumorcellen, tumorgroei en -metastasen en eventuele veranderingen gedurende therapie.

A

THESIS SUMMARY

Optical techniques offer great potential for applications in healthcare: they can be non-invasive, light is non-ionising, the optical instruments are generally cheap and portable, and optical interactions provide both structural and physiological information on biological tissue. The disadvantages of optical techniques are the limited penetration depth in tissue and deterioration of image contrast by optical scattering. The part of the circulation where arteries and arterioles branch into capillaries (microcirculation) is partially located just below the tissue surface. Therefore, we can probe this part of the circulation, where the exchange of oxygen and nutrients with cells takes place, with optical techniques. A dysfunctional microcirculation can damage tissues and ultimately lead to death, for example in the case of septic shock. Many other diseases are the cause, mediator or result of a dysfunctional microcirculation. Thus, microcirculation monitoring can aid diagnostics, give feedback during therapy or provide information on physiological processes. An optical technique that reliably visualizes the functional status of microcirculation has extensive clinical relevance.

Sidestream dark field (SDF) microscopy is a hand-held video microscope technique that directly visualizes the sublingual microcirculation, using the principle that green light is more strongly absorbed by blood than the surrounding tissue. The images show red blood cells as dark globules flowing through light-grey tissue, from which the vessel density, vessel geometry and flow velocity (up to 2 mm/s) can be quantified. **Chapter 2** introduces a group of techniques that visualize blood flow based on another principle: dynamic light scattering. Coherent laser light (same wavelength and phase) back scattered by tissue has travelled a large number of different paths through tissue resulting in a large number of different phases when arriving at the detector, which causes a random interference pattern ('speckles'). When there is movement in the tissue (e.g. blood flow) the interference pattern will fluctuate in time. The temporal fluctuations can be described by the temporal autocorrelation function (ACF), which depends on the optical properties, the movement type (random, directional) and velocity. When the speckles are imaged by a camera, the fluctuations will be integrated over the finite exposure time. Fast fluctuations logically appear more 'blurred' than slow fluctuations, where the blurring is quantified by the speckle contrast K. The mathematical relationship between K and the ACF is described in Chapter 2, introducing the important parameter τ_c as the characteristic time constant of the fluctuations. Flow velocity V and τ_c are inversely related. Techniques that spatially image speckles to measure blood dynamics are known as laser speckle flowmetry techniques. The simplicity of the hardware and algorithm as well as the sensitivity to a wide flow velocity range represent advantages of these techniques as non-invasive clinical microcirculation monitors.

The disadvantage of laser speckle flowmetry techniques is the absence of a quantitative relationship between contrast K (or τ_c) and flow velocity *in vivo*. In **Chapter 3** we therefore combine SDF microscopy and laser speckle contrast imaging (LSCI) to derive both blood flow velocities (SDF) and decorrelation times (LSCI) of the same vessels. The aim of this chapter is the validation of the integrated SDF-LSCI technique. The results show that K can reliably be calculated from the speckle images and that τ_c can be accurately estimated by fitting a model to K-values obtained at a range of exposure times. We designed an optical tissue-simulating phantom with flow channels to systematically assess τ_c as a function of V, which confirmed the linear relationship between $1/\tau_c$ and V. We subsequently investigated the relationship between $1/\tau_c$

and V for the sublingual microcirculation. The important conclusion drawn from this first *in vivo* experiment is that τ_c measured for a vessel in the focal plane depends on (unknown) additional dynamic scattering events that happen outside the vessel (e.g. muscle movements or out-of-focus vessels). This 'offset' decorrelation can be quantified using K-values measured for adjacent tissue regions. The offset-corrected *in vivo* τ_c values show an improved inverse relationship with V as compared to the uncorrected values. This chapter presents a first *in vivo* quantification for measuring blood flow velocities using SDF-LSCI.

The temporal autocorrelation function is crucial to accurately estimate τ_c (and V) from K-values. In **Chapter 4** we further investigate on modelling of the ACF and the relationship between τ_c and V. Dynamic light scattering theoretical frameworks predict that the ACF depends on the optical properties of the dynamic scatterers: properties that can be varied by changing the size and volume fraction of polystyrene sphere solutions flowing through the phantom channel. More specifically, the ACF depends on the scattering phase function (scatterer size) and multiple scattering (scatterer volume fraction) and influences the relationship between τ_c and V, described by the parameter α: $1/\tau_c = \alpha V$. The measurement of α in the phantom experiment resembles the theoretical prediction within certain conditions that are met in the microcirculation. Through modelling of the scattering phase function of red blood cells and estimation of the number of scattering events within a blood vessel α *in vivo* was predicted and matched perfectly with the experimental α found for microcirculatory vessels. This study provides the quantitative link between *in vivo* measured τ_c and V. In summary, correction for offset-decorrelation (Chapter 3) and rescaling for multiple scattering (Chapter 4) result in quantitative imaging of microcirculatory blood flow velocities using SDF-LSCI. Since vessel morphology can be derived from the images, the clinically relevant parameters blood flow and tissue perfusion can also be quantified. Chapters 2 through 4 represent the theoretical and experimental insights that demonstrate the potential for laser speckle flowmetry techniques to become quantitative clinical microcirculation imagers.

The microcirculation can also deliver nutrients and oxygen to unwanted tumour tissues, and tumours can trigger local growth of vessels to facilitate rapid tumour growth. Imaging the increase of local microcirculation lacks the specificity required to detect (small) tumours, however, the tumour microcirculation can be utilized to deliver drugs and other materials to the tumour. The second part of this thesis is therefore devoted to study luminescent nanoparticles that can enhance the optical contrast between tumour and normal tissue, which improves the detection ability of (small) tumour lesions. The luminescence as described in **Chapter 5** is the result of the upconversion process, where low energy light (long wavelength, excitation light) is absorbed and high energy light (short wavelength, emission light) is emitted after subsequent energy transfers between rare earth ions doped in an inorganic nanocrystal; upconversion nanoparticles (UCNPs). Since no known biological molecule is capable of upconversion, the upconversion signal can be spectrally separated from the background signal (e.g. autofluorescence) and the long lifetime of upconversion (~ milliseconds) enables temporal separation of the excitation light from the emitted light. These properties enable background-free detection of UCNPs in biological tissue with a high signal-to-noise ratio and excellent optical contrast. Additionally, the excitation wavelength in the near infrared can penetrate deeper into tissue compared with visible light, and with reduced scattering. These unique optical properties make UCNPs highly feasible for biomedical applications.

However, the optical contrast of UCNPs in tissue is primarily determined by the conversion efficiency of the upconversion process, which is typical only ~1% for UCNPs. In addition, the conversion efficiency linearly decreases with excitation intensity, resulting in a large reduction of emitted signal in deeper tissue layers where the excitation light is attenuated. In **Chapter 6** we critically evaluate the unique optical properties of UCNPs in the context of biological tissues to identify application niches for UCNPs. We obtain the conversion efficiency and spectral properties versus the excitation intensity with an experimental set-up for ensemble measurements, and a quantified optical microscope system for single particle measurements. The results show that the optical properties of single and ensemble UCNPs are similar, provide feedback on the synthesis quality, and are essential for modelling UCNP detection in biological tissue. In view of the high signal-to-noise ratio, but reduced signal with increasing imaging depth in tissue, potential applications include areas that require the detection of small amounts of particles in the (semi)ballistic regime. We experimentally confirm this by imaging a single UCNP through a 250-micrometer layer of haemolysed blood. We theoretically model the optical contrast of a single UCNP in skin using the optical properties of skin, UCNPs and the imaging system, which showed a superior UCNP-contrast as compared to a conventional fluorescent molecule. The maximal single-UCNP detection depth is estimated at 0.4 mm, which is clinically relevant for example to visualize tumour margins intra-operatively. Furthermore, the detection of small amounts of nanoparticles is clinically relevant for applications assessing biological liquids (blood, urine), thick tissue slices or subsurface tissues.

The clinical application of UCNPs to detect small tumour masses or tumour margins intra-operatively is further investigated in **Chapter 7**. As-synthesized UCNPs however, have hydrophobic surfaces that are not compatible with the hydrophilic *in vivo* environment. Therefore, the UCNPs are further prepared by coating them with amphiphilic polymers resulting in hydrophilic surfaces with functional groups. The UCNP surface properties are crucial for the interaction of the nanoparticles with cells. Functionalizing the UCNP surface with "tumour recognizing" proteins (antibodies) aims to induce a higher concentration of UCNPs in the tumour compared with normal tissue, resulting in a high tumour-to-normal tissue optical contrast. In Chapter 7 the UCNPs are functionalized with mini-antibodies that target a receptor that is over-expressed on breast cancer cells (Her2/neu receptor, SK-BR-3 cells). After *in vitro* incubation (and washing) of the functionalized UCNPs with tumour cells, the UCNP signal was 10 times higher compared to the control cells (that do not over-express the receptor) incubated with UCNPs. To evaluate the detection of UCNP-labelled breast cancer cells *in vivo*, we covered the cells with optical breast tissue simulating phantom layers. Microscopic imaging of the UCNP signal was feasible through up to 1.6 mm of phantom material. An optical model built on these results predicts a theoretical detection depth of up to 4 mm for a (small, $< 1 mm^3$) cancer lesion in breast tissue. Therefore, targeted delivery of UCNPs holds promise for the early detection of small tumours and an earlier onset of therapy.

Ample research is clearly still needed before UCNPs can simply be injected in the bloodstream and their distribution reveals the location of small tumours using optical techniques. In **Chapter 8** we continue towards *in vivo* scenarios by the delivery of UCNPs to small tumour lesions in chick embryos, in addition to the study on the toxicity of UCNPs to human cells. To date, cancer is often incurable and remains a complex disease, further complicated by the diversity between different tumour types but also between different tumour development stages. Since tumour development is highly associated with blood vessel

growth, monitoring tumour microcirculation can provide insight into the tumour structure. Combining optical techniques that enable the detection of both blood flow and nanoparticle delivery in tumour tissues (**Chapter 9**) can be constructive for research into the interaction between tumour cells, tumour growth and metastasis, as well as the tumour response to therapy.

List of Publications

(Partly) Included in thesis:

- **A. Nadort**, R. G. Woolthuis, T. G. van Leeuwen, and D. J. Faber, "Quantitative laser speckle flowmetry of the *in vivo* microcirculation using sidestream dark field microscopy," Biomedical optics express **4**, 2347-2361 (2013).
- **A. Nadort**, V. K. Sreenivasan, Z. Song, E. A. Grebenik, A. V. Nechaev, V. A. Semchishen, V. Y. Panchenko, and A. V. Zvyagin, "Quantitative imaging of single upconversion nanoparticles in biological tissue," PLoS One **8**, e63292 (2013).
- **A. Nadort**, K. Kalkman, T. G. van Leeuwen, and D. J. Faber, "Quantitative blood flow velocity imaging using laser speckle flowmetry" (in submission).
- E. A. Grebenik, **A. Nadort**, A. N. Generalova, A. V. Nechaev, V. K. Sreenivasan, E. V. Khaydukov, V. A. Semchishen, A. P. Popov, V. I. Sokolov, A. S. Akhmanov, V. P. Zubov, D. V. Klinov, V. Y. Panchenko, S. M. Deyev, and A. V. Zvyagin, "Feasibility study of the optical imaging of a breast cancer lesion labeled with upconversion nanoparticle biocomplexes," J. Biomed. Opt. 18, 076004-076004 (2013).
- Z. Song, Y. G. Anissimov, J. Zhao, A. V. Nechaev, **A. Nadort**, D. Jin, T. W. Prow, M. S. Roberts, and A. V. Zvyagin, "Background free imaging of upconversion nanoparticle distribution in human skin," Journal of biomedical optics 18, 061215-061215 (2013).
- A. E. Guller, A. N. Generalova, E.V. Petersen, A.V. Nechaev, I.A. Trusova, N.N. Landyshev, **A. Nadort**, E.A. Grebenik, S.M. Deyev, A.B. Shekhter and A.V. Zvyagin, "Cytotoxicity and non-specific cellular uptake of bare and surface-modified upconversion nanoparticles in human skin cells, " Nano Research (2014).
- K. Liu, J. A. Holz, Y. Ding, X. Liu, Y. Zhang, T. Langping, X. Kong, B. Priem, **A. Nadort**, S. A. G. Lambrechts, M. C. G. Aalders, W. J. Buma, P. D. Y. Liu, and H. Zhang, "Targeted labeling of early-stage tumor spheroid in chorioallantoic membrane model with upconversion nanoparticles," Nanoscale (2015).

Book chapter

- A.V. Zvyagin, Z. Song, **A. Nadort**, V. K. A. Sreenivasan, and S. M. Deyev, "Luminescent Nanomaterials for Molecular-Specific Cellular Imaging," in *Handbook of Nano-Optics and Nanophotonics* (Springer, 2013), pp. 563-596.

Not included in thesis

- A. van der Veen, J. van Dieen, **A. Nadort**, B. Stam, and T. Smit, "Intervertebral disc recovery after dynamic or static loading in vitro: is there a role for the endplate?," J. Biomech. **40**, 2230-2235 (2007).
- R. H. Bremmer, **A. Nadort**, T. G. Van Leeuwen, M. J. Van Gemert, and M. C. Aalders, "Age estimation of blood stains by haemoglobin derivative determination using reflectance spectroscopy," Forensic Sci. Int. **206**, 166-171 (2011).

A

Contribution to publications

- **A. Nadort**, R. G. Woolthuis, T. G. van Leeuwen, and D. J. Faber, "Quantitative laser speckle flowmetry of the *in vivo* microcirculation using sidestream dark field microscopy," Biomedical optics express **4**, 2347-2361 (2013)
  Design and realization of all experiments, performing the experiments, supervising R.G.Woolthuis, data analysis, paper writing

- **A. Nadort**, V. K. Sreenivasan, Z. Song, E. A. Grebenik, A. V. Nechaev, V. A. Semchishen, V. Y. Panchenko, and A. V. Zvyagin, "Quantitative imaging of single upconversion nanoparticles in biological tissue," PLoS One **8**, e63292 (2013).
  Design and realization of all experiments, performing the experiments, data analysis, paper writing

- **A. Nadort**, K. Kalkman, T. G. van Leeuwen, and D. J. Faber, "Quantitative blood flow velocity imaging using laser speckle flowmetry" (in submission).
  Design and realization of all experiments, performing part of the experiments, supervising K. Kalkman, data analysis, paper writing

- E. A. Grebenik, **A. Nadort**, A. N. Generalova, A. V. Nechaev, V. K. Sreenivasan, E. V. Khaydukov, V. A. Semchishen, A. P. Popov, V. I. Sokolov, A. S. Akhmanov, V. P. Zubov, D. V. Klinov, V. Y. Panchenko, S. M. Deyev, and A. V. Zvyagin, "Feasibility study of the optical imaging of a breast cancer lesion labeled with upconversion nanoparticle biocomplexes," J. Biomed. Opt. 18, 076004-076004 (2013).
  Design and realization of optical imaging and UCNP characterization and optical phantom experiments, performing these experiments, data analysis, paper writing. A. Nadort has not been involved in UCNP biofunctionalization and cell labelling experiments.

- Z. Song, Y. G. Anissimov, J. Zhao, A. V. Nechaev, **A. Nadort**, D. Jin, T. W. Prow, M. S. Roberts, and A. V. Zvyagin, "Background free imaging of upconversion nanoparticle distribution in human skin," Journal of biomedical optics 18, 061215-061215 (2013)
  Design of quantitative imaging experiment and experimental quantification of microscope parameters.

- A. E. Guller, A. N. Generalova, E.V. Petersen, A.V. Nechaev, I.A. Trusova, N.N. Landyshev, **A. Nadort**, E.A. Grebenik, S.M. Deyev, A.B. Shekhter and A.V. Zvyagin, "Cytotoxicity and non-specific cellular uptake of bare and surface-modified upconversion nanoparticles in human skin cells, " Nano Research (2014).
  Design and realization of quantitative imaging experiment, performing UCNP optical characterization and cellular uptake imaging experiment and confocal imaging, including data analysis and paper writing (relevant parts)

- K. Liu, J. A. Holz, Y. Ding, X. Liu, Y. Zhang, T. Langping, X. Kong, B. Priem, **A. Nadort**, S. A. G. Lambrechts, M. C. G. Aalders, W. J. Buma, P. D. Y. Liu, and H. Zhang, "Targeted labeling of early-stage tumor spheroid in chorioallantoic membrane model with upconversion nanoparticles," Nanoscale (2015).
  Part of design, realization and performance of chick embryo CAM tumour model and intravital imaging system

Portfolio

Name PhD student:	Annemarie Nadort
PhD period:	February 2011 - February 2015
Name PhD principal supervisors:	prof. dr. A.G.J.M. van Leeuwen (University of Amsterdam, AMC)
	prof. E. M. Goldys (Macquarie University, MQ)

1. PhD training

General courses		
» BROK ('Basiscursus Regelgeving Klinisch Onderzoek') and Good Clinical Practice certificate, AMC	2012	0.9 ECTS
» Research skills in physics, PHYS802, MQ	2012	4.0 ECTS
» Scientific writing retreat, MQ	2013	0.5 ECTS
Department seminars & colloquia	2011 - 2015	6.0 ECTS
International conferences		
Poster presentations		
» Gordon Research Conferences (GRC) Lasers in Medicine and Biology, Holderness, USA	2012	1.5 ECTS
Oral presentations		
» European Conferences on Biomedical Optics, ECBO, Munich, Germany	2011	1.5 ECTS
» SPIE Photonics West, San Francisco, USA	2011	1.5 ECTS
» Conference on Optics Atoms and Laser Applications KOALA, Melbourne, Australia	2011	1.5 ECTS
» MQ BioFocus Research Conference, Wisemans Ferry, Australia	2011	1.5 ECTS
» International Conference on Nanoscience and Nanotechnology, ICONN, Perth, Australia	2012	1.5 ECTS
» Australian and New Zealand Conference on Optics and Photonics, ANZCOP, 2013, Perth, Australia	2013	1.5 ECTS
» SPIE Photonics West, San Francisco, USA	2014	1.5 ECTS
» Australian Institute of Physics conference, AIP, Canberra, Australia	2014	1.5 ECTS

2. Teaching

Supervising

» Rutger Woolthuis (TU Delft, Master student) Laser speckle flowmetry Biomedical Engineering & Physics, AMC	2011	1.0 ECTS
» Koen Kalkman (TU Delft, Master student) Laser speckle flowmetry Biomedical Engineering & Physics, AMC	2013	1.0 ECTS
» Emma Baars (VU Amsterdam, Master student) Quantitative spectroscopy Biomedical Engineering & Physics, AMC	2013	2.0 ECTS

Lab demonstrations, Tutoring

» First year physics students, MQ	2014

3. Parameters of esteem

Grants

» Gerbrand de Jong Fund fund for PhD students in the field of medicine	2011 and 2014
» Prins Bernhard Culture fund fund for high potential young academic researchers	2011
» Macquarie University Research Excellence Scholarship	2011

Awards and Prizes

» Student Presentation Award, Biofocus Research Conference	2011
» Outstanding Poster Award, GRC Lasers in Medicine and Biology	2012
» Faculty of Science and Engineering Award for Excellence in Sessional Teaching (MQ)	2014

A

Curriculum Vitae

Annemarie Nadort (1983) was born in Zaanstad and raised in Wormer in The Netherlands. In 2001 she graduated from the Sint Michaël College in Zaandam. In 2004 she completed a Bachelor of Science degree at the VU University in Amsterdam and in 2008 she completed a Master of Science degree in Medical Physics (VU University) and a Master of Science degree in Forensic Sciences (University of Amsterdam), both with distinction. Her undergraduate traineeship was completed in the area of biomechanics (VU University hospital) and her graduate traineeships in the areas of experimental audiology (VU University hospital), biophotonics (Academic Medical Centre, Amsterdam), biometrics (Netherlands Forensics Institute) and forensic sciences (NSW Police Force, Australia). In 2009 she started a job in research and development at Microvision Medical Inc., in collaboration with the department of Biomedical Engineering and Physics of the Academic Medical Center, both in Amsterdam. In 2011 she initiated a joint PhD project at the University of Amsterdam, the Netherlands, and Macquarie University in Sydney, Australia, of which this thesis is the result.

A

MACQUARIE UNIVERSITY

ANIMAL RESEARCH AUTHORITY (ARA)

AEC Reference No.: 2013/007

Date of Expiry: 31 March 2014

Full Approval Duration:*1 April 2013 to 31 March 2014 (12 Months)*

This ARA remains in force until the Date of Expiry (unless suspended, cancelled or surrendered) **and will only be renewed upon receipt of a satisfactory Progress Report before expiry (see Approval email for submission details).**

Principal Investigator:
Dr Andrei Zvyagin
Physics and Astronomy
Macquarie University, NSW 2109
andrei.zvyagin@mq.edu.au
0451 925 116

Associate Investigators:

Mark Connor	0413 202 762
Annemarie Nadort	0405 036 690
Ekaterina Ivukina	0498 035 883

In case of emergency, please contact:
the Principal Investigator / Associate Investigator named above
Animal Welfare Officer - 9850 7758 / 0439 497 383,

A

The above-named are authorised by MACQUARIE UNIVERSITY ANIMAL ETHICS COMMITTEE to conduct the following research:

Title of the project: **High-sensitivity targeted imaging of tumours on the chick embryo chorio-allantoic membrane**

Purpose: **4 - Research: Human or Animal Biology**

Aims: **1. To assess methods to detect tumours, based on labeling tumours with luminescent nanoparticle-antibody complexes that adhere to the tumour;**
2. To graft small tumours on the chick embryo chorio-allantoic membrane
3. To develop nanoparticles that can attach to tumours and also have therapeutic effects

Surgical Procedures category: 3 - Minor Conscious Intervention

All procedures must be performed as per the AEC-approved protocol, unless stated otherwise by the AEC and/or AWO.

Maximum numbers approved (for the Full Approval Duration):

Species	Strain	Age/Sex/Weight	Total	Supplier/Source
13	" "	Day 11-17	100	Country Cacklers
		TOTAL	100	

Location of research:

Location	*Full street address*
MQ	Macquarie University, Building E7B, PC1 lab 109, NSW 2109
ASAM	Level 1, F10A, 2 Technology Place, Macquarie University, NSW 2109

Amendments approved by the AEC since initial approval: N/A
Conditions of Approval: N/A

Being animal research carried out in accordance with the Code of Practice for a recognised research purpose and in connection with animals (other than exempt animals) that have been obtained from the holder of an animal suppliers licence.

Dr Karolyn White (Deputy Chair, Animal Ethics Committee)

Approval Date: 14 March 2013

A

ACKNOWLEDGMENTS

At this stage of thesis writing, everything is hard. My fingers are sticky from the never-cleaned keyboard, my eyes are wondering if they'll ever see the sky again, and my bum and chair have become fused together like a cluster of nanoparticles (Chapter 6). Therefore, it's time to thank you all.

First of all, congratulations for arriving here, although research has shown that the majority of readers actually start here. Good on ya[§]. Although I feel this is going to be a relatively long acknowledgement compared to thesis standards, if you are not in here, or not enough to your liking, please don't take it personal. It might be that I really love you in real life, but that you haven't contributed much to the actual contents of this thesis or my 'professional' life. Still friends?

As a Joint-PhD candidate, I have many supervisors. The very first one that was added to the team was Dirk, back in the day when we were in a swept-source project. Though we haven't done much sweeping, it has been the source of some interesting science. Dirk, you must have been fed up with me (let's not pretend we were not fed up with each other at times). Mistakes (whatevs[§] 200 or 300 micrometer diameter, same difference) that ruin data analysis (but give rise to better ones), my impatience that maybe sometimes shined through in between the lines, chaotic, tangled VI's, and all of this on the background of a long distance relationship (professional of course) and a Skype icon. Thank *someone* we are rational physicists, even though I'm a woman. We never cried. I really, really appreciate your supervision. *Genau*.

Andrei, having you as a supervisor has been interesting and fruitful in many ways. My thesis experience has turned multicultural due to Dutch, Russian and Australian influences, all of which I'm very grateful for. I feel we have built a strong relationship over the years. I highly appreciate your support, valuable scientific feedback, helpful supervision though always letting me do my own thing, and continuous stream of research ideas. I'm grateful for working together a little while longer so that we can get some useful data out of these chick embryos...

Ewa, as director of the BioFocus group at the MQ Photonics Research Centre you have been the facilitator of my biophotonics project in Australia. I want to thank you for your constructive feedback during meetings and your inspiring ideas for new research projects, in addition to your success in keeping our research lines noticed in Australia and beyond.

Ton, you have been a stable factor as department head and later supervisor since I arrived as a Master student (see next paragraph) at the AMC. You can combine excellent scientific thinking with pragmatic managing skills and turn dramas into no dramas[§]. You and Dirk have given this thesis a thorough theoretical basis that wouldn't have been possible without you and the time you dedicated to our meetings.

Maurice, you had me at 'hello' at our first encounter in the AMC basement when we discussed my Master research project on blood stain age back in 2007. I have great memories of those days and the fact

§ Australian slang: Good on ya : goed gedaan!
Whatevs : whatever : wat maakt 't uit
No dramas, no worries, too easy: kun je áltijd zeggen

that I discovered that scattering (no... really?) needed to be included in the analysis has given me insights for life. It was the start of an endless relationship with the department. Thank you for being part of my PhD degree as well, welcoming me into the CAM project and giving me the necessary critique at times, although our scientific collaborations have been surpassed by our musical collaborations. On that note, Martin van Gemert, also from you I have fond memories of the duality of our light scattering theories and guitar-saxophone duets.

Keshen & Jean-Marc, thank you for inviting me into the Microvision Medical team. To be able to work on scientific research that is so close to clinical applications has inspired me throughout my PhD project. It also amazes me how much research is actually needed before there is a working clinical device, so thumbs up for your achievements. Thank you for giving me the time and freedom to do this research and ongoing support till the end. Hopefully there are future collaborations waiting for us. Eva and Zahid, it's great to have met you and I have always enjoyed working with you. When can I come for lunch again?

Rutger & Koen & Emma, speckle and spectroscopy students, thank you heaps§ for opting for a research project in microcirculation imaging. I have enjoyed working with you, to see your devotion to your research projects and want to thank you once again for contributing to this thesis. I wish you all a great career!

To the committees for the Dutch PhD defence and the Australian thesis examination: thank you so much for your time and effort to read these ~70.000 words. I feel honoured to receive feedback from true experts in the various fields of this thesis.

Kim & Mitra, my paranimphjes, I am so lucky to have you by my side. We are all generally the same height and will make a perfect picture. We will get through this together, Mitra will tackle the bolletjes questions and Kim will give legal advice throughout. She'll be right§. Thank you for superb organizing skills and for the inspiration for the stellingen that just didn't make it:

Carien, thanks for taking the pictures!

I have had so many great colleagues throughout the years and throughout the world, it makes me a lucky person. The order here makes no sense, I'm just typing whatever comes up in my head. Katya darling, you have been the person I have most intensely collaborated with in the research sense, and I mean *intense*. For people who have not noticed the logarithmic and densely spaced time points in figure 8.2: this doesn't happen between 9 and 5. Thank you for being a friend and knowledgeable biochemist. Let's meet in Moscow soon! Olivia, it's great to know you're keeping the fire burning in the chick incubator. Good luck with your PhD project, I'm happy you joined the team and looking forward to work with you the next months. Barb, the way you have multiple babies and

§ Australian slang: Heaps : Emma's favo ozzy woord: veel
She'll be right: het komt wel goed

do your PhD project is amazing. It is always a pleasure hanging out with the Wellmanns, from WA via Canberra to the eventful Macquarie Park: let's stay in contact and hang out in Berlin in the future. Varun, Vazzoes, Vazza you have been a long-lasting colleague slash friend at MQ and turning more and more into a surf dude. I highly appreciate working with you both in the lab and outside. Tristan, I can rely on you for many things, both professionally and inappropriately. Besides horse riding, you can English very good. Thank you so much for feedback on many parts of this thesis (but not all, if there are mistakes do not blame Tristan). Claire, Jana and Graham, as native Australian, Canadian and British proofreaders I have all my accents covered. Thanks! Ondra, walking past your desk many times a day has always been a pleasure. Thanks for being there.

Anna, you are the newest addition to our little OBIS group but we already had many interesting discussions and even a published paper. I feel there is more to come! Good luck during your project. Zhen, as a previous OBIS member thanks for showing me around at MQ and in the lab, and doing research together. Nice to have you back in Sydney! Krystyna (you have a great 50x objective), Ayad, Martin, Wei, Sandhya, David, Michael and the whole Biofocus crew: thank you for your feedback over the years on Friday afternoons. Jin's team, Lu, Tim, Lixhin, Jay and of course Jin, thanks for your collaboration in the past, current and future. Michael thank you for bringing the party to my 30th birthday party. Wan, you're the best nanoruby ball miller I know. Chris, congrats to us both for submitting our thesis. Maria, your spider's silk must have great optical properties, keep feeding them the good stuff. To all students in E7B-148/165: cheers!!

Rob, Aaron, Jipeng, Peter, Thanh-Phong, Andy, Andrew, Carlo: thanks for your collegiality, the smiles, the stories, the lunches. Douglas, BJ, Josh: us coasties know what living is. Peeps over in the HearingHub: it's not the same after the separation. Miss you Simon, Alex, Marty, Graham, Ali, Nick, Iza...

Ludmila, Maider, Iza, Nora, Bar, Katya, Stacey a.k.a. the great OSA OptChicas soccer team, I enjoyed our hot training sessions, and excellent tournament appearance. Dennis & Paul, thanks for teaching us schwalben up to perfection.

David Coutts and Judith Dawes, thank you for being approachable and supportive department heads, Rich Mildren, Dave Spence for your excellent HDR management, Gabriel for the chats and (not) finding DAQ cards, James Downes for letting me teach. Carol, Lisa, Laura, Liz: cheers to the admin group, as well as Gina and Sue for looking after the labs. I will get a bit more general: thank you great people at Physics & Astronomy!

Let's not forget Joe the hatchery manager for unlimited supply of fertile eggs. And to keep in the Joe section: Joe from the Faculty store for never-failing service. Thanks to the MQ METS workshop for indispensable hardware support.

Ik swop voor de gelegenheid even naar het Nederlands, want we zijn aangekomen bij de BEPH afdeling!! Waar zal ik beginnen... Mn meest trouwe kamergenoot: Marcel van Herk, wij waren toch de (in)stabiele factors van L0-159, het lijkt me terecht dat we nu allebei deze kamer verlaten. Succes met je nieuwe

baan aan de University of Manchester. Mn trouwste BEPH buddy Nienke, volgens mij begon ik als master student, nam jij het over als promovendus, kwam ik weer terug als IOP-partner en vervolgens ook promovendus terwijl jij intussen het postdocstokje in handen hebt. Het was fantastisch. Dank je voor vriendschap in de wetenschap, het verheffen van conferenties tot ware werkgerelateerde ecstasies, maar ook de mooie parawetenschappelijke momenten. Wij weten wat het is om in het Oosten te wonen, waar de no worries§ nog overheersen. Van Nienke naar de overige laserbabes: Bar (van VU partners naar AMC partners, leuk dat je langskwam down under!), Lida (altijd heerlijk positief en relaxed, dank voor de leuke post naar Daley Avenue), Merel (wij waren samen master student en nu beide dok(c)to(e)r! Vanaf het moment dat we op zoek waren naar cyanide wist ik dat er een ware anesthesist in je schuilde): zonder jullie zou ik er zelf, maar ook mijn beph-herinneringen, een stuk minder leuk uit zien! Allemaal succes in onze carrières, let's stay in touch!

Martijn, Rolf & Roy: ik heb jullie bro-code nooit begrepen... maar ik denk vaak aan jullie. Hoop dat we kunnen proosten op 1 april. Alle Jeroenen, jullie zijn toppers, jij ook Jeroen. Corianne, het is alweer lang geleden maar we waren productieve kamergenoten! Judith, het was altijd leuk om tussen de experimenten door even over muziek te praten, succes met BUN! Angela, dank voor je vele in-1-keer-raak bloedprik momenten, maar ook het organiseren van het labuitje met jou en Nienke was too easy§.

De mensen van de overkant: Nicolas, volgens mij zijn we ongeveer gelijk klaar? Veel succes met de volgende stappen! Ronni, waar jij komt schijnt de zon en passen er meer woorden in de lucht. Succes met je opleiding! Frank, op de een of andere manier herinner ik me vooral de opening van het Amsterdam LaserLab met jou?? Vitali, in principle you are a funny man. Maybe see you April 1st? Duc, thanks for teaching me Vietnamese, 1 April *tram phan tram?* Naza, Froukje, Cristina, Monique, Janina, Nadia, Lorena: The other side of the hall way is a happy place thanks to you. Jetty, dank voor je steun tijdens allerlei fondsaanvragen en dingen die via formulieren gaan. Martin, dank voor je verkoeling bij oververhitte laptops. Jos & Maria, jullie zijn een leuk stel. Iwan, zonder jou was AVA er niet. Erik, het was leuk om over bloed & nanodeeltjes in de hersenen te praten. Ed, dank voor de bruggen tussen vasculair en photonics, en ook de leuke gesprekken tijdens uitjes en lunches.

Dan even naar de kelder, het was altijd spannend (maar toch ook fijn) om daar te komen: Edwin, gaan we nog even schaatsen zo? Kai, thanks for our short but great collaboration (and Bram!). Jasmin, the chicks have brought us close together, I hope you will finish soon too and good luck in Boston. Annemieke, hoe gaat het met de biggetjes? Saskia, dank voor je bruikbare feedback tijdens meetings en leuke gesprekken daarbuiten. Richelle, met jou lunchen of autorijden is echt gezellig, wie weet lukt het paardrijden ook nog eens! Gerda, van de Ponteneur naar het NFI en AMC: gek dat we elkaar dan in Australië net hebben gemist :(Alan, thanks for getting the scientists in the row boats!

Jelmer, het was leuk om samen van student naar loonlijst te gaan, doe de groeten aan de VU! Paul, dank voor je hulp bij de speckle opstelling, maar ook als koffie-baken in de gang. Abel en de 'nieuwe' generatie promovendi, als ik niet zo blij zou zijn dat ik dit nu kan typen zou ik jaloers zijn! Enjoy :) Alle andere lieve Biomedical Engineering & PHysics-ers: het was leuk met jullie!

§ Australian slang: No dramas, no worries, too easy: kun je áltijd zeggen

Noortje, het was fijn om af en toe op het Voetenplein relativerende koffie te drinken met je! Veel succes met de zware laatste loodjes.

The Shakin Babies: wat kan ik zeggen, na al die jaren nog super strak. Eeuwige dank!

Tim Casey, you really know how to make red blood cells glow. Thanks for your excellent work in Paint 1.0. I owe you a coldie.

Zusjes Els & Marlies, jullie omringen mij in leeftijd en in expertise: het is zo lekker om tussen een wiskundige en een dokter-to-be in een proefschrift in biomedical optics te schrijven. Leuk dat je ook een halve BEPHer bent Els :) En Marlies, dank voor de reflectie en afleiding buiten werktijd. Pete, Ross & Jim: thanks for being supportive in-laws, I promise I will stop studying now...

Alle andere vrienden en familie: dank voor jullie interesse (en medelijden...)!
All other friends and family: thank you for your interest (and support to Ben...)!

Pap & mam, vanaf het plaatjes uitknippen voor werkstukken op de basisschool tot het solderen van LEDjes voor de opstelling op pagina 77, jullie hebben altijd voor me klaar gestaan tijdens mijn vele studies. Dank voor jullie onvoorwaardelijke steun en betrokkenheid, en het vertrouwen dat het wel goed komt met me aan die andere kant van de wereld. Kom nog maar vaak langs!

Ben, thanks for building our house while I was busy doing science. You're a keeper.

Lastly and the most important: I would like to thank my red blood cells. The majority of this thesis would not have been written without them, I dare to say I wouldn't even be here without them. They have always assisted in the validation of laser speckle contrast ideas and they were there to cover up upconversion nanoparticles to show their detectability through blood. Always flawless, looking like perfect pancake-donuts, rolling and gliding, flowing and slipping through my vessels, coming out when I gently asked them and punctured my finger. Red blood cells I love you. And, for the record, you should love yours too. We all should acknowledge our red blood cells right now. Here's to everybodies red blood cells!

Get a dog up ya[§].

Annie.

§ Australian slang: Get a dog up ya: an instruction to take your alcoholic beverage and drink it